Cross Section Measurements for the Nucleosynthesis of Heavy Nuclei and Type Ia Supernovae

Tsimba Nsangu

Doctor of Philosophy

University of York

Physics

July 2014

Abstract

In this work, two rather different experiments with their respective analysis have been described. The first experiment concerned the ^{20}Ne(d,p)^{21}Ne transfer reaction and the second the ^{12}C+^{12}C fusion reaction.

An experiment of ^{20}Ne(d,p)^{21}Ne transfer reaction was performed in Munich, Germany using the Quadrupole Dipole Dipole Dipole (Q3D) magnetic spectrograph. This experiment has aimed at the investigation of spectroscopic information around the Gamow window of the ^{17}O(α,γ)^{21}Ne located between E_x = 7.65-8.05 MeV. The stated experiment was performed using an ^{21}Ne implanted target on carbon and covered the excitation energies varying from 6.9 MeV to 8.5 MeV. Sixteen states were identified, three of which, the 8.328(6) MeV, 6.977(17) MeV and 6.960(2) MeV have first been observed in this work. Within the Gamow window however, only one state, the 7.955(2) MeV by correspondence to the 7.9603(10) Mev as recorded in literature, has been identified. Out the sixteen states, this work made eleven firm assignments and two "tentative" assignments.

The ^{12}C+^{12}C fusion reaction was performed at TRIUMF, Canada using TUDA, the TRIUMF UK Detector Array. The experiment covered the centre of mass located between 3.4 to 4.02 MeV. The aim of this work was the determination of the cross section, which would help, at theses energies, reduce uncertainties observed in present data sets. Analysis such ADCs and TDCs calibrations, different cuts selection necessary for particle identification are presented.

Contents

List of Figures

List of Tables

Acknowledgments

The list here would certainly be endless.. For a start however, the author would like to thank God for, well, everything really.

I would start by thanking my supervisor Dr. Alison Laird for her support and guidance throughout the course of my Ph.D. I must have been, well one of those supervisee (there am I always knocking on your door and disturbing your meetings..Sorry for that!). A really big thank you.

I would also like to thank various York academics, past and present who have helped in a way or another during my time here. So thanks very much to Christian Aa Diget with input and useful dicussion when struggling with interpretations, to Brian Fulton who has helped proofread a part of my thesis, to Mike Bentley for his attentive attitude, to Edward Simpsons who helped starting running the DWBA software, to Paul Davies for help using ROOT at the start of my PhD, to Gemma Wilson with the occasional advice with the TWOFNR code. I would particularly also like to thank Benjamin Kay whose expertise has provided direct vital input in data analysis methodology.

Thanks as well to physicists from other facilities. Thank you to Anuj Parikh who had taken the time to explain the process of acquisition of the Munich data and to Nicolas de Séréville for taking time to help with the somehow complicated French visas process in regard to the experiment.

I would, furthermore like to thank various other members of the Nuclear Physics Group, past and present, such Philip Adsley for proofreading my thesis and whose in parallel (d,t) analysis, helped give insight into my own analysis. Oh my.., proofreading my freshly written attempt at the English language, poor you! I mean I think everyone gets the picture by reading this certainly almost French written acknowledgment.

Thank you to other students, that is Ed, Jess, Jos, Nuray, Adelle and Victoria for allowing me to endlessly go on about everything that goes through my head. You know there were a time where I used to be quiet. I know, it sounds like a myth but it is true! Thanks to everyone else within the group who has helped in any way.. Simply because I have not put that in does mean it is forgotten.

Thanks to people from my church who have without realising helped in many ways, thanks to my dear friends Eline and Anthony..

Now, I would like to come down on thanking different members of my family. Everyone here has helped in a way or another but a beyond thank to my Mum Felicité for her constant prayers and advice! Thousand of thanks Mum. Thanks very much as well to my uncle "Papa Jp" as we say and my aunt "Maman Godé" for helping with those horrendous fees. Thanks to all my siblings Bénédicte, Christelle, Hervé and Aurelie for always have been a great support. Really feel blessed to be part of such a close family!

Finally, to the person with whom I shared this passion for "the stars..", to you Dad, Mason Nsangu Ngimbi, who I miss so much....

Declaration

I, Tsimba Nsangu, declare that this thesis is a presentation of original work and I am the sole author. This work has not previously been presented for an award at this, or any other, University. All sources are acknowledged as References.

The following publication, by the author, contains part of work included in this thesis

- C.T.Nsangu *et al.*, Journal of Physics: Conference Series 665 (2016) 012026, ^{20}Ne(d,p)^{21}Ne Transfer Reaction in relation to the s-process abundances.

CHAPTER 1

Introduction

> Surely there is something in the unruffled calm of nature that overawes our little anxieties and doubts: the sight of the deep-blue sky, and the clustering stars above seem to impart a quiet to the mind.
>
> Jonathan Edwards

1.1 Nuclear Astrophysics

A significant and important question that has been of great interest for mankind is the explanation of the origin and constitution of the building blocks that constitute the matter around us, and the very nature of what lies far beyond the horizon. This curiosity has led mankind to multiple discoveries and scientific advancement. Looking on the largest scale, it has resulted, over millennia, in astronomy which later on has led to astrophysics. Astrophysics applies physical laws to the laboratory of space and can therefore be seen as a branch of astronomy which looks into space's physical properties. Looking on the smaller scale, it has led to the study of protons and neutrons which are the two fundamental building blocks of nuclear material. These two very different areas of science evolved over time with no obvious connection.

The fact that nucleosynthesis had a connection to cosmology was an insight of Robert Oppenheimer but this was just an unproven speculation, since the first paper on stellar

nucleosynthesis appeared in 1946, two years before, the well-established cosmological model was published [1]. Investigations over the years have shown that as humans we are all connected to distant space and time through a common heritage that are the chemical elements that make up our bodies [2]. The search to understand how nuclear processes influence astrophysical phenomena has indeed been driving experimental and theoretical research. The field known as nuclear astrophysics was born. One of the main and basic goals of nuclear astrophysics is to understand energy generation in stars and explain how chemical elements are synthesised in stellar events.

Today, half a century has passed since the foundation of nuclear astrophysics and this field has now reached maturity [3]. Nuclear astrophysics is today a multidisciplinary subject combining nuclear physics with astrophysics, observational astronomy and cosmochemistry.

In this thesis, two very different nuclear experimental investigations using stable beams for two very different astrophysical purposes are performed. One involves reducing the uncertainties in the cross section of a fusion reaction which plays a role into narrowing the present uncertainties into star evolution. The other encompasses the extraction of further spectroscopic information using a transfer reaction which plays a role into the abundances in nucleosynthesis of elements.

The remainder of this chapter will focus on giving a brief description of the relevant Nuclear Astrophysics background. The thesis afterwards is somehow divided into two parts, the first of which focuses on the the ^{20}Ne(d,p)^{21}Ne transfer reaction and the second of which focuses on ^{12}C+^{12}C fusion reaction. Therefore, chapter 2 outlines the theory of thermonuclear reaction and transfer reaction. Chapter 3 describes the astrophysical purposes and relevance of present work regarding the ^{20}Ne(d,p)^{21}Ne transfer reaction. Chapter 4 describes the experimental set up and procedure of the ^{20}Ne(d,p)^{21}Ne reaction. Chapter 5, data analysis of the same reaction and chapter 6, the results and interpretation. The chapter afterwards starts with the ^{12}C+^{12}C and outlines the astrophysical purposes and relevance of present work. Chapter 8 describes the ^{12}C+^{12}C experimental set up. Chapter 9 and chapter 10, the data analysis and preliminary results linked to the same reaction. Chapter 11 will finally finish by giving a general summary and proposals for further work.

Following is however the continuation of the present chapter with the nucleosynthesis of elements as the next section.

1.2 Nucleosynthesis of Chemical Elements

1.2.1 Nucleosynthesis of Elements below the iron peak

The big bang nucleosynthesis model was proposed by Gamow, Alpher, Herman and collaborators in the 1940s in order to explain the origin of chemical elements [4, 5]. This process however only explains well the abundance of lighter elements such ^{2}H, ^{3}He, ^{4}He and ^{7}Li. In order to explain the current abundances, it was suggested by Hoyle in 1946 that all heavy elements are synthesized in stars through thermonuclear reactions [6].

The minimum mass required to form a star is 0.08 $M_{\odot}$ [3]. Once a temperature of around 10^{6} K is reached, protostars start by fusing deuterium. Stars will thereafter reach the equilibrium configuration where gravitational force is balanced by thermal (internal) pressure. When the central temperature reaches approximatively T$\sim 10^{7}$ K, thermonuclear reactions are induced and become the star's main source of energy.

The first hydrostatic burning stage to take place is hydrogen burning which converts the hydrogen into an alpha particle by transforming four protons into helium through the proton-proton chain (pp-chain) and the CNO cycle. This stage which characterised stars as being in the Main Sequence, is by far the longest in the life of a given star. One of the straightforward consequences of hydrogen burning is the enrichment of the core of the star in helium.

When hydrogen is exhausted, if the temperature of $T \sim 10^{8}$K is reached in the core, helium burning occurs. This process converts the helium into carbon through the triple α process. During this stage, a certain quantity of oxygen is also produced through alpha capture on the carbon. If the core is massive enough, the next process referred as carbon burning converts the carbon into neon, sodium and magnesium. There is then a very short phase of neon burning which converts neon into magnesium. Thereafter, there is oxygen burning where an oxygen nuclei fuses with another oxygen. The main reactions produce sulphur, phosphorus, silicon, magnesium. Lastly, there is the silicon burning where the silicon can not fuse with itself due to the high Coulomb barrier. This process which operates at temperature above 10^{9} K witnesses the photodisintegration of silicon nuclei which then allow the gradual conversion by successive alpha capture of silicon to sulphur, argon and other elements up to iron. Figure 1.1 shows the solar relative abundances that has been normalised to silicon atoms 10^{6}.

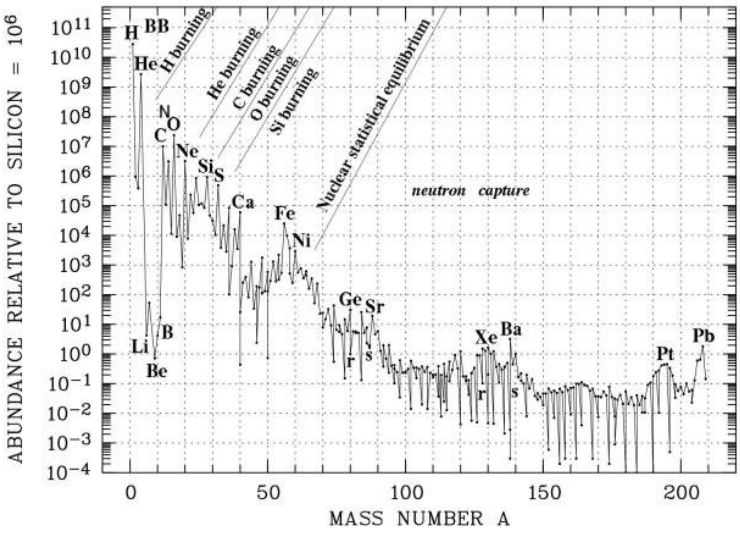

Figure 1.1: *Relative solar abundances of elements. Number abundances are normalized to the number of silicon atoms. This figure pictures nucleosynthesis of elements with corresponding burning stages. Adapted from [7].*

1.2.2 Nucleosynthesis of elements beyond the iron peak

Beyond iron, alpha capture ceases due to the high Coulomb barrier. Heavier nuclei are formed by exposing lighter seed nuclei to a source of neutrons, such that neutron capture reactions can be initiated [3]. Neutron capture followed by β-decay is responsible for the nucleosynthesis of most of the elements heavier than iron. Neutron capture can either operate at slow rates (s-process) or at high rates (r-process). The s-process operates from the seed of ^{56}Fe up to ^{209}Bi and follows the line of stability. While certain nuclei are accessible to both the s-process and the r-process paths, there are 27 trans-iron elements which are purely processed by r-process. Elements such as thorium, uranium and plutonium are effectively known to be the very proof of the occurrence of this process [8] which is located along the neutron dripline.

The third mechanisms thought to be responsible for the production of the neutron-deficient isotopes that lie on the proton-rich side of the valley of stability is referred to as the p-process [9].

The s-process

Neutron capture is said to be slow when the β-decay timescale is much shorter that the time between two successive neutron captures. This leads the s-process path to be located along the line of β stability. The s-process can occur at any stage of the stars life depending on the neutron availability. Although it is thought to mainly occur in

Asymptotic Giant Branch (AGB) and Thermally Pulsing Asymptotic Giant Branch [1], it has also been observed in red giants[1] with the detection in the outer layers of the star of elements such as technetium[2] [10].

As previously stated, the *s*-process operates with iron as seed and proceeds in zigzag fashion through most stable isotopes, terminating at ^{209}Bi because there are no stable nuclei above $A = 209$ through which the process could continue [11].

The *s*-process abundances depend on the magnitude of the neutron-capture cross sections and the total neutron availability and thus exposure. Nuclide with very small cross sections will lead to an increase in abundance while those with higher cross sections will very quickly be destroyed and therefore lead to a much lower abundance. Adding to this list of *s*-process abundance possible impacting factors are isotopes with either high abundance or high neutron cross section which can both capture a large amount of free neutrons, reducing thereby the amount of neutrons available for the *s*-process. A nuclide is said to be a neutron source when it adds neutrons allowing the *s*-process to occur. A neutron poison removes neutrons available for the $s-$process affecting therefore negatively the abundance of this process. While a neutron absorber only temporarily removes the neutron, meaning after the neutrons are absorbed, they are recycled later on through another mechanism making them again available for the *s*-process.

The solar system *s*-process abundance indicates the existence of three distinct constituents of the *s*-process [3]. The first is the weak *s*-process which operates in the helium core or carbon burning shell of massive star and is responsible for the production of nuclei with A$\leq$ 90. The ^{22}Ne(α,n)^{25}Mg is thought to be at the origin of the production of most of the neutrons. This process is thought to be a secondary process because, ^{22}Ne the main neutron source and the seeds which happen to be mainly iron, have a secondary origin [12]. ^{22}Ne comes indeed from the initial C, N and O and is produced via the ^{14}N(α,γ)^{18}F($\beta^{+}\nu$)^{18}O(α,γ)^{22}Ne reaction. However during helium burning, the neutron poison are of secondary origin through ^{25}Mg and primary origin through mainly ^{16}O. ^{25}Mg acts as neutron poison through ^{25}Mg(n,γ)^{26}Mg and ^{16}O through ^{16}O(n,γ)^{17}O [13]. During carbon burning, the neutron inhibitors are thought to only be primary elements, mainly ^{20}Ne and ^{24}Mg [12].

The second component is the main *s*-process which operates mainly in helium shell flashes in low mass Thermally Pulsing Asymptotic Giant Branch (TP-AGB)[3] stars and is

[1]Red Giant, AGB, TP AGB stars are well explained in the next section

[2]Short half life of 4.2 millions years in comparison to the average age of billions of year of the star, indeed suggests its recent formation

[3]Defined in the next section

responsible for the production of nuclei with $90 \geq A \geq 205$. In this case the ^{13}C(α,n)^{16}O reaction which uses ^{13}C present in the CNO cycle represents the predominant neutron source. However the ^{22}Ne(α,n)^{25}Mg neutron source is also marginally activated during a thermal pulse, altering sensitively certain abundance ratios of nuclei which are part of the *s*-process paths.

The third component is the strong *s*-process which is thought to operate in low mass, low metallicity[4] TP-AGB stars. The strong *s*-process is thought to have ^{13}C as the main neutron source through the ^{13}C(α,n)^{16}O reaction [3]. ^{16}O can at times act as neutron poison through the ^{16}O(n,γ)^{17}O reaction.

There is also a non-standard *s*-process that occurs in very low metallicity massive rotating stars [12] where the standard weak *s*-process in massive stars is less efficient and where the contribution from the carbon shell becomes very small. Indeed, contrary to the fact that at solar metallicity the main effect of rotation on the *s*-process production is the expansion of the convective helium core due to additional mixing and therefore a behaviour like non-rotating more massive stars; at low metallicity, the repercussion of rotation is more important. The outward part of core helium burning, carbon and oxygen are mixed into hydrogen rich regions leading to a strong production of nitrogen, part of which may enter the convective helium core and be transformed into primary ^{22}Ne by α-captures. Consequently, by comparison to the non-rotating models, the ^{22}Ne availability in the helium-core is strongly improved [14].

Iron seeds and in general elements lighter than strontium allows the nucleosynthesis of isotopes beyond the mass region between strontium and barium depending on the neutron exposure [15]. Theoretical models predict high abundance of ^{16}O layers in low-metallicity stars [3].Given the lack of ^{25}Mg, ^{16}O becomes the most dominant neutron absorber via the ^{16}O(n,γ)^{17}O reaction.

Finally, it is important to underline that not every star goes through every single processes. Whether or not a star reaches heavy burning stages is strongly dependent on the initial mass of the star. A short description of stellar evolution for stars of different masses is now given.

[4] Also said to be metal-poor or early generation

1.3 Stellar Evolution

1.3.1 Evolution of Low Mass and Intermediate Mass star

A gas cloud must be compact enough for the attractive force due to gravity to counterbalance the dispersive effects of the internal pressure and begin the process of condensation into a cluster of stars [16]. Gas cloud contracts to form a protostar. When the protostar reaches a mass of at least 0.08 $M_\odot$, the energy released by the gravitational energy increases and is converted into enough thermal energy to slow down the collapse and approaches hydrostatic equilibrium. The first thermonuclear reaction is induced. When hydrogen is exhausted in the core, stars with masses $M \lesssim 0.4\ M_\odot$ do not reach the required temperature of $T\sim 10^8$ K to fuse helium into carbon. These extremely low mass stars end up as a stable He white dwarf.

For low and intermediate stars of masses $0.4\ M_\odot \lesssim M \lesssim 4M_\odot$, after the exhaustion of hydrogen in the core, hydrogen burning continues in the shell via CNO cycle. The core then contracts and the hydrogen shell becomes hotter leading the star to expand dramatically and being classified as a *red giant*. The envelope becomes convective and grows in size. The first dredge-up occurs which bring to surface matter that have previously experienced CNO cycle. This leads the temperature to rise in the core. When the temperature reaches $T\sim 10^8$ K, helium burning starts leading the star to be classified to be in the *horizontal branch of the HR diagram*. After the exhaustion of the helium in the core, the core contracts again and leads the star to be classified as being in the *Asymptotic Giant Branch (AGB)* . AGB stars suffer from strong mass loss due to the wind caused by thermal pulse. Thermal pulses are explosion caused by the sudden energy released due to the ignition produced by the instability in the helium shell above the degenerate carbon/oxygen core. This instability which results in periodic increase of temperature in helium shell is indeed due to the fact that for most of the time, latent hydrogen shell located the helium shell is the main nuclear energy source.

This wind removes the AGB star's envelope and leaves the degenerate core. The star therefore ends up as a long-lived carbon/oxygen cooling white dwarf.

In stars with higher mass $4M_\odot \lesssim M \lesssim 8M_\odot$, when the AGB star stage is reached, the process of helium burning continues in the shell and the star undergoes a second dredge-up. From this stage, the evolution becomes rather complicated. The He-burning shell becomes thermally unstable and undergoes periodic thermal pulses. Such stars are the ones referred as TP-AGB stars. One of the salient properties of a TP-AGB star is

that the periodic thermal pulses alternating with mixing episodes give rise to a unique nucleosynthesis of in particular ^{12}C, ^{14}N, and elements heavier than iron [17]. Since the surface abundance in ^{12}C increases after every dredge-ups, AGB stars can turn into a carbon star with a number ratio of C/O>1 given that they can undergo up to seven dredge ups.

The mechanisms of the wind which drives material off the surface of AGB stars are not yet completely understood. It is clear however that stars with higher mass suffer stronger mass loss. It is also known that the duration of a given TP-AGB star, the loss of the hydrogen rich shell and the growing mass of its CO core, limit the number of thermal pulses that a given star can undergo. If the mass loss is weak, the CO core may reach the *Chandrasekhar mass* ($M_{Ch} \approx 1.4 M_{\odot}$) which leads to carbon being ignited in the centre of the core. However if the mass loss is strong, the CO core does not reach the Chandrasekhar mass and end up as CO white dwarf.

1.3.2 Evolution of Massive stars: Mass $M \gtrsim 10M_{\odot}$

Every star with mass $M \gtrsim 10M_{\odot}$ will reach high enough temperatures to ignite the carbon. It will therefore pass the carbon burning stage up to the silicon burning stage. During each process, burning operates in the core of the star and remnants of previous stages occupy the outer shells located right beneath the remnant of the previous stage. This will result with the star presenting several layers of different composition separated by thin nuclear burning shells surrounding a core mainly composed of iron. Figure 1.2 is a graphical representation of the different layers composition after the silicon burning.

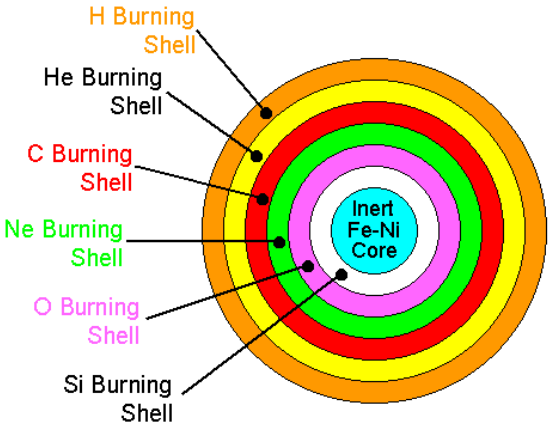

Figure 1.2: *Graphical Representation of different layers composition after silicon burning. Adapted from [18].*

At this stage, the core has no further source of nuclear energy at its disposal. The core acquires mass as a consequence of nuclear burning in the overlying shells. When the core mass reaches the Chandrasekhar mass, the electron degeneracy pressure is unable to counteract gravity [3]. The core then collapses very rapidly under gravity and results in a supernova explosion. The supernova explosion then leaves a black hole or a neutron star. Carbon burning is also thought to occur in binary stars, leading into our consideration of the description of those stellar binary systems.

1.4 Binary Systems

Up to 50% of stars in the Galaxy are part of binary systems. Close binary stellar systems are made of two stars orbiting around each other and significantly influencing each others' evolution. There is a concept referred to as the *inner Lagrangian point* which exists between two massive bodies of a close binary system and is defined as where the gravitational pull of each body cancels each other out. Due to centrifugal forces involved, this point becomes a pair of extended equipotential surfaces referred to as the *Roche lobe*. The Roche lobe of a given star may get filled when the stars evolves off the main sequence and becomes a red giant because the star expands [19]. Material is then free to flow from that star through the inner Lagrangian point onto its companion. Binary systems may be formed of different kinds of progenitors. Figure 1.3 shows an illustration of a binary system where the Lagrangian point and Roche Lobe can be seen.

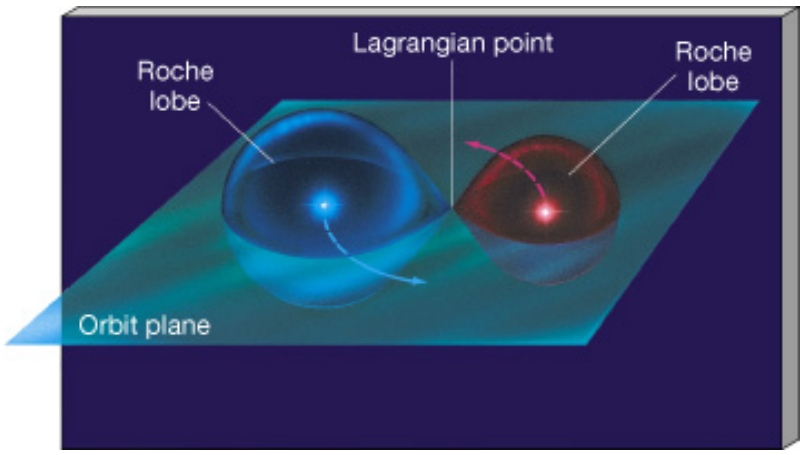

Figure 1.3: *Graphical Representation of a binary system where each star can be seen as surrounded by the Roche Lobe which meet at the Lagrangian point. Taken from ref.[20].*

1.4.1 Type Ia-Supernovae

Type 1a Supernovae are the brightest explosions in the modern universe and are used as *"standard candles"* for cosmological distance determination. Indeed, their light curves are somewhat homogeneous and their intrinsic brightness is known. Therefore by measuring their luminosity, it becomes possible to estimate their distance using the inverse square law which stipulates that the brightness of an object is inversely proportional to the distance squared. They have subsequently been used in the quest to outline the geometrical structure of the Universe through calibrated light curve interpretation [21].

One of the current views of type Ia-supernovae is that they result from a binary system in which one of the pair is a carbon-oxygen white dwarf accreting matter from its companion main-sequence or red giant star [19]. The more specific nature of the progenitor though, be it a Chandrasekhar-mass white dwarf, sub-Chandrasekhar mass dwarf, or even two merging white dwarfs, is lacking and is still debated [22]. The essential fact being that when the density at the centre of the CO white dwarf increases, the temperature rises and reaches the range of T =1.8-2.5 GK, which leads carbon to ignite. The ignition of carbon in the degenerate core of a white dwarf close to the Chandrasekhar limit can either result in the propagation of an explosion driving nuclear burning by a shock wave referred to as supersonic wave or an explosion inducing burning by thermal conduction of the degenerate electrons referred to as subsonic wave.

The following figure 1.4 is a graphical representation of type Ia supernovae formation mechanism.

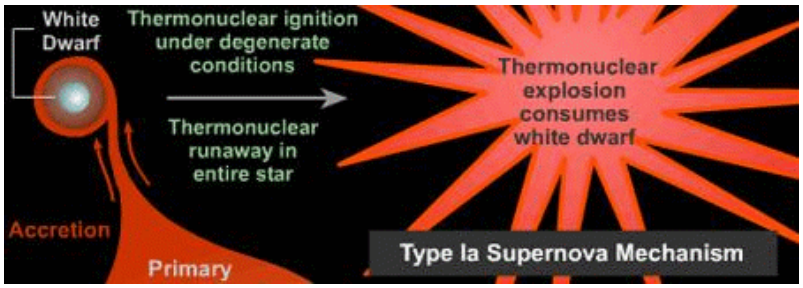

Figure 1.4: *Graphical Illustration of a type Ia supernovae mechanism. Taken from ref. [23].*

1.4.2 X-ray bursts

X-ray bursts result from a close binary system where one of the pair is a main sequence star and the other is a neutron star. They normally arise because hydrogen or helium is accreted onto a neutron star which causes matter to settle on the surface. As a result, the temperatures near the neutron star surface rise and reach 10^7 K and persistent thermal emission occurs at X-ray energies.

1.4.3 Superburst

Superbursts are long, energetic, rare explosions in low mass X-ray bursts. They are indeed similar to X-ray bursts except they last two or three orders of magnitude longer. Superbursts are thought to last too long and have too high an energy to be explained by the burning of hydrogen or helium.

It has therefore been suggested that an unstable burning of carbon at a greater depth could be the origin of the superbursts [24]. This unstable carbon burning would be due to the ash left over from the *rp*-process on the surface of a neutron star. This model is heavily debated and there are presently only few models which attempt to investigate the feasibility of this process.

Thereafter Figure 1.5 is an artistic representation of a neutron stars accreting matter from red giants.

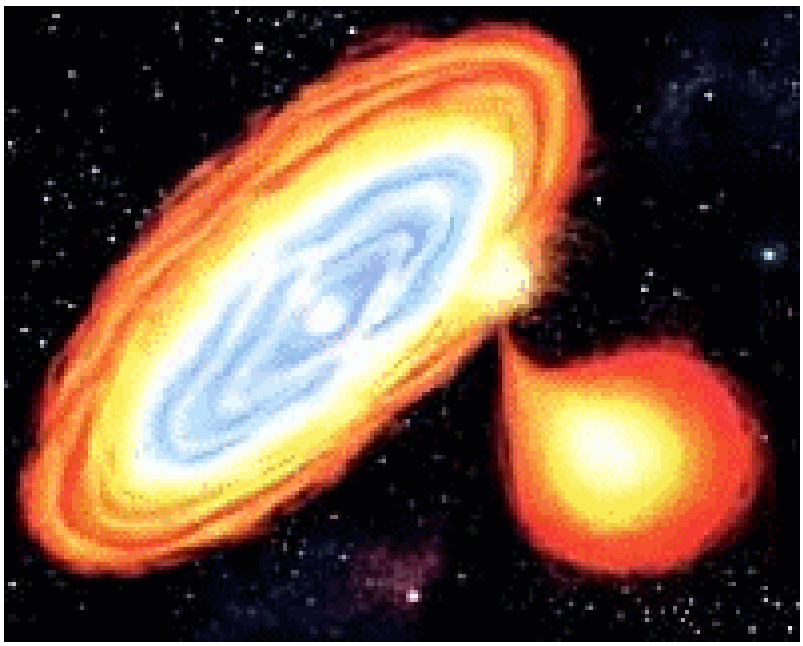

Figure 1.5: *Graphical Illustration of neutron stars accreting matter from red giants. Taken from ref. [25].*

1.5 Shortcomings and Uncertainties

1.5.1 Shortcomings of stellar evolution and uncertainties in Supernovae type Ia and superburst

It can be seen from the star evolution section 1.3 that the crucial mass between the two extremely different evolutionary paths is only approximate(8-10 $M\odot$). The uncertainty in the mass cut off is directly linked to the uncertainty in the rate of the $^{12}C+^{12}C$ reaction which triggers the carbon burning.

Furthermore, different models of type Ia supernovae mechanisms exist [3]. There is still a debate on the validity of a given one. This therefore leads to uncertainties on type Ia supernovae timescales.

The difficulty in type Ia supernovae modeling arises from the uncertainties linked to the degenerate burning of carbon.

Concerning superbursts, although as stated in section 1.4.3 that certain models suggest unstable carbon burning such that the ash is heated up and carbon ignited in the crust of a neutron star. Model with known carbon fusion reaction rates, fails to explain the ignition of carbon since the amount of ^{12}C in the ash does not seem to be sufficient to trigger the superburst [26].

1.5.2 Uncertainties in *s*-Process Abundances

As described in section 1.2.2 on the *s*-process, very low metallicity massive rotating stars are thought to have ^{16}O as the dominant neutron poison. ^{16}O absorbs a neutron via the ^{16}O(n,γ)^{17}O reaction. However neutrons can be made available again for the *s*-process via the ^{17}O(α,n)^{20}Ne reaction depending on the strength of the competing reaction channel ^{17}O(α,γ)^{21}Ne. Neutron recycling is highly dependent on the ratio of $^{17}O(\alpha,n)^{20}Ne$ reaction rate to the $^{17}O(\alpha,\gamma)^{21}$Ne reaction rates. However, despite its importance the ratio of the involved reaction rates is highly uncertain and the fate of ^{16}O as either neutron poison or neutron absorber is yet to be confirmed.

Only two theoretical predictions by Caughlin and Fowler [27] and Descouvemont [28] exist and at low energies (below 1 MeV), they are different by three orders of magnitude. For low metallicity massive rotating stars, the temperature of interest for the *s*-process for the core helium burning is in the region of 0.3 $\times$ 10^9 K which corresponds in the centre of mass to an energy range of 0.3-0.7 MeV. For the carbon shell burning however, temperatures of interest are higher and are located in the region of 0.8-1.3 $\times$ 10^9 K, which corresponds to an energy range of 0.7 to 1.8 MeV in the centre of mass. The ^{17}O(α,n)^{20}Ne reaction has already been measured in the energy range between 0.56 and 10.1 MeV, see for example recent measurements by Best *et al.* in [29]. Furthermore, extrapolations to lower energies are also available through the Nuclear Astrophysics Compilation of Reaction Rates (NACRE compilation) [30]. For the ^{17}O(α,γ)^{21}Ne reaction however, there is a lack of experimental data. Indeed, not until recently were the first two direct measurements of ^{17}O(α,γ)^{21}Ne made by Taggart *et al.*[15] and Best et *al.* [31] in the region covering 0.6-1.6 MeV and 0.75-1.65 MeV respectively.

CHAPTER 2

Theory of Thermonuclear Reactions and One-Nucleon Transfer Reactions

There are different types of nuclear reactions, some are multi-step processes compound reactions and some are characterised by a single-step process and direct reactions. Nuclear reactions indeed take place when two nuclei collide, to generate different products than the initial particles. Direct reactions take place within a very short timescale (order of 10^{-22}s) while compound reactions are observed to take something around 10^{-16}s to 10^{-18}s [11]. This chapter covers the nuclear theory of transfer reactions on focusing on single particle transfer properties alongside thermonuclear nuclear related theory.

2.1 Cross Sections

2.1.1 Differential Cross Sections

The cross section is a quantitative representation of the probability to form reaction products from two colliding particles. The differential cross section, however, is obtained from the probability to observe reaction products particles within a particular direction, here represented as angle (θ,ϕ) with respect to beam axis. The number of outgoing particles going through the solid angle is proportional to the number of beam particles and the areal density of the target and the probability of interaction. The differential cross section can be written as

$$\frac{d\sigma}{d\Omega} = \frac{Y}{I_b \times N_t \times \Delta\Omega}, \tag{2.1}$$

where Y is the yield, I_b is the number of beam particles, N_t is the target number density and $\Delta\Omega$ is the solid angle. The total angle-integrated cross section is determined by integrating $\frac{d\sigma}{d\Omega}$ over all angles

$$\sigma = \int_{\Delta\Omega} \frac{d\sigma}{d\Omega}\, d\Omega \tag{2.2}$$

2.1.2 Cross Sections

The total cross section can then be defined as [3]:

$$\sigma = \frac{\frac{N_R}{t}}{\left[\frac{N_b}{(tA)}\right] N}, \tag{2.3}$$

where $\frac{N_R}{t}$ is the number of interactions per time, $\frac{N_b}{(tA)}$ the number of incident particles per area per time and N the number of target nuclei per area within the beam.

2.2 Thermonuclear Reactions in Stellar Environment

In stellar conditions, thermonuclear reactions occur when two nuclei collide and interact to produce a new nuclear species. In a stellar environment, the only kinetic energy available to nuclei is their thermal motion. Consequently, reactions initiated by this motion are referred as thermonuclear reactions [3]. In stellar environments, a charged particle x interacts with a charged particle y only after overcoming their mutual Coulomb barrier. The Coulomb barrier which represents the electrostatic energy between two nuclei

$$V_c = \frac{Z_x Z_y e^2}{4\pi\varepsilon_0 r}, \tag{2.4}$$

where Z_x and Z_y are respectively the charge of particle x and y, and r the interaction radius which in Fermi can be estimated as

$$R = 1.36(A_x^{\frac{1}{3}} + A_y^{\frac{1}{3}}) + 0.5 \tag{2.5}$$

where A_x and A_y are respectively the mass number of the interacting particle x and y.

In general, as described in Ref.[3], motion within stars is non-relativistic and non-degenerate which implies that nuclei velocities can be characterised by a Maxwell-Boltzmann

distribution. The probability of a nuclear reaction to occur depends on the relative velocities between the reactants. If the velocity distributions of the interacting particles at thermodynamic equilibrium are described by the Maxwell-Boltzmann distributions, then the relative velocities will also be described by the Maxwell-Boltzmann distribution. This implies that the probability that the relative velocity has a value between ν and $\nu + d\nu$ can be given by:

$$P(\nu)d\nu = \left(\frac{\mu}{2\pi kT}\right)^{\frac{3}{2}} \times e^{\frac{-\mu\nu^2}{2KT}} \times 4\pi\nu^2 d\nu, \tag{2.6}$$

where μ is the reduced mass, k is the Boltzmann constant and T is the temperature.

2.2.1 Tunneling through the barrier and Gamow Window

It is important to underline that stars evolve slowly by adjusting their temperature, which implies that typical thermal energies are not high enough to overcome the Coulomb barrier. This could have implied for thermonuclear reactions not to be feasible on a classical point of view. However, this is not the case as particles are able to penetrate the Coulomb barrier through the quantum tunneling effect. This probability of barrier penetration is given as in Ref.[32] by

$$P \approx \exp\left(-2\pi\eta\right) = \exp\left[-\left(\frac{E_G}{E}\right)^{\frac{1}{2}}\right], \tag{2.7}$$

where $2\pi\eta$ is the Sommerfeld parameter defined as the probability of penetrability of the Coulomb barrier, ν the relative velocity and E_G the Gamow energy defined in general by

$$E_G = \left[\frac{(2\mu)^{\frac{1}{2}}\pi e^2 Z_x Z_y}{\hbar}\right]^2 \tag{2.8}$$

where μ is the reduced mass, Z_x and Z_y the charge of the projectile and target.

The Gamow energy, in keV, can be written as

$$E_G = \left(\frac{bkT}{2}\right)^{\frac{2}{3}} = 1.22(Z_x^2 Z_y^2 \mu T_6^2)^{\frac{1}{3}}, \tag{2.9}$$

and the Gamow window, in keV, by

$$\Delta_G = \frac{4}{3^{\frac{1}{2}}}(E_0 kT)^{\frac{1}{2}} = 0.749(Z_x^2 Z_y^2 \mu T_6^5)^{\frac{1}{6}}, \tag{2.10}$$

with T_6 being the the temperature in 10^6 K. The Gamow window can thus be seen as the small energy window, referred to as well as Gamow peak $E = E_G \pm \frac{\Delta_G}{2}$, at which for a

given stellar temperature T, nuclear reaction takes place. Figure 2.1 shows the Maxwell Boltzmann energy distribution alongside the tunneling through the barrier probability and the resulting Gamow peak.

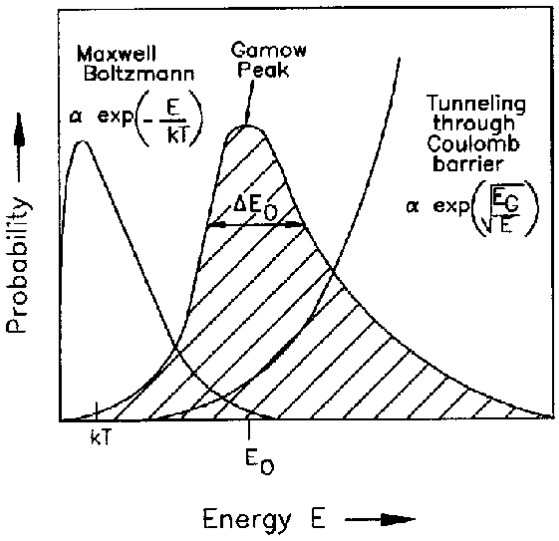

Figure 2.1: *Illustration of the Maxwell Boltzmann energy distribution and the Quantum tunneling. From Ref.[33].*

2.2.2 Reaction Rates and S-factor

The reaction rate is found by combining the relative velocity and the cross section of each interacting particles.

For the reaction rate per particle pair we obtain:

$$< \sigma\nu >= \int_0^\infty \nu P(\nu)\sigma(\nu)d\nu = \int_0^\infty \nu P(E)\sigma(E)dE \tag{2.11}$$

This implies that

$$< \sigma\nu >= \left(\frac{8}{\pi\mu}\right)^{\frac{1}{2}} \frac{1}{(KT)^{\frac{1}{2}}} \int_0^\infty \nu e^{-\frac{E}{KT}} \sigma(E)dE \tag{2.12}$$

The astrophysical S factor $S(E)$, is mainly used in nuclear astrophysics as it removes the Coulomb component from the cross section. The relationship between the S factor and the cross section is then mathematically given by

$$\sigma_{react} = \frac{S\,(E)}{E} \exp\left(-2\pi\eta\right) \tag{2.13}$$

2.3 Compound Nuclear Reactions

The theory of compound nucleus reactions was first developed by Hauser and Feshbach in 1952. The main hypothesis is based on the scenario that an incoming particle reaches a target with a smaller impact parameter compared to the size of the nucleus radius. A compound nucleus can be seen as in intermediate state during which the projectile and the target can go through successive collisions. The projectile and target then stay together long enough to reach statistical equilibrium which allows for example, a single nucleon to receive enough energy to be able to escape the system [11]. A number of different exit channels are possible from compound system. This model therefore suggest that the probability of decay to any channels is independent of the formation process.

Representatively, the reaction can be written as

$$a + X \ \rightarrow \ C^* \ \rightarrow Y + b \tag{2.14}$$

The compound nucleus model works best for lower beam energies where the likehood of the projectile being trapped is higher. Furthermore it also works best for medium and heavy nuclei where the interior is large enough to absorb the beam energy [11].

Each decay channel will have its own decay width [1]. The energy width Γ of the state is defined as the spread in energy of the state and is the product of the decay probability by $\hbar$.

2.3.1 Resonance

In a compound reaction, a resonant reaction is the one where the bombarding energy E is equal to Q + E = E_r with Q representing the Q-value of the reaction. This thereafter leads to the formation of an excited state with energy E_r.

When considering narrow or single resonance, the cross section is given by the Breit-Wigner equation [2]. Thus it can be written as:

$$\sigma_{xy} = g_x(J)\frac{\pi}{k_x^2}(1+\delta_{xy})\frac{\Gamma_x\Gamma_y}{(E-E_r)^2+\left(\frac{\Gamma}{2}\right)^2}, \tag{2.15}$$

where $k_x$is the wave number in the entrance channel, $g_x(J)$ a statistical factor which takes into account the effects of spin and angular momentum and is defined as

$$g_x(J) = \frac{2J+1}{(2j_x+1)(2j_y+1)} \tag{2.16}$$

[1]Decay width are defined as decay rates into a given open channel.

with j_x, j_y and J are the spin numbers in the two reactants and the compound nucleus respectively.

The reaction rates can also be re-written as:

$$< \sigma\nu >= \left(\frac{2\pi}{\mu KT}\right)^{\frac{3}{2}} \hbar^2(\omega\gamma)_R exp\left(-\frac{E_R}{KT}\right) f, \tag{2.17}$$

where μ is the reduced mass, $\omega = g_1(J)(1+\delta_{xy})$, $(\omega\gamma)_R$ is the strength of the resonance[2], $\gamma = \frac{\Gamma_x\Gamma_y}{\Gamma}$ and f the electron screening effects in stars [3] and $\Gamma_x\Gamma_y$ being partials energy widths of the two reactants.

2.4 Transfer Reactions

Direct reaction are reactions where the projectile interacts mostly at the target surface. Transfer reactions are classified as direct reactions in which nuclei separate immediately after making a glancing contact. For the case of direct reactions in general, the projectile can exchange some angular momentum, some energy or transfer nucleons. Furthermore, direct reactions take place near or at the surface and therefore have a large impact parameter. Figure 2.2 shows a graphic representation of one nucleon transfer process.

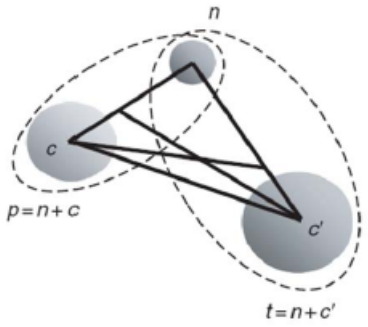

Figure 2.2: *Graphical representation of one nucleon transfer process from [34].*

2.4.1 The Nucleon-Nucleus Interaction

Considering the original many body nucleon nucleus interaction: The Schrödinger equation for the nucleon N-nucleus A (N+A) interaction will be written as [34, 35]:

$$H\left(r_0;r_1,r_2,r_3,...,r_A\right)\psi\left(r_0;r_1,r_2,r_3,...,r_A\right) = E\left(r_0;r_1,r_2,r_3,...,r_A\right), \tag{2.18}$$

[2]Resonance strength is defined as resonance parameters which measure the width ratio $g_x\gamma = g_x(J)\frac{\Gamma_x\Gamma_y}{\Gamma}$ which refers to the integrated cross section.

[3]Meaning atomic electron clouds act as screening potential.

where $H\left(r_0;r_1,r_2,r_3,...,r_A\right)$ represents N+A Hamiltonian, $\psi\left(r_0;r_1,r_2,r_3,...,r_A\right)$ the total N+A wavefunction and E the total energy.

The Hamiltonian can however be split into three distinct part: The first part representing the projectile kinetic energy (T_0), the second part representing the projectile interaction with all nucleons from the target ($\sum_{i=0}^{A} V\left(r_{0i}\right)$) and the third part representing the target internal Hamiltonian H_A. Mathematically therefore the Hamiltonian can be written as:

$$H\left(r_0;r_1,r_2,r_3,...,r_A\right) = T_0 + \sum_{i=0}^{A} V\left(r_{0i}\right) + H_A\left(r_1,r_2,r_3,...,r_A\right), \tag{2.19}$$

The target internal Hamiltonian is straightforward and forms a complete set which can be written as:

$$H_A\left(r_1,r_2,r_3,...,r_A\right)\phi_i\left(r_1,r_2,r_3,...,r_A\right) = \epsilon_i\phi_i\left(r_1,r_2,r_3,...,r_A\right) \tag{2.20}$$

where $\phi_i\left(r_1,r_2,r_3,...,r_A\right)$ and ϵ_i are respectively the target internal wavefunction and energy.

The general solution of the system N+A can be written in term of the target internal solution:

$$\psi\left(r_0;r_1,r_2,r_3,...,r_A\right) = \sum_{ij} \varphi_i\left(r_0\right)\phi_i\left(r_1,r_2,r_3,...,r_A\right), \tag{2.21}$$

where $\varphi_i\left(r_0\right)$ is the projectile wavefunction.

The target is considered to remain in the ground state represented by the wave function "ϕ_0". If the projection operator P which is defined as P= $|\phi_0\rangle\langle\phi_0|$ and which characterised the elastic component of the solution as $P\phi = \epsilon_0\phi_0$ is introduced. Moreover, if the Q operator which takes into account all "non scattering" components and is therefore defined as Q=1-P is also introduced, then the general equation

$$H\left(P+Q\right)\phi = E\left(P+Q\right)\phi \tag{2.22}$$

Which can be rewritten as

$$\left(E-H\right)\left(P+Q\right)\phi = 0 \tag{2.23}$$

By the consideration of properties such $P^2\phi = P\phi$, $Q^2\phi = Q\phi$ and $PQ\phi = QP\phi = 0$ and by multiplying P. It can be written

$$(E - PHP)P\phi = (PHQ)Q\phi \tag{2.24}$$

Thereafter, multiplying by Q, it can be written

$$(E - QHQ)Q\phi = (QHP)P\phi \tag{2.25}$$

This leads $Q\phi$ to be written as

$$Q\phi = \frac{1}{E - QHQ}QHPP\phi \tag{2.26}$$

Therefore expression 2.23 can be written as

$$\left\{E - T_0 - \left\langle \phi_0 | \sum_{i=0}^{A} V\left(r_{0i}\right) | \phi_0 \right\rangle - \left\langle \phi_0 | VQ \frac{1}{E - QHQ} QV | \phi_0 \right\rangle \right\} \epsilon_0 = 0. \tag{2.27}$$

The scattering equation can then also be written as

$$\left(E - T_0 - \nu(r_0)\right) \epsilon_0 = 0 \tag{2.28}$$

With the effective potential $\nu(r_0)$ written as:

$$\nu(r_0) = \left\langle \phi_0 | \sum_{i=0}^{A} V\left(r_{0i}\right) | \phi_0 \right\rangle - \left\langle \phi_0 | VQ \frac{1}{E - QHQ} QV | \phi_0 \right\rangle \tag{2.29}$$

This potential is however generally non-local, this means that, the potential which acts at one position of space may be dependent on the value of the wave function at a different position [35]. This really make it complicated to find a given solution. The eigenvalue equation can be written as

$$\left(E - T_0\right) \epsilon_0 \left(r_0\right) = v_0 \left(r_0\right) \epsilon_0 \left(r_0\right) + \int f \left(r, r_0'\right) \epsilon_0 \left(r_0'\right) dr_0' \tag{2.30}$$

$f\left(r, r_0'\right)$ here represents a function which contains both r_0 and r_0'.

2.4.2 Optical Model

Given the above complications and even though progress concerning a microscopic approach has been made, using a phenomenological approach remains useful. The optical model replaces the microscopic potential by a potential obtained phenomenologically:

$$\left(E - T_0 - U_{OMP}\right) \epsilon_0 = 0, \tag{2.31}$$

where E represents the total energy, T_0 is the projectile kinetic energy and U_{OMP} represents the phenomenological optical potential.

This approach is based on the consideration of the interaction of the projectile with the nucleus as whole, with the nucleus being represented by a potential. The potential parameters are obtained by considering fitting theoretical calculations to experimental scattering data. With the aim of making this approach more physical, the shape of the potential is obtained from general features of the nucleon-nucleon interactions general features and from the matter and charge distribution within the nucleus as described in References [36, 37, 38]. The interaction of the projectile with the nucleus is then described and represented by the use of a complex potential in analogy to the refraction and absorption of a light wave by a medium of complex refractive index. Indeed, the optical potential can therefore be defined as an effective potential based on the description of two interacting particles. The main idea behind being the fact that a given projectile on a target nucleus can either be elastically scattered or undergo a reaction.

The optical potential is then generally parametrised as:

$$U(r) = U_C(r) + U_r(r) + iU_i(r) + U_{so}(r), \tag{2.32}$$

where $U_C(r)$ is the Coulomb potential, $U_r(r)$ is the real part, $U_i(r)$ is the imaginary part and $U_{so}(r)$ the spin-parity term.

The terms in the potential are defined as:

- The radial form of the Coulomb interaction $U_C(r)$ is defined as the one of a uniform charged sphere of radius R_C

$$U_C(r) = \begin{cases} \frac{Z_1\, z_2\, e^2}{2\, R_C}\left(3 - \frac{r^2}{{R_C}^2}\right) & \text{if } r \leq R_C \\ \frac{Z_1\, z_2\, e^2}{R_C} & \text{if } r \geq R_C \end{cases} \tag{2.33}$$

- The real part $U_r(r)$ represents the real central volume potential of the potential depth ($V_r(r)$) and $f_r(r)$ has the Woods-Saxon form, leading $U_r(r)$ to be written as

$$U_r(r) = -V_r(r)\, f_r(r) \tag{2.34}$$

- The imaginary part $U_i(r)$ represents the imaginary central surface potential of depth W_D, $f_i(r)$ a Woods-Saxon potential parameter and a_i the surface diffuseness parameter. This imaginary part can mathematically be written as

$$U_i(r) = 4a_i W_D \frac{df_i(r)}{dr} \tag{2.35}$$

- The spin-orbit term $U_{so}(r)$ represents the surface spin-orbit potential of the depth V_{so}. For $f_{so}(r)$, given that the radial form of this potential approximates the nuclear density distribution, a Woods-Saxon formfactor is generally used. m_p is the projectile mass, c the velocity of light, ℓ the orbital angular momentum and s the spin operator:

$$U_{so}(r) = \left(\frac{\hbar}{m_p c}\right)^2 V_{so} \frac{1}{r} \frac{df_{so}(r)}{dr} \ell \cdot s \tag{2.36}$$

$f_{so}(r)$, the Woods-Saxon parameter is explicitly formulated as

$$f_{so}(r) = \left[1 + exp\left(\frac{r-R}{a_{so}}\right)\right]^{-1} \tag{2.37}$$

With R the nuclear radius defined as $R = rA^{\frac{1}{3}}$, A the target mass number. a_{so} is the surface diffusivity parameter and r the radius.

The real and imaginary volume terms are generally taken as Woods-Saxon for nuclei with A $\geq$ 30, while for lower mass a Gaussian geometry is sometimes considered [38]. In general, the real and imaginary surface terms are either considered to be the derivative of the Woods-Saxon shape as shown earlier or a Gaussian, both of which gives similar results.

Optical model parameters are phenomenologically obtained by the fitting of calculated elastic scattering cross sections of a particular experiment. This gives rise to what referred as "local optical potential". During fitting, fitting optimisation related difficulty may arise (such expansion of χ^2 around the minimum)[34]. There is another option than local optical potential in the so-called "global optical potentials". These global potentials are obtained through a simultaneous fitting of elastic scattering data of a large number of nuclides across a wide energy range. Global potentials aim at acquiring single set of parameters suitable for a wide range of systems, leading therefore however to the possibility for specific local effects to be uniformed. There is however still the possibility of using parameters set for a given energy. Consequently in general, global potentials reduce the fluctuations in the result. This leads to the fact that a global potential is best to be used when a general trend is required rather than an accurate cross section at given energies [39].

Furthermore, it is important to characterise the behaviour of the transferred nucleon before the transfer, meaning within the projectile, and after it has been transferred, which implies within the residual nucleus.

As explained in References [40] and [41], different choices of bound state related potential parameters do reproduce well the shape of angular distributions but do vary substantially the magnitude of the cross section.

In a transfer reaction settings, the optical potentials are used to distort incoming and outgoing wave which were considered plane waves. The distortion of the plane waves which used the Plane Wave Born Approximation as model, by the introduction of the optical potential, is referred as the Distorted Wave Born Approximation (DWBA).

2.4.3 The (d, p) Transfer Reaction

Given that this work will focus on the (d, p) transfer reaction. This section gives an overview of the transfer reaction theory for this particular case. The following sections gives insight into the theory involving this type of reaction.

It is usually sufficient to use perturbation theory to evaluate the transition matrix, therefore the cross section is easily evaluated given the usual weak coupling between the elastic channel and the transfer (d, p) reaction [36]. Reactions produced by deuterons show some particular features, given the fact that the deuteron binding energy comes to approximately 1 MeV per nucleon compared to an average of 8 MeV binding energy in most nuclides. Furthermore the distance at which nucleon are spaced within the deuteron is relatively long. Because of these properties, deuteron induced reactions may result in the absorption of a single nucleon while the other will continue its journey mainly within the same direction by predominantly remaining beyond the nucleus boundary [37]. In this instance, as described in Ref.[36], it is shown that the cross section is of the form:

$$\frac{d\sigma\left(k_{\alpha i},k_{\beta j}\right)}{d\Omega}=\frac{M_{\alpha}k_{\beta j}}{M_{\beta}k_{\alpha i}}\left|f\left(k_{\alpha i},k_{\beta j}\right)\right|^{2}, \tag{2.38}$$

where M_α and M_β represent the transition matrix of the incident and outgoing channel respectively channel. $k_{\alpha i}$ and $k_{\beta j}$ the relative momentum in the entrance and outgoing channel respectively. $f\left(k_{\alpha i},k_{\beta j}\right)$ is the reaction amplitude. In the Born approximation, the reaction amplitude is written as:

$$f\left(k_{\alpha i},k_{\beta j}\right)=\frac{M_{\beta}}{2m\hbar^{2}}\langle\phi_{\beta j}\left(k_{\beta j}\right)\left|\mathrm{H}_{\beta}-\bar{\mathrm{H}}_{\beta}\right|\phi_{\alpha i}\left(k_{\alpha i}\right)\rangle, \tag{2.39}$$

where H_β and $\bar{\mathrm{H}}_\beta$ are respectively the total and the asymptotic form of the Hamiltonian in the final state and $\phi_{\alpha i}$ and $\phi_{\beta j}$ waves are eigenfunctions of the H_β and $\bar{\mathrm{H}}_\beta$ respectively. This equation can be re-written as to include a short range interaction

$$f\left(k_{\alpha i},k_{\beta j}\right)=\frac{M_{\beta}}{2m\hbar^{2}}\langle\phi_{\beta j}\left(k_{\beta j}\right)\left|\mathrm{V}_{pn}+\mathrm{V}_{pC}-\bar{\mathrm{V}}_{pR}\right|\phi_{\alpha i}\left(k_{\alpha i}\right)\rangle \tag{2.40}$$

where the suffixes refer to proton, deuteron, target core, residual nucleus and $\bar{\mathrm{V}}_{pR}$ is the optical potential for the scattering of protons by the residual nucleus. The basic assumption for the transfer reaction mechanism that only the neutron interacts with the target leads to $\mathrm{V}_{pC} \approx \bar{\mathrm{V}}_{pR}$ meaning $\left(\mathrm{V}_{pC}-\bar{\mathrm{V}}_{pR}\right)$ is insignificant. This allows the reaction amplitude to be written as:

$$f\left(k_{\alpha i},k_{\beta j}\right)=\frac{M_{\beta}}{2m\hbar^{2}}\langle\phi_{\beta j}\left(k_{\beta j}\right)\left|\mathrm{V}_{pn}\right|\phi_{\alpha i}\left(k_{\alpha i}\right)\rangle \tag{2.41}$$

2.4.4 The Plane Wave Theory

In earlier investigations [42] into transfer reaction cross section calculations, the distortion of the wavefunctions brought on by the nuclear and Coulomb fields was not taken into account resulting in what is referred to as the "Plane Wave Theory". For the (d,p) transfer reaction, the deuteron and proton plane waves are respectively represented by $\exp\left(ik_{d}\ldots r_{d}\right)$ and $\exp\left(-ik_{p}\ldots r_{p}\right)$, with r and k being respectively the interaction radius and the wave number. The plane-wave expressions only depend on r and k and the transferred neutron angular momentum ℓ_{n}. With this theory, it is possible to obtain good fit around the peak which allows ℓ_{n} to be deduced, however absolute spectroscopic factors are usually underpredicted by a factor of ten or more [42]. In short, the plane wave theory may be successful overall when the velocities of the incoming deuteron and outgoing proton are relatively the same such that the proton is not expected to strongly engage with the residual nucleus. This theory is indeed absolutely inconsistent in the fact that it ignores totally the distortion produced by the nuclear field on the incoming and outgoing wave. The plane wave can not give much information on the nuclear structure or reaction mechanism. Neglecting the nuclear and Coulomb distortions makes without doubt this theory incomplete.

2.4.5 The Distorted Wave Born Approximation(DWBA)

Plane wave theory shortcomings led to the development of the distorted wave theory by Tobocman and many others [42]. In this theory, the nuclear and Coulomb distortion are taken into account by the addition of an optical model. This theory therefore includes the combined effect of the nuclear and Coulomb fields into the projectile and ejectile waves functions. The waves are obtained from the optical potentials that depicts the

equivalent elastic scattering interaction and the relevant energies. The elastic scattering characterises only the asymptotic form of these wave functions which are then thereafter used to evaluate the overlap integral [36].

In the earlier work on DWBA, for a (d, p) reaction for example, the product of the neutron-proton interaction and deuteron internal wave function was described by a zero-range term. Zero-range approximation allow the reduction of the reaction amplitude from the six-dimensional integral to a three dimensional integral.

The interaction can then mathematically be represented as:

$$V_{pn}\left(r_{pn}\right)\phi_d\left(r_{pn}\right) = V_0\delta\left(r_{pn}\right), \tag{2.42}$$

with $r_{pn} \equiv r_p - r_n$ and $V_0 = \int \phi_d\left(r_{pn}\right)\ V_{pn}\left(r_{pn}\right)\ dr_{pn}$.

With this theory, overall it has been found that there is a better estimate of the angular momentum and more accurate spectroscopic factors. One of the improvements on DWBA is to use a realistic expression for the $V_{pn}\left(r_{pn}\right)$ and for the deuteron internal wave function $\phi_d\left(r_{pn}\right)$. Practically, since $V_{pn}\left(r_{pn}\right)$ is not well known, a good finite-range approximation of $V_{pn}\left(r_{pn}\right)$ and $\phi_d\left(r_{pn}\right)$ product happens to be satisfactory. For example, a finite-range Gaussian interaction of range r_G in which the parameters are adjusted such that the Fourier transform has the same zero and low-momentum components as that of the zero range approximation can be used. The expression used may then be written as:

$$V_{pn}\left(r_{pn}\right)\phi_d\left(r_{pn}\right) = V_G \exp\left(-\frac{|r_{pn}|^2}{{r_G}^2}\right), \tag{2.43}$$

with the strength V_G defined similarly by inversion as the zero range potential V_0.

It is worth emphasising that the resulting cross section obtained with this finite-range interaction gives very similar shape than the one obtained with the zero-range approximation with a magnitude change of about 20 %. It has been found that the zero-range approximation usually overemphasize nuclear interior contribution which leads to a cross section overestimation [36].

There is a calculation referred to as Local Energy Approximation (LEA) which allows, by a simple modification of the three dimensional overlap integral, to obtain a very close result than the one obtained by the full finite range approximation. When fitting optical potential with elastic scattering data, there is only a guarantee of the correctness of the wave functions at larger distances. The use of the non-local component of the optical potential allow the inclusion of the nuclear interior. As defined in [36], the relation by Perey is written as:

$$\psi_{n1}(r) = \frac{\psi_1(r)}{1 + \frac{2m\beta^2}{\hbar^2} V(r)^{\frac{1}{2}}}, \tag{2.44}$$

where $\psi_1(r)$ is the wave function obtained with elastic scattering data and $V(r)$ is the equivalent local potential, and β is the Gaussian form non locality range.

DWBA for a (d, p) Transfer Reaction

Most transfer reaction experiments are analysed using the DWBA theory. The (d, p) transfer reaction is the most extensively studied of the one-nucleon transfer reactions [43]. DWBA, as explained previously, includes an overlap function that gives details about the single-particle structure

$$\langle \psi_B(1,\, 2,...,\, A,\, A+1) | \psi_A(1,\, 2,...,\, A) \rangle \tag{2.45}$$

The (d, p) reaction experiments purposes are mainly spectroscopic: Spin and parity of nuclear levels, spectroscopic factor, and their spreading of the single-particle strength [43].

Angular Momentum Transfer in direct reactions

From the passage from the initial to the final states in transfer reactions, as described in Ref.[32], there is an angular momentum transfer between the incident particle and the target. The angular momentum in question originates from the momentum transfer at the point of contact which then influences the ejectile angular momentum distribution. By considering the classical scenario of a projectile with a momentum set as p_p which interacts within a target surface, at a radius R and an ejectile of momentum p_e with θ as relative angle. The total momentum can then be written as:

$${p_{total}}^2 = {p_p}^2 + {p_e}^2 - 2 \times p_p \times p_e \cos\theta = (p_p - p_e)^2 + 4 \times p_p \times p_e \times \sin^2\frac{\theta}{2} \tag{2.46}$$

where the transferred angular momentum is equal to $L = \sqrt{\ell(\ell+1)}\hbar \leq p_{total} R$, with R=1.25 $\times A^{\frac{1}{3}}$. As it can be seen the ejectile direction, θ, is dependent on the total angular momentum p_{total} and consequently is also L dependent.

Spectroscopic Factor

The general definition of the spectroscopic factor including its computation for diverse scenarios are in details covered by Macfarlane and French [44]. As a summary, the spectroscopic factor of the final state is extracted by comparing the experimental cross section to the DWBA calculation. Mathematically, it can be written as:

$$\left(\frac{d\sigma}{d\Omega}\right)_{Measured} = {C_P}^2 {S_{njl}}^P \cdot {C_R}^2 {S_{n'j'l'}}^R \left(\frac{d\sigma}{d\Omega}\right)_{DWBA}, \tag{2.47}$$

where ${C_P}^2{S_{njl}}^P$ and ${C_R}^2{S_{n'j'l'}}^R$ represent the projectile and residual nucleus spectroscopic products in which the C are the Clebsch-Gordan isospin coupling coefficients and S are the associated spectroscopic factors.

2.4.6 DWBA Shortcomings - Adiabatic Approximation for the Deuteron Optical Potential

Although it is reasonable to expect to obtain an optical potential that well-reproduces an elastic scattering cross section, the problem becomes more difficult for complex particles. When considering the (d, p) transfer reaction, deuteron breakup and the distortion effect of the deuteron in the field is not taken into account [43]. As a matter of fact, the DWBA formalism breaks down whenever the final state is unbound with the construction of the final wavefunction using the usual potential. The consideration of the Adiabatic model for the deuteron optical potential initiated by Johnson and Soper in 1970 [45] takes into account deuteron breakup.

With this approximation, the deuteron potential is defined to be

$$U_d\,(r) = \left(\frac{1}{D_0}\right) \int [U_n(r + \frac{1}{2}s) + U_p(r - \frac{1}{2}s)] V_{pn}(s) \phi_d(s) ds, \tag{2.48}$$

with U_p and U_n, the nucleon optical potentials that corresponds to the energies of half the deuteron beam energy and ϕ_d the deuteron wave function. This equation shows that the distorted waves that are produced by this potential contained not only the elastic waves but also approximately in a way the outgoing waves associated with the breakup of the deuteron into low energy relative ^{3}S states.

This model has a distinct advantage compared to its elastic scattering deuteron potentials in the fact that a faster fall off with angle and stronger oscillations are observed. This adiabatic potential U_d is different from the usual sum $U_p + U_n$ in the fact it has, with assumption of having the same geometry, has a larger diffuseness.

It produces a stronger localisation in ℓ space than elastic potentials. It is important to underline that the validity of this approximation improves with higher energies [43].

Further details on DWBA and adiabatic model shortcomings and suggested way to remedy it such the consideration of the adiabatic model on (d, p) with non-local potentials, can be found in published papers by Timofeyuk in Refs.[46] and [47].

CHAPTER 3

Astrophysical Motivation of the ^{20}Ne(d,p)^{21}Ne at Relevant Energies

> The sun has one kind of splendor, the moon another and the stars another; and star differs from star in splendor.
>
> Corint.

The first part of this thesis focuses on a single-nucleon transfer reaction designed to investigate excited states in ^{21}Ne relevant to the astrophysically important ^{17}O(α,γ)^{21}Ne and ^{17}O(α,n)^{20}Ne reactions. This chapter covers the motivation that drove the measurement of the ^{20}Ne(d,p)^{21}Ne transfer reaction performed at the Maier-Leibnitz Laboratorium in Munich and describes the scope of this present work.

3.1 Astrophysical relevance of the ^{20}Ne(d,p)^{21}Ne transfer reaction

The s-process abundances, as described in section 1.2.2, are dependent on lighter nuclei which can either act as neutron poisons or neutron sources.

As described within the same section, there is also a non standard s-process that occurs in very low metallicity massive rotating stars [12]. In particular in a standard weak s-process, the abundance contribution does not originate from a primary significant source of neutrons but rather from the star's metallicity. It is this metallicity which both provides the s-process seeds, which happen to mainly be iron and the secondary neutron sources. Secondary sources in this case come from the initial C, N and O via

the $^{14}N(\alpha,\gamma)^{18}F(\beta^{+}\nu)^{18}O(\alpha,\gamma)$ reactions resulting in ^{22}Ne. The ^{22}Ne$(\alpha,n)^{25}$Mg reaction, which only ignites when the appropriate temperature is reached, is indeed thought to be at the origin of the production of most of the neutrons [14], leading therefore to more massive star to have more ^{22}Ne neutron sources.

When referring to rotating stars, the main effect of rotation on the *s*-process production is the expansion of the convective helium core due to additional mixing and therefore a behaviour like non-rotating more massive stars; at low metallicity, the effect of rotation is more important. At very low metallicity, with the removal of ^{22}Ne, the standard weak *s*-process in massive stars becomes as a consequence much less effective. In this instance, in the outward part of core Helium burning, carbon and oxygen are mixed into hydrogen rich regions leading to a strong production of nitrogen, part of which may enter the convective Helium core and be transformed into primary ^{22}Ne by α-captures. Consequently, by comparison to non-rotating models, the ^{22}Ne availability in the Helium-core is strongly enhanced [14] leading to a higher neutron flux.

In stars of higher metallicity, during helium burning, the neutron poisons are of primary origin through mainly ^{16}O and of secondary origin through ^{25}Mg. At very low metallicity, since there is a lack of elements higher than helium, it is safe to state that ^{25}Mg is insignificant. The consideration of the products of helium burning, ^{12}C and ^{16}O, allowed the possibility of the consideration of both as potential neutron poison or absorber despite their low thermal cross section. Theoretical model predicts a rich abundance of ^{16}O layers in low-metallicity stars [3], which leads to the ^{16}O becoming the most dominant neutron absorber or poison through the ^{16}O$(n,\gamma)^{17}$O reaction. The standing of ^{16}O as either neutron poison or neutron absorber in low metallicity massive stars is determined by the neutron recycling process through the subsequent ^{17}O$(\alpha,n)^{20}$Ne reaction [14] which is however counteracted by the competing channel ^{17}O$(\alpha,\gamma)^{21}$Ne. Hence, the neutron recycling process is highly dependent on the ratio of the ^{17}O$(\alpha,\gamma)^{21}$Ne and ^{17}O$(\alpha,n)^{20}$Ne reaction rates.

The ^{17}O$(\alpha,n)^{20}$Ne reaction, which results from the strong interaction is expected to dominate by two orders of magnitude over the ^{17}O$(\alpha,\gamma)^{21}$Ne reaction which emanates from the electromagnetic interaction. The ratio is however more complicated as strong resonances in the (α,γ) reaction for example would negatively affect the *s*-process abundances [48].

Two theoretical predictions exist. The theoretical calculations by Caughlan and Fowler (CF88) [27] predict the $(\alpha,\gamma)/(\alpha,n)$ ratio to be 0.1 below 1 MeV and 5×10^{-4} above 1 MeV. These calculations are based on Hauser-Feshbach calculations at low energies and

experimental data on the $^{18}O(\alpha,\gamma)^{22}Ne$ reaction at higher energies.

The calculation by Descouvemont [28] however uses the three cluster Generator Coordinate Method (GCM) where the ^{21}Ne nucleus is described by mixing of different configurations of $^{16}O+\alpha+n$ such $(\alpha + {}^{16}O) + n$ and $(n + {}^{16}O) + \alpha$. The ^{21}Ne wave functions are in this instance produced from ^{16}O α internal wave functions defined in the harmonic oscillator basis for which further detailed description on the subject can be found in Ref. [28, 49]. Here Descouvemont predicts a ratio of 10^{-4} over all relevant energies. Given that the centre of mass energies varies from 0.3 to 0.7 MeV and 0.7 to 1.8 MeV for core helium burning and the carbon shell burning respectively, the two theoretical predictions disagree by three orders of magnitude along a broad enough range of energies relevant to the *s*-process. The disagreement in particular at low energies results in significant difference in the predicted abundances of the *s*-process. Figure 3.1 shows the $^{17}O(\alpha,\gamma)^{21}Ne$ and $^{17}O(\alpha,n)^{20}Ne$ reaction rates as a function of temperature with the CF88 and Descouvemont calculations.

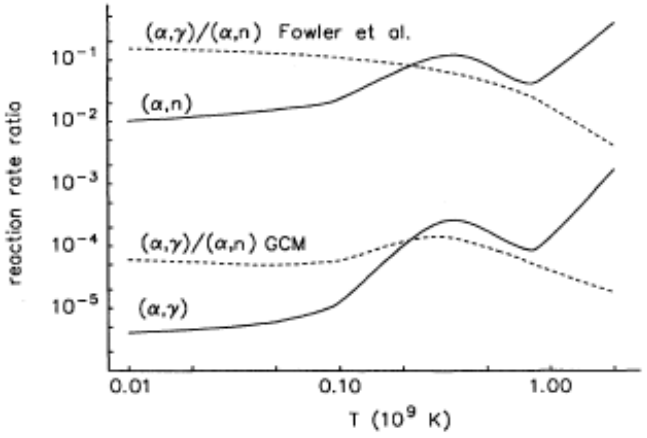

Figure 3.1: *Different Reaction Rates Ratios as a function of temperature. The ratio of Descouvemont's reaction rates of* (α,γ) *and* (α,n) *to the values of CF88 is represented as solid lines and* $(\alpha,\gamma)/(\alpha,n)$ *ratios are depicted as dashed lines. Taken from Ref.[28]*

Figure 3.2, taken from Ref.[14] shows the two predictions of the overproduction factor X/X_{ini} based on both theoretical calculations where one can see clear variations, which is in particular highlighted by the variations between strontium and barium. This overproduction factor X/X_{ini} was obtained using the one-zone *s*-process nucleosynthesis calculation following the end of Helium burning.

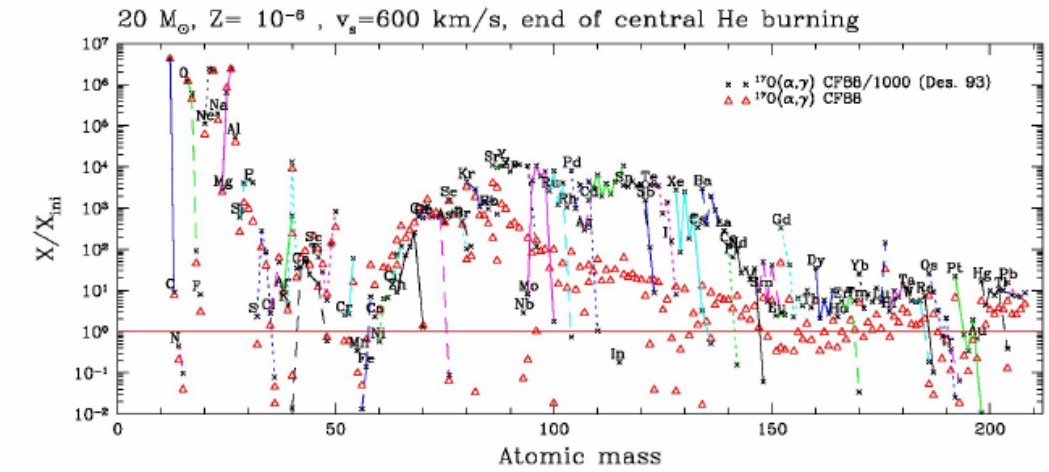

Figure 3.2: *The overproduction factor X/X_{ini} using the one-zone s-process nucleosynthesis calculation following the end of helium burning. Descouvemont's lower rate [28] of $^{17}O(\alpha,\gamma)^{21}Ne$ leads to a strong increase of s-process overproduction (up to three orders of magnitude) between strontium and barium. Taken from Ref.[14].*

3.2 Ratio of the ^{17}O(α,γ)^{21}Ne to the ^{17}O(α,n)^{20}Ne Rate Experimental Investigations

Experimental constraints on both reaction rates are hence crucial. Concerning the ^{17}O(α,n)^{20}Ne reaction, as stated in section 1.5.2, measurements at relatively low energies (between 0.56 - 10.1 MeV) exist [29, 50]. Additionally extrapolations to lower energies are available through the NACRE compilation [30]. However, for the ^{17}O(α,γ)^{21}Ne reaction, experimental data are quite scarce. Indeed, only two recent direct measurements of this reaction exist. One of the experiments was performed in 2009 by Taggart *et al.* [15, 48], scanning the energies range between 0.6 and 1.6 MeV in the centre of mass and the other measurement was performed by Best *et al.*[31] in the energy region between 0.750 –1.650 MeV in the centre of mass.

3.2.1 $^{17}O(\alpha,\gamma)^{21}Ne$ Measurement at TRIUMF

For this measurement, the DRAGON - Detector of Recoils And Gammas Of Nuclear reactions was used. DRAGON is located in the ISAC facility, at The TRIUMF Laboratory in Vancouver, Canada and is purposely constructed for nuclear astrophysics radiative capture experiments. The facility consists of a recoil mass separator, a windowless gas target, a γ-ray array and a heavy-ion detector system for which further details can be found in references [51, 52]. This measurement found the following selected resonances, which can be seen alongside their associated uncertainty in Table 3.1.

E_{cm}(MeV)	$\omega\gamma$(MeV)	error(%)
0.621	0.714	28.1
0.717	23.160	24.6
0.806	3.000	19.4
1.116	33.560	13.1

Table 3.1: *Selected Resonances of DRAGON experiment used for reaction rate calculation [48].*

These selected resonances were then used for reaction rate calculations and compared directly to the reaction rate which are part of the CF88 results. For comparison to the Descouvement calculations however, the reaction rates shown later were obtained by processing the same reaction rate codes as the one used to calculate the DRAGON results. Figure 3.3 shows the DRAGON result calculated reaction rate for which relative contributions are considered alongside those of CF88 and Descouvemont.

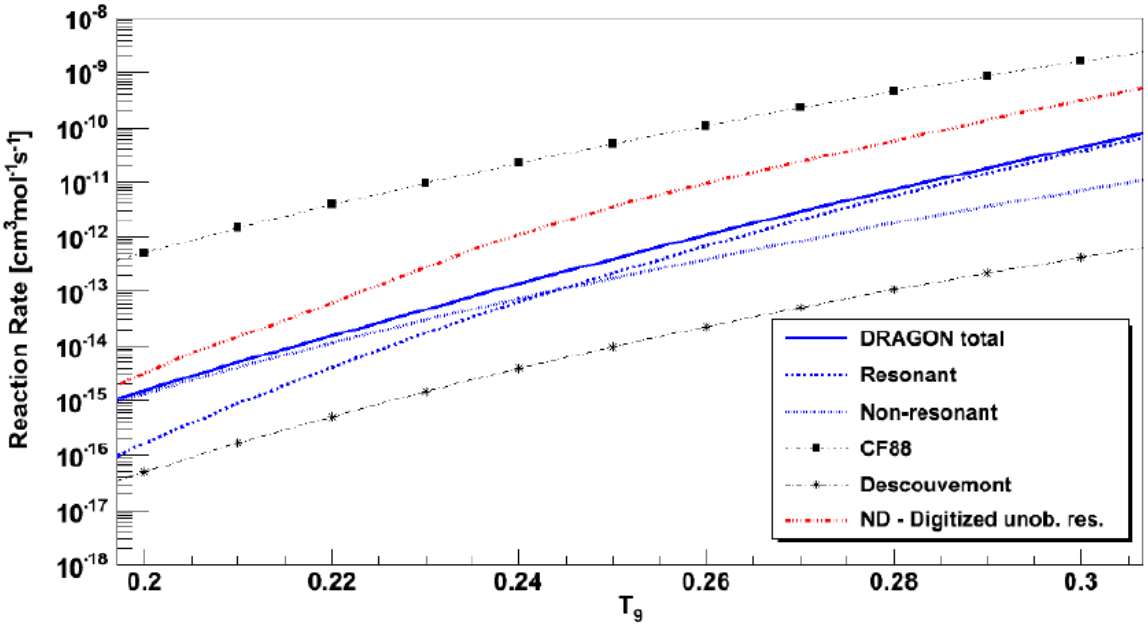

Figure 3.3: *Figure from [48] showing DRAGON reaction rate relative contribution (in blue) with Descouvemont [28], CF88 [27] calculations and Best data in red* [1] *[31].*

This calculation was based on the assumption of contribution to reaction rates being from single resonances with zero contribution for all off-resonance regions. Given the lack of further data, these assumptions appeared to be adequate at giving at the very least a dependable lower approximation of the $^{17}O(\alpha,\gamma)^{21}Ne$ rate. Given the fact that this experiment did not reach the lowest end of the Gamow window, an extrapolation had to be made and so a mix of fitting methods was used as extensively detailed in Reference [48]. The fitting to establish off-resonance data, while still considering the contribution of resonant states separately, allows for the calculation of the non-resonant contribution to the reaction rate. A range of fitting parameters were then tested, as well as the effect of including those likely but not certain selected resonances described earlier in Table 3.1. The extrapolation used to the non resonant region increased strongly the associated errors on the reaction rate calculation[48]. Nevertheless, the results attained were adequate to contribute to an important constraint on the reaction rate, very helpful given the extremely large discrepancies between the two available theoretical models [27, 28].

This experiment concluded that the S-factor calculation from the GCM of Descouvemont significantly underpredicted the data in the region covered by the measurement. The DRAGON data indeed resulted in a far stronger (α,γ) channel than the one predicted by the Descouvemont's calculations. This is really striking when comparing the reaction

[1] Described thereafter in the following section

rate around the strong E_{cm} = 0.8 MeV resonance where the GCM underpredicts by a factor of 100 the experimental data. It is important to note however that this is not necessarily in disagreement if the GCM prediction is considered to represent the non-resonant contribution to the cross section. Furthermore, it is also worth noting that the data did not support the CF88 predictions either.

3.2.2 $^{17}O(\alpha,\gamma)^{21}Ne$ Measurement at Notre Dame

This measurement was performed using γ spectroscopy at the University of Notre Dame Nuclear Science Laboratory, United States. The experiment utilised a helium beam directed onto a tantalum-backed target into which H_2O enriched to 90.1 % in ^{17}O had been added[31]. The target thickness chosen resulted in a beam energy spread of about 12 keV for an α beam of 1 MeV. This measurement found resonances listed in Table 3.2. Resonance energies are given for the laboratory and centre of mass frame.

E_α(MeV)	E_{cm}(MeV)	E_x(MeV)	$\omega\gamma$(MeV)
1.002(2)	0.811	8.159(2)	7.6(9)
1.386(2)	1.122	8.470(2)	1.2(2)
1.619(2)	1.311	8.659(2)	136.0(17)

Table 3.2: *Resonances from the Notre Dame experiment [31].*

These three resonance contributions were then used to calculate the stellar reaction rate of the $^{17}O(\alpha,\gamma)^{21}Ne$ reaction around a temperature of 1 GK. The team found at T = 1 GK, a reaction rate $N_A\ \langle\sigma\mu\rangle = 1.8 \times 10^2$ and $N_A\ \langle\sigma\mu\rangle$(CF88) = 4.6×10^{-2} $cm^3\ mol^{-1}\ s^{-1}$. The calculations related to this particular experiment were at odds with the Descouvemont predictions and initially confirmed the CF88 calculations in Ref. [31]. However, in order to estimate an upper limit of the reaction rate, this team assumed that all unobserved states within the covered experimental range (E_x = 7.960 and 8.465 MeV) displayed resonances in the (α,γ) channel with strengths just below their detection limit. It was then found that in this case, the rate would increase by 10% or more [31]. There was another experiment later by the same team detailed in Ref.[29] on $^{17}O(\alpha,n)^{20}Ne$. This new measurement allowed them to compare the (α,n) and the (α,γ) rates. In this case the team found that both rates were weaker than those suggested by NACRE and CF88 respectively at He burning temperatures. To exemplify, the recommended (α,n) rate was about 1/4 of that in NACRE and the rate of the (α,γ) channel about 1/4 of the CF88 rate (both in this case at T$\sim$ 0.3GK). Figure 3.4, taken from [29], shows the result of their work where one can see the comparison of *s*-process elemental abundances obtained at the

end of convective He-core burning, relative to the initial abundance distribution. In this figure, the effect of the (α,γ) and (α,n) rates, shown in red stars, are directly compared to the abundances that result from using the (α,n) rate adopted from the NACRE [30] and CF88 rate modified by Descouvement [28, 53], shown in blue squares. This figure is plotted by the team as a function of atomic number for ease in comparison with Figure 3.2.

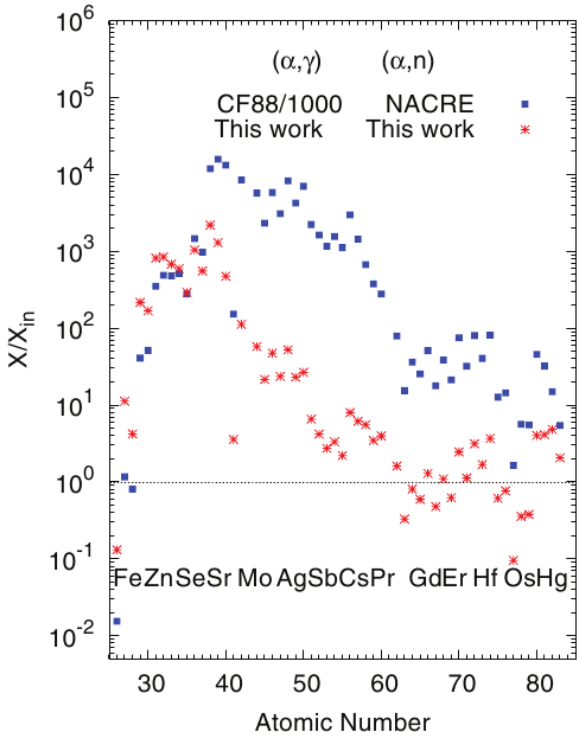

Figure 3.4: *Overproduction factor where the red lines are based on Best et al. $^{17}O(\alpha,\gamma)^{21}Ne$ and $^{17}O(\alpha,n)^{20}Ne$ measurements while the blue lines are based on Descouvemont $^{17}O(\alpha,\gamma)^{21}Ne$ rate and NACRE $^{17}O(\alpha,n)^{20}Ne$ rate.*

3.2.3 Summary of the $^{17}O(\alpha,\gamma)^{21}Ne$ to the $^{17}O(\alpha,n)^{20}Ne$ Rate Experimental Data

In each measurement, different extrapolations to lower energies as described earlier were made. Both teams based their reaction rate calculation on their respective measured or selected resonances and, in both cases as again described earlier, different hypothesis to estimate upper or lower limit of the rate were performed. Both experiments predict an increased rate in comparison to the Descouvemont prediction but at the same time a much lower rate than the one predicted by CF88, with measurements by Best having a higher value than those made by Taggart. Figure 3.5 better summarises the overall experimental effort where respective single resonances were in turn considered in regard to

both theoretical predictions. The comparison were illustrated in Ref.[48] where Best data were extracted and reaction rates recalculated in order to allow a direct comparison. Both results suggested therefore a stronger $^{17}O(\alpha,\gamma)^{21}Ne$ channel which implied, as explained in previous section, less recycled neutrons, with Best results suggesting the highest rate.

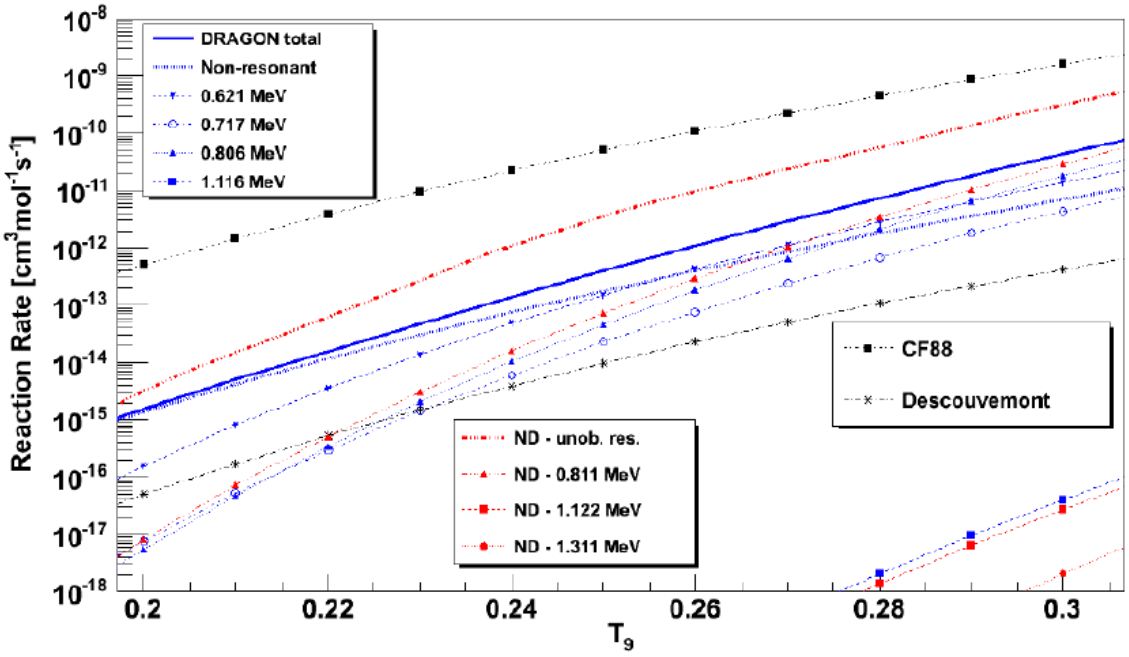

Figure 3.5: *Figure from [48] showing DRAGON and Best [31] reaction rate where single resonances contribution were in turn considered. Descouvemont [28] and CF88 [27] calculations are also shown.*

Those upper and lower limit assumptions were based by the consideration of different possible scenarios on level densities properties of ^{21}Ne around the Gamow window of $^{17}O(\alpha,\gamma)^{21}Ne$. The α-particle threshold in ^{21}Ne corresponds to an excitation energy of 7.35 MeV, therefore, the structure of ^{21}Ne around this energy determines the low temperature reaction rate of $^{17}O(\alpha,\gamma)^{21}Ne$. As stated previously, the Gamow window for core helium burning corresponds to E_{cm} = 0.3-0.7 MeV which translates to excited states of ^{21}Ne located between E_x = 7.65-8.05 MeV.

3.2.4 ^{21}Ne Spectroscopic Information

Within the region covering the excitation energies located between E_x = 7.65-8.05 MeV, very little spectroscopic information is known. There are six known states within that region for which most of the spectroscopic properties such spin-parity are not all

known. Figure 3.6 shows the ^{21}Ne level scheme around the Gamow window where the six adopted values ranging from E_x = 7.6491-7.9821 MeV can be seen. Table 3.3 shows the adopted values alongside known spectroscopic properties such as spin and parity established using values from all the previous studies (also indicated).

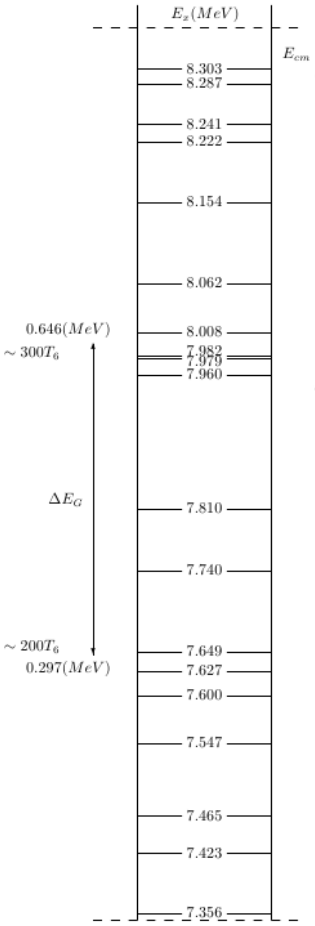

Figure 3.6: *^{21}Ne Level Scheme between 0 to 1 MeV above the α threshold where the region of interest, the $^{17}O(\alpha,\gamma)^{21}Ne$ Gamow window during helium core burning, is indicated. Modified from Ref.[48]*

Energy Level (keV)	J^{π}	Method of identification
7649.1(10)	$(7/2,5/2)^{+}$	^{18}O(α,$n\gamma$) *[54, 55, 56]* ^{12}C(^{13}C,$\alpha\gamma$)*[57]* ^{19}F(^{3}He,p),(^{3}He,$p\gamma$)*[58, 59]* ^{13}C(^{12}C,α)*[60]*
7740(10)	-	^{19}F(^{3}He,p),(^{3}He,$p\gamma$) *[58, 59]*
7810(10)	-	^{19}F(^{3}He,p),(^{3}He,$p\gamma$) *[58, 59]* ^{13}C(^{12}C,α)*[60]*
7960.3(10)	$(11/2^{-})$	^{16}O(^{7}Li,$np\gamma$) *[61, 62]*
7979(10)	$3/2^{-}$	^{19}F(^{3}He,p),(^{3}He,$p\gamma$) *[58, 59]* ^{21}Ne(n,n')*[63, 64]*
7982.1(6)	$(7/2,11/2)^{+}$	^{18}O(α,$n\gamma$) *[54, 55, 56]* ^{12}C(^{13}C,$\alpha\gamma$)*[57]* ^{13}C(^{12}C,α)*[60]*

Table 3.3: *Information of excited states within Gamow Window.*

3.3 Current Status on Spectroscopic Information in ^{21}Ne

The structure of ^{21}Ne in general and, above the α-threshold in particular, has been studied using many methods over the years as Table 3.3 shows. For the studies of spectroscopic information of states up to E_x= 6.9 MeV, the ^{18}O(α,$n\gamma$), ^{12}C(^{13}C,$\alpha\gamma$), ^{19}F(^{3}He,p),(^{3}He,$p\gamma$), ^{13}C(^{12}C,α), ^{16}O(^{7}Li,$np\gamma$) reactions were used. In addition to that, the single-particle ^{20}Ne(d,p)^{21}Ne transfer reaction was also used for most states around that region. However the ^{20}Ne(d,p)^{21}Ne transfer reaction had never been used for states above E_x= 6.9 MeV in ^{21}Ne (See Ref. [65], [66], [67] and [68]).

Most previous experiments on ^{20}Ne(d,p)^{21}Ne were performed up to only the late 1970s. This can effectively be seen by surveying the literature, see for example experiments by Chambon *et al.* [65], by Howard *et al.* [66], by Lambert *et al.* [67], by Heikkinen and Pixley [69], by Vegh and Valek [70]. In all those experiments, only gaseous targets of ^{20}Ne, either enriched or of natural isotopic composition, were used. Moreover, in most experiments [66, 67, 69, 70], a Van de Graaf accelerator was used [2] and different types of magnetic deflector used for the separation of protons groups from deuterons or other possible contaminants [65, 67, 70] while for proton detection, various types of detectors were used (semiconductors detectors, gas based detectors).

The highest incident beam energy used was of 16.4 MeV [65], [68] while as stated previously the highest excitation energies reached was of E_x= 6.9 MeV.

[2] Description briefly given in the next chapter

3.4 The ^{20}Ne(d,p)^{21}Ne transfer reaction at astrophysically relevant energies

In order to address the need for further spectroscopic information on ^{21}Ne around the Gamow window of the ^{17}O(α,γ)^{21}Ne reaction, an experiment on the ^{20}Ne(d,p)^{21}Ne transfer reaction was performed in July 2012. The measurement aimed at covering the excitation energies in ^{21}Ne located between E_x = 7.65-8.05 MeV and proposed to constrain energies and J^π values of known states in ^{21}Ne as well as search for new states within the region of interest.

CHAPTER 4

^{20}Ne(d,p)^{21}Ne Experimental Setup

> Worry does not empty tomorrow of its sorrows; it empties today of its strength.
>
> Corrie Ten Boom

The ^{20}Ne$(d,p)^{21}$Ne transfer reaction experiment which constitutes part of this work was performed at the Maier-Leibnitz Laboratorium (MLL) of Munich, Garching, Germany. The MLL is a joint facility between the Technische Universität of Munich and the Ludwig-Maximilians-Universität (LMU) of Munich. The Laboratory is centred around a tandem Van de Graaff accelerator, a polarised hydrogen source, Accelerator Mass Spectrometry (AMS) ion source, ultra clean ion source and negative ion injector. The facility is used for very different research areas such as the Cluster of Excellence "Origin and Structure of the Universe" as described on the Munich homepage [71] in which different discipline of physics work together. That includes nuclear and particle physicists, astronomers and astrophysicists. Experiments range, therefore, from pure nuclear structure related activities to biophysics experiments [71].

The facility includes different equipment such as a Bragg Chamber, gas filled magnet, different scattering chambers and a magnetic spectrograph consisting of a quadrupole and three dipoles.

Figure 4.1 shows an outlook of the Laboratory facility.

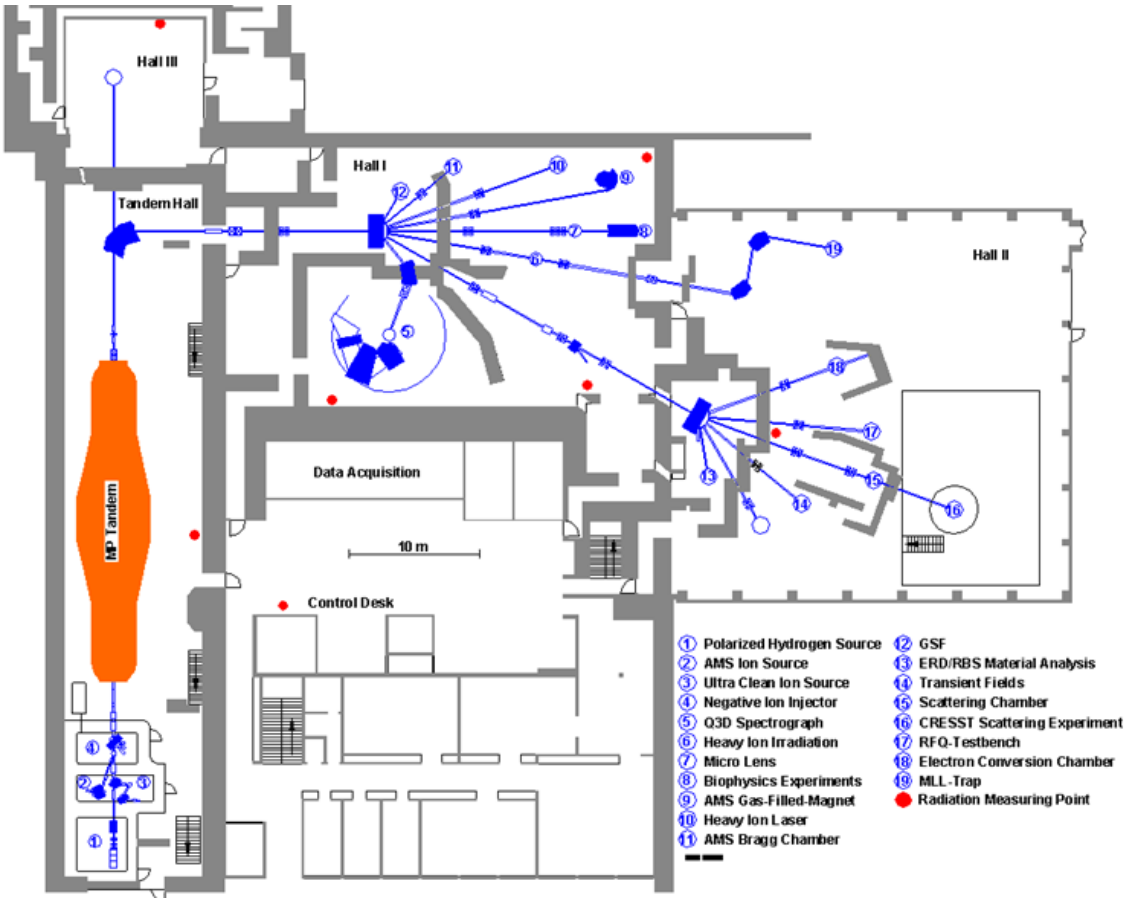

Figure 4.1: *Schematic overview of the Maier-Leibnitz-Laboratorium facility.*

This $^{20}\mathrm{Ne}(d,p)^{21}\mathrm{Ne}$ transfer reaction experiment took place at the Quadrupole Dipole Dipole Dipole (Q3D) magnetic scpectrograph. In the following chapter, the experimental setup of the Q3D end of the facility during the experiment will be detailed. The production and acceleration of the beams will also be described, including an overview of the tandem Van de Graaff accelerator itself. The experiment electronics and data acquisition and specific details on the experiment will also be presented.

4.1 Beam Production and Transportation

The deuteron beam was produced by an ion source and accelerated by the Tandem Van de Graaff accelerator. Tandem accelerators are accelerators of electrostatical type which have as main components a high voltage generator, terminal and vacuum acceleration tube. The central terminal in Tandem is retained at a positive potential. Tandem accelerators allow charged particles to be accelerated in two phases. Negatively charged ions are created by an ion source. These negative ions are then introduced towards the terminal where they are accelerated and stripped of electrons by passing through a thin foil in the terminal. This stripping results in the ions being positively charged. The resulting positive ions then, are additionaly accelerated and driven away from the terminal and directed toward the high energy extremity of the accelerator.

Figure 4.2 is a view of the Munich tandem accelerator.

Figure 4.2: *Photograph showing the Munich Tandem Van de Graaff Accelerator from [72].*

The Munich Tandem Voltage can reach up to 15 Mega Volts [73]. Particles such as protons can therefore reach a kinetic energy of up to 30 MeV and heavier nuclei can reach higher energies. The following figure 4.3 shows a schematic of a Tandem accelerator.

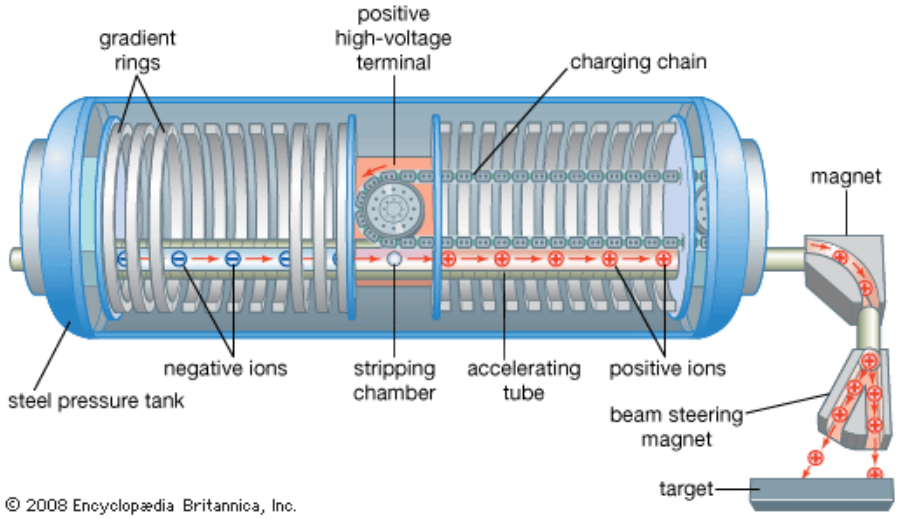

Figure 4.3: *Sketch of the Tandem Accelerator. From [74].*

The negative ion injector of the Munich tandem has three platforms: one with a polarised ion source, one with an ion source for Accelerator Mass Spectrometry and one with an ion source for routine operation [75].

Around a dozen measurement areas are available, among them the high precision Quadrupole Dipole Dipole Dipole magnetic spectrograph which is an excellent tool for high precision nuclear spectroscopy.

4.2 The Munich Quadrupole Dipole Dipole Dipole Magnetic Spectrograph(Q3D)

The Q3D magnetic spectrograph has an energy resolution of $\delta E/\mathrm{E} = 2 \times(10)^{-4}$ [76]. In the Q3D magnetic spectrograph, after ejectiles have left the target and entered the spectrograph, they are focused to the focal plane by the quadrupole. Figure 4.4 shows a picture showing one side of the Munich Q3D spectrograph.

Figure 4.4: *Picture of the Munich Q3D Magnetic Spectrograph.*

The magnetic field of the three dipole magnets separates the trajectories of the particles according to their magnetic rigidity. Magnetic rigidity is a concept which is explained in the following section.

4.2.1 Charged Particle Motion

A charged particle (of charge Q) moving with velocity v in a uniform magnetic field of strength B experiences a force referred to as the Lorentz force F and defined as

$$F = Qv \times B \tag{4.1}$$

This force provides a centripetal acceleration bending the particle in a circular path and is therefore equal to its mass multiplied by its acceleration towards the centre of its circular path:

$$F = QvB = \frac{mv^2}{\rho} \tag{4.2}$$

where ρ is the radius of curvature of the path. Rearranging the previous equation leads to

$$B\rho = \frac{mv}{Q} \tag{4.3}$$

where $B\rho$ is known as the magnetic rigidity.

4.2.2 Munich Q3D Characteristics

As stated beforehand, the magnetic field separates the trajectories of the particles according to their magnetic rigidity. However particles that possess small differences in magnetic rigidity will follow slightly different bending radii. This leads to the position at which a particular type of ion crosses the focal plane to be uniquely related with its momentum [77].

The Q3D magnetic spectrograph can be very useful in the investigation of high precision nuclear structure. In this particular case, the energy distribution of a given type of ejectiles have to be measured and all other nuclei passing through the Q3D spectrograph have to be ignored. This consideration leads to the necessity of having a focal plane detector which not only has the capacity to measure the incident ions position but also provide for particle identification.

Figure 4.5 shows a detailed schematic of the Q3D spectrograph with details of the position of the Faraday cup[1] and a multipole magnet [2]. As it can be seen, the quadrupole and the dipole I are followed by a corrective element, a multipole fields which can be produced perpendicular to the beam direction for compensation of kinematic effects [78].

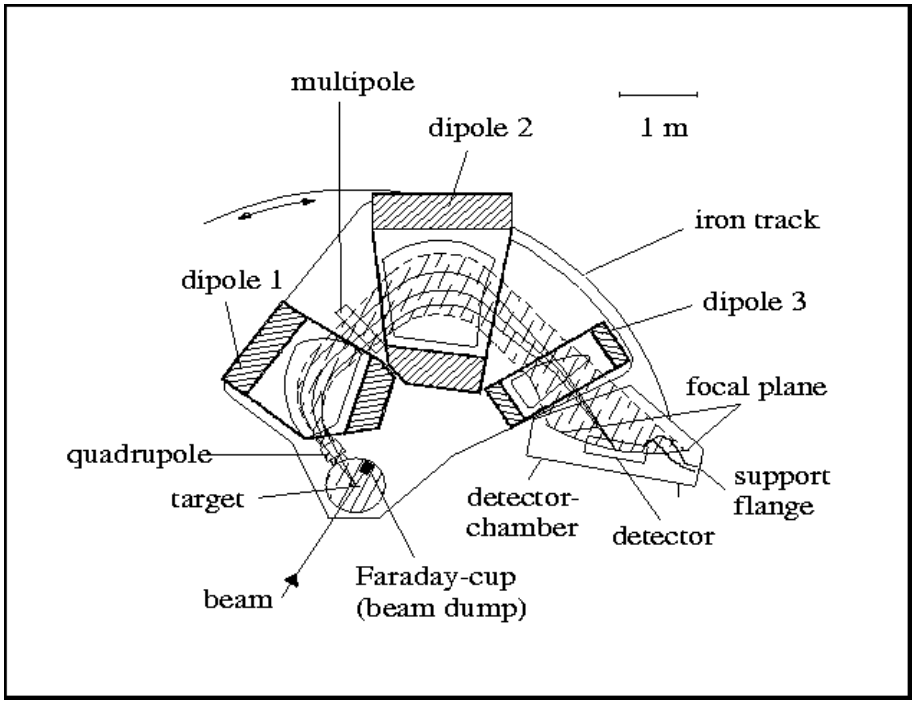

Figure 4.5: *Detailed Sketch of the Q3D Magnetic Spectrograph [77].*

Kinematic broadening

As explained in Ref.[79], the energy of the different particles vary with angle, which implies that a correction is essential in order to allow it to remain at the same spot. This correction is therefore there to avoid loss of resolution and kinematic broadening of the peaks in the energy spectrum and is provided by the multipole field and the curved edges of the dipole fields.

If as in Ref.[79], the kinematic factor K is defined as

$$K = -\frac{1}{p}\frac{dp}{d\theta}, \tag{4.4}$$

where θ is the reaction angle. Which can be written as

$$K = \frac{\sqrt{\frac{M_b \times M_0 \times E_b}{E_0}} \times \sin\theta}{M_0 + M_R - \sqrt{\frac{M_b \times M_0 \times E_b}{E_0}} \times \cos\theta}, \tag{4.5}$$

[1]Used to collect the beam.
[2]Meaning either quadrupole, hexapole, octupole and decapole

In the Q3D series of spectrographs, the detector displacement is defined as

$$\Delta z = -DM\rho K \tag{4.6}$$

where D represents the dispersion, M the magnification, ρ the curvature and K the kinematic factor. The dispersion is usually large in Q3D spectrograph and the magnification M is unity or larger. Thus, the detector displacement is usually very substantial even for average values of kinematic factor. This fact implies that for these instruments, a very satisfactory method of correction is usually needed. The defocussing multipole, which can be seen in Figure 4.5, is consequently ultimately located preferably close to the middle of the spectrograph and has as one of its function to push the x-image [3] back to the detector.

The curved focal plane has a full length of 1.8 m. Over the past decades, different types of detectors were developed with the principal aim to cover most of the focal plane length and to have a sufficient position resolution of less than 0.5 mm with no periodic effects in the position determination. Furthermore the detector has to have a good particle identification capacity and the capability to withstand the high background condition [80]. The detector described by J.Ott and al. in [76] fulfilled all the criteria except for the fact that it only had an useable active length of 35 cm. The same concept was used to build the presently used detector which has a well increased active length of 90 cm.

[3] Noting that a particle is assumed to be emitted from (or passing through) point x, y in the plane z = 0.

4.3 Munich Q3D Cathode Strip Detectors with Single-Strip Readout

The active length of the Q3D focal plane detector has been increased to nearly 90 cm. This however still only makes use of half the length of the full Q3D focal plane. Despite this fact, it still presents some distinct advantages which alongside its characteristics are described here.

4.3.1 The detector

The detector is composed of two proportional gas filled detectors followed by a scintillator. The first proportional detector provides the energy loss related data to provide particle identification and the second the position information.

The outer dimensions of the detector housing is as follow: length of 1600 mm, width of 190 mm and height of 250 mm and the inner dimensions are length 1520 mm, width and height 170 $\times$ 170 mm [80]. The scintillator has a thickness of 7 mm and a height of 14 mm. Figure 4.6 shows a schematic cut through the detector where the arrangement of the gas filled detectors and scintillator can be seen.

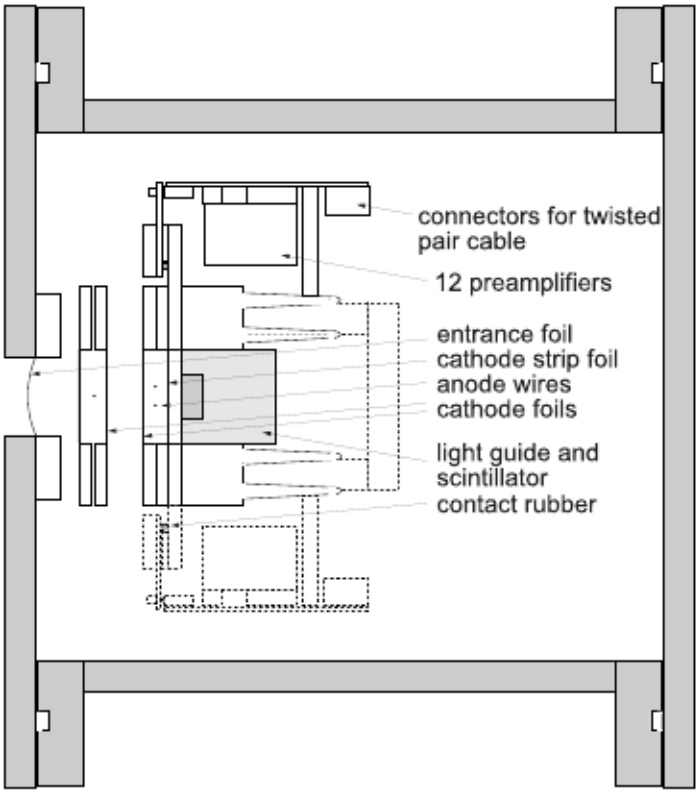

Figure 4.6: *Schematic cut through the focal plane detector where incoming particles enter from the left [80].*

Particles enter the gas filled detector and ionise the gas generating free electrons which create an avalanche around the anode wire. The avalanche created is proportional to the energy loss of the particle. Therefore when an incoming particle penetrates the first proportional detector, a separate readout of the upper and lower anode wire gives rise to two separate energy loss (ΔE) signal. The particle then continues and penetrates the second proportional detector, which is constituted of 255 segmented cathode strip foils which are 3.5 mm long, 3.0 mm wide and are separated from each other by 0.5 mm. Within this detector, the avalanche previously produced simultaneously induces a positively charged Gaussian shape distribution on the neighbouring cathode strip foils the centroid of which provides the position of where the particle crossed the anode wire. The particle then proceeds and stops in the scintillator. The combination of both ΔE signals with that of energy collected from the scintillator provide an excellent particle identification and focal plane position known within 0.1 mm.

Figure 4.7 shows the working principle of the multiwire proportional chamber (MWPC) where segmented cathode strip can be seen.

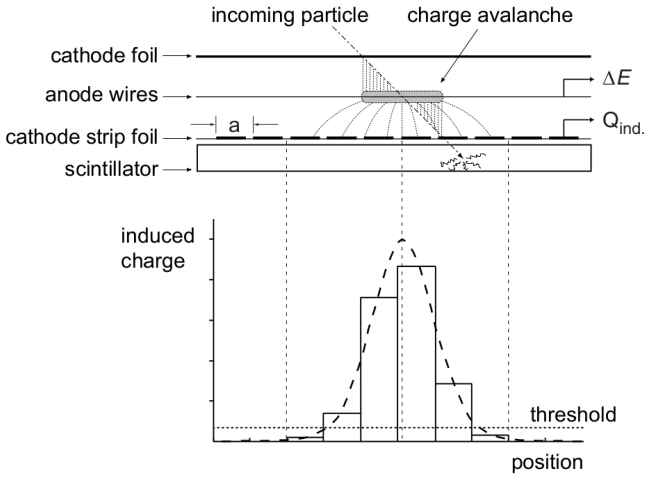

Figure 4.7: *Focal Plane Detector Working Principle [80].*

The detector presents some distinct advantages as is the fact that in contrast to a longer detector, a shorter detector means that the energy calibration is very well described by a second order polynomial.

Furthermore, during data analysis the Gaussian fit method used for offline data analysis produces no systematic errors in the position determination [80].

4.4 Detector Electronics

The second proportional detector, as described earlier, comprises 255 read-out cathode strips. Each cathode strip is fitted with a charge sensitive preamplifier. The signal output of each preamplifier is then given to a peak-hold-discriminator unit [76]. When a signal above the threshold is detected by one of the strips, a digital signal is sent to the Application Specific Integrated Circuit (ASIC) which then scans all fired strips and determines whether it is valid. An event is considered to be valid when 3 to 7 of the neighbouring strips have fired (referred to as having a multiplicity between 3 and 7). The multiplicity of 3-7 is, as detailed in Ref.[76], expected for particles entering the detector at angles located between 40-50 degrees which is the angle at which the reaction products enter the detector. The ASIC finishes its work in about 2.5 μs. If the event is not

valid, then all components are reset. The coincidence between the wire planes and the scintillator signal triggers the digital position information read-out which consists of the start trip number, the values of the charge on the 3-7 strip number and the multiplicity. The ASIC signal is not included. As a consequence, no position information is read when the ASIC is busy working with invalid events such as the ones with either wrong multiplicities or even with multiple correct multiplicities. Each time the ASIC is busy, there is therefore no output and counts are registered by the zero-values in the positions spectra. This zero-values position therefore monitors the detector correlated deadtime. This detector correlated correction can easily be performed during the analysis. The average correction needed is usually of the order of less than 10% [80]

4.5 Data Acquisition

The data acquisition related software can be divided into two parts with different charateristics. The first is an online data acquisition based system which calculates the position of an event with the centre of gravity method. This method generates a systematic error which leads to periodic structure in the spectrum. This periodicity therefore reflects the periodic structure of the cathode foil.
The second part of the data acquisition system is an offline based process. It is performed by a different method of replaying the data. In this case, a Gaussian fit method is used for the charge distribution on the cathode strip. In this case, the periodic structure is eliminated and event positions can be determined with a precision better than 0.1 mm [76].

During the experiment, for each run, scaler 1 and scaler 3 were recorded. Scaler 1 gives the beam current integrator (BCI) value [4] and scaler 3 gives BCI multiplied by the Data Acquisition (DAQ) dead time. This implies that the DAQ is live for Scaler 1 - Scaler 3. Appropriate corresponding correction can easily be performed during the analysis process.

[4] Can also be defined as the measure of the charge deposited in the Faraday cup.

4.6 Experimental Conditions Consideration

Before the experiment took place, there were a few important points that needed investigation, such as the possibility of unwanted ejectiles from reactions of contaminants in the target reaching the focal plane and masking the peak of interest. It is important to note that outgoing ions with magnetic rigidity comparable to reactions on the target nuclei will follow a similar bending radius to the particles of interest. As described in the following section 4.7, implanted ^{20}Ne in a ^{12}C target was used. This will lead to the possibility of having ^{12}C reaction products, alongside reaction products of other common contaminants such of ^{28}Si and ^{16}O, with similar bending radius on the focal plane spectra. However it was also expected that as a result of kinematic broadening, other reactions products will be out of focus and broadened compared to the one resulting from the ^{20}Ne reaction products. By therefore calculating the magnetic rigidity of possible other contaminants, it was possible to project the extent of contamination on the focal plane spectra and the change in magnetic rigidity separation as incident beam energies changed. To this effect, magnetic rigidity against angle was checked for 15 MeV, 18 MeV, 20 MeV, 22 MeV and 25 MeV beam energies within the region of interest alongside ^{12}C(d,p)^{13}C, ^{13}C(d,p)^{14}C, ^{22}Ne(d,p)^{23}Ne, ^{16}O(d,p)^{17}O. Figures 4.8 and 4.9 show examples of some of the plots made during this planning. In these plots, angles varying from 0-180 as a function of the magnetic rigidity can be seen.

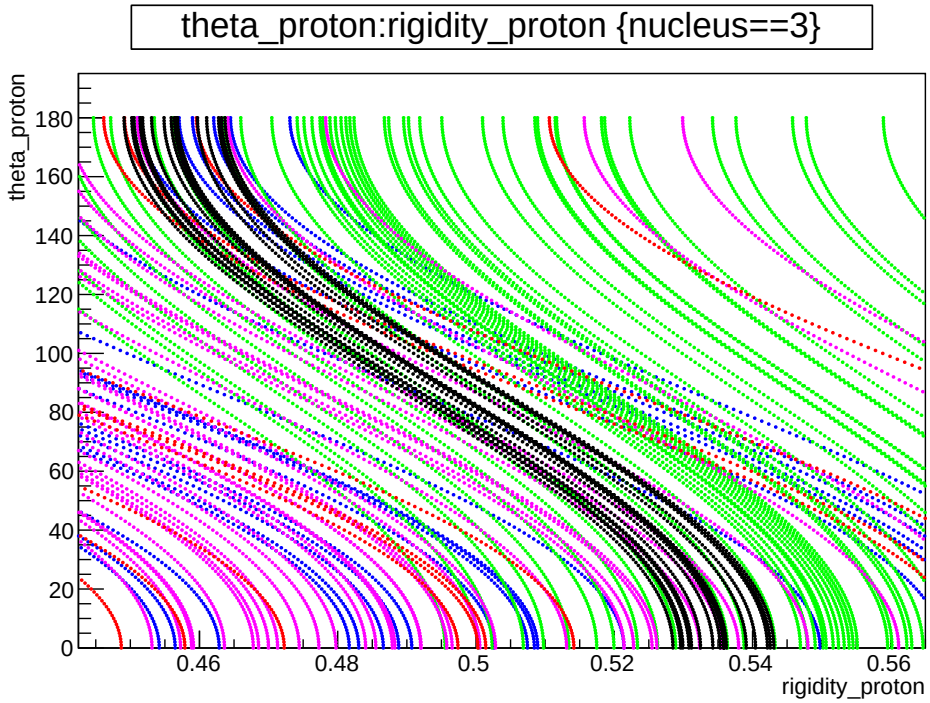

Figure 4.8: *Kinematics for 18 MeV beam energy of* $^{20}Ne(d,p)^{21}Ne$ *(black) alongside expected contaminants such* $^{12}C(d,p)^{13}C$*(red),* $^{13}C(d,p)^{14}C$*(blue),* $^{22}Ne(d,p)^{23}Ne$*(Green),* $^{16}O(d,p)^{17}O$*(Magenta).*

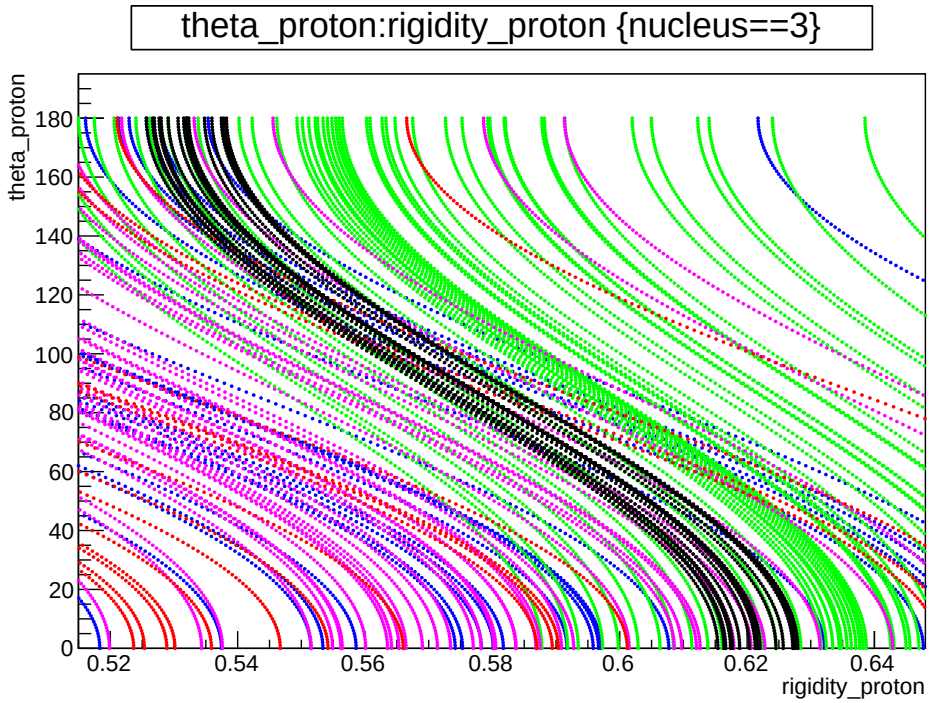

Figure 4.9: *Kinematics for 23 MeV beam energy of* $^{20}Ne(d,p)^{21}Ne$ *(black) alongside expected contaminants such* $^{12}C(d,p)^{13}C$*(red),* $^{13}C(d,p)^{14}C$*(blue),* $^{22}Ne(d,p)^{23}Ne$*(Green),* $^{16}O(d,p)^{17}O$*(Magenta).*

4.7 The Experiment

The experiment which took place from the 24^{th} July 2012 to the 30^{th} July 2012 used a 22 MeV deuteron ($^2H^+$) beam and ^{20}Ne implanted targets.

The 22 MeV beam energy was chosen to populate ^{21}Ne excitation energies within the region of interest and because it would have allowed a quick jump to 24 MeV which was the beam energy of choice for a ^{20}Ne(d,t)^{19}Ne experiment planned to run within the same experimental campaign. 22 MeV allowed in addition a well spaced separation of different excited states of ^{21}Ne and no protons from (d,p) reactions on ^{12}C and ^{13}C on the focal plane. Some contamination from (d,p) on ^{16}O was expected. The ^{21}Ne excitation energies located within the focal plane of the Q3D spectrograph covered ranged from 6.9 MeV to up to 8.5 MeV.

Beam intensities from 500 nA to up to 1 uA were used during the experiment as the beam was gradually increased.

Different targets were available with different thicknesses as given in table 4.1 below.

TARGET ORIGIN	TARGET SPECIFICATION
Dresden2	7 ug/cm^2 of ^{20}Ne in 40ug/cm^2 of ^{12}C
Dresden5	7 ug/cm^2 of ^{20}Ne in 40ug/cm^2 of ^{12}C
Yale	4.67ug/cm^2 of ^{20}Ne in 40ug/cm^2 of ^{12}C
Yale	18ug/cm^2 of ^{20}Ne in 40ug/cm^2 of ^{12}C
Seattle	7.6ug/cm^2 of ^{20}Ne in 40ug/cm^2 of ^{12}C
ORNL	6 ug/cm^2 of ^{20}Ne in 30ug/cm^2 of ^{12}C

Table 4.1: *Different available targets during experiment.*

Only two different set of targets were used, both produced at Dresden-Rossendorf (Dresden2 and Dresden5). Dresden5 was used first and covered the major part of the experiment.

The original thickness were as stated on the previous table, of 7ug/cm^2 of ^{20}Ne in 40ug/cm^2 of carbon. During the experiments, measurements were taken at various angles ranging from 8° to 35°.

CHAPTER 5

$^{20}Ne(d,p)^{21}Ne$ Data Analysis

> The beginning of wisdom is this: Get wisdom. Though it cost all you have, get understanding.
>
> Proverbs

In this chapter the procedure for sorting, particle identification, calibrating and extracting the yield from the experimental data is described. The methods used to calibrate the data using $^{28}Si(d,p)^{29}Si$ measurements is detailed alongside the determination of excitation energies of identified ^{21}Ne states. Furthermore the methods used for raw yields extraction and calculation of differential cross section are also recounted.

5.1 Data sorting and Particle Identification

The data used, as explained in Section 4.5 were obtained through the offline based replay where the Gaussian fit method is used [80]. Figure 5.1 shows a spectrum generated by the Gaussian fit method. For generating the position spectrum the events are sorted such that the width of one strip (3.5 mm) corresponds to 10 channels.

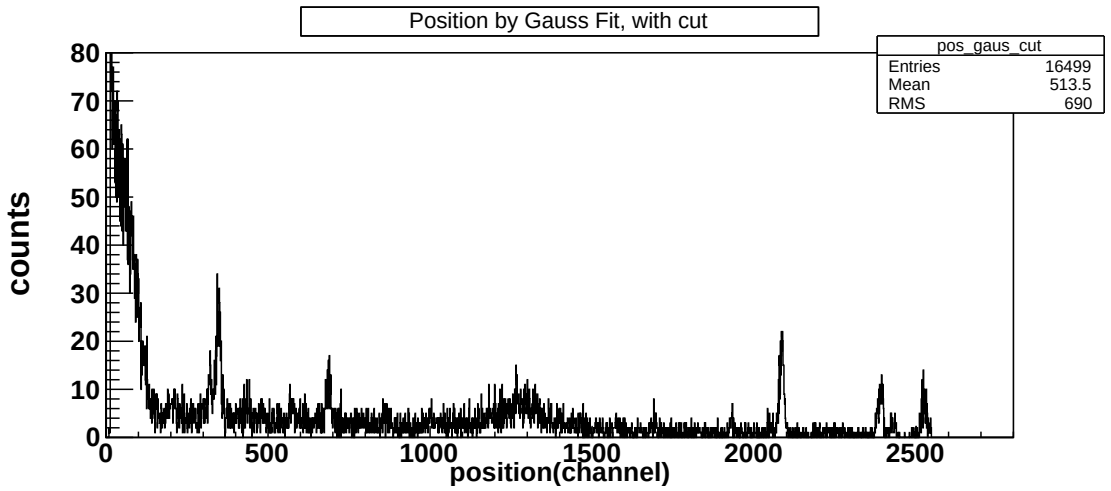

Figure 5.1: *Position spectrum of protons from the $^{20}Ne(d,p)^{21}Ne$ reaction with cut made on outgoing proton, E_d= 22 MeV at a lab angle of 20° (Run 175).*

Given that a variety of reaction channels are capable of producing outgoing products with magnetic rigidity similar to those of the outgoing protons from the ^{20}Ne$(d,p)^{21}$Ne reaction, they may lead to the possibility of detecting multiple types of particles on the focal plane. There is indeed for example the potential of having deuterons or even tritons on the focal plane spectra.

For particle identification, as mentioned in the previous chapter, the combination of energies losses from the anodes (ΔE) with the residual energy signals from the scintillator, was used. It was expected that lower mass particles would be expected to lose less energy through gas detector which meant few electrons collected at the anodes. Thus when considering one of the anode signals versus the other, different reaction products were expected to be located along the diagonal with the lower mass particle expected to occupy the lowest place. On the other hand, energies deposited in the scintillator are expected to be highly dependent on the reaction process Q value and initial energy. Indeed, the reaction product with higher residual energy would deposit more energy. Figures 5.2 and 5.3 show energy loss in anode 1 against energy loss in anode 2 before and after the proton cut was applied. Protons can be clearly seen and differentiated from scattered deuterons. Figures 5.4 and 5.5 show anode energy loss versus residual energy in the scintillator before and after the proton cut was applied. The ^{20}Ne$(d,p)^{21}$Ne reaction has a positive Q value (4.537 MeV), therefore the protons compared to the scattered deuterons are on the higher end concerning their residual energies. The selection of the particle of interest was performed when the data were resorted during the generation of the offline version of the measurements. This provided a way of eliminating most of the undesired

background signals by not jeopardising the signals generated by the outgoing protons. Only events remaining after the cut are included in the final focal plane spectra.

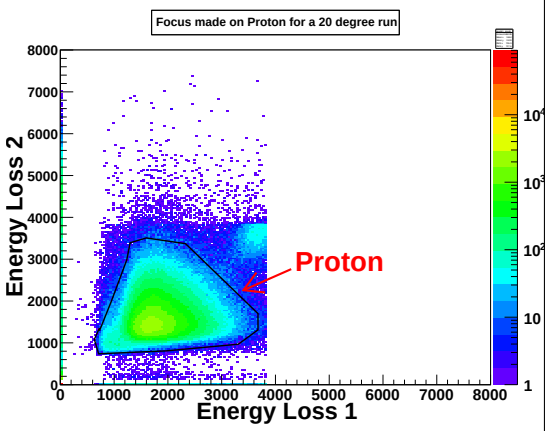

Figure 5.2: *Two dimensional histogram showing energy loss collected on one anode versus energy loss collected on the other anode where the proton, particle of interest is shown.*

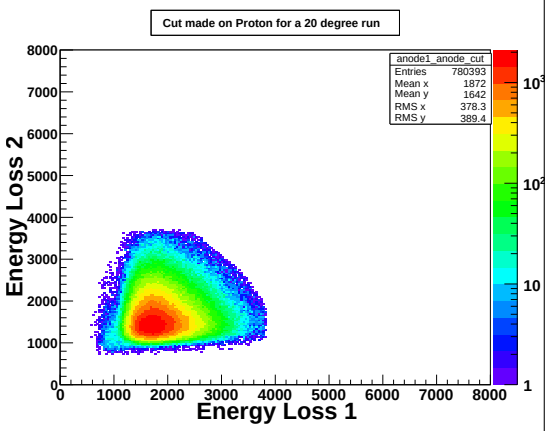

Figure 5.3: *Two dimensional histogram showing energy loss collected on one anode versus energy loss collected on the other anode after cut has been applied to select the proton.*

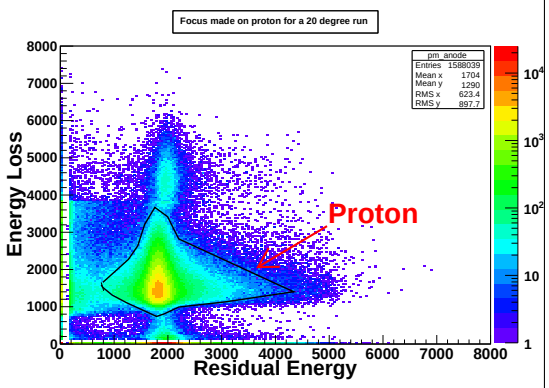

Figure 5.4: *Histogram showing energy loss signal from one arbitrary anode versus residual energy collected by the scintillator where the proton is shown.*

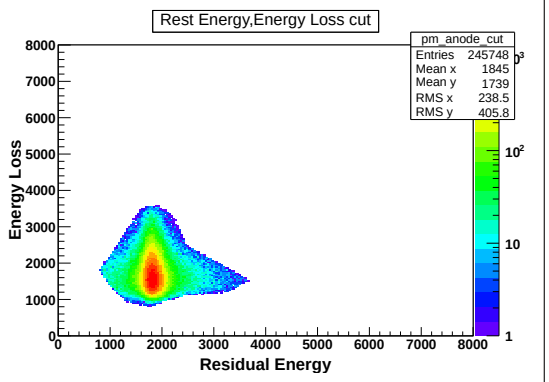

Figure 5.5: *Histogram showing energy loss signal from the anode versus residual energy collected by the scintillator where the proton only has been selected.*

5.2 Data Calibration

For calibration purposes, ^{28}Si(d,p)^{29}Si reaction measurements were taken at the same excitation energies and same B-field settings as the ^{20}Ne(d,p)^{21}Ne data.

5.2.1 $^{28}Si(d,p)^{29}Si$ Data and level Identification

Given that the excitation energy of interest lay between E_x = 7.65-8.05 MeV, the focus (central point) of the focal plane was taken to be 7.7 MeV. Measurements were taken at 8°, 11°, 13°, 15°, 20°, 25°, 30° and 35°. Known ^{29}Si states, which are available in the literature [68], were identified in the focal plane spectra.

Major contaminants such as ^{17}O nuclei resulting from ^{16}O(d,p)^{17}O were also identified and associated to states found in literature[68]. With a view to help with ^{29}Si identification, all measurements taken at different angles were set at an identical focal plane position range. In order to identify specific ^{29}Si states, the focal plane Plotter simulations package (codes can be found in Ref. [81]) were used. Plotter is one of the four Java Class simulation packages which allow to plot position spectra on the focal plane detector for various reaction channels.

Figure 5.6 shows all Silicon runs at different angles, all set at the same range.

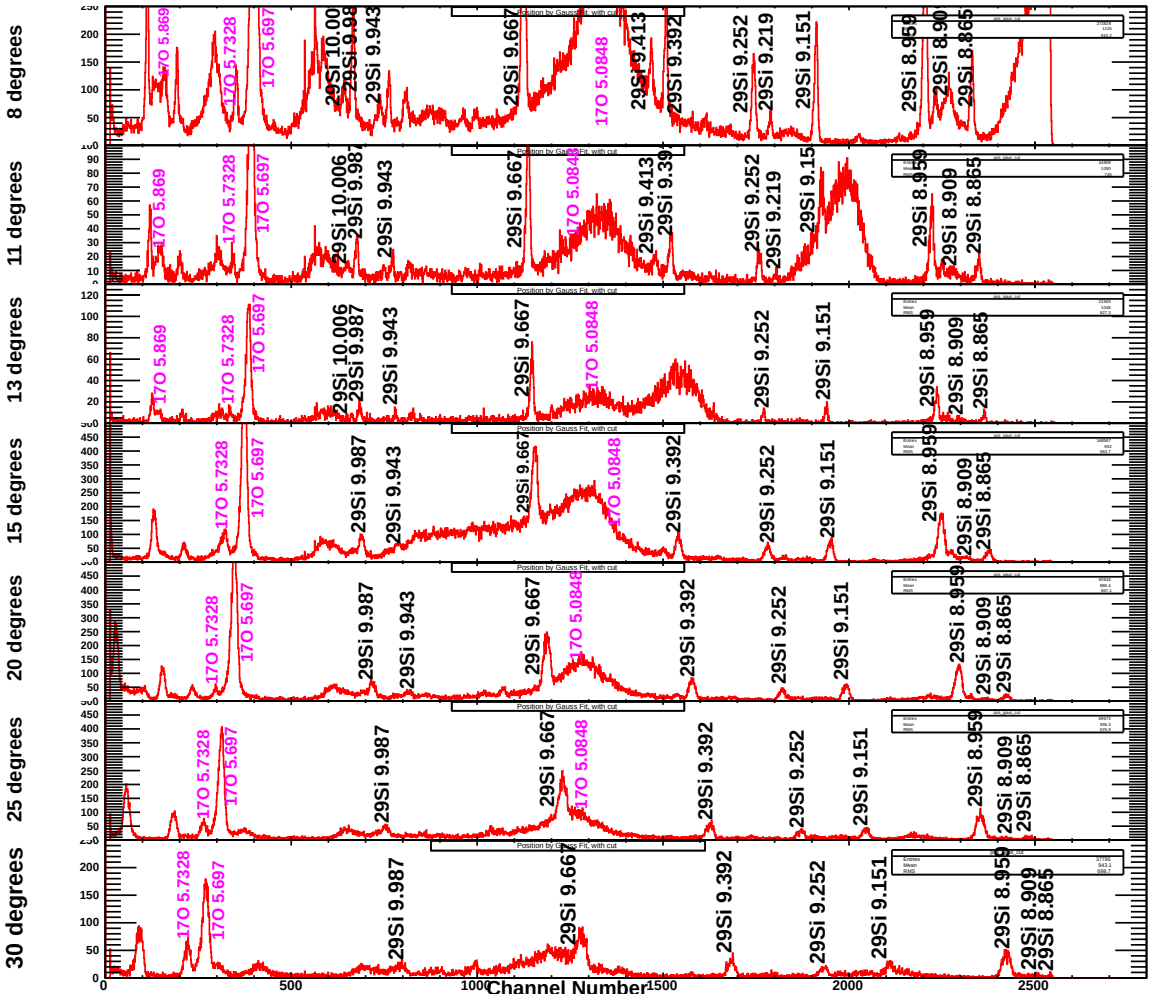

Figure 5.6: *Set of focal plane excitation energy spectra for the $^{28}Si(d,p)^{29}Si$ runs at 8°, 11°, 13°, 15°, 20°, 25° and 30° respectively. Different ^{29}Si levels alongside main ^{17}O contaminants are indicated.*

For nuclei of the same species, a linear relationship between the excitation energy against position in the focal plane (channel number) was expected. For different species however, the linear relationship has to be established between the magnetic rigidity of each state against the position in the focal plane. Calculations in this case were performed using JRelkin [81]. JRelkin is a relativistic Kinematics Program and another of the four Java Class simulation packages.

5.2.2 Magnetic Rigidity (Bρ) Calculation

The proton magnetic rigidity measured for known states of the ^{28}Si(d,p)^{29}Si and ^{16}O(d,p)^{17}O reactions were calculated and, plotted against the channel number of the associated peak in the focal plane spectrum (see Figure 5.7) very well described by a second order polynomial.

This fit provides a calibration, enabling to extract the magnetic rigidity of states of interest in the main reaction from the channel number of the relevant peak in the focal plane spectrum.

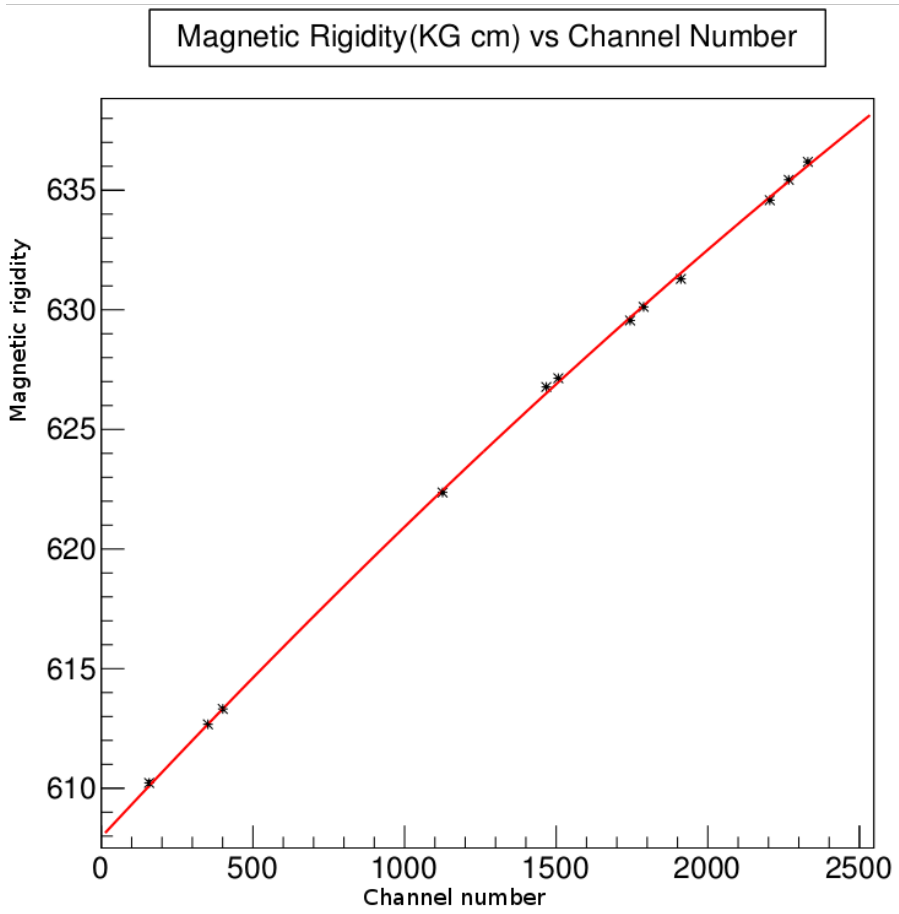

Figure 5.7: *Magnetic rigidity against channel number fitted with a second order polynomial with as parameters* p_0*=608.04 ± 0.15,* p_1*=0.0136 ± 0.0003,* p_2*=-6.62×10^{-7} ± 1.09×10^{-7}.*

5.2.3 Energy of ^{21}Ne States

For the second part of the calibration, in order to directly establish the relationship between magnetic rigidity and excitation energies of a given isotope (in this case ^{21}Ne, ^{29}Si and ^{17}O), an expression of excitation energy as a function of the magnetic rigidity was determined for each nucleus. The expression was only obtained for the region of interest. This meant that for ^{21}Ne, the expression was found for states located within E_x = 6-9 MeV. Figure 5.8 shows the relationship between the ^{21}Ne excitation energies and a given magnetic rigidity that resulted from a first order polynomial fitting. This subsequently implied that it was possible to determine the excitation energy of any ^{21}Ne state located within this range from the focal plane position.

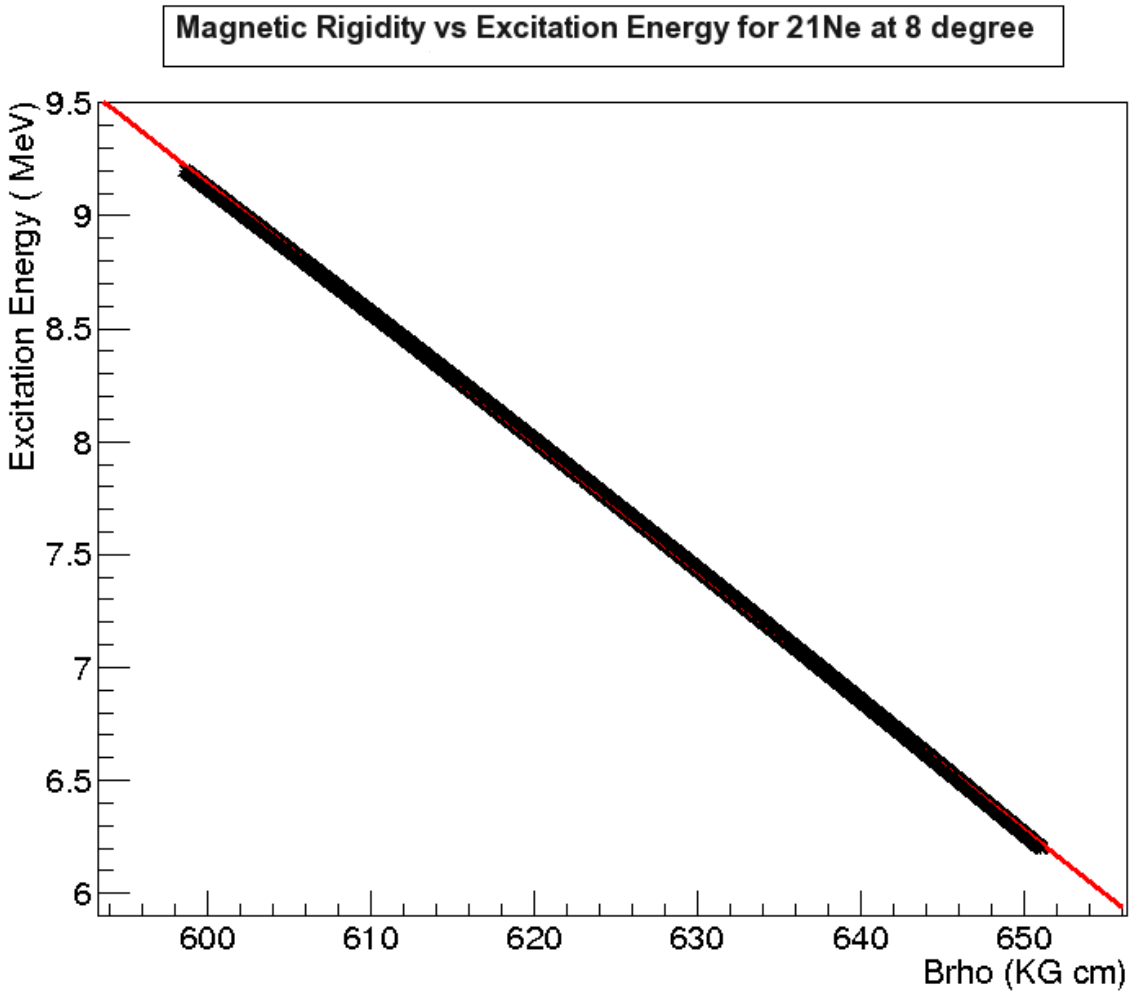

Figure 5.8: *This graph shows the relationship between different ^{21}Ne excited states and magnetic rigidity. A first order polynomial was fitted with following parameters p_0=43.4859±3.0009×10^{-3}, p_1=-5.72362±4.7969×10^{-6}.*

Identification of ^{21}Ne States

For identification, kinematic broadening and shift with angle of all nuclei not in focus (of which contaminants are part), resulted in the ^{21}Ne states being easily identifiable. The peaks for lighter contaminants move towards higher excitation energies with increase in angle and in concomitant manner for heavier contaminants move towards lower excitation energies. Calculations of the relative change in magnetic rigidity through increasing angle confirmed this predicted behaviour. Effectively, as explained in details in Ref.[79], the focus being made on ^{21}Ne states translate to applying a kinematic correction on the kinematic broadening. This correction as detailed in the previous chapter, allows the residual nucleus to be left at the same spot on the detector for the same state and thus is therefore independent of direction of emission.

Figure 5.9 shows ^{20}Ne(d,p)^{21}Ne proton related spectra at different angles ranging from 8° to 30° on the same graph as ^{28}Si(d,p)^{29}C proton spectra at all angles. The proton spectrum from the ^{12}C(d,p)^{13}Si reaction at 8° is also shown. This figure was useful in identifying contaminants as the positions of silicon and oxygen related states can be seen moving while neon related state positions remained mainly fixed.

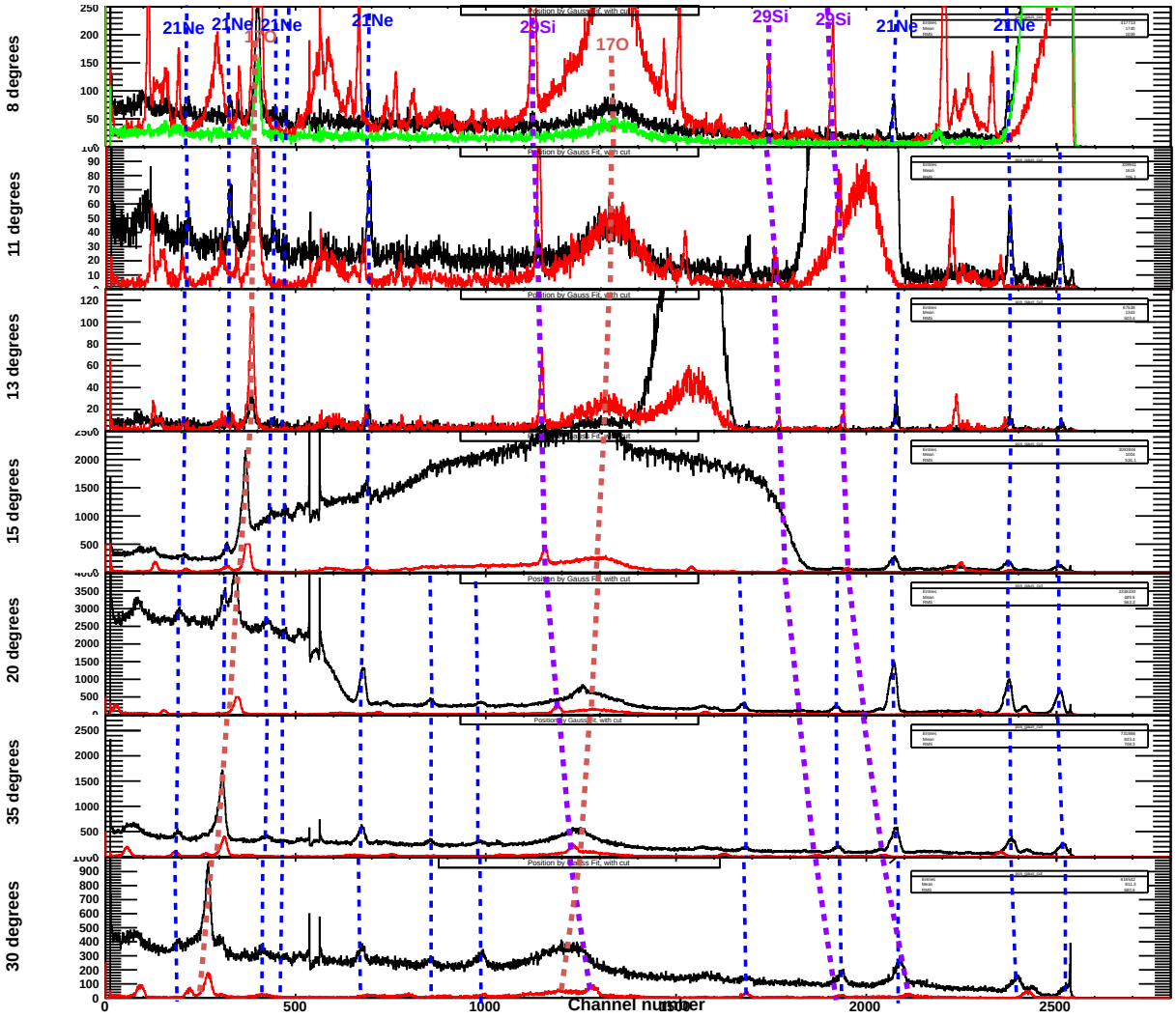

Figure 5.9: *Proton spectra at 8°, 11°, 13°, 15°, 20°, 25° and 30° respectively as a function of channel number. This figure shows Ne runs (black), Si runs used during calibration (red) and C run at 8° only (green). It can be seen that* ^{21}Ne *remain mostly fixed with angles while* ^{29}Si *and* ^{17}O *evolve.*

A very small shift on the ^{21}Ne position on the focal plane was observed. This shift of up to 17 keV was due certainly to the error in setting the main dipole field. The excitation energy of each identified ^{21}Ne state was determined from the calibration from knowledge of their position on the focal plane. The excitation energies of previously published states determined from the calibrations were in agreement for most states($\leq$ 25 keV). All ^{21}Ne peaks were observed at most angles. However at some angles, contaminants fell within the region occupied by states of interest leading to the obscuring of some ^{21}Ne peaks.

5.3 Background Estimation and Raw Yields Extraction

During the experiment, ^{12}C(d,p)^{13}C measurements were intended to be taken for background estimation. However due to time constraints ^{12}C(d,p)^{13}C data ended up only to be taken at 8° angle. The background was then mostly established by using the ^{20}Ne(d,p)^{21}Ne data. Apart from statistics uncertainties, different systematic uncertainties such as the exact shape of the background, exact region or appropriate background range and background scaling were to be taken into account.

Those different considerations led to a methodology in the background estimation of each state at each angle. The following approach allowed not only to estimate the background and obtain the yield but more importantly to estimate different uncertainties associated with that extraction.

The extraction of the background turned out not to be straightforward given the presence of rather substantial contaminants peaks throughout the spectrum. What turns out to be important for the background estimation of given peak are the background shape itself and the range around the peak from which it is estimated.

1. In order to determine the uncertainties in the focal plane position range, the first step was to choose two sets of ranges in the neighbouring of the peak which was as free as possible of contaminant peaks: One range covered an extended enough region to give an averaged shaped and the second much shorter range but not in direct immediate neighbouring to give the background shape at a closer range of the given peak.

2. For addressing the shape related uncertainties, for both ranges, then fit a first and a second order polynomial which by direct look at the data spectra mimicked quite well the suspected background shape. This led to a total of four different background estimations. The estimation in different systematic errors such as on region estimation, error arising from 1st and 2nd order polynomial fitting, background scaling error was made. The estimation in the background range was expected to have the highest uncertainties.

3. After different fittings had been performed, the estimated background was subtracted.

4. Thereafter a Gaussian was fitted to the subtracted peak and raw yield extracted. At this stage, the integral (direct count number) was also extracted. The integral at this stage only serves as mere comparison of the quality of the fit. For few peaks and for methodology accuracy purpose, yields extracted by these steps were checked and found to be similar to yields extracted by direct combination first or second polynomial plus Gaussian fit.

The following few subsections illustrate more clearly the different steps taken by going through the detailed yield extraction methodology for one of the ^{21}Ne states at a particular angle. The 7.239 MeV state for the run 278 which is a 20° run, is arbitrary chosen for illustration purpose.

5.3.1 Focal plane position range related uncertainties

Figure 5.10 shows the ^{21}Ne 7.239 MeV peak for which the centroid position on the focal plane is 2069 channels. Ranges selected varied from 1600-2500 and 1900-2150 on the focal plane.

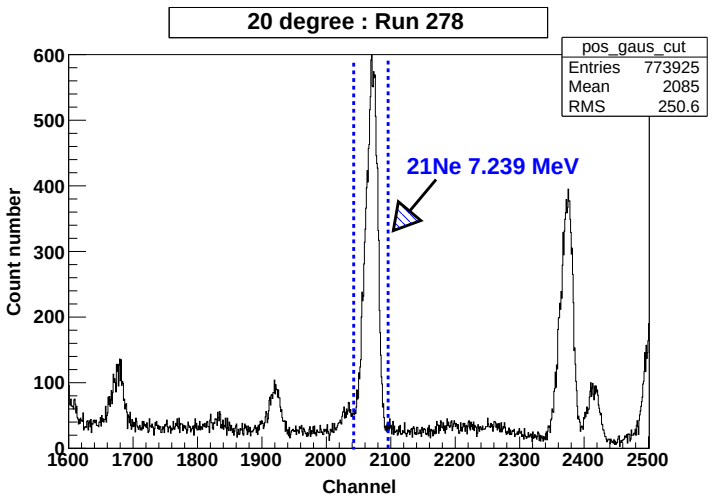

Figure 5.10: *Proton spectra at 20°. In this figure the ^{21}Ne 7.239 MeV peak alongside its position on the focal plane can be clearly seen. Run 278 which is one of the five run at 20°. This run has been picked arbitrarily for illustration purpose.*

5.3.2 Uncertainties related to Background Shape

For channel number range varying from 1600-2500, a first and second order polynomial were fitted. The mentioned first and second order polynomial are respectively shown alongside with details of fit in Figures 5.11 and 5.12.

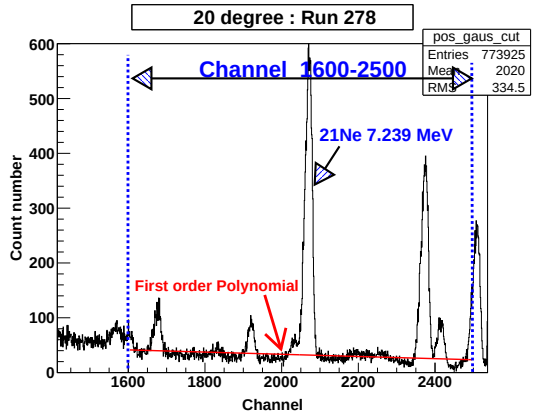

Figure 5.11: *Proton spectra of run 278 where range of selection is shown. In this figure, position ranging from channel number 1600-2500 with first order polynomial fit is shown. Fit parameters:* p_0*=57.8111±10.1534,* p_1*= -0.0109±0.0050.*

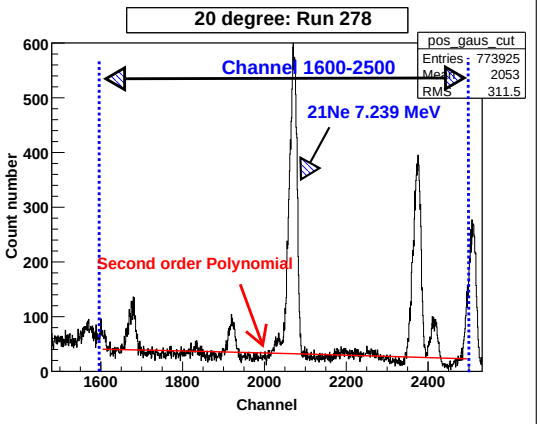

Figure 5.12: *Proton spectra of run 278 where range of selection is shown. In this figure, position ranging from channel number 1600-2500 with second order polynomial fit is shown. Fit parameters:* p_0*=-3021.44±352.11,* p_1*= 3.02±0.35,* p_2*=-0.001 ±8.510×*10^{-5}

Alongside for channel number range varying from 1900-2150, a first and second order polynomial were fitted as well. This can be respectively seen alongside with fitting details in Figure 5.13 and 5.14.

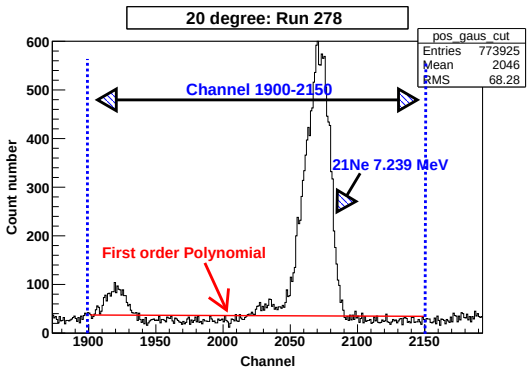

Figure 5.13: *Proton spectra of run 278 where range of selection is shown. In this figure, position ranging from channel number 1900-2150 with first order polynomial fit is shown. Fit parameters:* p_0*=73.4345±1.5087,* p_1*= -0.0200±0.0007.*

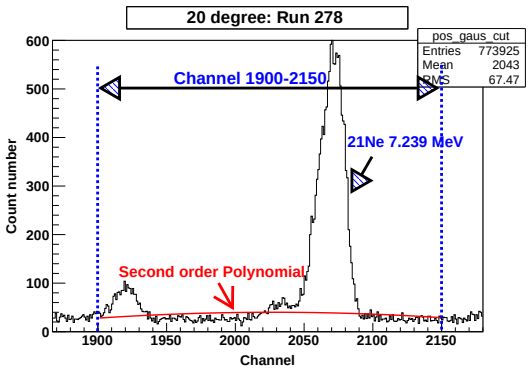

Figure 5.14: *Proton spectra of run 278 where range of selection is shown. In this figure, position ranging from channel number 1900-2150 with second order polynomial fit is shown. Fit parameters:* p_0*=52.306±13.472,* p_1*= 0.007±0.013,* p_2*=-4.988* $\times 10^{-6}$ *±3.161* $\times 10^{-6}$

Table 5.1 shows on the other hand a summary of the fit parameters.

Channel number range	Polynomial Order	Fit Parameters
1600-2500	First order polynomial	p_0=57.8111±10.1534, p_1= -0.0108698±0.0050050
1600-2500	Second order polynomial	p_0=-3021.44±352.11, p_1= 3.01949±0.34641, p_2=-0.000744528 ±8.51009×10^{-5}
1900-2150	First order polynomial	p_0=73.4345±1.50868, p_1= -0.0200222±0.0007149
1900-2150	Second order polynomial	p_0=52.306±13.472, p_1= 0.0006759±0.0131343, p_2=-4.98821×10^{-6} ±3.16064 ×10^{-6}

Table 5.1: *Details on uncertainties related to Background Shape on fit parameters.*

5.3.3 Gaussian fitting and total uncertainties determination

Using a set of ROOT codes the four different background estimations were subtracted from the spectra. A Gaussian was fitted to each subtracted spectra which allowed the raw yield to be obtained in each case. The different uncertainties which were included in the error calculation were obtained through the raw yield variation in each of the four cases. The following figure 5.15 shows the subtracted spectra for one of the four previous background (the 2nd order polynomial, range varying from 1900-2150) with Gaussian fit.

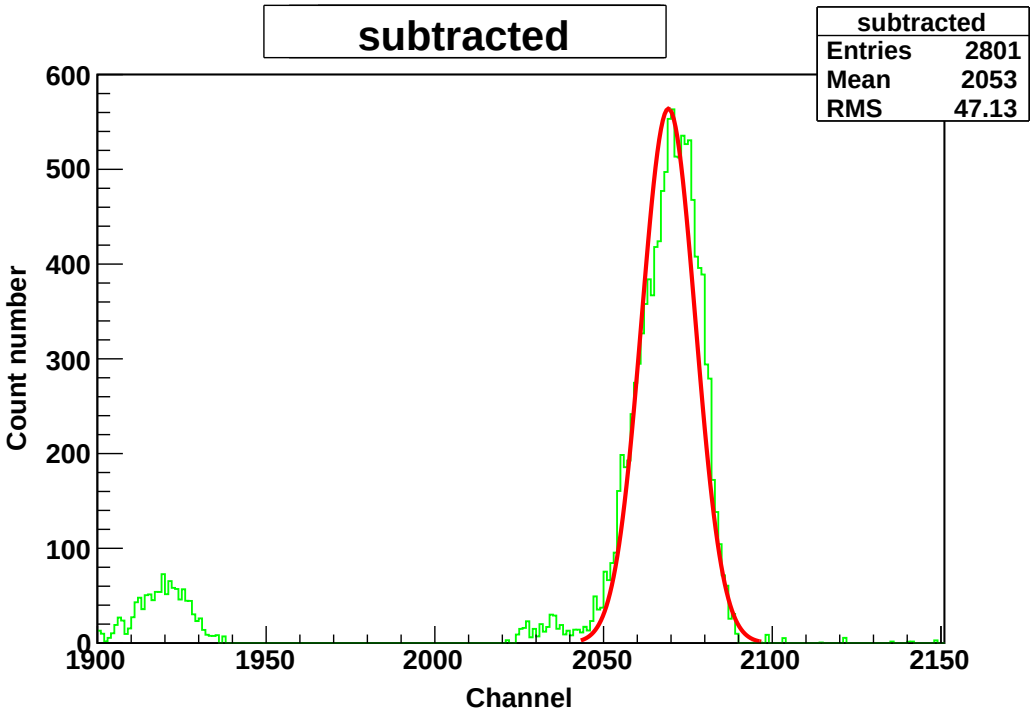

Figure 5.15: *Subtracted proton spectra from the second order polynomial, ranging from 1900-2150 for run 278. In this figure, the Gaussian fit can be seen.*

In few cases and for methodology accuracy purpose, yields extracted by these steps were checked and found to be similar to yields extracted by direct combination first or second polynomial plus Gaussian fit. An example which illustrates a second order polynomial plus Gaussian fit is shown in figure 5.16. Both methods were found to give similar results.

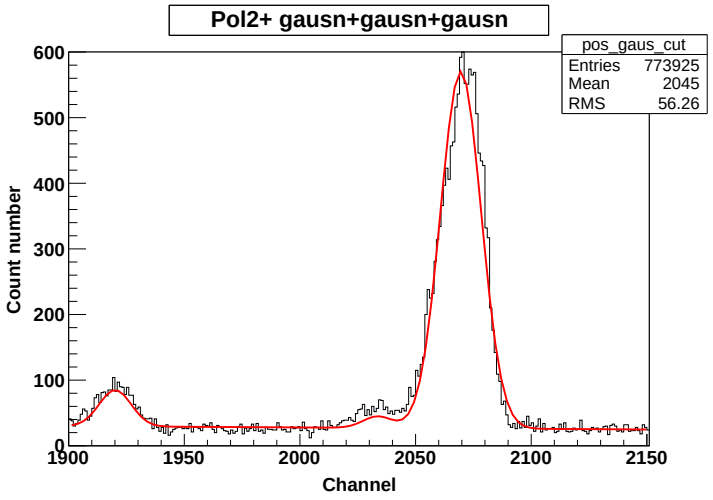

Figure 5.16: *Proton spectra showing second order polynomial plus Gaussian fit. This figure shows the second order plus three different Gaussian, made to take into account contaminants peaks within 1900-2150 range.*

5.4 Differential Cross Sections

The reaction cross section is a quantitative representation of the probability to form reaction products from two colliding particles. The following gives an overview of the determination of its different components:

The yield was determined by correcting the raw yield for the DAQ deadtime and the detector correlated deadtime.

If the raw yield is noted as Y_{raw}, the DAQ correlated efficiency is noted as ε_1, the detector correlated efficiency as ε_2 and the corrected yield as $Y_{corrected}$, the corrected yield is then be written as

$$Y_{corrected} = \frac{Y_{raw}}{\varepsilon_1 \times \varepsilon_2} \tag{5.1}$$

The description given in section 4.5 give the characterisation of both collected integer, known as SCALER 1 and SCALER 3. As explained previously, SCALER 1 gives a value of the Beam Current Integrator (BCI) and SCALER 3 (BCI_{dt}) measures the correlated deadtime, which leads for the associated efficiency to be

$$\varepsilon_1 = \frac{BCI - BCI_{dt}}{BCI} \tag{5.2}$$

Concerning the ε_2 correction, based on fact that the 0-values in the positions spectra, as described in detail in section 4.5 of the previous chapter, monitors the detector correlated deadtime. The detector correlated deadtime efficiency is given by

$$\varepsilon_2 = \frac{Overall\ count\ -\ 0\ channel\ count}{Overall\ count} \tag{5.3}$$

Leading the corrected yield to be

$$Y_{corrected} = Y_{raw} \times \frac{BCI}{BCI\ -\ BCI_{dt}} \times \frac{Overall\ count}{Overall\ count\ -\ 0\ channel\ count} \tag{5.4}$$

The number of beam particles is calculated by the integrated charge collected at the Faraday cup. In this case, a pulse was dispensed each time a charge of 2 μC was reached. For a beam with Q as the total accumulated charge or the integrated beam current and

charge state q, the number of beam particle was calculated as

$$I_b = \frac{Q}{q \times e} \tag{5.5}$$

During the experiment, because of a mechanical malfunction, for most runs the spectrograph aperture size was fixed for the x-slit at +- 19 mm and y-slit at 24.5 mm; which came to having a solid angle of 13.5 msr. The target number density, as stated in Section 4.7, was 7 ug/cm^2. During the course of the experiment, although the original nominal target thickness was known, the implanted ^{20}Ne was progressively released from the carbon foil. The leakage rate of ^{20}Ne was not monitored which therefore contributes an additional very significant uncertainty to the target thickness. Thus due to this fact, only either the relative differential cross section or ratio of cross section at different angles may be used to infer the angular momentum and therefore the spin-parity of different states.

5.5 Procedure Details for inferring angular momentum

In a straightforward case, angular momentum assignments would have been inferred by a direct comparison through the angular distribution cross sections curves of each identified state. Indeed the variation of the differential cross section of outgoing protons as a function of the observed angles are representative of the orbital angular momentum transferred in the reaction. A direct investigation with the DWBA angular distributions would have sufficed. However, given the uncertainties of the target's true thickness, this was not possible.

The following step was to look into the possibility of a direct comparison of the ratio of the differential cross section of two states, on the basis and acceptance of actual confirmed l assignments meaning by using such states as referenced or starting point. Within the energy range of this work, only three states with known spin parity values exist. That is the ^{21}Ne 8.360 MeV, 8.303 MeV and 8.062 MeV [68]. A scaling or re-adjustment of the data which helped take into account of the suggested target leakage based on the DWBA angular distribution of these states was used in this work.

5.5.1 DWBA parameters

The DWBA related programs used for this work detailed description along with downloadable source codes can be found in Ref.[82]. TWOFNR, as it is called is the extended version of the program TWOSTP which calculates the scattering differential cross sec-

tion for general form of the distorted wave Born approximation up to second order [82]. TWOFNR is an extension in the way that it allows for a finite-range generalisation of the TWOSTP set of codes. The version used in this work is the Surrey shortened version of the TWOFNR code which allows one-step transfer reaction related calculations using either the DWBA or the Johnson-Soper/Johnson-Tandy adiabatic approximation available to take account of breakup effects. The data input generation for this program is interactively accomplished by a front-end code referred to as FRONT. This FRONT program is FORTRAN based and allows to create data sets for a range of light-ion induced transfer reactions. It includes as well a range of microscopic and phenomenological optical potentials to choose from.

As stated in 2.4.2, the potential parameters are obtained by considering fitting theoretical calculations to experimental data. In this work, the sensitivity of using different suitable parameters obtained from the built in potential available through TWOFNR was briefly investigated and no major shape change was observed. The only observable changed were detected in the curve scale which does not constitute an issue for the present work. For this work, Johnson and Soper zero-range adiabatic method [45] were used to take into account the deuteron breakup. For the outgoing protons, the phenomenological potential of Bechetti-Greenles [83] were used. Given that this work energy range is located beyond the neutron separation energies, the approximation of a false binding of 0.1 MeV (in order to take into account of the high excitation states) was used for calculations. Figure 5.17 shows an example of the output when performing theoretical calculation with this code. This is the ℓ=0, where a direct comparison between simple DWBA and Adiabatic approximation input can be seen.

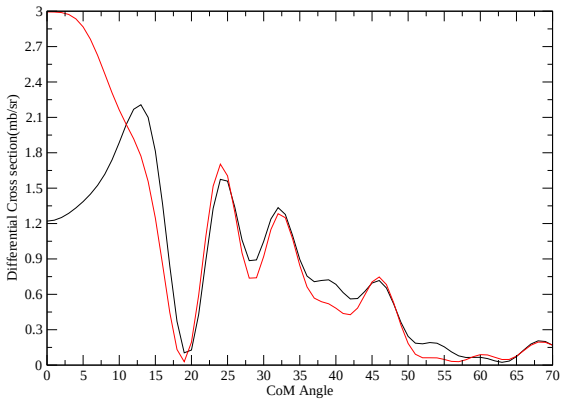

Figure 5.17: *ℓ=0 angular distribution where the output with DWBA input is seen in red and the one with the Adiabatic Approximation is seen in black.*

CHAPTER 6

^{20}Ne(d,p)^{21}Ne Results and Interpretation

In this chapter, results of the different analysis steps presented in the previous chapter are outlined. The states identified in this work are presented and compared to the information contained in the literature, here mostly contained in Reference [84]. Furthermore, the outline of the procedure used to determine the angular momentum of different ^{21}Ne states is presented.

6.1 Identified ^{21}Ne States

In total, sixteen ^{21}Ne peaks were identified. Excitation energies were estimated as described in section 5.2. Out of the sixteen, only thirteen correspond to states that are mentioned in the literature [84]. Table 6.1 gives a summary of these results. In the table, different ^{21}Ne states measured excitation energy can be seen beside existing known values from literature as detailed in Ref.[84].

Measured Energies (MeV)	Literature Energies (MeV)
6.960(2)	-
6.977(17)	-
7.032(13)	7.0226(10)
7.055(13)	7.0421(5)
7.239(11)	7.226(5)
7.330(9)	7.320(5)
7.485(7)	7.465(10)
7.558(10)	7.547(10)
7.955(2)	7.9603(10)
8.039(12)	8.062(10)
8.167(15)	8.1549(6)
8.301(9)	8.303(10)
8.328(6)	-
8.349(3)	8.360(10)
8.437(3)	8.430(10)
8.520(4)	8.522(3)

Table 6.1: *This table shows the different measured ^{21}Ne state energies with current values which can be found in literature [84].*

The measured peaks at 8.328(6) MeV, 6.977(17) MeV and 6.960(2) MeV, which are clearly seen in Figure 6.1, are not found in the literature.

All peaks were observed at most angles. It is important to note the fact that only uncertainties due to energy determinations at different angles have been considered when presenting these results. In total 32 different levels can be found in literature between the 7.0226 MeV and 8.522 MeV states. Of those 32, only 13 could be associated to the proton peaks observed in the data. Figure 6.2 illustrates the spectra of the outgoing protons at different angles: 8°, 11°, 13°, 15°, 20°, 25°, 30° and 35°. Within the Gamow window, 7.955(2) MeV has been the only observed peak.

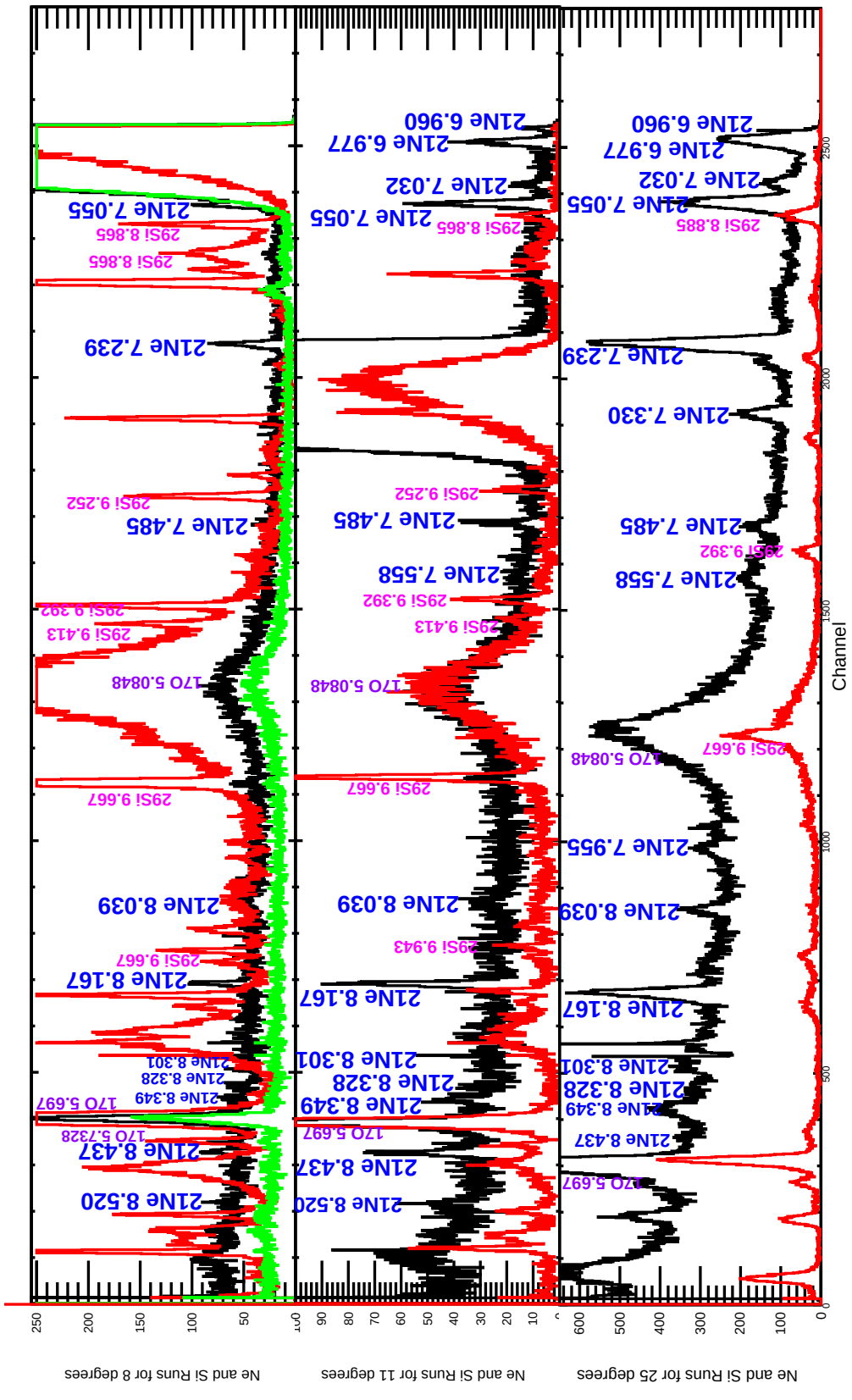

Figure 6.1: *Proton spectra where new measured peaks (8.328(6) MeV, 6.977(17) MeV and 6.960(2) MeV) can be seen. This figure shows Ne runs (black), Si runs used during calibration (red) and C run (green).*

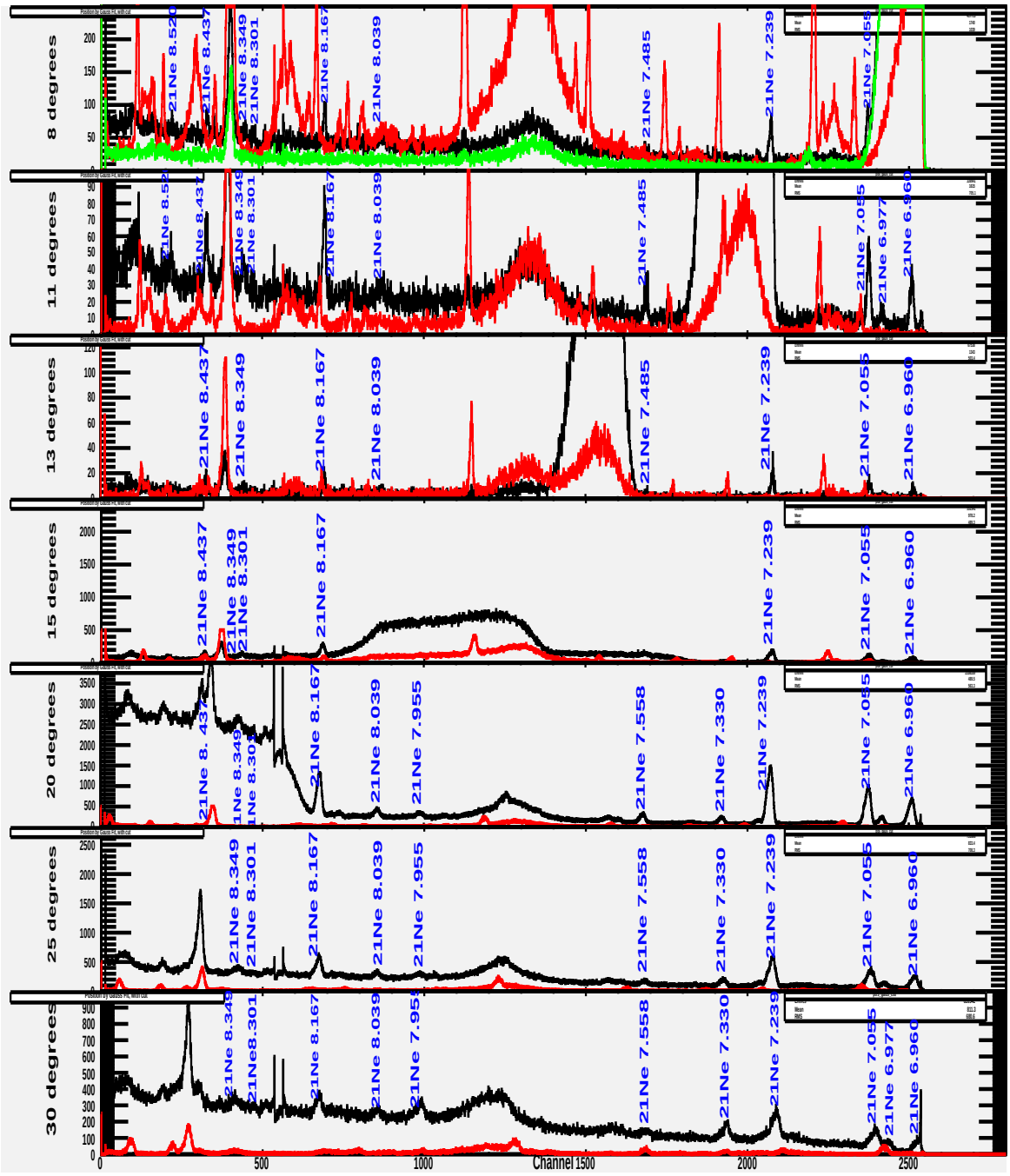

Figure 6.2: *Proton spectra at different angles where identified* ^{21}Ne *peak can be seen. Here, the spectra can be seen at 8°, 11°, 13°, 15°, 20°, 25°, 30° and 35°. This figure shows Ne runs (black), Si runs used during calibration (red) and C run at 8° only (green).*

6.2 Angular Distribution

The differential cross sections were calculated for each state at all angles at which it was observed as detailed in section 5.4. They were all calculated in the laboratory frame. Thereafter, differential cross sections and associated angles were converted from the laboratory frame to the centre of mass (CoM) frame using different set of equations detailed and explained in the appendix Chapter B. A ROOT code was written for that purpose, and for subsequent results, only the CoM values are shown. The differential cross sections with angles in the laboratory frame alongside with their respective Run number are shown in the appendix Chapter C.

6.3 Uncertainties in the Cross section and Investigation into Target Thickness Related Problem

Concerning the uncertainties into the calculation of the different cross section, as described in section 5.3, different variations into the background had already given in the experimental error. The following systematic error were to be considered: Beam intensity uncertainties were taken to be 10 % [85] and the acceptance error were deduced to be 10 % (5 % errors on each slits) [86]. The consideration of the beam intensity uncertainties were taken to be 10 % to take into account the uncertainty brought in by the line intensity. This uncertainty remains, for all angular momentum measurements, quite significant. Indeed, the current measured in a Faraday-cup could already be too high, if electrons which are set free by the beam can leave the cup. At this stage, the current is then integrated by a commercial instrument which gives one signal per 1/1000th of the charge corresponding to the setting. However, this has to be calibrated and also has an offset to be adjusted. These signals are then counted by a scaler and the dead time of the data acquisition is, as described in the previous Chapter, taken into account by another scaler. The uncertainty linked to the scaler is negligible but the other effects are not and may be reasonably accounted for by a 10 % uncertainty [87].

During the experiment, as mentioned previously in section 5.4, as expected with implanted targets [88, 89, 90, 91, 92], neon leakage seemed to be observed.

Despite the fact that both ^{20}Ne implanted targets had the same nominal thickness of 7 μg/cm^2, there were distinct differences such as background difference and stronger ^{21}Ne peak intensity when using Dresden2 compared to when using Dresden5. Both targets have as a consequence been treated separately.

Given the difficulty of using the angular distribution as they were, the primary intention was the use of angular momentum ratios by using the ^{21}Ne 8.360 MeV, 8.303 MeV and 8.062 MeV states which have known spin-parity as references and normalise the data accordingly.

Most runs with same setting (meaning same target, same angle, same focus) were taken consecutively. It was therefore expected, despite the suspected Neon loss, to have the cross section with same setting to have equivalent values within error. The data in appendix C allow a direct insight and as it can be seen most of the values expected to be equivalent were so. There were however few irregularities in need of investigation before proceeding that occurred for either a given run or simply for a very specific value. The primary plan was to find a way of investigating the suspected Neon loss.

It is important to underline that during the course of the experiment, the Neon loss suspicion arose when the neon counts in a strongly populated peak for 3 successive runs in Dresden2 were seen to drop. Those runs were only unfortunately 1 hour apart and does not give any insight of what may have been happening over the course of the whole experiment (7 days).

6.3.1 Literature for Neon loss on Implanted targets

In Ref.[90], ^{21}Ne, ^{24}Mg, ^{28}Si, ^{32}S, and ^{36}Ar targets were all implanted into 30 μg/cm^2 carbon foils by ion implantation. In this paper, C. Wrede and team highlight the difficulty to produce thin and solid targets that are constituted of ^{21}Ne, ^{24}Mg, ^{28}Si, ^{32}S, and ^{36}Ar that are similar. The difficulty is especially present in the event of charged particle product given that their energies depend strongly on the targets areal density, uniformity, composition, and composition depth profile. The aim in this case was the production of isotopically pure 3-6 μg/cm^2 targets. Each of those targets were found to be stable under a beam of $\approx$ 400 enA, 32 MeV ^{3}He$^+$ for approximatively 24 hours. Despite this stability, a loss of implanted material of 10% or less were still present from a day of cumulative beam.

6.3.2 Contaminants for Neon loss estimation

In the investigation into the fluctuations of data concerning Neon contents, one another primary intention was to attempt to use present contaminants for that purpose. Contaminants such as ^{29}Si or ^{17}O would not be expected to be lost during the measurement as in the case of ^{21}Ne. ^{28}Si as a contaminant would have been expected to already be present in the carbon backing material. Just as for ^{16}O, once the target chamber was locked and pumped out, the loss would have been expected to be minimal. ^{29}Si turned out to be too weak in Neon measurements at different angles to allow any quantitative estimate. The ^{17}O however was visible and could have allowed an approximate idea of the Neon variations throughout different runs if again runs with same setting at same angle were taken after at least a day during the measurement. This again was not the case Data with the same settings were only taken an hour apart and therefore contaminants unfortunately could not for the general purpose meaningfully help in the task.

6.3.3 Closer Look on Inconsistent Values

There were small variations observed in several states for the corresponding 11.7° CoM angle, from run 219 to run 220, Dresden5. However, not all states are in perfect agreement. For the majority of states there is an agreement and out of the ten observed states where both run 219 and run 220 are present, five of them fall within 1 standard deviation (S.D) for the two runs, a further state within 2 S.D and again a further state within 3 S.D.

During the experiment, between runs 219 and 220, there was a change in the beam current from 600 to 900 nA and a much shorter running time (17 min) for 219 compared to 220 (47 min) which gave a BCI of 337694 for run 219 compared to 1277124 for run 220. Run 219 was therefore weakly populated, and for most states has a higher level of uncertainty than run 220, compromising its reliability. Averages of the data were weighted however, giving subsequently more weight to the more reliable run, 220.

Similar observations were made in some states at 15.9° CoM angle (runs 166-170, Dresden5). Similarly, there seem to be several fluctuations, and not all states are in perfect agreement though the majority are. Out of the eleven observed states where both runs are present, in four of them both runs fall within 1 S.D. A further of five states have both runs fall within 2 S.D and two further states see the runs fall within 2.5 S.D.

Run 166 was weakly populated as well and had higher uncertainties for the majority of the eleven measured states, limiting the overall reliability. Averages were again weighted, giving more weight for most states, to the more reliable run (170).

Further down, for the Dresden2 case, some states at 21.2° CoM angle, considering runs 278, 279 and 280, an interesting pattern emerges. Although the majority of runs are in good agreement and lie within 2 S.D (for example, out of the fourteen observed states, nine of them fall within 1 S.D for both runs), there appears to be a progressive reduction when chronologically comparing runs 278, 279 and 280, which suggest a small loss of Neon in the target. In subsequent data, averages calculated as weighted averaged values have been used. It is also important to highlight that in the following runs at different angles, that is for runs 282, 283 and 284 for states at 26.5° CoM angle and for runs 286, 287 and 288 for states at 31.8° of the Dresden2 data, weighted averaged values were used in the analysis.

It should be noted that runs 224 and 225 (preceding run 226, intended to be the only run at 8.5° CoM angle), were both faulty due a setting issue, details of which can be found within Table A.1 within the appendix. There were a wrong V_a setting used during those runs. It is also important to highlight that both runs during the experiment were interrupted and therefore very short and ought to be discarded. Run 226 was found to have an unusually high BCI deadtime BCI_{dt}=18.9%, and a very high detector correlated deadtime of 15.7%, leading to it having the yield correction factor at least 25-30% which is notably higher than other runs (as defined in section 5.4). Furthermore, given the peculiarity of the settings change in runs 224 and 225 preceding this run and this recorded anomaly, it has subsequently been disregarded in any following calculations.

Furthermore, it is necessary to mention that at 37.1°, only one single run exists. Run 291, the very last run of the experiment, had a relatively short running time, and therefore weakly populated for most states, making it very difficult to use in most cases. The 37.1° could not therefore be used for most states, namely the ^{21}Ne 8.167 MeV, ^{21}Ne 7.955 MeV, ^{21}Ne 7.558 MeV, ^{21}Ne 7.330 MeV, ^{21}Ne 7.239 MeV, ^{21}Ne 7.055 MeV, ^{21}Ne 7.032 MeV, ^{21}Ne 6.977MeV.

6.4 Angular Momentum Assignments - State by State

In this section, the results of the analysis are presented and discussed state by state. For each state, the discussion includes the different considerations alongside the conclusion leading to each angular momentum assignment (or the lack of it). Each state has been given a labeling convention that prioritised the prior angular momentum knowledge. The following set of figures in each case therefore involve a mixture of TWOFNR-based DWBA, Angular distributions curve that helped toward making assignments.

6.4.1 ^{21}Ne 8.349 MeV - Ne I

This state has a confirmed spin of 3/2 and a positive parity. For this state, it was possible to extract the differential cross section at 11°, 13°, 15°. Only data at a single angle (15°) were extracted for Dresden2. Thus for this state, only Dresden5 was considered. Figure 6.3 shows the angular distribution in the CoM as extracted.

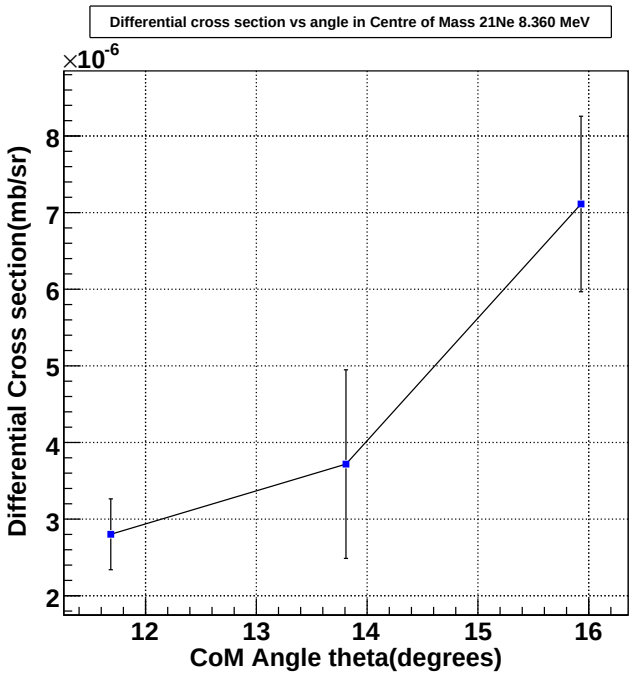

Figure 6.3: *Experimental angular distribution as extracted from data for Dresden5.*

Given the presence of only three data points, it was not possible to directly use this state as "reference state". However the idea was to use this state later on after the normalisation factor would have been calculated by using another state as reference. Figure 6.4 shows the theoretical angular distribution for ℓ=2, J$^\pi$=$(3/2)^+$ using TWOFNR.

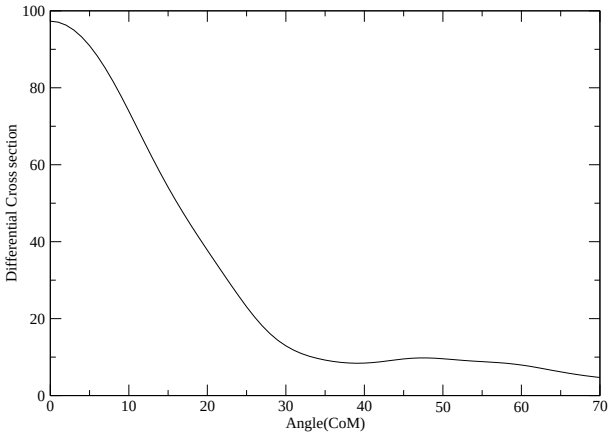

Figure 6.4: *DWBA ℓ=2 curves, J^π=$(3/2)^+$ using TWOFNR.*

The ratio of the theoretical angular momentum to different data points for this state was calculated. This ratio, which can be seen in Figure 6.5, allowed to highlight the variation between the theoretical curves and the data.

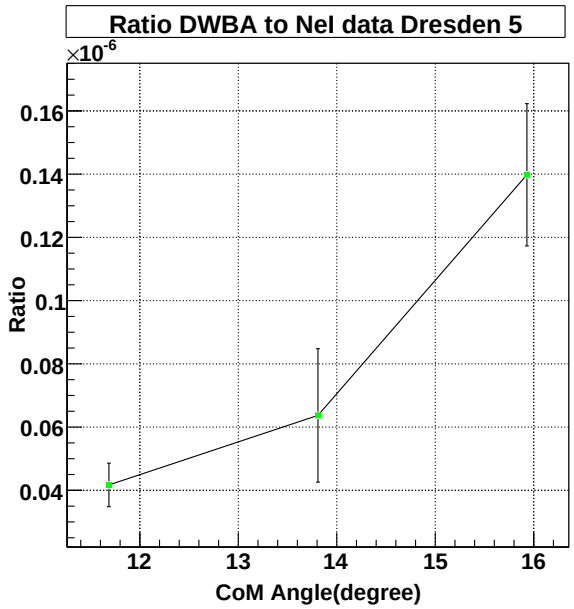

Figure 6.5: *Ratio of DWBA ℓ=2 curves to the ^{21}Ne 8.349 MeV Dresden5 experimental values.*

6.4.2 ^{21}Ne 8.301 MeV - Ne II

This state has a confirmed spin of 3/2 and a negative parity. Angular distributions at 11°, 13°, 15°, 20°, 25°, 30° were extracted for Dresden5 and at 15°, 20°, 25°, 30° and 35° for Dresden2. Figures 6.6 and 6.7 show respectively the angular distribution for Dresden5 and Dresden2 as extracted.

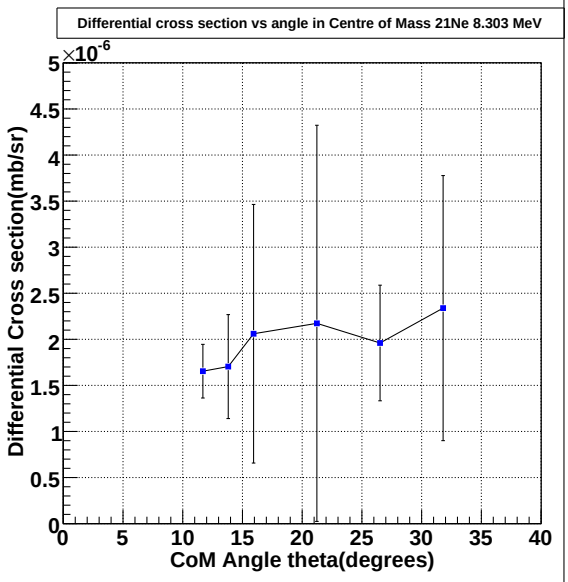

Figure 6.6: *Experimental angular distribution as extracted from data for Dresden5 for ^{21}Ne 8.301 MeV.*

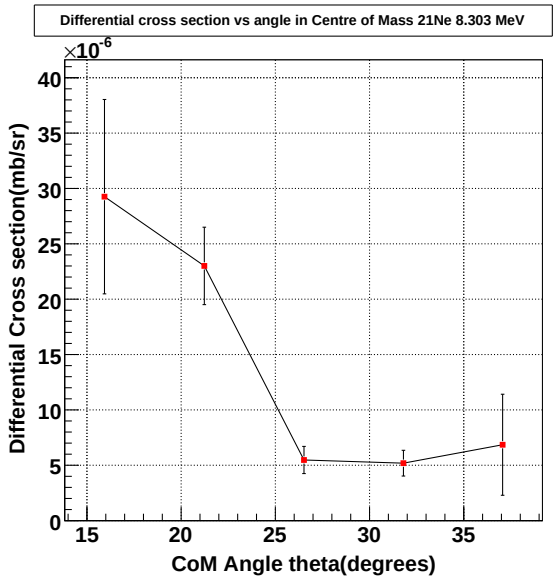

Figure 6.7: *Experimental angular distribution as extracted from data for Dresden2 for ^{21}Ne 8.301 MeV.*

Despite the fact that this state has been measured at a wide range of angles, it is found to be weakly populated which led to cross section errors as large as 100 % for one of the measurements at 15° when using Dresden2. This peak could not principally be used as the main reference state. However, given a much better coverage than NeI, this peak was used as a confirmation of the normalisation used thereafter. Again, the theoretical angular distribution for ℓ=1, $J^{\pi}=(3/2)^{-}$ using TWOFNR is seen in Figure 6.8. The ratio of this theoretical curve to the data was calculated for both targets. Ratio to both Dresden5 and Dresden2 data of this state are respectively shown in Figures 6.9 and 6.10.

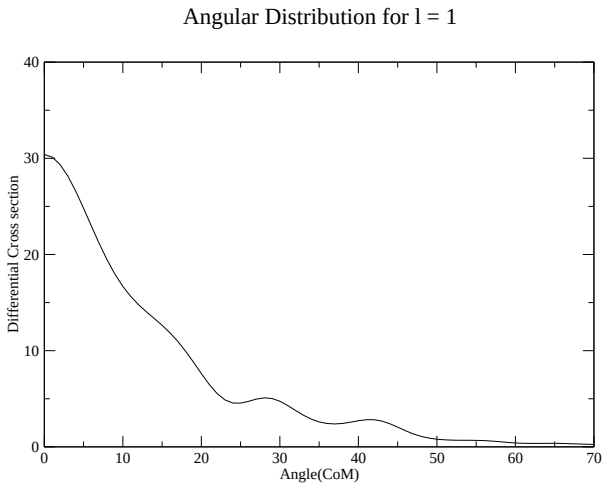

Figure 6.8: *DWBA ℓ=1 curves, J^{π}=$(3/2)^{-}$ using TWOFNR.*

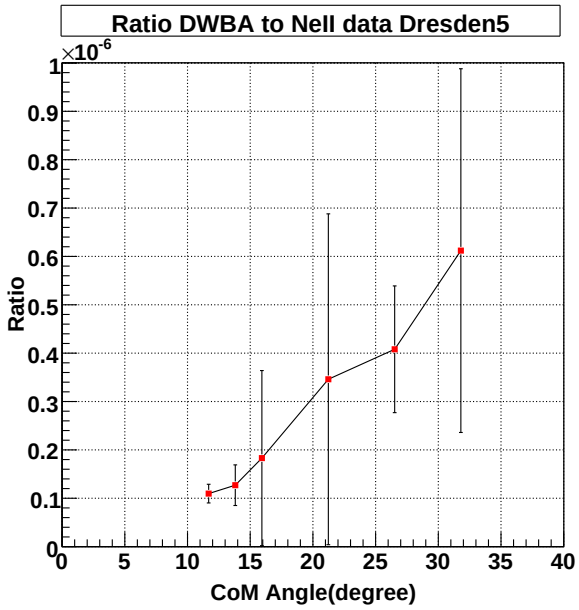

Figure 6.9: *Ratio of DWBA ℓ=1 curves to the ^{21}Ne 8.301 MeV Dresden5 experimental values.*

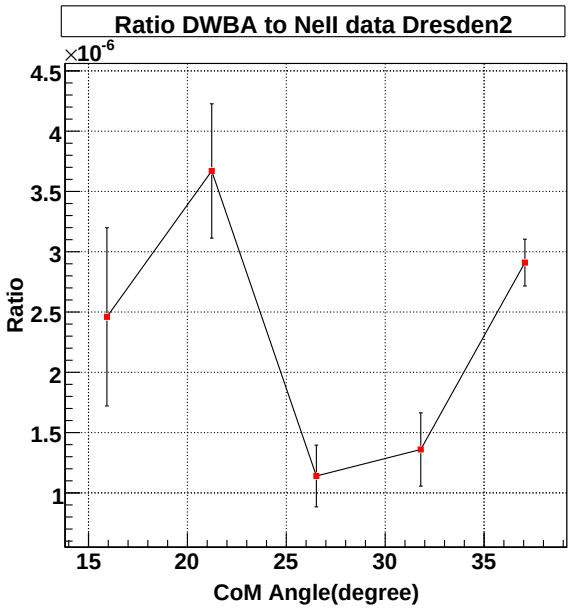

Figure 6.10: *Ratio of DWBA ℓ=1 curves to the ^{21}Ne 8.301 MeV Dresden2 experimental values.*

6.4.3 ^{21}Ne 8.039 MeV - Ne III

This state has a confirmed spin of 3/2 and a positive parity. Angular distributions were determined for 11°, 13°, 20°, 25° and 30° for Dresden5 and for 20°, 25°, 30° and 35° for Dresden2. Both are respectively shown in Figures 6.11 and 6.12.

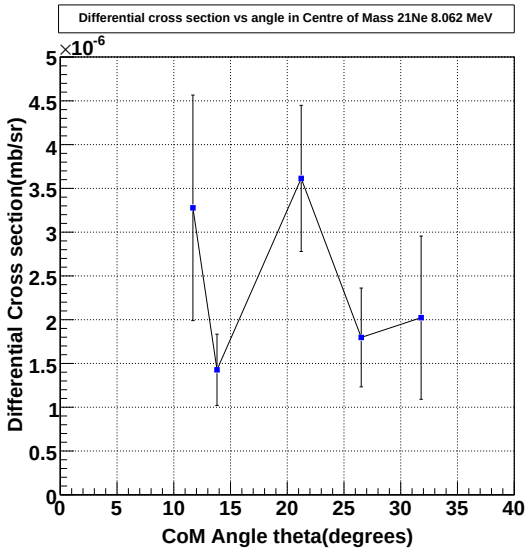

Figure 6.11: *Experimental angular distribution as extracted from data for Dresden5 for ^{21}Ne 8.0862 MeV.*

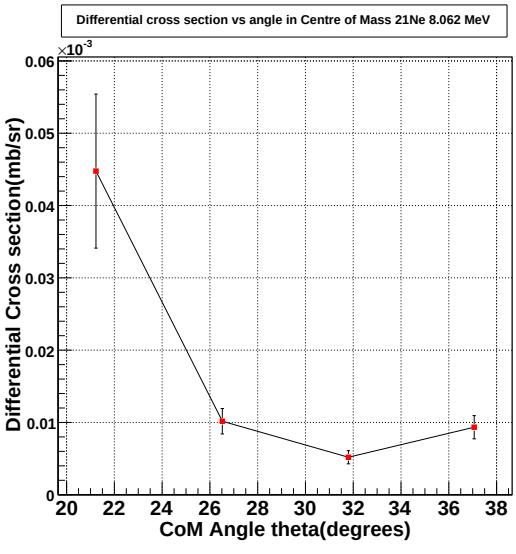

Figure 6.12: *Experimental angular distribution as extracted from data for Dresden2 for ^{21}Ne 8.062 MeV.*

This peak happened to be well populated with enough angular coverage compared to ^{21}Ne 8.349 MeV and ^{21}Ne 8.301 MeV. It therefore presented itself to be a better candidate as the potential "reference state". Angular distribution theoretical calculations were, as mentioned in the previous chapter, performed using TWOFNR. J^{π} of this state being known, despite not knowing the exact behaviour of the implanted Neon, theoretical angular distribution for the ℓ=2, $J^{\pi}= (3/2)^{+}$ were to serve as the starting point toward the interpretation of this work results. This state has the same spin parity as NeI for which the theoretical angular distribution is shown in Figure 6.4.

The scaling ratio of the theoretical curve to Dresden5 experimental data was calculated for different angles covered by the data (that is 11°, 13°, 20°, 25° and 30°) and is shown in Figure 6.13 alongside ratio of NeI and NeII.

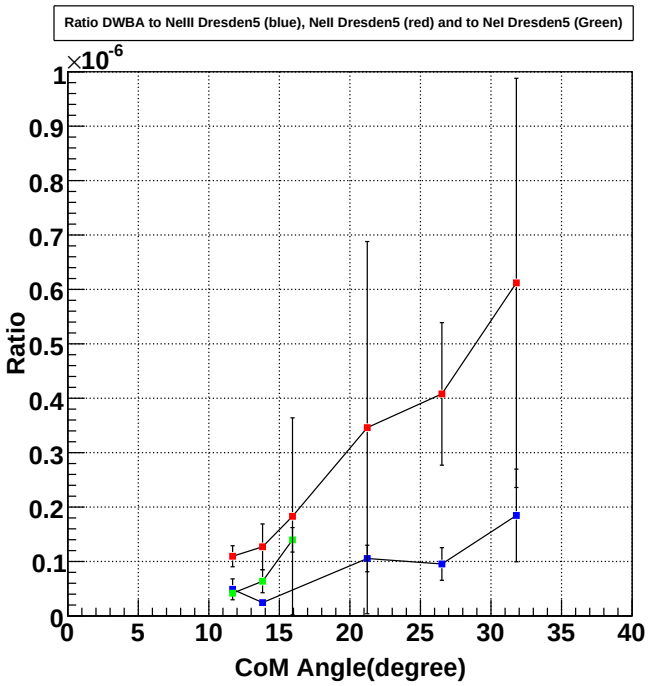

Figure 6.13: *Ratio of DWBA ℓ=2 curves to Dresden5 experimental values for NeI, NeIII and DWBA ℓ=1 curve to Dresden5 experimental values for NeII. NeI being in Green, NeII in red and NeIII in blue.*

These ratios do agree within error quite well at higher angle. At 11.7° and 13.8°, NeI appears to have twice the strength than the NeIII.

Going through the data as listed in appendix C, for both targets, measurements at different angle were taken with no particular order. From there, in order to go forward, and re-order the data so it can be rightly weighted, a way of normalising the data had to found.

NeIII, being chosen as the reference state, was firstly normalised in such a way that the ratio between the theoretical angular distribution and Dresden5 data would remain constant. In this case, this constant was chosen to be unity for ease of comparison and relative strength estimation to other states. Table 6.2 shows the previously displayed ratio values at different angle for NeIII, Dresden5.

CoM Angle	Ratios values including respective errors
11.7	$(4.88\pm1.92)\times 10^{-8}$
13.8	$(2.44\pm0.69)\times 10^{-8}$
21.2	$(1.06\pm 0.24)\times 10^{-7}$
26.5	$(9.54\pm 2.99)\times 10^{-8}$
31.8	$(1.85\pm 0.85)\times 10^{-7}$

Table 6.2: *Theoretical angular distribution to ^{21}Ne 8.039 MeV ratio. The inverse of the ratio shown were used as normalisation factor for all Dresden5 data.*

These ratios represent the "normalisation factor" whose inverse were applied to all data, taking appropriately the error into account. The experimental angular distribution for the Dresden5 data of the ^{21}Ne 8.039 MeV state can be seen in Figure 6.14 alongside the theoretical calculations for the ℓ=0, ℓ=1, ℓ=2, ℓ=3, ℓ=4 and ℓ=5 angular distributions. Table 6.3 shows the resulting Chi-square fitting parameters of the data to those calculated angular distributions.

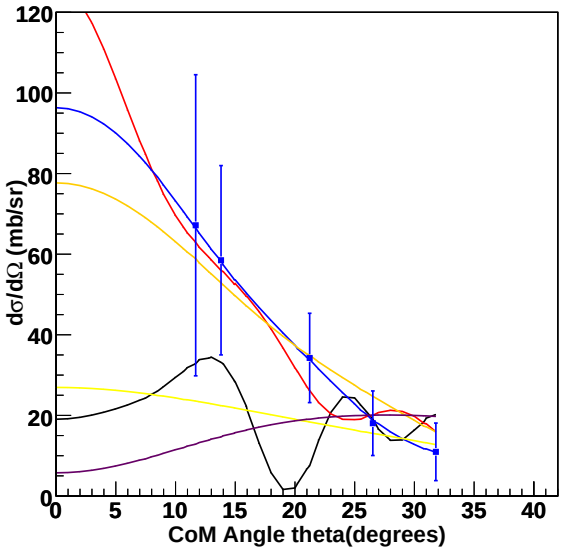

Figure 6.14: *Normalised Dresden5 data for ^{21}Ne 8.039 MeV with different theoretical angular distribution calculated using TWOFNR. ℓ=0 can be seen in black, ℓ=1 in red, ℓ=2 in blue, ℓ=3 in Orange, ℓ=4 in yellow and ℓ=5 in Magenta.*

	ℓ=0	ℓ=1	ℓ=2	ℓ=3	ℓ=4	ℓ=5
Chi-Square Values	9.531	1.104	0.007	0.772	3.895	9.062
Degree of Freedom	4	4	4	4	4	4
Relative Scaling Factor	15.62±3.80	4.17±0.83	0.99±0.19	0.91±0.18	1.43±0.31	3.54±0.85

Table 6.3: *Chi-Square test resulting parameters for NeIII Dresden5. This table shows the parameters obtained when fitting experimental data with theoretical calculations.*

For NeIII, as expected, a perfect match with the ℓ=2 ($J^{\pi} = (3/2)^{+}$) angular momentum was obtained for Dresden5. The Chi-square fit of which can be seen in Figure 6.15.

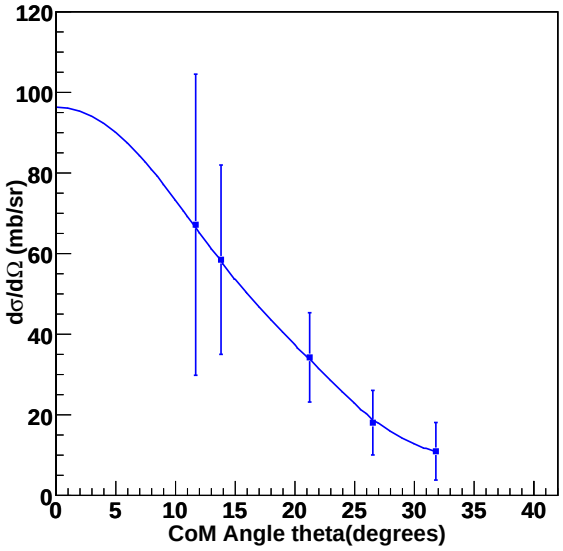

Figure 6.15: *Normalised Dresden5 data for ^{21}Ne 8.039 MeV with ℓ=2 theoretical angular momentum calculated using TWOFNR.*

Concerning Dresden2 data, Figure 6.16 shows the scaling ratio at different angle of ℓ=2 theoretical calculation to Dresden2 experimental data at different covered angles and Table 6.4 shows the corresponding values. For this target, normalisation of the data was also performed and resulting "renormalised " data (where available) used for further discrimination of the angular momentum for different states.

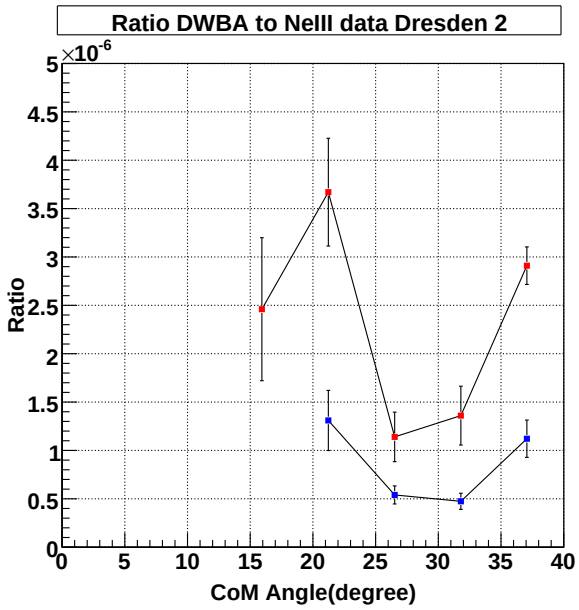

Figure 6.16: *Ratio of DWBA ℓ=2 curves to Dresden2 experimental values for NeIII and DWBA ℓ=1 curve to Dresden2 experimental values for NeII. NeII being in red and NeIII in blue.*

CoM Angle	Ratios values including respective errors
21.2	$(1.31\pm0.31)\times 10^{-6}$
26.5	$(5.40\pm0.93)\times 10^{-7}$
31.8	$(4.74\pm 0.83)\times 10^{-7}$
37.1	$(1.12\pm 0.19)\times 10^{-6}$

Table 6.4: *Theoretical angular distribution to ^{21}Ne 8.039 MeV ratio. The inverse of the ratio shown were used as normalisation factor for all Dresden2 data.*

Therefore, in Figure 6.17, the Chi-square fit for the Dresden2 experimental data of the NeIII state can be seen alongside the theoretical angular distributions curves (ℓ=0, ℓ=1, ℓ=2, ℓ=3, ℓ=4, ℓ=5). The table afterwards (Table 6.5) shows the corresponding fitting parameters.

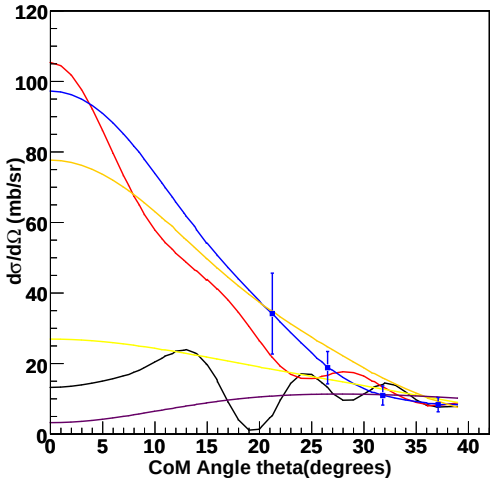

Figure 6.17: *Normalised Dresden2 data for ^{21}Ne 8.039 MeV with different theoretical angular distribution calculated using TWOFNR. ℓ=0 can be seen in black, ℓ=1 in red, ℓ=2 in blue, ℓ=3 in Orange, ℓ=4 in yellow and ℓ=5 in Magenta.*

	ℓ=0	ℓ=1	ℓ=2	ℓ=3	ℓ=4	ℓ=5
Chi-Square Values	9.260	2.128	6.453e-05	0.938	3.400	7.994
Degree of Freedom	3	3	3	3	3	3
Relative Scaling Factor	2.00±0.28	3.47±0.46	1.00±0.13	0.79±0.103	0.96±0.13	2.00±0.28

Table 6.5: *Chi-Square test resulting parameters for NeIII Dresden2. This table shows the parameters obtained when fitting experimental data with theoretical calculations.*

For the Dresden2 set of data, as expected, the ^{21}Ne 8.039 MeV state is also in perfect agreement with the ℓ=2 ($J^{\pi} = (3/2)^{+}$) angular momentum. Figure 6.18 shows the resulting Chi-squared test fit on the data for the ℓ=2 theoretical angular momentum.

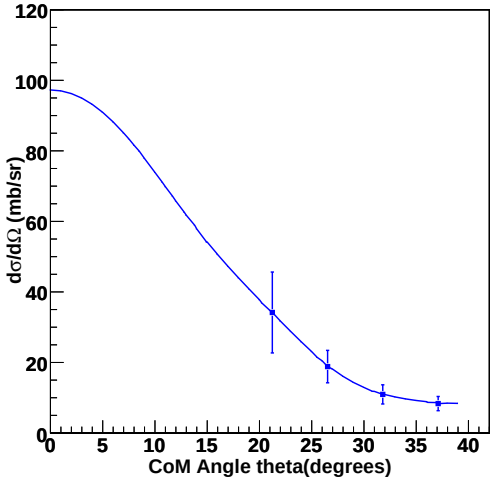

Figure 6.18: *Normalised Dresden2 data for ^{21}Ne 8.039 MeV with ℓ=2 theoretical angular distribution calculated using TWOFNR.*

The step subsequently was to use NeI and NeII as a first check. However NeI is only defined at 11.7°, 13.8°, 15.9° giving the overlap angular range at only 11.7° and 13.8°. Therefore the check was inconclusive for this state. In NeII case, however the match was in agreement with the literature (ℓ=1, $J^{\pi}=(3/2)^{-}$) for both Dresden5 and Dresden2 targets. Figure 6.19 shows the resulting fit for Dresden5 and Figure 6.21, the resulting fit for Dresden2. The corresponding parameters of the data to different theoretical angular distributions are both recorded in Tables 6.6 and 6.7 for the Dresden5 and Dresden2 data respectively. Figure 6.20 shows the Dresden2 data fitted with different theoretical angular momentums.

	ℓ=0	ℓ=1	ℓ=2	ℓ=3	ℓ=4	ℓ=5
Chi-Square Values	2.477	0.401	0.643	0.873	1.957	3.815
Degree of Freedom	3	3	3	3	3	3
Relative Scaling Factor	16.04±4.96	4.19±1.18	1.01±0.29	0.87±0.25	1.37±0.41	3.40±1.12

Table 6.6: *Chi-Square distribution resulting parameters for NeII Dresden5 target. This table shows the parameters obtained when fitting experimental data with theoretical calculations.*

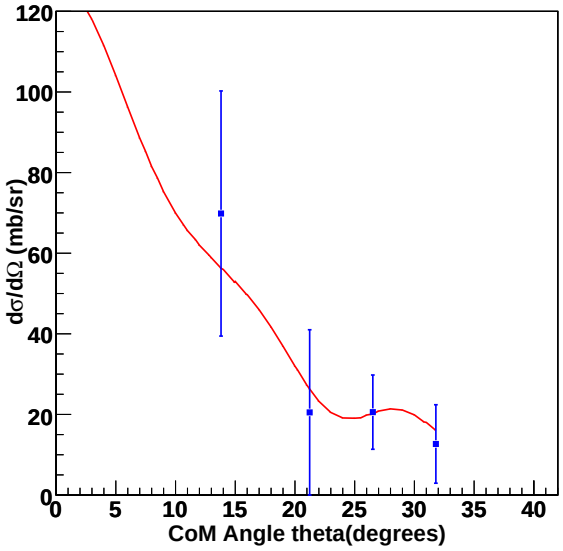

Figure 6.19: *Normalised Dresden5 data for ^{21}Ne 8.301 MeV with ℓ=1 theoretical angular distribution calculated using TWOFNR.*

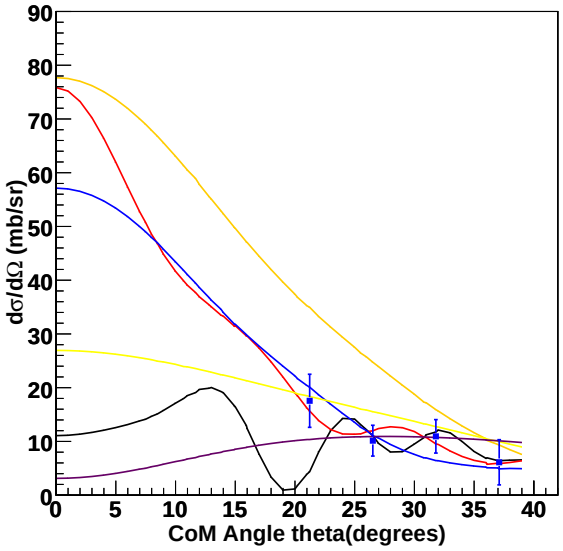

Figure 6.20: *Normalised Dresden2 data for ^{21}Ne 8.301 MeV with all theoretical angular distribution calculated using TWOFNR.ℓ=0 can be seen in black, ℓ=1 in red, ℓ=2 in blue, ℓ=3 in Orange, ℓ=4 in yellow and ℓ=5 in Magenta.*

	ℓ=0	ℓ=1	ℓ=2	ℓ=3	ℓ=4	ℓ=5
Chi-Square Values	7.319	0.767	2.555	1.642	1.149	3.106
Degree of Freedom	3	3	3	3	3	3
Relative Scaling Factor	9.07±1.60	2.50±0.40	0.59±0.10	0.49±0.08	0.77±0.12	1.93±0.32

Table 6.7: *Chi-Square distribution resulting parameters for NeII for the Dresden2 data. This table shows the parameters obtained when fitting experimental data with theoretical calculations.*

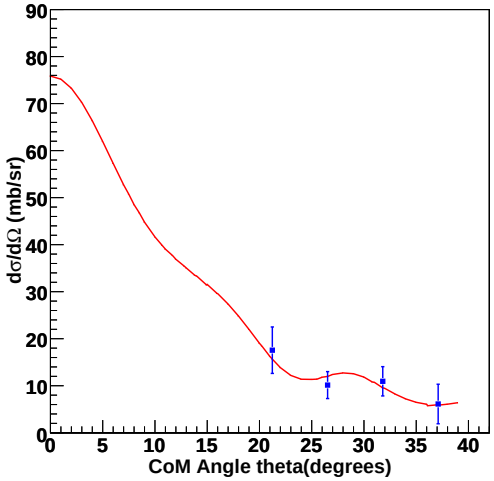

Figure 6.21: *Normalised Dresden2 data for ^{21}Ne 8.301 MeV with ℓ=1 theoretical angular distribution calculated using TWOFNR.*

6.4.4 ^{21}Ne 8.520 MeV - Ne IV

This state has no spin-parity assignments in literature. For this state, the differential cross section was only extracted at 11° for Dresden5. No data were taken for Dresden2. Thus no spin assignment was possible using the present data.

6.4.5 ^{21}Ne 8.437 MeV - Ne V

This state has no spin-parity assignments in literature. In Figures 6.22 and 6.23, angular distribution at 11°, 13°, 20°, 25° and 30° can be seen for Dresden5 and at 20°, 25°, 30° and 35° for Dresden2 respectively.

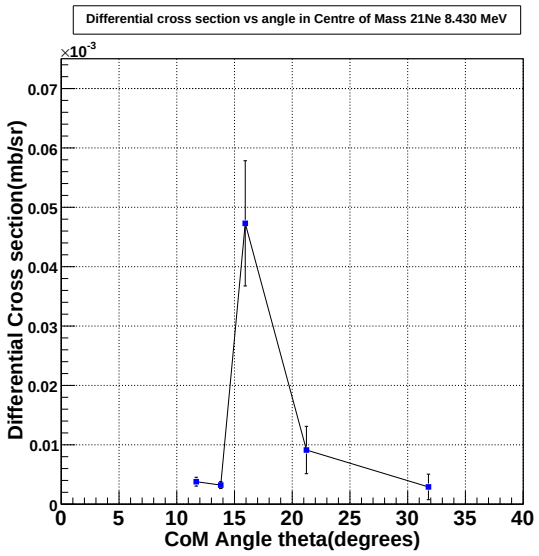

Figure 6.22: *Experimental angular distribution as extracted from data for Dresden5 for ^{21}Ne 8.437 MeV.*

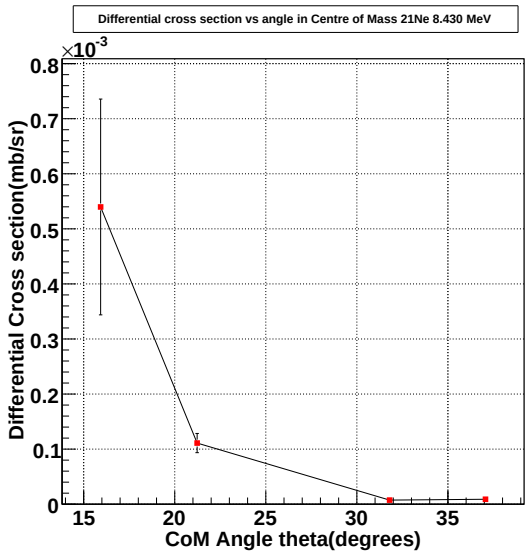

Figure 6.23: *Experimental angular distribution as extracted from data for Dresden2 for ^{21}Ne 8.437 MeV.*

For the ^{21}Ne 8.437 MeV, Dresden5 data, beside the Chi-square fit to different theoretical angular distributions can be seen in Figure 6.24. Table 6.8 shows the associated values of deriving parameters.

It is important to underline that for all states, normalised values of data only appear when normalisation factors in table 6.2 are available. Therefore the difference in angles availability between raw data and normalised data in Figures 6.22 and 6.24, 6.23 and 6.26 and in all Figures thereafter.

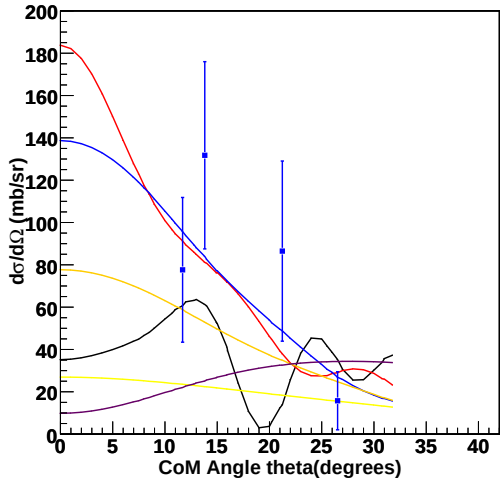

Figure 6.24: *Normalised Dresden5 data for ^{21}Ne 8.437 MeV with different angular distributions. ℓ=0 can be seen in black, ℓ=1 in red, ℓ=2 in blue, ℓ=3 in Orange, ℓ=4 in yellow and ℓ=5 in Magenta. Theoretical angular distribution calculated using TWOFNR.*

	ℓ=0	ℓ=1	ℓ=2	ℓ=3	ℓ=4	ℓ=5
Chi-Square Values	7.711	3.706	2.886	4.371	6.940	11.896
Degree of Freedom	3	3	3	3	3	3
Relative Scaling Factor	28.83±8.41	6.05±1.52	1.43±0.35	1.35±0.35	2.35±0.67	6.06±2.20

Table 6.8: *Chi-Square test resulting parameters for NeV Dresden5. This table shows the parameters obtained when fitting experimental data with theoretical calculations.*

Dresden5 data indicates the transfer angular momentum to be ℓ=2. No discrimination between either $J^{\pi}=(3/2)^{+}$ or $J^{\pi}=(5/2)^{+}$ was possible with the present data. Figure 6.25 shows the normalised Dresden5 with the ℓ=2 theoretical angular distribution.

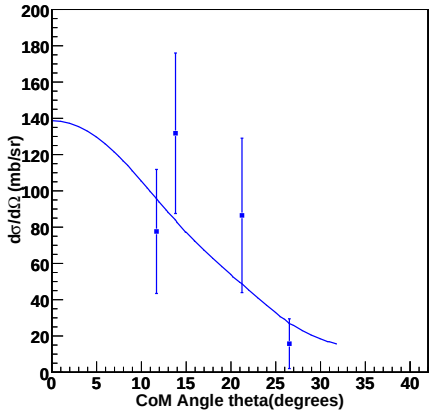

Figure 6.25: *Normalised Dresden5 data for ^{21}Ne 8.437 MeV with ℓ=2 angular distribution. Theoretical angular distribution calculated using TWOFNR.*

For the Dresden2 set of data, normalisation was also performed. Figure 6.26 shows the resulting plot of the data with different theoretical angular distributions while Table 6.9 displays the associated parameters.

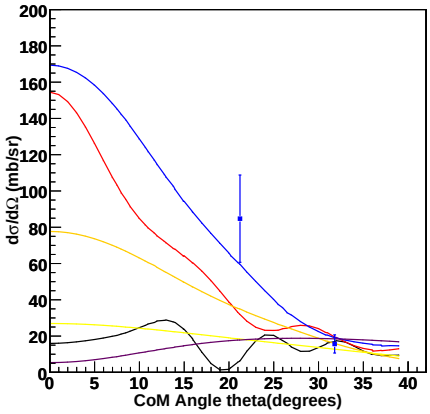

Figure 6.26: *Normalised Dresden2 data for ^{21}Ne 8.437 MeV with ℓ=0, ℓ=1, ℓ=2, ℓ=3, ℓ=4, ℓ=5 theoretical angular distribution. ℓ=0 is seen in black, ℓ=1 in red, ℓ=2 in blue, ℓ=3 in Orange, ℓ=4 in yellow and ℓ=5 in Magenta.Theoretical angular distribution calculated using TWOFNR.*

	ℓ=0	ℓ=1	ℓ=2	ℓ=3	ℓ=4	ℓ=5
Chi-Square Values	10.690	5.390	1.550	3.610	6.120	8.050
Degree of Freedom	1	1	1	1	1	1
Relative Scaling Factor	13.07 ± 3.86	5.08±1.24	1.74±0.38	1.23±0.29	1.51±0.38	3.31±0.88

Table 6.9: *Chi-Square test resulting parameters for NeV Dresden2. This table shows the parameters obtained when fitting experimental data with theoretical calculations.*

With a Chi-square of the resulting fit of 1.55, Dresden2 indicates an ℓ=2 assignment as well, plot of which, is shown in Figure 6.27.

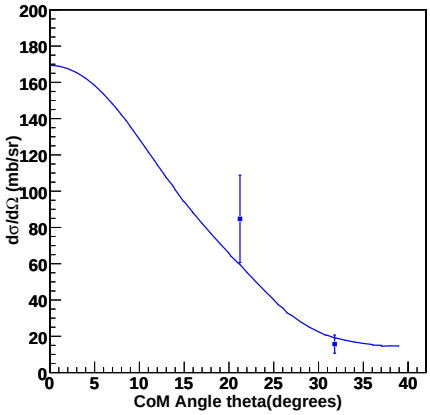

Figure 6.27: *Normalised Dresden2 data for ^{21}Ne 8.437 MeV with the ℓ=2 theoretical angular distribution. Theoretical angular distribution calculated using TWOFNR.*

For this state, this work concluded, based on Dresden5 and Dresden2 data, to a firm assignment of ℓ=2 (J^{π}=$(3/2)^{+}$ or J^{π}=$(5/2)^{+}$).

6.4.6 ^{21}Ne 8.328 MeV - Ne VI

This state has no spin-parity assignments in literature given that it has firstly been observed in this work. For this state, angular distribution, which is shown in Figures 6.28 and 6.29, were extracted at 11°, 13°, 15° and 20° for Dresden5 and only at 15° and 20° in Dresden2 case.

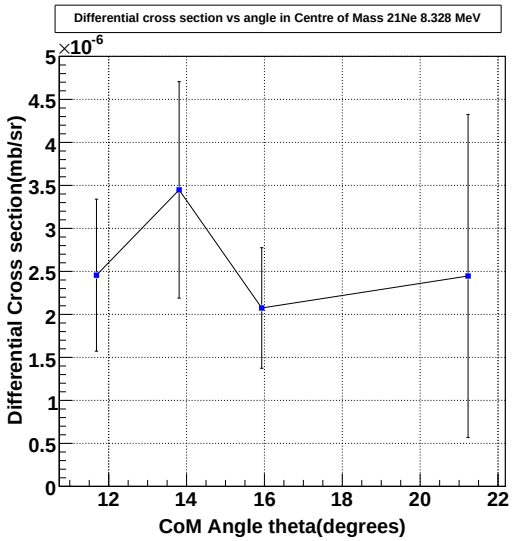

Figure 6.28: *Experimental angular distribution as extracted from data for Dresden5 for ^{21}Ne 8.328 MeV.*

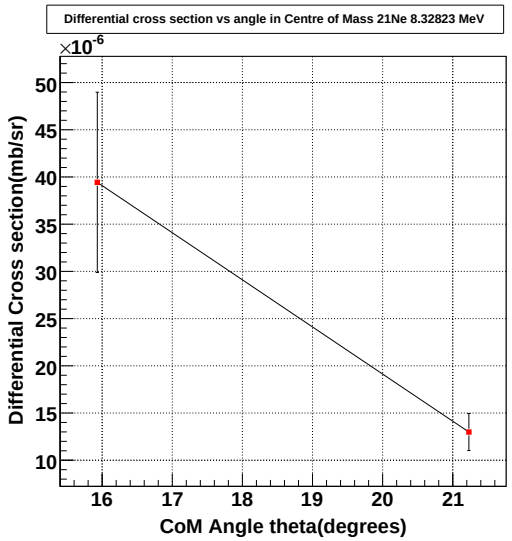

Figure 6.29: *Experimental angular distribution as extracted from data for Dresden2 for ^{21}Ne 8.328 MeV.*

For angular momentum assignments, both targets were used separately as in with previous states. Figure 6.30 shows the Dresden5 data with different possible theoretical angular distributions. The Chi-square parameters resulting from the fits of the data to those theoretical calculations are listed in Table 6.10.

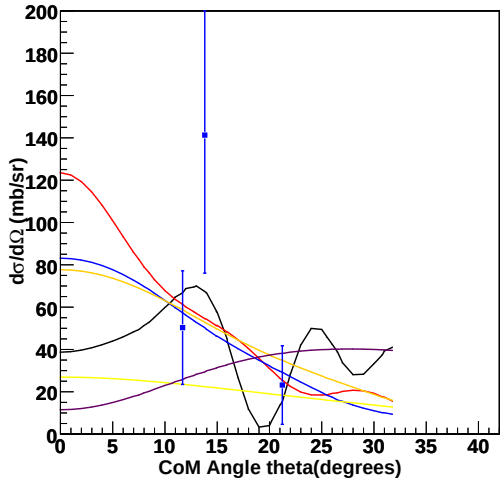

Figure 6.30: *Normalised Dresden5 data for ^{21}Ne 8.328 MeV with both angular distribution. In this graph, ℓ=0 is seen in black, ℓ=1 in red, ℓ=2 in blue, ℓ=3 in Orange, ℓ=4 in yellow and ℓ=5 in Magenta. Theoretical angular distribution calculated using TWOFNR.*

	ℓ=0	ℓ=1	ℓ=2	ℓ=3	ℓ=4	ℓ=5
Chi-Square Values	1.839	1.953	2.120	2.270	2.726	4.431
Degree of Freedom	2	2	2	2	2	2
Relative Scaling Factor	31.72±11.27	4.06±1.45	0.85±0.31	0.91±0.33	1.94±0.73	7.09±3.07

Table 6.10: *Chi-Square test resulting parameters for NeVI Dresden5. This table shows the parameters obtained when fitting experimental data with theoretical calculations.*

Dresden5 data lead on ℓ=0 ($J^{\pi}=(1/2)^{+}$) angular momentum assignment. Figure 6.31 shows the normalised data data alongside the ℓ=0 theoretical curve.

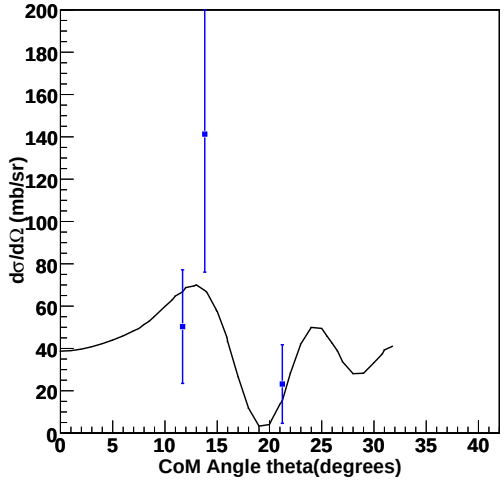

Figure 6.31: *Normalised Dresden5 data for ^{21}Ne 8.328 MeV with ℓ=0 angular distribution. Theoretical angular distribution calculated using TWOFNR.*

For this state, the work concluded on a tentative ℓ=0 ($J^{\pi}=(1/2)^{+}$) assignment. This assignment was made solely based on the Dresden5 data as no normalised Dresden2 data were available for this state.

6.4.7 ^{21}Ne 8.167 MeV - Ne VII

This state has a suspected spin of 9/2 and a suspected positive parity. For this state, angular distribution was extracted for 11°, 13°, 15°, 20°, 25° and 30° in Dresden5 case and for 15°, 20°, 25°, 30° and 35° for Dresden2. Figures 6.32 and 6.33 show the extracted values.

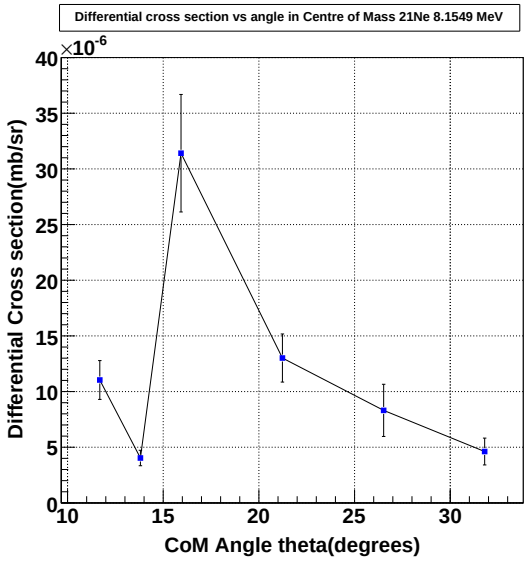

Figure 6.32: *Experimental angular distribution as extracted from data for Dresden5 for ^{21}Ne 8.167 MeV.*

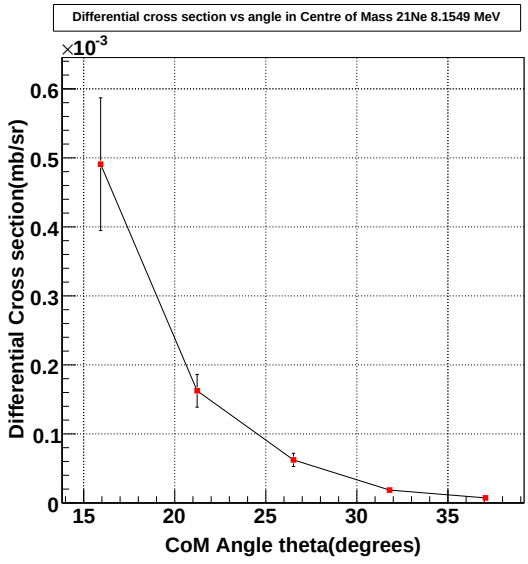

Figure 6.33: *Experimental angular distribution as extracted from data for Dresden2 for ^{21}Ne 8.167 MeV.*

For this state, normalised data of the Dresden5 target can be seen alongside ℓ=0, ℓ=1, ℓ=2, ℓ=3, ℓ=4 and ℓ=5 theoretical curves as shown in Figure 6.34. The Chi-square parameters resulting from fit with different theoretical curves can be seen in Table 6.11.

As explained in section 6.3.3, 37.1° CoM data could not be used for the following states: NeVII (Figure 6.36), NeVIII (Figure 6.42), NeIX (Figure 6.48), NeXI (Figure 6.60), NeXII (Figure 6.66), NeXIII (Figure 6.72), NeXIV (Figure 6.78), NeXV (Figure 6.84).

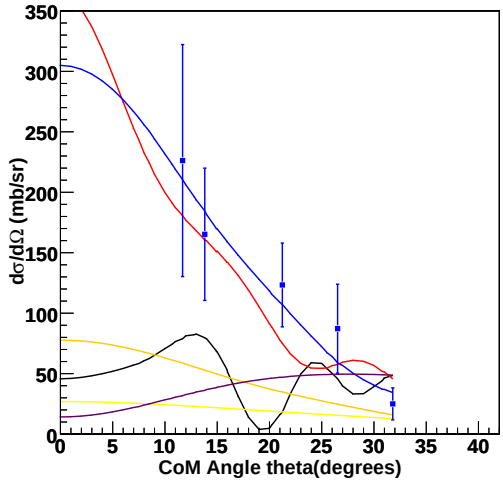

Figure 6.34: *Normalised Dresden5 data for ^{21}Ne 8.167 MeV with ℓ=0 in black, ℓ=1 in red, ℓ=2 in blue, ℓ=3 in Orange, ℓ=4 in yellow and ℓ=5 in Magenta. Theoretical angular distribution calculated using TWOFNR.*

	ℓ=0	ℓ=1	ℓ=2	ℓ=3	ℓ=4	ℓ=5
Chi-Square Values	18.494	5.289	1.452	3.469	10.196	18.815
Degree of Freedom	4	4	4		4	4
Relative Scaling Factor	37.48 ± 8.82	11.97±2.14	3.13±0.53	2.80±0.49	4.04±0.79	8.74±2.07

Table 6.11: *Chi-Square test resulting parameters for NeVII Dresden5. This table shows the parameters obtained when fitting experimental data with theoretical calculations.*

The ℓ=2 ($J^{\pi}=(3/2)^{+}$) with a Chi-square value of 1.452, relative strength of 3.13±0.53, seems in good agreement with all data points. Whereas for the ℓ=4 (Chi-square value 10.196, relative strength of 4.04±0.79) suggested in previous study, does not agree with the data. Figure 6.35 shows Dresden5 normalised data with ℓ=2 theoretical angular momentum.

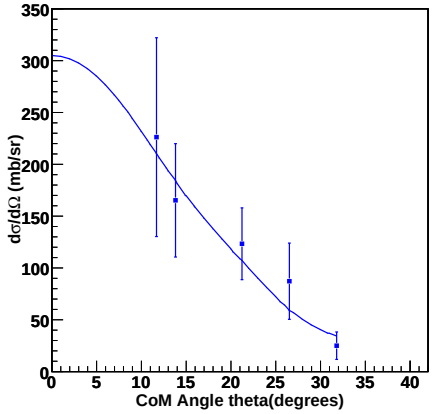

Figure 6.35: *Normalised Dresden5 data for ^{21}Ne 8.167 MeV ℓ=2($J^{\pi}=(3/2)^{+}$). Theoretical angular distribution calculated using TWOFNR.*

A quick investigation by renormalising Dresden2 data, shown in Figure 6.36, for this state, allowed to support the ℓ=2 transfer assignment ($J^{\pi}=(3/2)^{+}$ or $J^{\pi}=(5/2)^{+}$). The Chi-square test fit was performed and corresponding parameters recorded for different curves in Table 6.12. The final fit of the data with the ℓ=2 theoretical angular distribution, can be seen in Figure 6.37.

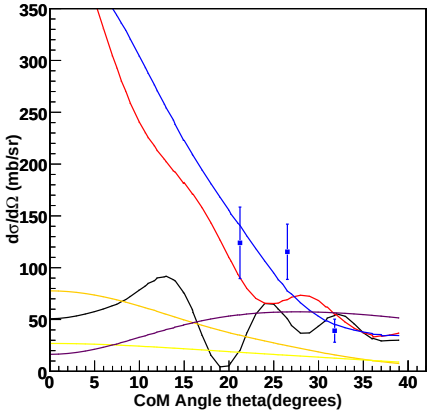

Figure 6.36: *Normalised Dresden2 data for ^{21}Ne 8.167 MeV with ℓ=0 in black, ℓ=1 in red, ℓ=2 in blue, ℓ=3 in Orange, ℓ=4 in yellow and ℓ=5 in Magenta. Theoretical angular distribution calculated using TWOFNR.*

	ℓ=0	ℓ=1	ℓ=2	ℓ=3	ℓ=4	ℓ=5
Chi-Square Values	16.697	5.988	2.536	3.072	6.979	11.217
Degree of Freedom	2	2	2	2	2	2
Relative Scaling Factor	41.59 ±7.94	14.41±2.33	4.11±0.64	3.23±0.50	4.38±0.72	10.13±1.77

Table 6.12: *Chi-Square test resulting parameters for NeVII Dresden2. This table shows the parameters obtained when fitting experimental data with theoretical calculations.*

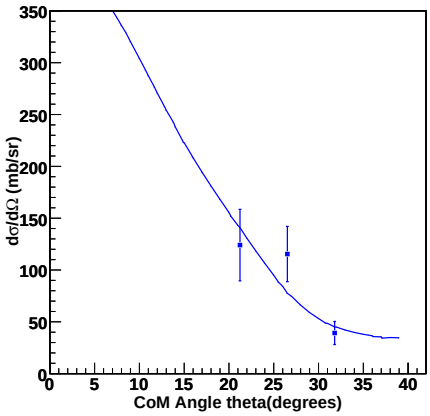

Figure 6.37: *Normalised Dresden2 data for ^{21}Ne 8.167 MeV ℓ=2($J^{\pi}=(3/2)^{+}$). Theoretical angular distribution calculated using TWOFNR.*

For this state, ℓ=2 is in good agreement with both Dresden5 and Dresden2 the data points. Therefore, considering Dresden5 data and Dresden2 data, it is possible to firmly assign ℓ=2(J^{π}=$(3/2)^{+}/(5/2)^{+}$) angular momentum.

6.4.8 ^{21}Ne 7.955 MeV - Ne VIII

This state has a suspected J^{π} of $(11/2)^{-}$. Angular distributions were determined at 20°, 25° and 30° for Dresden5 and 20°, 25°, 30° and 35° for Dresden2. Figures 6.38 and 6.39 show the measured values.

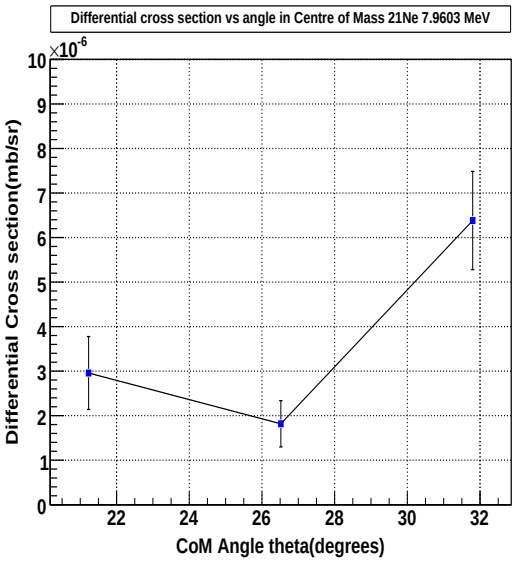

Figure 6.38: *Experimental angular distribution as extracted from data for Dresden5 for ^{21}Ne 7.955 MeV.*

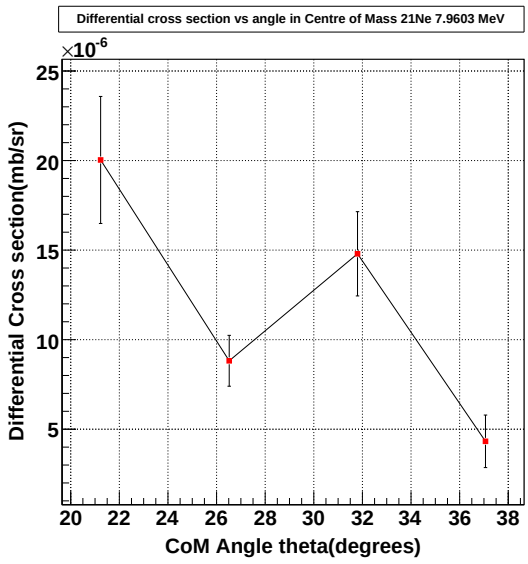

Figure 6.39: *Experimental angular distribution as extracted from data for Dresden2 for ^{21}Ne 7.955 MeV.*

Calculations were performed using Dresden5 data. Figure 6.40 shows the different theoretical curves alongside the data. Respective Chi-square fit parameters are recorded in Table 6.13.

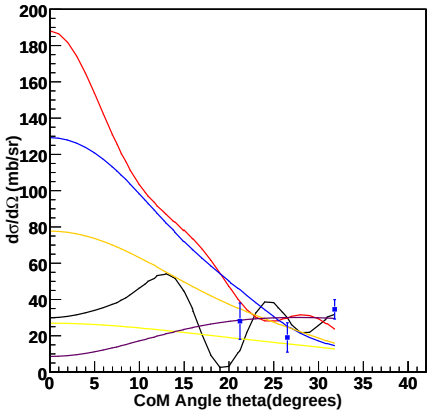

Figure 6.40: *Normalised Dresden5 data for ^{21}Ne 7.955 MeV where ℓ=0 can be seen in black, ℓ=1 in red, ℓ=2 in blue, ℓ=3 in Orange, ℓ=4 in yellow and ℓ=5 in Magenta. Theoretical angular distribution calculated using TWOFNR.*

	ℓ=0	ℓ=1	ℓ=2	ℓ=3	ℓ=4	ℓ=5
Chi-Square Values	4.708	7.043	17.546	12.004	5.814	2.706
Degree of Freedom	2	2	2	2	2	2
Relative Scaling Factor	24.54±3.46	6.19±0.89	1.33±0.22	1.19±0.18	1.97±0.28	5.31±0.73

Table 6.13: *Chi-Square test resulting parameters for NeVIII Dresden5. This table shows the parameters obtained when fitting experimental data with theoretical calculations.*

Using Dresden5 data, an ℓ=5(J^{π}=$(11/2)^{-}$) assignement can be made, fit of which can be seen in Figure 6.41.

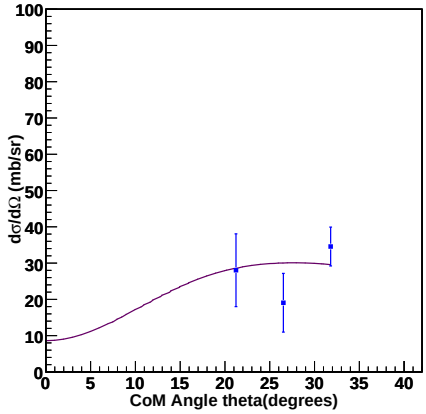

Figure 6.41: *Normalised Dresden5 data for ^{21}Ne 7.955 MeV with ℓ=5(J^{π}=$(11/2)^{-}$) angular momentum. Theoretical angular distribution calculated using TWOFNR.*

The same investigation was performed with the Dresden2 data. Figure 6.42 shows diverse theoretical curves alongside the data and Table 6.14 the different corresponding Chi-square test fit parameters.

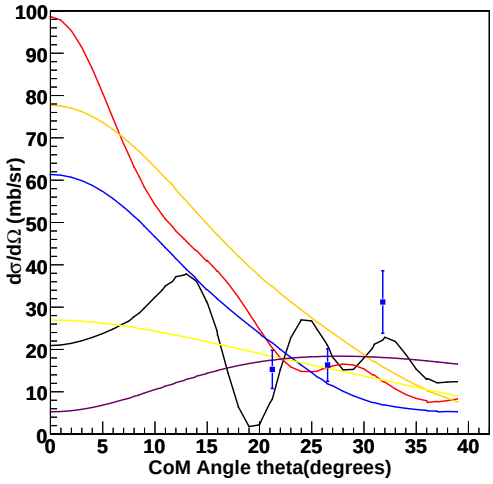

Figure 6.42: *Normalised Dresden2 data for ^{21}Ne 7.955 MeV where ℓ=0 is in black, ℓ=1 in red, ℓ=2 in blue, ℓ=3 in Orange, ℓ=4 in yellow and ℓ=5 in Magenta. Theoretical angular distribution calculated using TWOFNR.*

	ℓ=0	ℓ=1	ℓ=2	ℓ=3	ℓ=4	ℓ=5
Chi-Square Values	5.352	7.787	14.118	10.337	6.603	3.663
Degree of Freedom	2	2	2	2	2	2
Relative Scaling Factor	17.15±2.65	3.25±0.52	0.63±0.11	0.59±0.10	1.07±0.17	3.25±0.49

Table 6.14: *Chi-Square test resulting parameters for NeVIII Dresden2. This table shows the parameters obtained when fitting experimental data with theoretical calculations.*

Dresden2 data favoured as well the ℓ=5 ($J^{\pi}=(11/2)^{-}$) with a Chi-square of 3.663 and relative strength of 3.25±0.49.

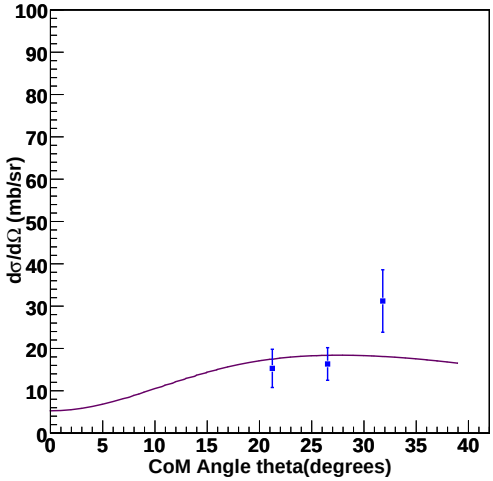

Figure 6.43: *Normalised Dresden2 data for ^{21}Ne 7.955 MeV where ℓ=5($J^{\pi}=(11/2)^{-}$) angular momentum can be seen alongside. Theoretical angular distribution calculated using TWOFNR.*

For this state, based on both Dresden5 and Dresden2 data, a firm ℓ=5(J$^{\pi}$=$(11/2)^{-}$) was assigned for this state, which is in agreement with the literature suggested spin parity of $(11/2)^{-}$.

6.4.9 ^{21}Ne 7.558 MeV - Ne IX

This state has no spin-parity assignments in literature. Angular distributions were deduced at 20°, 25° and 30° in Dresden5 and 20°, 25°, 30° and 35° belonging to Dresden2. In Figures 6.44 and 6.45, both of values can be seen.

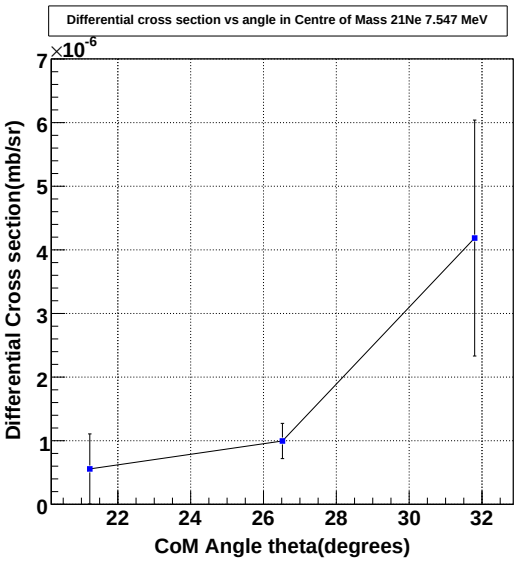

Figure 6.44: *Experimental angular distribution as extracted from data for Dresden5 for ^{21}Ne 7.558 MeV.*

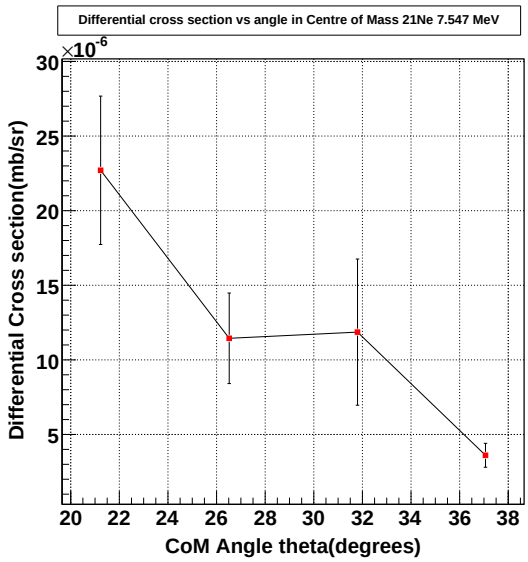

Figure 6.45: *Experimental angular distribution as extracted from data for Dresden2 for ^{21}Ne 7.558 MeV.*

Normalisation was performed for data of both targets. For the Dresden5 data, Figure 6.46 shows the different theoretical curves alongside the data resulting from the Chi-square fitting. Table 6.15 shows the associated key parameters.

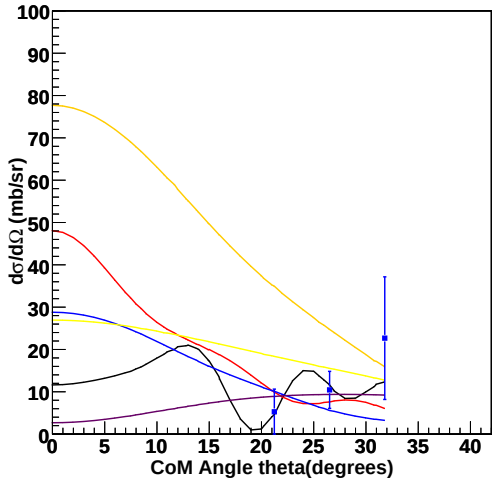

Figure 6.46: *Normalised Dresden5 data for ^{21}Ne 7.558 MeV where ℓ=0 is in black, ℓ=1 in red, ℓ=2 in blue, ℓ=3 in Orange, ℓ=4 in yellow and ℓ=5 in Magenta. Theoretical angular distribution calculated using TWOFNR.*

	ℓ=0	ℓ=1	ℓ=2	ℓ=3	ℓ=4	ℓ=5
Chi-Square Values	0.599	2.497	3.862	2.938	2.157	1.380
Degree of Freedom	2	2	2	2	2	2
Relative Scaling Factor	9.52 ±3.26	1.58±0.62	0.30±0.13	0.29±0.12	0.53±0.20	1.66±0.60

Table 6.15: *Chi-Square test resulting parameters for NeIX Dresden5. This table shows the parameters obtained when fitting experimental data with theoretical calculations.*

For this state, this work was unable using Dresden5 data, to fully discriminate between ℓ=0 or an ℓ=5 assignment. Both of which are shown in Figure 6.47.

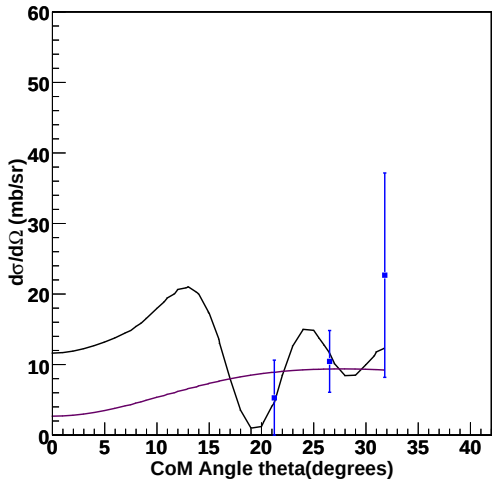

Figure 6.47: *Normalised Dresden5 data for ^{21}Ne 7.558 MeV where ℓ=0(J^{π}=$(1/2)^{+}$) in black and ℓ=5(J^{π}=$(11/2)^{-}$) in Magenta. Theoretical angular distribution calculated using TWOFNR.*

To further discriminate the angular momentum assignments, Dresden2 data were used. The same investigation was performed. Data were normalised and Chi-square fit performed. Both Figure 6.48 and Table 6.16 show respectively the resulting fits and keys parameters.

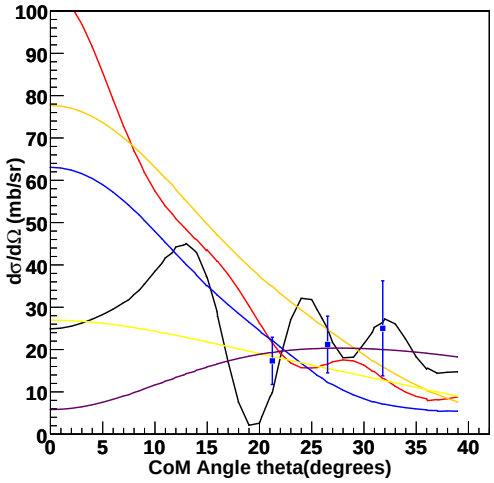

Figure 6.48: *Normalised Dresden2 data for ^{21}Ne 7.558 MeV with ℓ=0, which can be seen in black, ℓ=1 in red, ℓ=2 in blue, ℓ=3 in Orange, ℓ=4 in yellow and ℓ=5 in Magenta. Theoretical angular distribution calculated using TWOFNR.*

	ℓ=0	ℓ=1	ℓ=2	ℓ=3	ℓ=4	ℓ=5
Chi-Square Values	2.135	2.187	5.105	3.191	1.561	0.340
Degree of Freedom	2	2	2	2	2	2
Relative Scaling Factor	20.40 ± 4.30	3.44±0.73	0.65±0.15	0.63±0.14	1.15±0.24	3.59±0.73

Table 6.16: *Chi-Square test resulting parameters for NeIX Dresden2. This table shows the parameters obtained when fitting experimental data with theoretical calculations.*

The Dresden2 data confirmed ℓ=5 ($J^{\pi}=(11/2)^{-}$), with Chi-square parameter fit of 0.340, to be a better fit to the data.

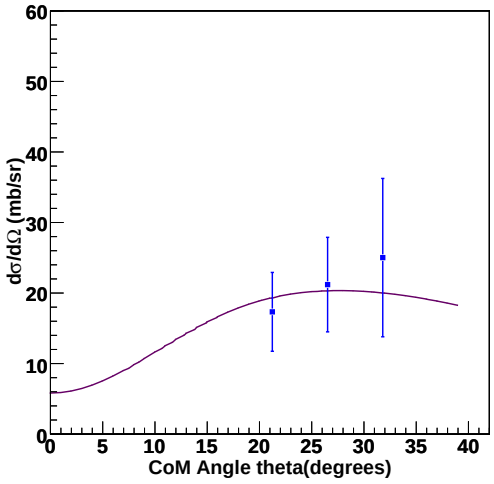

Figure 6.49: *Normalised Dresden2 data for ^{21}Ne 7.558 MeV where ℓ=5(J^{π}=$(11/2)^{-}$) can be seen. Theoretical angular distribution calculated using TWOFNR.*

For this work, therefore, based on both Dresden5 and Dresden2 data, a firm assignment of ℓ=5(J^{π}=$(11/2)^{-}$) was made.

6.4.10 ^{21}Ne 7.485MeV - Ne X

This state has a suspected J^{π} of $(1/2)^{-}$ or $(3/2)^{-}$. Figures 6.50 and 6.51 show the extracted values for Dresden5 (11°, 13°, 15°, 20° and 25°) and for Dresden2 (20°, 25° only).

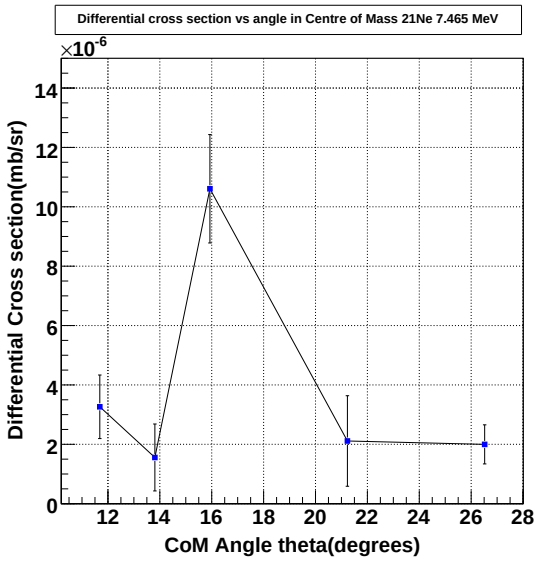

Figure 6.50: *Experimental angular distribution as extracted from data for Dresden5 for ^{21}Ne 7.485 MeV.*

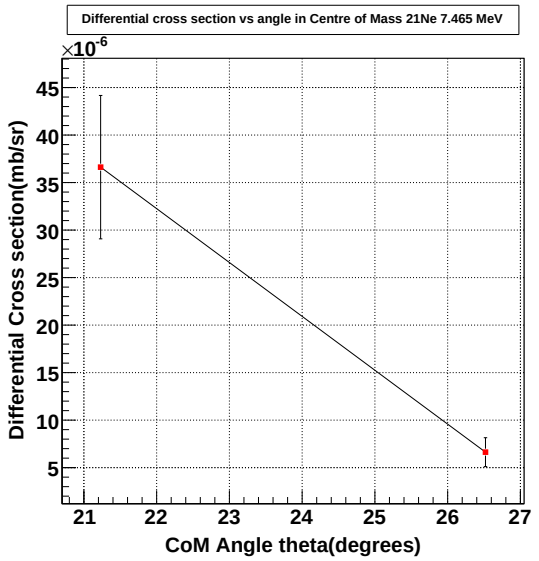

Figure 6.51: *Experimental angular distribution as extracted from data for Dresden2 for ^{21}Ne 7.485 MeV.*

For the ^{21}Ne 7.558 MeV, both the Dresden5 and Dresden2 data were taken into account. Figure 6.52 shows the resulting chi-square fits for the Dresden5 data on different theoretical curves and Table 6.17 shows the resulting main parameters.

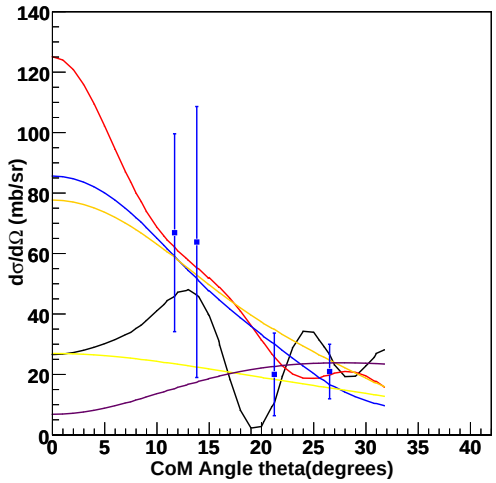

Figure 6.52: *Normalised Dresden5 data for ^{21}Ne 7.558 MeV in which ℓ=0 is in black, ℓ=1 in red, ℓ=2 in blue, ℓ=3 in Orange, ℓ=4 in yellow and ℓ=5 in Magenta. Theoretical angular distribution calculated using TWOFNR.*

	ℓ=0	ℓ=1	ℓ=2	ℓ=3	ℓ=4	ℓ=5
Chi-Square Values	0.482	0.256	0.912	0.935	1.748	3.693
Degree of Freedom	3	3	3	3	3	3
Relative Scaling Factor	21.77 ± 6.21	4.12±1.12	0.88±0.25	0.83±0.23	1.47±0.43	4.21±1.33

Table 6.17: *Chi-Square test resulting parameters for NeX Dresden5. This table shows the parameters obtained when fitting experimental data with theoretical calculations.*

Using Dresden5 data, an assignment of ℓ=1 (as suggested by the literature) could be made. Figure 6.53 shows angular distribution alongside normalised Dresden5 data that led to this conclusion.

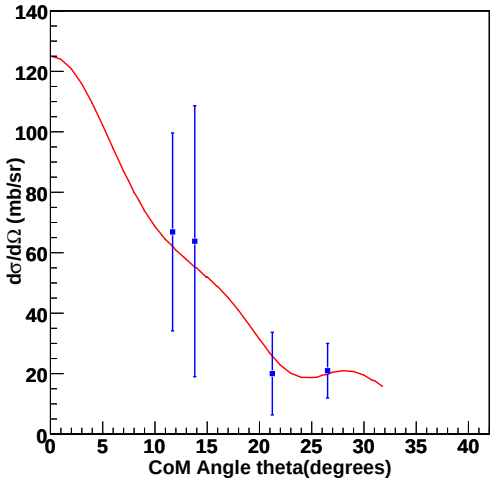

Figure 6.53: *Normalised Dresden5 data for ^{21}Ne 7.558 MeV where ℓ=1 can be seen. Theoretical angular distribution calculated using TWOFNR.*

For the Dresden2 data, Figure 6.54 shows the key results of the Chi-square fitting and in Table 6.18, the associated parameters can be seen.

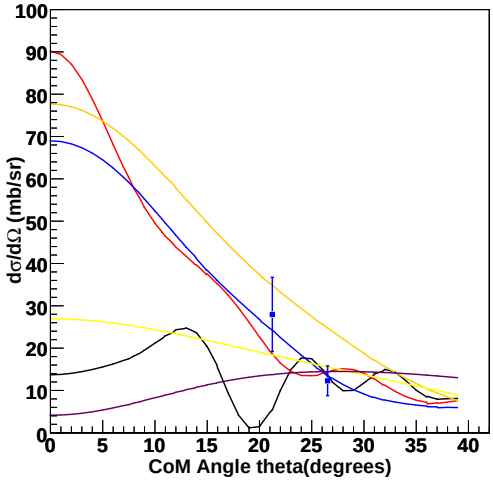

Figure 6.54: *Normalised Dresden2 data for ^{21}Ne 7.558 MeV where ℓ=0 can be seen in black, ℓ=1 in red, ℓ=2 in blue, ℓ=3 in Orange, ℓ=4 in yellow and ℓ=5 in Magenta. Theoretical angular distribution calculated using TWOFNR.*

	ℓ=0	**ℓ=1**	**ℓ=2**	**ℓ=3**	**ℓ=4**	**ℓ=5**
Chi-Square Values	6.779	1.444	0.269	1.105	1.915	3.013
Degree of Freedom	1	1	1	1	1	1
Relative Scaling Factor	11.222± 2.85	2.97±0.65	0.71±0.15	0.57±0.12	0.93±0.21	2.56±0.58

Table 6.18: *Chi-Square test resulting parameters for NeX Dresden2. This table shows the parameters obtained when fitting experimental data with theoretical calculations.*

For Dresden2, there were only one degree of freedom (two data points), despite the fact, the fit was performed and ℓ=1 fall within acceptable range while ℓ=2 seems to agree better. Figure 6.55 shows the data alongside ℓ=1 and ℓ=2 angular distributions.

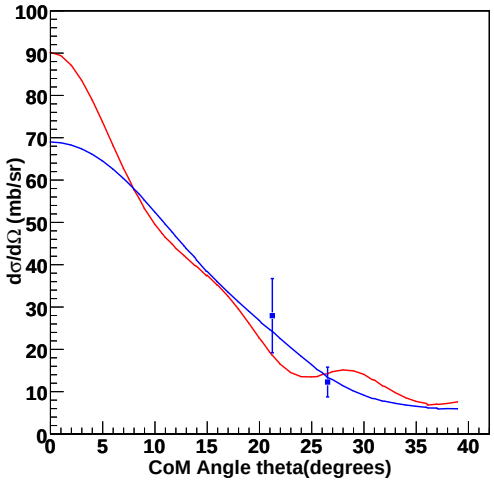

Figure 6.55: *Normalised Dresden2 data for ^{21}Ne 7.558 MeV where ℓ=1 (red) and ℓ=2 (blue) angular momentum can be seen. Theoretical angular distribution calculated using TWOFNR.*

For this state, this work concluded on a firm assignment of ℓ=1 ($(1/2)^-$ or $(3/2)^-$) based on both Dresden5 and Dresden2 data. While with the Dresden2 data, it was not possible to clearly discriminate between ℓ=1 and ℓ=2, the Dresden5 data, which has more data points, clearly allowed this discrimination. Dresden5, confirmed without a doubt the ℓ=1 assignment, and momentum assignment of this state confirmed the spin/parity literature suggestion.

6.4.11 ^{21}Ne 7.330 MeV - Ne XI

This state has no spin-parity assignments in literature. In Figures 6.56 and 6.57 are shown the angular distribution at 15°, 20°, 25° and 30° for Dresden5 and 20°, 25°, 30° and 35° in Dresden2 case.

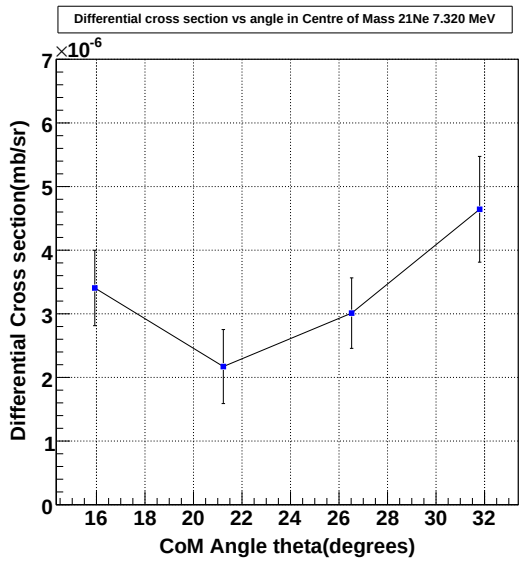

Figure 6.56: *Experimental angular distribution as extracted from data for Dresden5 for ^{21}Ne 7.330 MeV.*

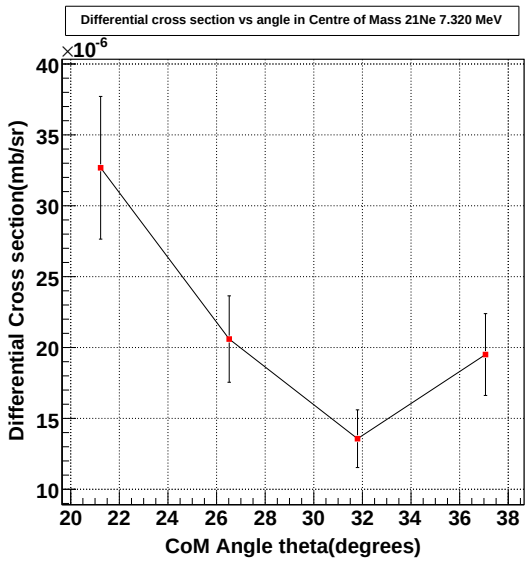

Figure 6.57: *Experimental angular distribution as extracted from data for Dresden2 for ^{21}Ne 7.330 MeV.*

Concerning angular momentum assignment for the ^{21}Ne 7.558 MeV, both Dresden5 and Dresden2 data were used during the investigation. Figure 6.58 and Table 6.19 show respectively the resulting fits and parameters for the Dresden5 data.

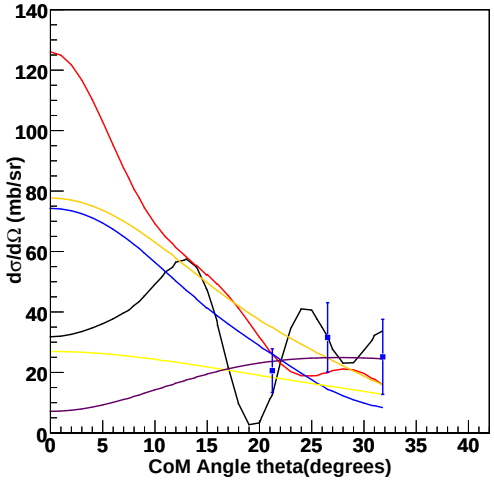

Figure 6.58: *Normalised Dresden5 data for ^{21}Ne 7.558 MeV with ℓ=0 in black, ℓ=1 in red, ℓ=2 in blue, ℓ=3 in Orange, ℓ=4 in yellow and ℓ=5 in Magenta. Theoretical angular distribution calculated using TWOFNR.*

	ℓ=0	ℓ=1	ℓ=2	ℓ=3	ℓ=4	ℓ=5
Chi-Square Values	1.720	2.165	4.666	3.033	1.588	0.524
Degree of Freedom	2	2	2	2	2	2
Relative Scaling Factor	26.05 ± 6.13	4.15±0.99	0.76±0.20	0.75±0.18	1.40±0.33	4.39±1.00

Table 6.19: *Chi-Square test resulting parameters for NeXI Dresden5. This table shows the parameters obtained when fitting experimental data with theoretical calculations.*

Dresden5 data favoured ℓ=5 ($J^{\pi}=(11/2)^{-}$) as angular momentum assignment. Figure 6.59 shows the normalised data which can be seen with the theoretical ℓ=5 angular distribution.

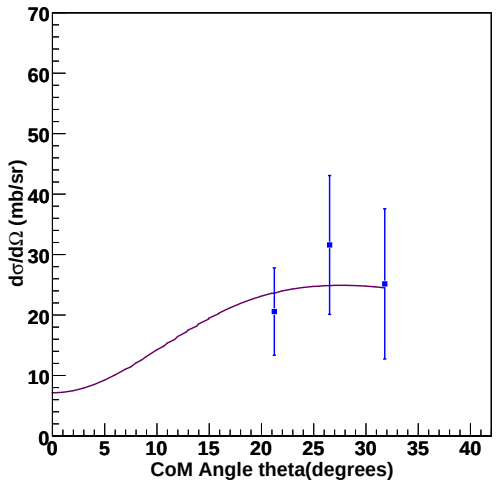

Figure 6.59: *Normalised Dresden5 data for ^{21}Ne 7.558 MeV where ℓ=5($J^{\pi}=(11/2)^{-}$) is shown. Theoretical angular distribution calculated using TWOFNR.*

For Dresden2 data, Figure 6.60 and Table 6.20 show the result of the fit associated with the different theoretical angular momentums.

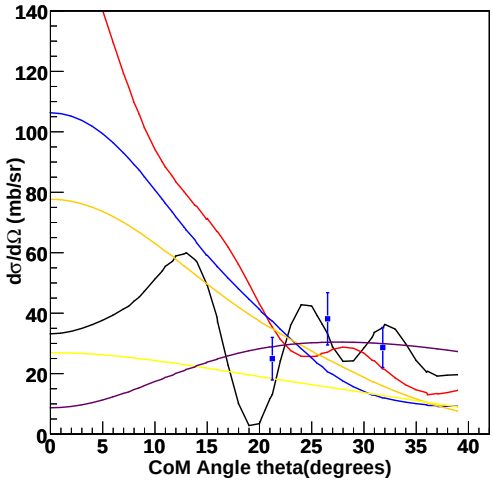

Figure 6.60: *Normalised Dresden5 data for ^{21}Ne 7.558 MeV where ℓ=0 is in black, ℓ=1 in red, ℓ=2 in blue, ℓ=3 in Orange, ℓ=4 in yellow and ℓ=5 in Magenta. Theoretical angular distribution calculated using TWOFNR.*

	ℓ=0	ℓ=1	ℓ=2	ℓ=3	ℓ=4	ℓ=5
Chi-Square Values	4.158	4.979	13.610	8.024	3.410	1.151
Degree of Freedom	2	2	2	2	2	2
Relative Scaling Factor	27.18 ± 3.98	5.65±0.83	1.09±0.18	1.05±0.16	1.86±0.27	5.37±0.76

Table 6.20: *Chi-Square test resulting parameters for NeXI Dresden2. This table shows the parameters obtained when fitting experimental data with theoretical calculations.*

Dresden2 data favoured the ℓ=5 ($J^{\pi}=(11/2)^{-}$) likewise as angular momentum assignment. Figure 6.61 shows the normalised data which can be seen with the theoretical ℓ=5 angular distribution.

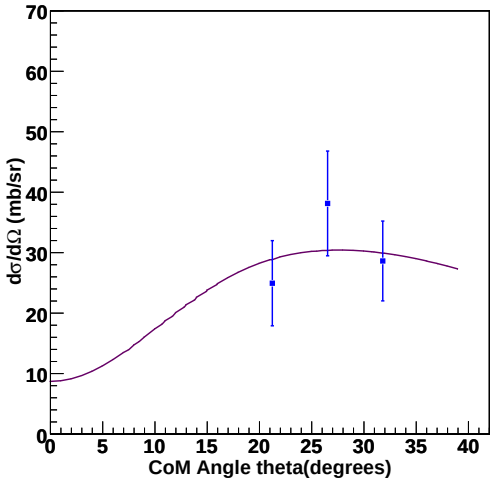

Figure 6.61: *Normalised Dresden5 data for ^{21}Ne 7.558 MeV where ℓ=5($J^{\pi}=(11/2)^{-}$) can be seen. Theoretical angular distribution calculated using TWOFNR.*

For this state therefore, based on both Dresden5 and Dresden2 data, this work made a firm ℓ=5 ($J^{\pi}=(11/2)^{-}$) as angular momentum assignment.

6.4.12 ^{21}Ne 7.239 MeV - Ne XII

This state has no spin-parity assignments in literature. From the data, it was possible to obtain the angular distribution for Dresden5 at 13°, 15°, 20°, 25°, 30° and for Dresden2 at 15°, 20°, 25°, 30° and 35°. Figures 6.62 and 6.63 show those results.

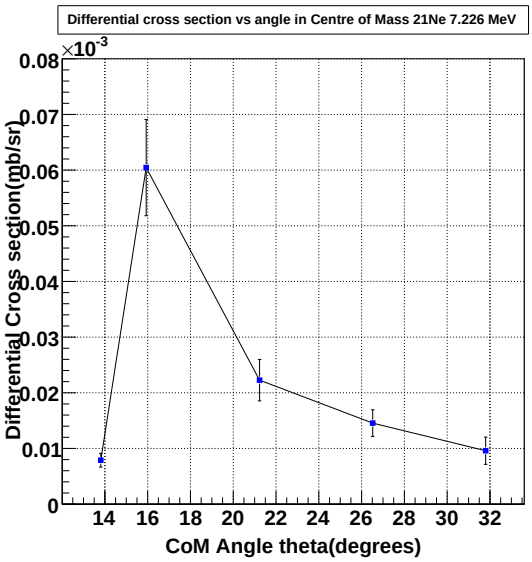

Figure 6.62: *Experimental angular distribution as extracted from data for Dresden5 for ^{21}Ne 7.239 MeV.*

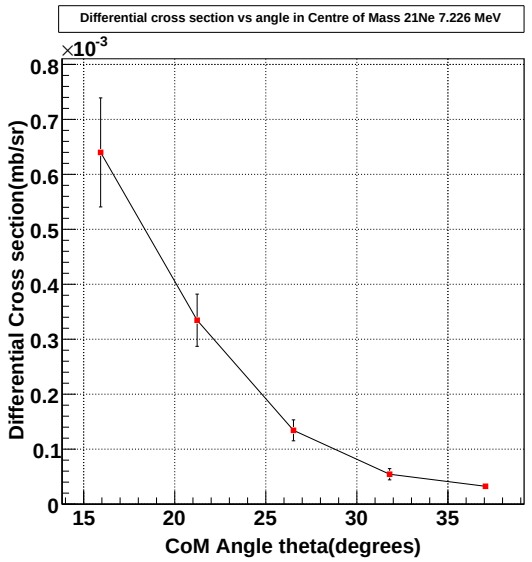

Figure 6.63: *Experimental angular distribution as extracted from data for Dresden2 for ^{21}Ne 7.239 MeV.*

Just as well, the first half of the results concentrates on the Dresden5 data while the second half on Dresden2. In Figure 6.64 and Table 6.21, the resulting fits and parameters of the Chi-square test for the Dresden5 data with ℓ=0, ℓ=1, ℓ=2, ℓ=3, ℓ=4 and ℓ=5 angular distributions can be seen.

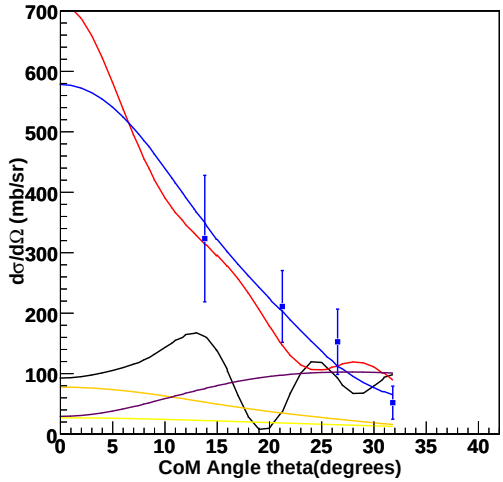

Figure 6.64: *Normalised Dresden5 data for ^{21}Ne 7.239 MeV with different angular momentum. ℓ=0 can be seen in black, ℓ=1 in red, ℓ=2 in blue, ℓ=3 in Orange, ℓ=4 in yellow and ℓ=5 in Magenta. Theoretical angular distribution calculated using TWOFNR.*

	ℓ=0	ℓ=1	ℓ=2	ℓ=3	ℓ=4	ℓ=5
Chi-Square Values	15.145	3.616	0.882	1.917	6.672	13.385
Degree of Freedom	3	3	3	3	3	3
Relative Scaling Factor	75.96± 17.59	23.41±4.26	5.94±1.04	5.27±0.93	7.84±1.51	18.11±4.01

Table 6.21: *Chi-Square test resulting parameters for NeXII Dresden5. This table shows the parameters obtained when fitting experimental data with theoretical calculations.*

Based on Dresden5 data, ℓ=2 ($J^{\pi}=(3/2)^{+}$ or $J^{\pi}=(5/2)^{+}$) is the unequivocal angular momentum for this state. Figure 6.65 shows the theoretical curve alongside normalised data that led to this conclusion.

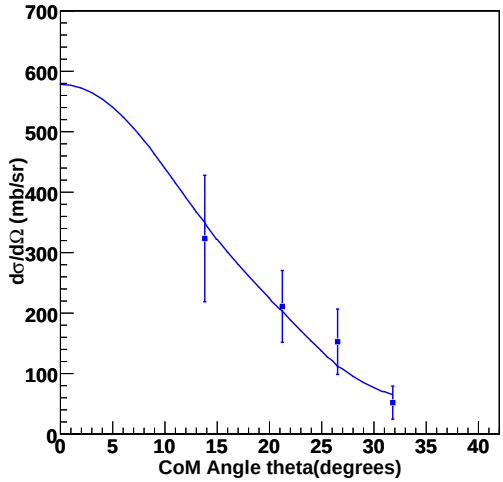

Figure 6.65: *Normalised Dresden5 data for ^{21}Ne 7.239 MeV where ℓ=2 ($J^{\pi}=(3/2)^{+}$ or $J^{\pi}=(5/2)^{+}$) can be seen. Theoretical angular distribution calculated using TWOFNR.*

The same investigation was performed for the Dresden2 data. The data were renormalised and Chi-square fits carried out. Figure 6.66 and Table 6.22 show respectively the resulting fits and main parameters.

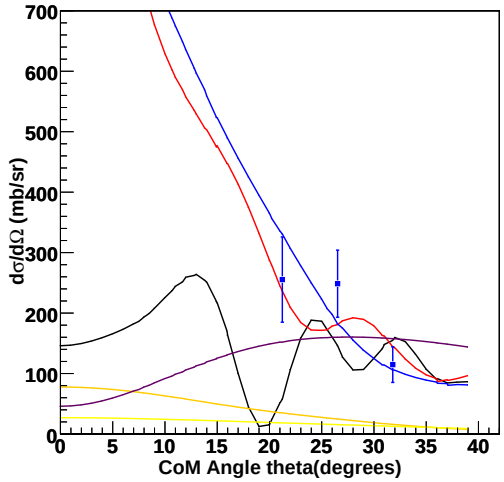

Figure 6.66: *Normalised Dresden2 data for ^{21}Ne 7.239 MeV where ℓ=0 is in black, ℓ=1 in red, ℓ=2 in blue, ℓ=3 in Orange, ℓ=4 in yellow and ℓ=5 in Magenta. Theoretical angular distribution calculated using TWOFNR.*

	ℓ=0	ℓ=1	ℓ=2	ℓ=3	ℓ=4	ℓ=5
Chi-Square Values	13.145	2.550	2.677	1.135	3.143	6.817
Degree of Freedom	2	2	2	2	2	2
Relative Scaling Factor	119.59 ± 20.16	37.70±5.57	9.66±1.43	8.01±1.17	11.65±1.73	28.28±4.39

Table 6.22: *Chi-Square test resulting parameters for NeXII Dresden2. This table shows the parameters obtained when fitting experimental data with theoretical calculations.*

Based on Figure 6.66 when considering the trend of the data and Table 6.22, ℓ=2 alongside ℓ=1 or even ℓ=3 (based on Chi-square fitting alone) happened to be the possible angular momentum choice of this state. More data point, based on this target alone, would have been needed to lift the ambiguity. Figure 6.67 shows the data alongside both ℓ=2 and ℓ=1 angular distributions.

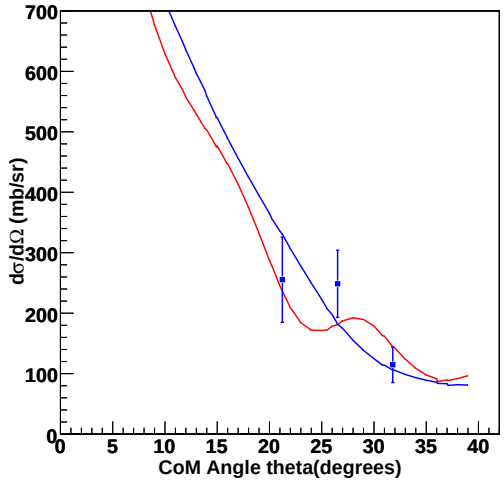

Figure 6.67: *Normalised Dresden2 data for ^{21}Ne 7.239 MeV where ℓ=2(J^{π}=$(3/2)^{+}$) is shown. Theoretical angular distribution calculated using TWOFNR.*

Dresden2 data has less degree of freedom and for this state, does not give an unambiguous assigned, with possible candidates being either ℓ=2 alongside ℓ=1 or even ℓ=3. However, given the presence of Dresden5 data undisputed confirmation on the ℓ=2, in this work, a firm assignment of ℓ=2 (J^{π}=$(3/2)^{+}$ or J^{π}=$(5/2)^{+}$) was made.

6.4.13 ^{21}Ne 7.055 MeV - Ne XIII

This state has a suspected J^{π}=$(9/2)^{+}$. Angular distribution at 11°, 13°, 15°, 20°, 25°, 30° for Dresden5 and 15°, 20°, 25°, 30° and 35° that have been extracted, are shown in Figures 6.68 and 6.69.

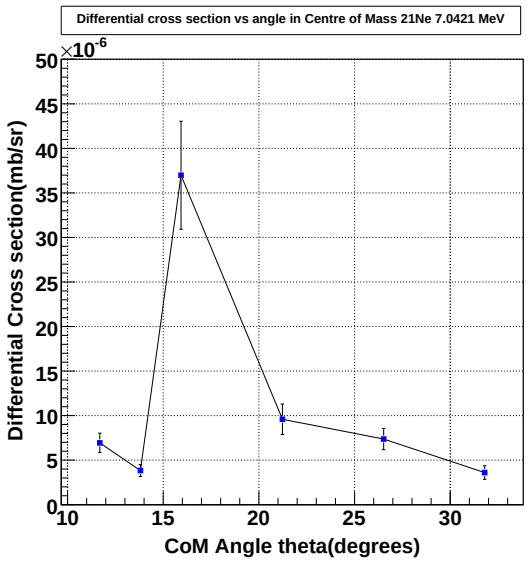

Figure 6.68: *Experimental angular distribution as extracted from data for Dresden5 for ^{21}Ne 7.055 MeV.*

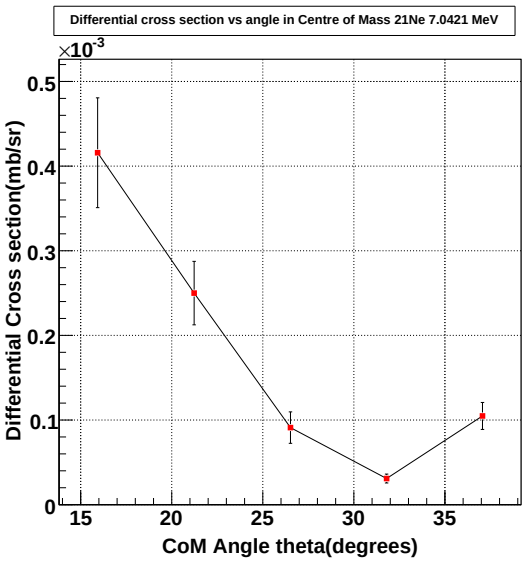

Figure 6.69: *Experimental angular distribution as extracted from data for Dresden2 for ^{21}Ne 7.055 MeV.*

Figure 6.70 shows normalised Dresden5 data with different theoretical angular distributions for which Chi-square fits were performed. The table afterwards (Table 6.23) shows the associated parameters.

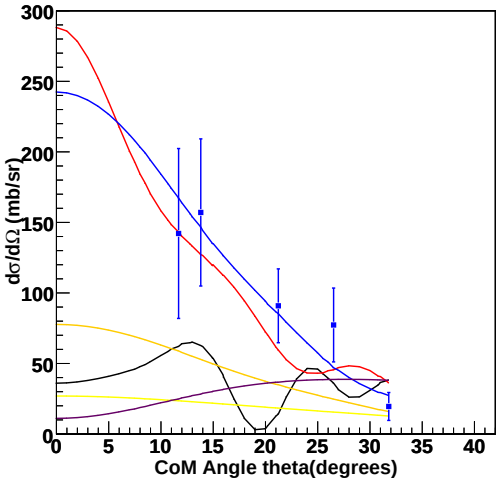

Figure 6.70: *Normalised Dresden5 data for ^{21}Ne 7.055 MeV. ℓ=0 is in black, ℓ=1 in red, ℓ=2 in blue, ℓ=3 in Orange, ℓ=4 in yellow and ℓ=5 in Magenta. Theoretical angular distribution calculated using TWOFNR.*

	ℓ=0	ℓ=1	ℓ=2	ℓ=3	ℓ=4	ℓ=5
Chi-Square Values	19.677	6.095	2.222	4.149	11.132	19.877
Degree of Freedom	4	4	4	4	4	4
Relative Scaling Factor	29.52 ± 6.66	9.48±1.65	2.49±0.41	2.20±0.37	3.15±0.59	6.83±1.55

Table 6.23: *Chi-Square test resulting parameters for NeXIII Dresden5. This table shows the parameters obtained when fitting experimental data with theoretical calculations.*

Dresden5 favoured an assignment of ℓ=2 (Chi-square value of 2.222, relative strength 2.49±0.41), for which the resulting fit can be seen in Figure 6.71.

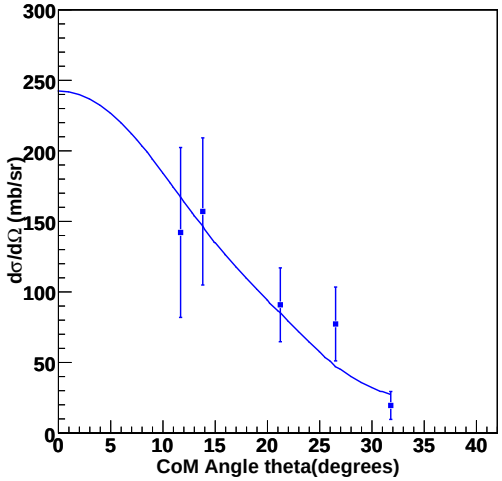

Figure 6.71: *Normalised Dresden5 data for ^{21}Ne 7.055 MeV where ℓ=2 in blue can be seen. Theoretical angular distribution calculated using TWOFNR.*

The Dresden2 data were as well, normalised as previously explained and the following, which can be seen in Figure 6.72 and Table 6.24, obtained.

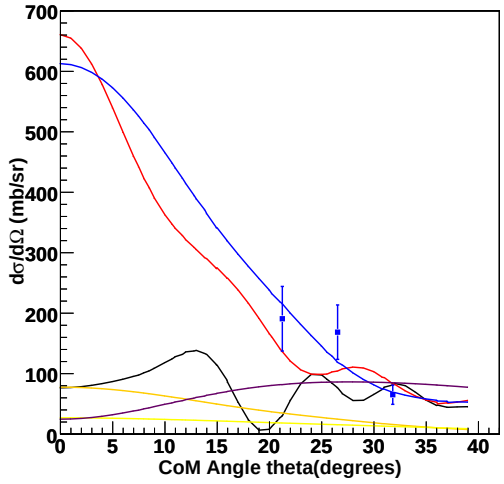

Figure 6.72: *Normalised Dresden2 data for ^{21}Ne 7.055 MeV where ℓ=0 angular momentum is seen in black, ℓ=1 in red, ℓ=2 in blue, ℓ=3 in Orange, ℓ=4 in yellow and ℓ=5 in Magenta. Theoretical angular distribution calculated using TWOFNR.*

	ℓ=0	ℓ=1	ℓ=2	ℓ=3	ℓ=4	ℓ=5
Chi-Square Values	14.229	4.351	1.508	1.893	5.277	9.052
Degree of Freedom	2	2	2	2	2	2
Relative Scaling Factor	62.72 ± 11.58	21.74±3.47	6.30±0.97	4.91±0.76	6.60±1.07	15.23±2.59

Table 6.24: *Chi-Square test resulting parameters for NeXIII Dresden2. This table shows the parameters obtained when fitting experimental data with theoretical calculations.*

For Dresden2 alike, an assignement of ℓ=2 was favoured. Details of which can be seen in Figure 6.73.

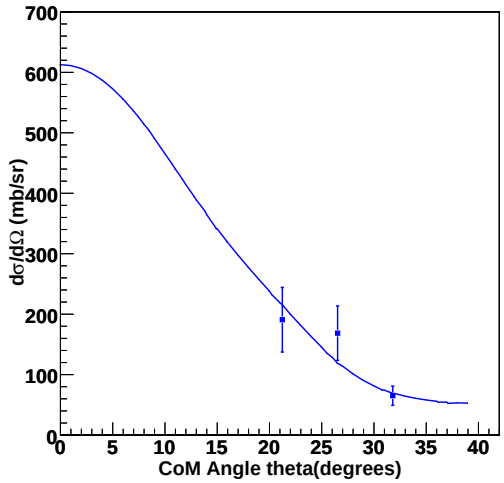

Figure 6.73: *Normalised Dresden2 data for ^{21}Ne 7.055 MeV where ℓ=2 angular momentum in blue is shown. Theoretical angular distribution calculated using TWOFNR.*

For this state, ℓ=2 is in good agreement with both Dresden5 and Dresden2 data points. Therefore, considering Dresden5 data and Dresden2 data, it is possible to firmly assign ℓ=2(J^{π}=$(3/2)^{+}$/$(5/2)^{+}$) as angular momentum, despite the suggested ℓ=4 of the literature.

6.4.14 ^{21}Ne 7.032 MeV - Ne XIV

This state has a suspected spin of 7/2 and a suspected positive parity. Data allowed the extraction of the angular distribution at 13°, 15°, 20°, 25°, 30° for Dresden5 and at 15°, 20°, 25°, 30° and 35° for Dresden2. Those are shown in Figures 6.74 and 6.75.

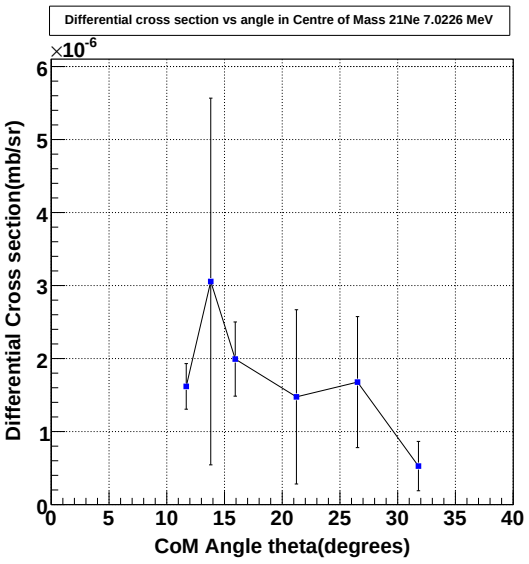

Figure 6.74: *Experimental angular distribution as extracted from data for Dresden5 for ^{21}Ne 7.032 MeV.*

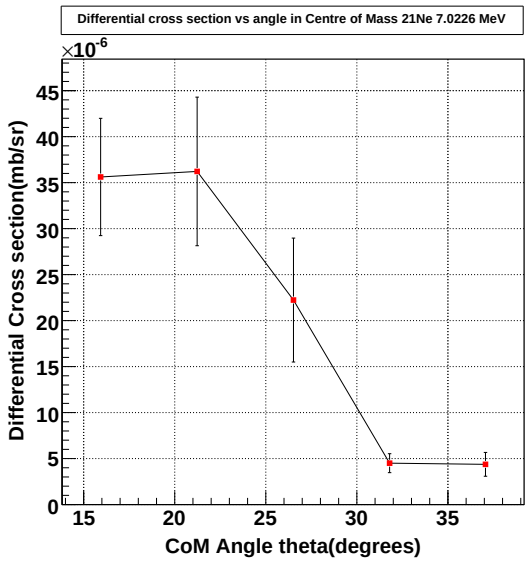

Figure 6.75: *Experimental angular distribution as extracted from data for Dresden2 for ^{21}Ne 7.032 MeV.*

Results for the Dresden5 data can be seen in Figure 6.76 and Table 6.25. Both the figure and table give details of the fitting of the data on different angular momentums using the Chi-square test method. Therefore, Figure 6.76 shows normalised Dresden5 where ℓ=0, ℓ=1, ℓ=2, ℓ=3, ℓ=4 and ℓ=5 theoretical curves can be seen and Table 6.25 associated parameters.

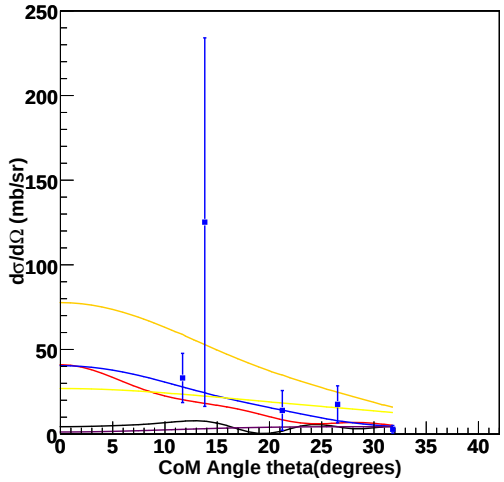

Figure 6.76: *Normalised Dresden5 data for ^{21}Ne 7.032 MeV where different angular momentum can be seen. ℓ=0 is in black, ℓ=1 in red, ℓ=2 in blue, ℓ=3 in Orange, ℓ=4 in yellow and ℓ=5 in Magenta. Theoretical angular distribution calculated using TWOFNR.*

	ℓ=0	ℓ=1	ℓ=2	ℓ=3	ℓ=4	ℓ=5
Chi-Square Values	7.461	4.047	2.358	3.788	6.203	8.205
Degree of Freedom	4	4	4	4	4	4
Relative Scaling Factor	3.58 ± 1.65	1.35±0.47	0.42±0.13	0.32±0.11	0.39±0.16	0.77±0.39

Table 6.25: *Chi-Square test resulting parameters for NeXIV Dresden5. This table shows the parameters obtained when fitting experimental data with theoretical calculations.*

Dresden5 data, favoured an ℓ=2 angular momentum assignement. Figure 6.77 shows normalised Dresden5 where the ℓ=2 theoretical curve can be seen.

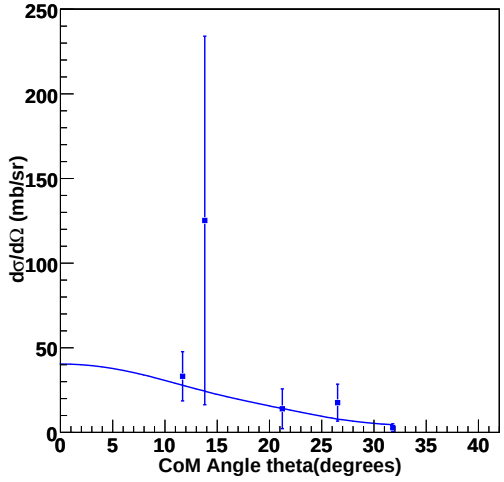

Figure 6.77: *Normalised Dresden5 data for ^{21}Ne 7.032 MeV where ℓ=2 can be seen. Theoretical angular distribution calculated using TWOFNR.*

Dresden2 data were also renormalised and can be seen in Figure 6.78 alongside theoretical angular distributions. Table 6.26 shows the resulting Chi-square fit parameters.

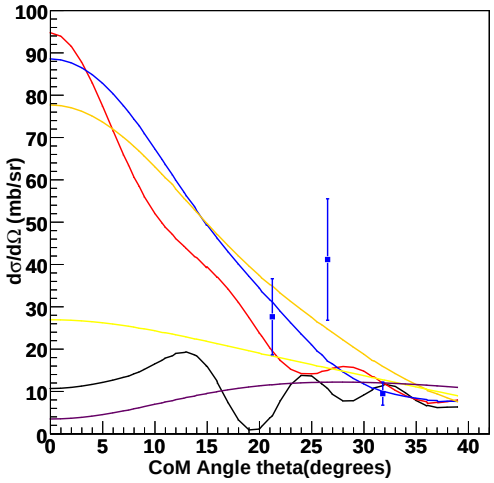

Figure 6.78: *Normalised Dresden2 data for ^{21}Ne 7.032 MeV where ℓ=0 is in black, ℓ=1 in red, ℓ=2 in blue, ℓ=3 in Orange, ℓ=4 in yellow and ℓ=5 in Magenta. Theoretical angular distribution calculated using TWOFNR.*

	ℓ=0	ℓ=1	ℓ=2	ℓ=3	ℓ=4	ℓ=5
Chi-Square Values	11.762	4.930	2.988	3.240	5.589	8.120
Degree of Freedom	2	2	2	2	2	2
Relative Scaling Factor	8.76 ± 2.07	3.12±0.63	0.91±0.18	0.71±0.14	0.95±0.19	2.15±0.46

Table 6.26: *Chi-Square test resulting parameters for NeXIV Dresden2. This table shows the parameters obtained when fitting experimental data with theoretical calculations.*

Dresden2 data, with a Chi-square value of 2.988, alike favoured an ℓ=2 ($J^{\pi}=(3/2)^{+}$ or $J^{\pi}=(5/2)^{+}$) angular momentum assignement. Figure 6.79 shows the normalised Dresden2 data for the 7.032 MeV where the ℓ=2 theoretical angular distribution can be seen.

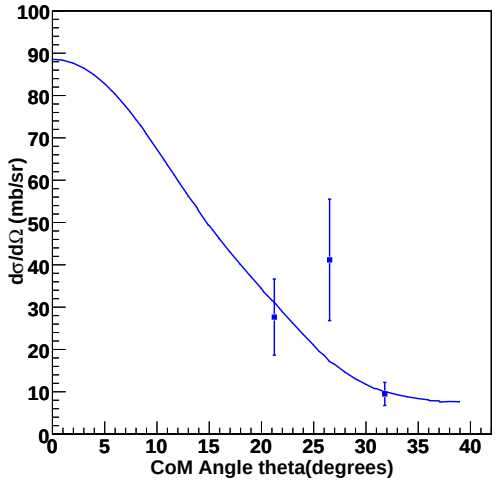

Figure 6.79: *Normalised Dresden2 data for ^{21}Ne 7.032 MeV where ℓ=2 angular momentum (blue), can be seen. Theoretical angular distribution calculated using TWOFNR.*

By considering both Dresden5 and Dresden2 data, a firm assignment of ℓ=2 ($J^{\pi}=(3/2)^{+}$ or $J^{\pi}=(5/2)^{+}$) was unequivocally made for this work.

6.4.15 ^{21}Ne 6.977MeV - Ne XV

This is a new state, not found in literature. Angular distributions extracted for this state are shown in Figures 6.80 and 6.81. For Dresden5, it can be seen at 11°, 13°, 15°, 20°, 25°, 30° and for Dresden2 at 15°, 20°, 25°, 30° and 35°.

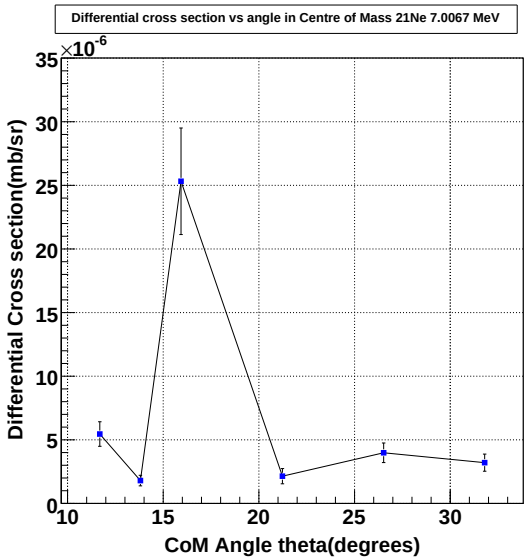

Figure 6.80: *Experimental angular distribution as extracted from data for Dresden5 for ^{21}Ne 6.977 MeV.*

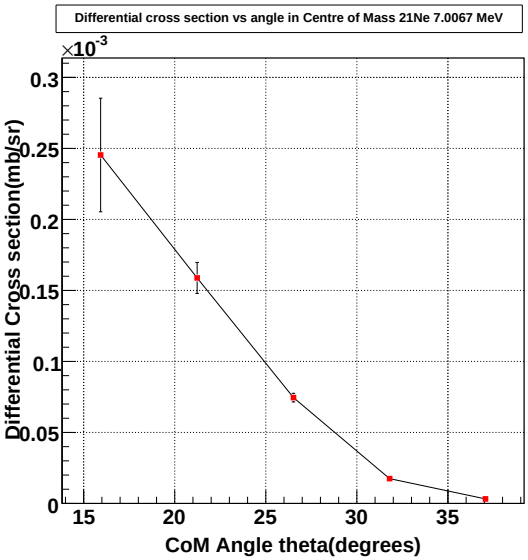

Figure 6.81: *Experimental angular distribution as extracted from data for Dresden2 for ^{21}Ne 6.977 MeV.*

The determination of the angular momentum assignement was performed using both targets for this state. Both data sets were renormalised and Chi-square fits performed.

Figure 6.82 shows the Chi-square fits results for the Dresden5 data while Table 6.27 shows the associated parameters.

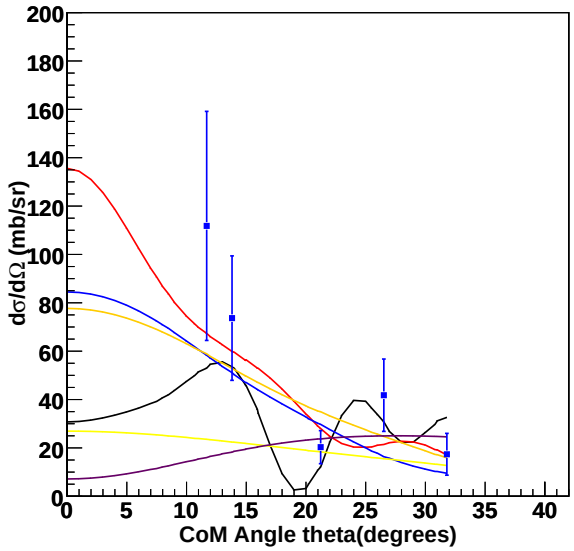

Figure 6.82: *Normalised Dresden5 data for ^{21}Ne 6.977 MeV where both theoretical angular momentum can be seen. ℓ=0 is seen in black, ℓ=1 in red, ℓ=2 in blue, ℓ=3 in Orange, ℓ=4 in yellow and ℓ=5 in Magenta. Theoretical angular distribution calculated using TWOFNR.*

	ℓ=0	ℓ=1	ℓ=2	ℓ=3	ℓ=4	ℓ=5
Chi-Square Values	7.251	4.286	7.654	6.959	7.710	10.941
Degree of Freedom	4	4	4	4	4	4
Relative Scaling Factor	25.18 ± 4.83	4.46±0.81	0.87±0.17	0.85±0.16	1.53±0.30	4.41±0.91

Table 6.27: *Chi-Square test resulting parameters for NeXV Dresden5. This table shows the parameters obtained when fitting experimental data with theoretical calculations.*

When considering Dresden5, the suspected assignment of ℓ=1 can be made for the state. Figure 6.83 shows the theoretical angular distribution with the normalised Dresden5 data.

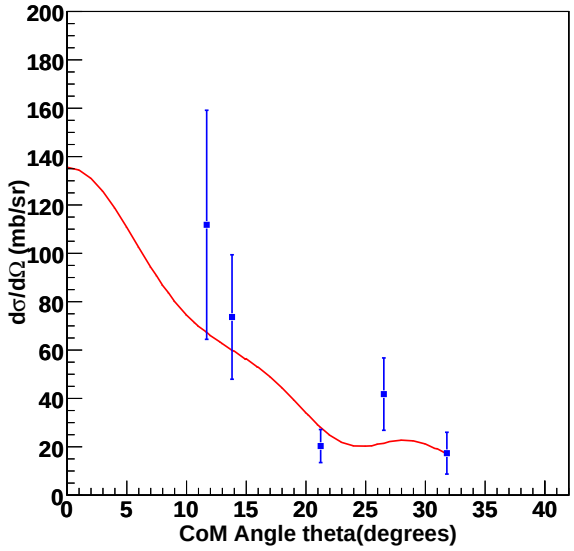

Figure 6.83: *Normalised Dresden5 data for ^{21}Ne 6.977 MeV where ℓ=1 in red, can be seen. Theoretical angular distribution calculated using TWOFNR.*

For the Dresden2 data, Figure 6.84 and associated Table 6.28 show the Chi square fits and parameters respectively for the ^{21}Ne 6.977 MeV.

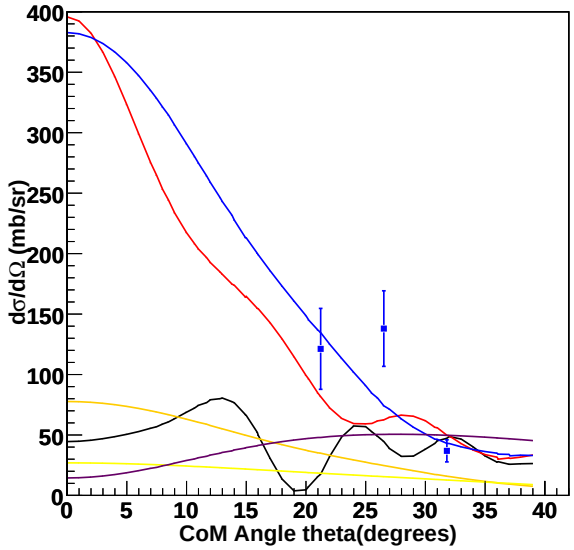

Figure 6.84: *Normalised Dresden2 data for ^{21}Ne 6.977 MeV where both theoretical angular momentum can be seen. ℓ=0 is seen in black, ℓ=1 in red, ℓ=2 in blue, ℓ=3 in Orange, ℓ=4 in yellow and ℓ=5 in Magenta. Theoretical angular distribution calculated using TWOFNR.*

	ℓ=0	ℓ=1	ℓ=2	ℓ=3	ℓ=4	ℓ=5
Chi-Square Values	19.836	9.233	4.811	5.822	10.313	14.626
Degree of Freedom	2	2	2	2	2	2
Relative Scaling Factor	36.49 ± 6.76	13.02±2.07	3.93±0.59	3.01±0.46	3.93±0.63	8.920±1.52

Table 6.28: *Chi-Square test resulting parameters for NeXV Dresden2. This table shows the parameters obtained when fitting experimental data with theoretical calculations.*

Based on Dresden2 alone, no assignments was possible as none of the theoretical curves fall within the acceptable range for a Chi-square distribution with degree of freedom of 2. Therefore, in this work, based on Dresden5 alone, only a tentative angular momentum assignment of ℓ=1 could be made.

6.4.16 ^{21}Ne 6.960 MeV - Ne XVI

This state has firstly been observed in this work. Figures 6.85 and 6.86 show the distribution for Dresden5 at 11°, 15°, 20° and 25° and for Dresden2 at 20°, 25°, 30° and 35°.

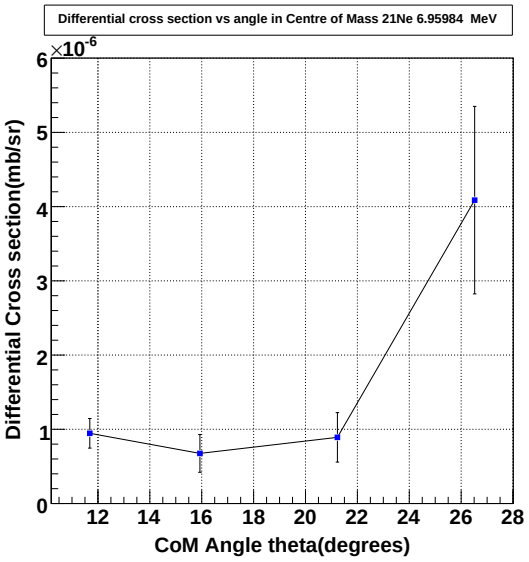

Figure 6.85: *Experimental angular distribution as extracted from data for Dresden5 for ^{21}Ne 6.960 MeV.*

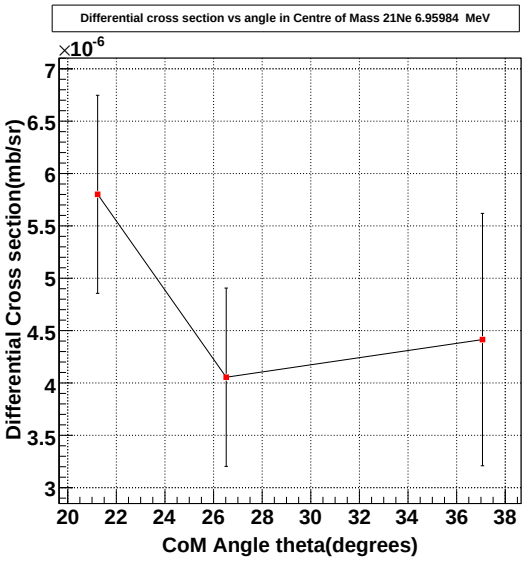

Figure 6.86: *Experimental angular distribution as extracted from data for Dresden2 for ^{21}Ne 6.960 MeV.*

For the angular momentum assignement of this state, both targets were also used. Both sets of data were renormalised and used accordingly. For the Dresden5 data, results of the fits can be seen in Figure 6.87 and Table 6.29 for different angular momentum (ℓ=0, ℓ=1, ℓ=2, ℓ=3, ℓ=4 and ℓ=5).

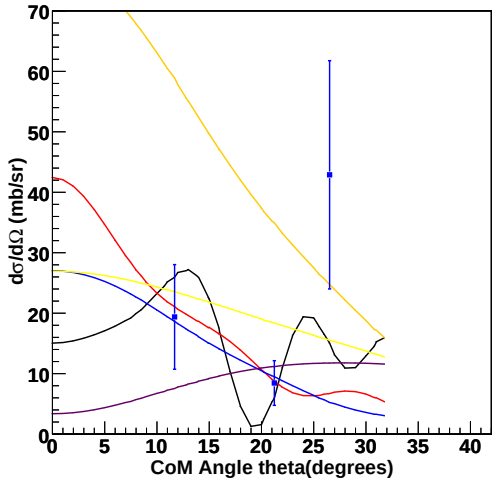

Figure 6.87: *Normalised Dresden5 data for ^{21}Ne 6.960 MeV where ℓ=0 is seen in black, ℓ=1 in red, ℓ=2 in blue, ℓ=3 in Orange, ℓ=4 in yellow and ℓ=5 in Magenta. Theoretical angular distribution calculated using TWOFNR.*

	ℓ=0	ℓ=1	ℓ=2	ℓ=3	ℓ=4	ℓ=5
Chi-Square Values	3.212	3.721	4.069	3.859	4.010	5.133
Degree of Freedom	2	2	2	2	2	2
Relative Scaling Factor	12.33 ± 3.53	1.40±0.41	0.28±0.08	0.29±0.09	0.59±0.18	2.077±0.65

Table 6.29: *Chi-Square test resulting parameters for NeXVI Dresden5. This table shows the parameters obtained when fitting experimental data with theoretical calculations.*

The result, based on Dresden5 data alone, for this state was quite ambiguous. However the result based on the Chi-square fit, which can be see in Figure 6.88, pointed to a possible ℓ=0 assignment.

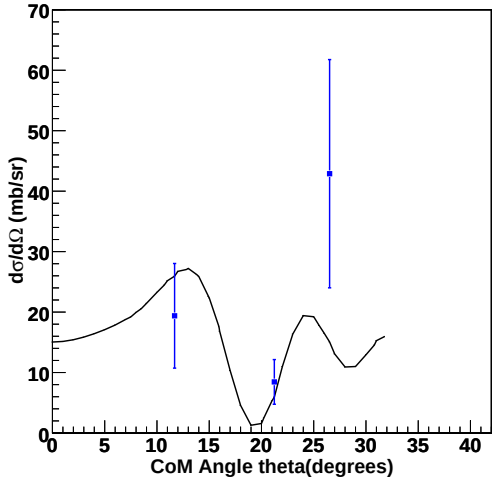

Figure 6.88: *Normalised Dresden5 data for ^{21}Ne 6.960 MeV where ℓ=0 is shown. Theoretical angular distribution calculated using TWOFNR.*

For the Dresden2 data, results of the fits to different theoretical angular distribution can be seen in Figure 6.89 and Table 6.30.

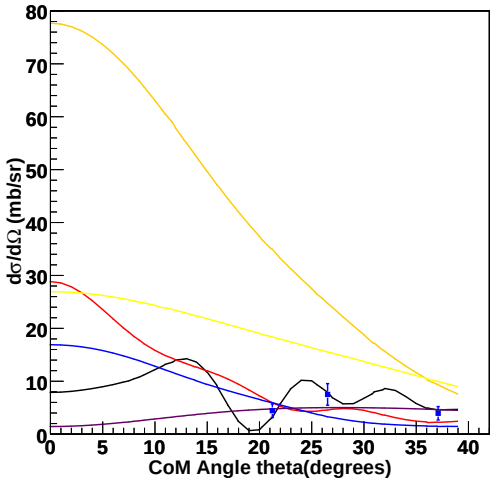

Figure 6.89: *Normalised Dresden2 data for ^{21}Ne 6.960 MeV with different angular momentum. ℓ=0 is seen in black, ℓ=1 in red, ℓ=2 in blue, ℓ=3 in Orange, ℓ=4 in yellow and ℓ=5 in Magenta. Theoretical angular distribution calculated using TWOFNR.*

	ℓ=0	ℓ=1	ℓ=2	ℓ=3	ℓ=4	ℓ=5
Chi-Square Values	1.356	5.355	9.617	7.498	3.185	1.879
Degree of Freedom	2	2	2	2	2	2
Relative Scaling Factor	6.47 ± 1.11	0.95±0.17	0.17±0.03	0.17±0.03	0.31±0.06	0.89±0.15

Table 6.30: *Chi-Square test resulting parameters for NeXVI Dresden2. This table shows the parameters obtained when fitting experimental data with theoretical calculations.*

Dresden2 data, with a Chi-square value of 1.356, alike unequivocally favoured an ℓ=0 angular momentum assignement.

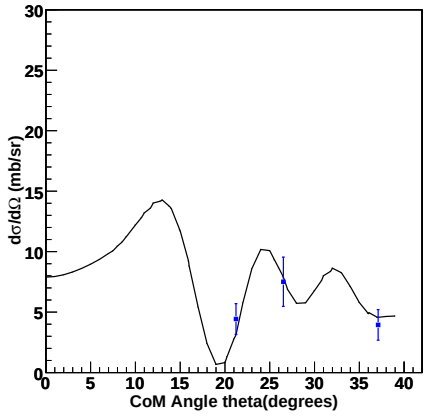

Figure 6.90: *Normalised Dresden2 data for ^{21}Ne 6.960 MeV where ℓ=0 is shown. Theoretical angular distribution calculated using TWOFNR.*

When considering both set of data, for this work, for the ^{21}Ne 6.960 MeV state, a firm ℓ=0 ($(1/2)^+$) angular momentum assignment was made.

6.5 Further Discussion

As a summary the following spin-parity assignments for different states are presented in Table 6.31.

Neon state	ℓ	$\mathbf{J}^\pi$
NeI	-	-
NeII	1	$(3/2)^-$
NeIII	**2**	$(\mathbf{3/2})^+$
NeIV	-	-
NeV	2	$(3/2)^+/(5/2)^+$
NeVI	(0)	$(1/2)^+$
NeVII	2	$(3/2)^+/(5/2)^+$
NeVIII	5	$(11/2)^-$
NeIX	5	$(11/2)^-$
NeX	1	$(1/2)^-/(3/2)^-$
NeXI	5	$(11/2)^-$
NeXII	2	$(3/2)^+/(5/2)^+$
NeXIII	2	$(3/2)^+/(5/2)^+$
NeXIV	2	$(3/2)^+/(5/2)^+$
NeXV	(1)	$(1/2)^-/(3/2)^-$
NeXVI	0	$(1/2)^+$

Table 6.31: *Summary of assigned ℓ and corresponding J^π for identified states. States where only tentative assignments were made are placed within brackets.*

Discrimination between ambiguous ℓ assignment for some states could have been improved by having a precise measurement of target thickness variation over time. Normalising the data to a known state, added uncertainties to an already large set of errors making it at time difficult to make firm ℓ assignments. Added to the knowledge of the "true" target thickness, the knowledge of the background shape would have led to smaller uncertainties and helped with the quest. A better coverage, especially at lower angle would have made it easier as most curves have very distinct features at these low angles.

CHAPTER 7

The ^{12}C $+^{12}$ C Fusion Reaction

7.1 Astrophysical importance of the ^{12}C $+^{12}$ C reaction

As explained in section 1.3, a star with mass M $\leq$ 8 $M_{\odot}$, will evolve to a white dwarf and one with M$\geq$ 10 $M_{\odot}$ will end as either a black hole or a neutron star. The crucial mass between these two extremely different evolutionary paths is only an approximation: 8-10 M$\odot$. The uncertainty in this mass range is directly related to the uncertainty in the reaction rate of the ^{12}C $+^{12}$ C reaction. The temperature at which the core carbon starts fusing material is 0.6-1.0 GK, and the Gamow peak in the centre of mass corresponding to these temperatures is E_{cm}=1.72-2.42 MeV.

As can be seen in section 1.3, ^{12}C plays a key role in AGB and TP-AGB stars. Improved knowledge of the ^{12}C $+^{12}$ C reaction will help to constrain the mass boundary and help the understanding of the role played by this reaction in TP-AGB stars.

The ^{12}C+^{12}C fusion reaction also plays an important role in binary systems producing Type 1a supernovae and superbursts.

Type 1a Supernovae, as explained in section 1.4.1, are important for cosmological distance determination. Once the density at the centre of the CO white dwarf increases, there is a rise in temperature and ignition of carbon. Further knowledge of the carbon fusion that triggers this explosion will help improve supernovae mechanisms and give an insight into their timescales.

Concerning superbursts, as explained in section 1.4.3, for unstable carbon burning at a deeper depth to be the origin of the superbursts. Given that presently no model with

actual known carbon fusion reaction rates have been able to explain the ignition, greater knowledge of the carbon fusion reaction is required.

7.2 Current Status on $^{12}C + ^{12}C$

7.2.1 The $^{12}C + ^{12}C$ Fusion Reaction

The $^{12}C + ^{12}C$ fusion reaction gives rise to a multitude of reaction products. This reaction has a Coulomb barrier height of 6.3 MeV. The cross section of this reaction falls gradually to less than one nanobarn for energies between 1 and 3 MeV [93].

The two carbon nuclei fuse to form the compound nucleus ^{24}Mg, which has enough excitation energy to either decay by particle emission or de-excite via γ-ray emission. Alpha, proton and neutron emission are the dominant evaporation channels within the energy range of interest, hence the production of ^{20}Ne, ^{23}Na and ^{23}Mg. The following set of equations show the different reaction products with their respective Q-value and Figure 7.1 shows the $^{12}C + ^{12}C$ energy levels.

$$^{12}C + ^{12}C \rightarrow ^{20}Ne + \alpha (Q = 4.61 \text{ MeV}) \quad (7.1)$$

$$^{12}C + ^{12}C \rightarrow ^{23}Na + p (Q = 2.24 \text{ MeV}) \quad (7.2)$$

$$^{12}C + ^{12}C \rightarrow ^{23}Mg + n (Q = 2.59 \text{ MeV}) \quad (7.3)$$

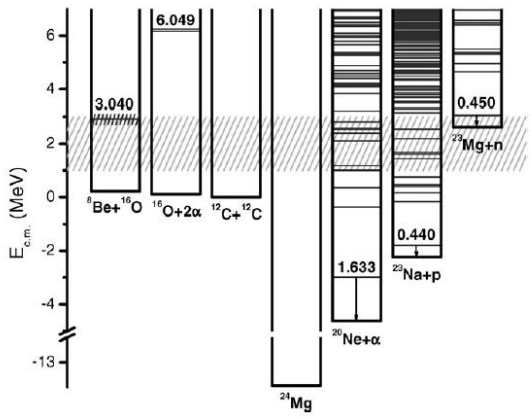

Figure 7.1: *$^{12}C + ^{12}C$ energy level diagram [93]. The shaded region indicates the astrophysically relevant energies.*

7.3 Previous Work on $^{12}C + ^{12}C$

Considerable effort has been devoted over the years to measure the $^{12}C + ^{12}C$ cross section at astrophysical energies, either by charged particle detection [94] or γ-ray spectroscopy [93, 95, 96, 97].These data have shown unexpected resonance structure in the excitation functions for $^{12}C + ^{12}C$ exit channels.

Initially, the resonances were observed at higher energies [95] and attributed to single particle states. Later on however, resonances were observed at lower energies and it became obvious that they needed to be extended to even lower energies [98]. These observed resonances scales however are too large to represent compound nucleus resonances and too small to be attributed to single particle states as they occur at around 100 keV apart [99]. This led to the implication of possible intermediate structure.

The previous cited experiments obtained useful data over a wide range of energies down to E_{cm}=2.1 MeV [97]. Although most authors agree with the rise of the S-factor at low energies [94, 93, 95, 96, 97], there remains major discrepancy. For example the work performed by L. Barron-Palos *et al.* in [93] and Mazarakis *et al.* in [94] seem to agree with the rise in the S factor at low energies while the work performed by Beckel *et al.*[100] disagree.

Figure 7.2, from [101] shows the extent of the disagreement when considering the cross section where a large spread in the data can be seen.

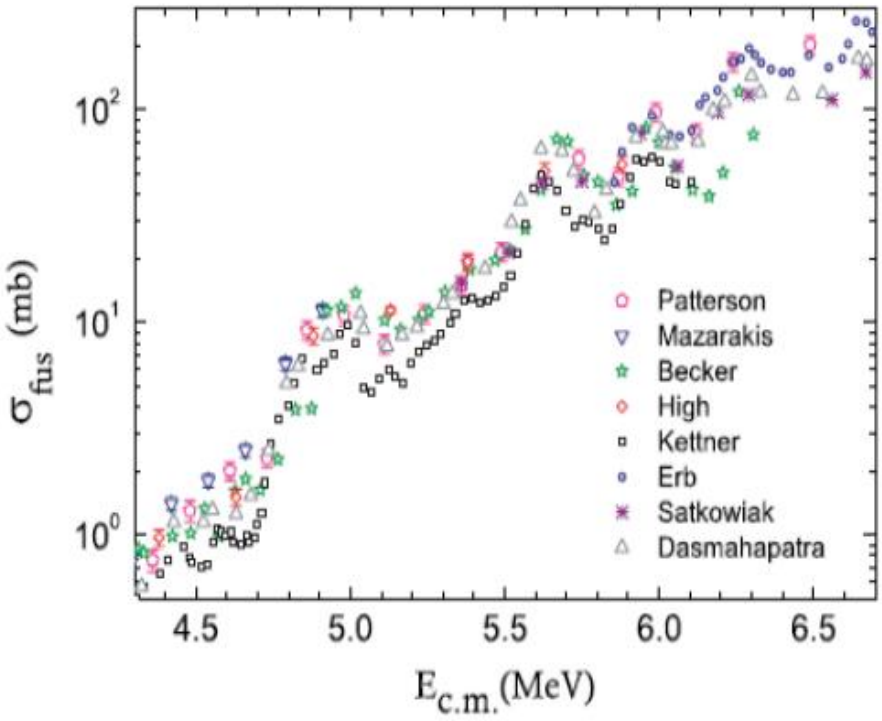

Figure 7.2: *Total fusion cross section measured in different* ^{12}C+^{12}C *experiments [101].*

It is important to underline that the ^{12}C +^{12} C cross section can either be obtained by charged particle detection or by γ ray spectroscopy. None of the γ-ray spectroscopic experiments measure the total cross section directly as only excited states can be detected. The ground state cross section in this case is obtained through calculations based on charged particle experiments. Furthermore in order to compare data from both methods, since there is no neutron channel data in both cases, α and p branching ratios need considering. Aguilera *et al.* made those necessary adjustments, further details of which can be found in [101]. Figure 7.3 shows the S factor from different experiments alongside theoretical predictions.

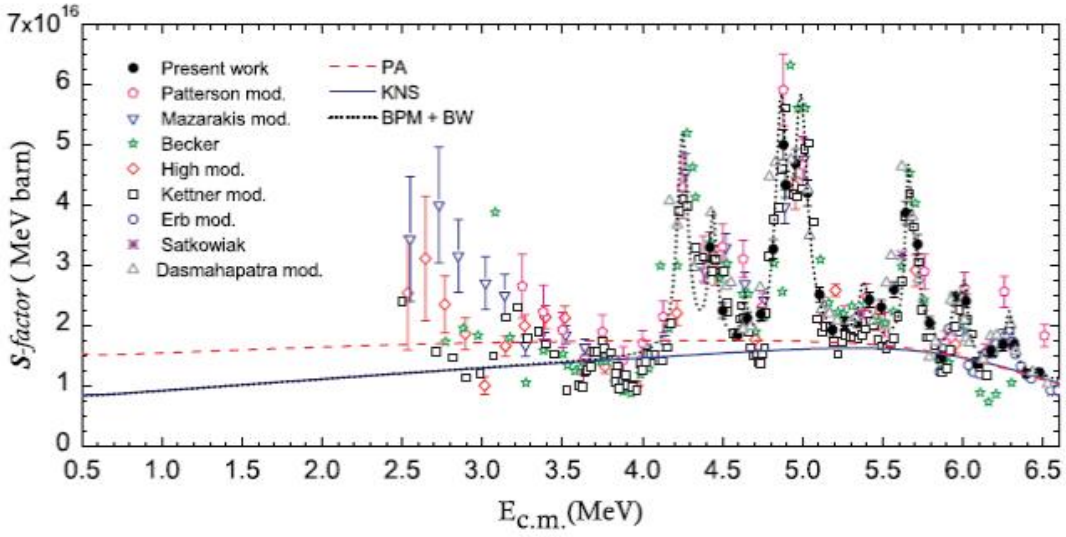

Figure 7.3: *S-factor for different* $^{12}C + ^{12}C$ *experiments [101]. Different lines show different theoretical predictions.*

7.4 Present work

The aim of the current work is to investigate $^{12}\mathrm{C} + ^{12}\mathrm{C}$ fusion reactions at the centre-of-mass energy range of 3.40 - 4.02 MeV. As explained earlier, the energy of interest starts at around 1 MeV. The energy range of this work is located at the higher end of the astrophysical range. This experiment is designed to set basis for experiments at much lower energies. Thus it should help provide a constraint to the present discrepancies in the studied energy range. This will also provide as well a premise for further investigation into the possible contributions of resonances to the cross section.

CHAPTER 8

Measuring ^{12}C $+^{12}$ C at Low Energies With the TRIUMF UK Detector Array Scattering Chamber

The ^{12}C+^{12}C reaction, data on which is the subject of the remainder of this work, was performed at TRIUMF located in Vancouver, Canada. TRIUMF is Canada's national laboratory for particle and nuclear physics.

The ^{12}C $+^{12}$ C measurement was carried out using the TRIUMF UK Detector Array (TUDA) scattering chamber. The beam was provided by OLIS (Off Line Ion Source) and accelerated by ISAC (ISotope Separator AND a*C*celerator). OLIS is used for the production of a range of stable beams for ISAC experiments and is constituted of a microwave driven cusp source for single and double charge ions, a surface ion source for low energy, and a multi-charge ion source [102].

8.1 ISAC-I

ISAC facility focuses on the post-acceleration of radioactive and stable nuclear beams varying from 0.15 to 1.5 MeV/u. It is constituted of a primary accelerator Radio Frequency Quadrupole (RFQ), a secondary accelerator Drift Tube Linac (DTL), the Low-Energy Beam Transport (LEBT) segment, the Medium-Energy Beam Transport (MEBT) segment and the High-Energy Beam Transport (HEBT) segment. Figure 8.1 shows the overview of ISAC facility.

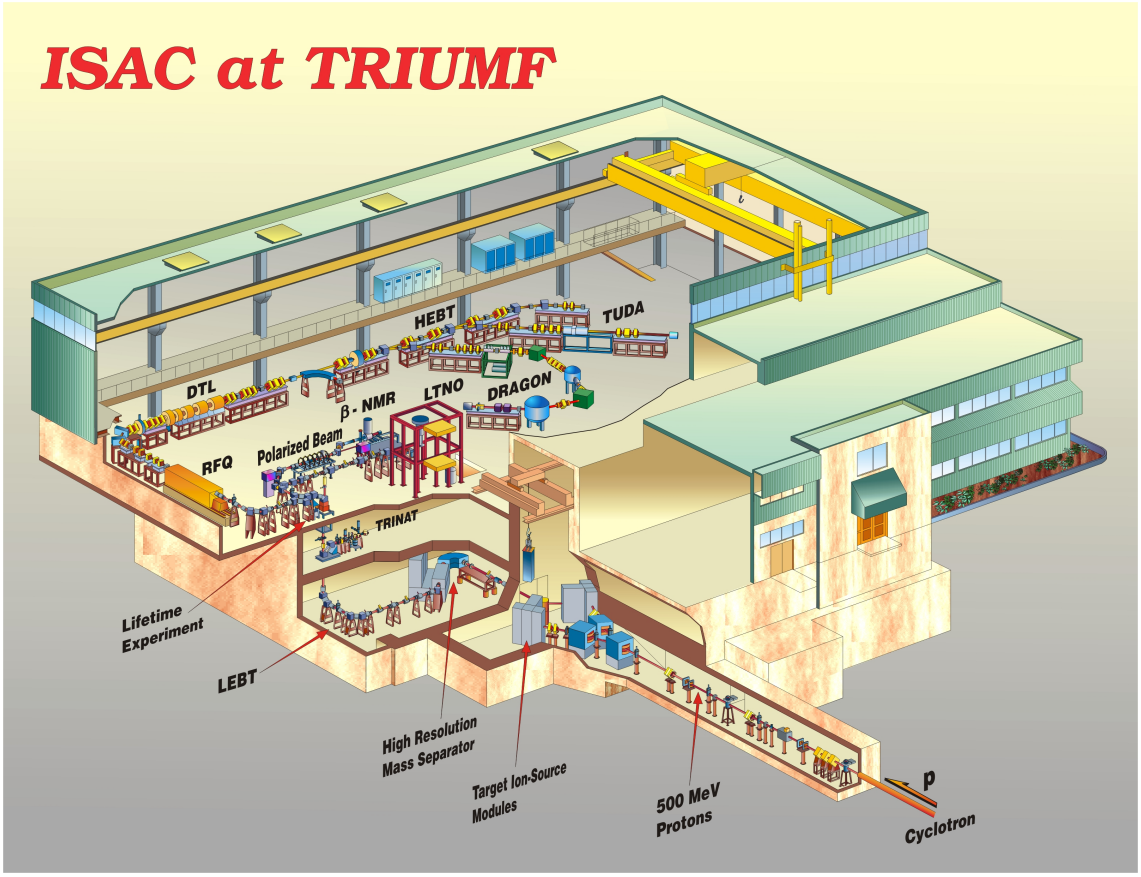

Figure 8.1: *A schematic representation of ISAC beam hall [103].*

8.2 TUDA Layout

TUDA, shown in Figure 8.2, consists of a main scattering chamber and an associated instrumentation copper shack. The scattering chamber is composed of two cylindrical segments connected by a rectangular section and arranged in such a way that it is coaxial with the beam. TUDA is used for studying charged particle reactions and allows for either solid or gas targets to be mounted in the chamber. TUDA is equipped with a target ladder and vacuum pump (located in rectangular section), a collimator assembly located at the entrance of the chamber and an anti-scatter collimator mounted upstream to provide protection against primary scattering. Furthermore it is fitted with upstream and downstream four vane beam monitors and a beam dump Faraday Cup [104]. TUDA allows variable upstream and downstream positioning of the charged particle detectors which are perpendicular to the beam axis.

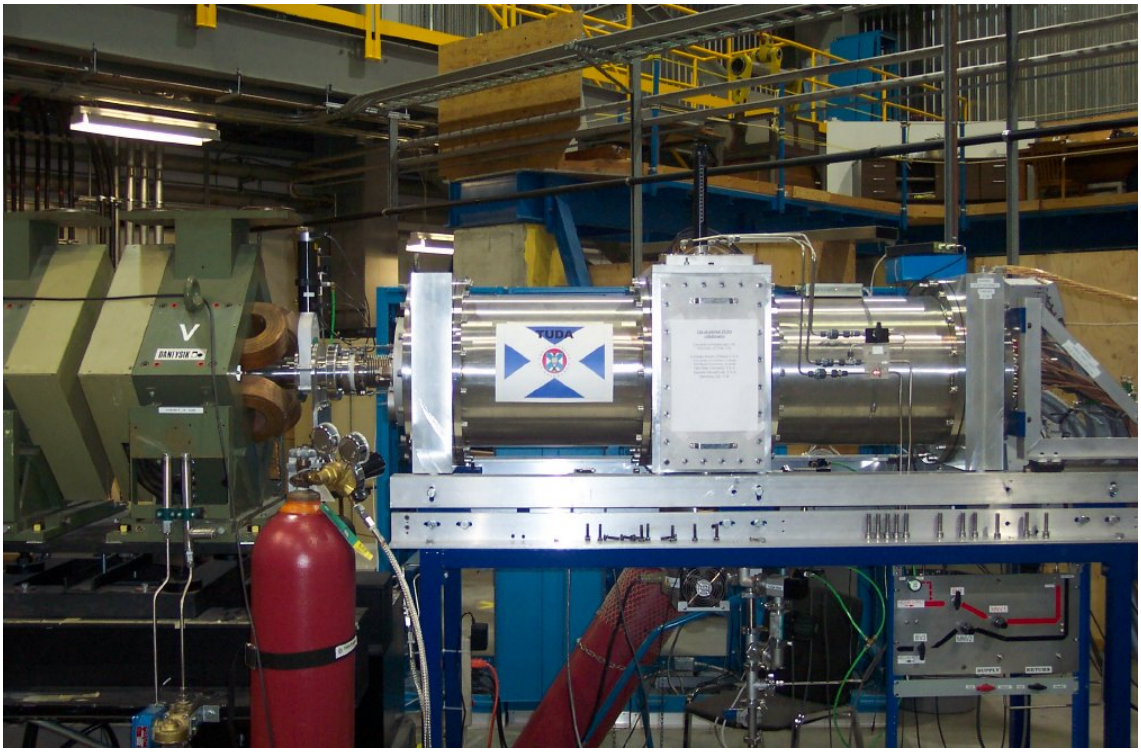

Figure 8.2: *A photograph showing TUDA [103].*

The Louvain-Edinburgh Detector Array (LEDA) and S2[1] configuration was used.

[1]Both defined in later sections.

8.3 LEDA - Segmented Detector

LEDA is a segmented single sided silicon detector with an active area consisting of 8 sectors and 16 radial strips each. Thus it has a total of 128 separate strips. Each strip is 4.9 mm wide. They are joined by a 100 μm interstrip section. LEDA can be used in a number of different configurations to provide the required angle coverage. Figure 8.3 shows a schematic view of LEDA which has been positioned inside TUDA and Figure 8.4 shows a photograph of a LEDA array.

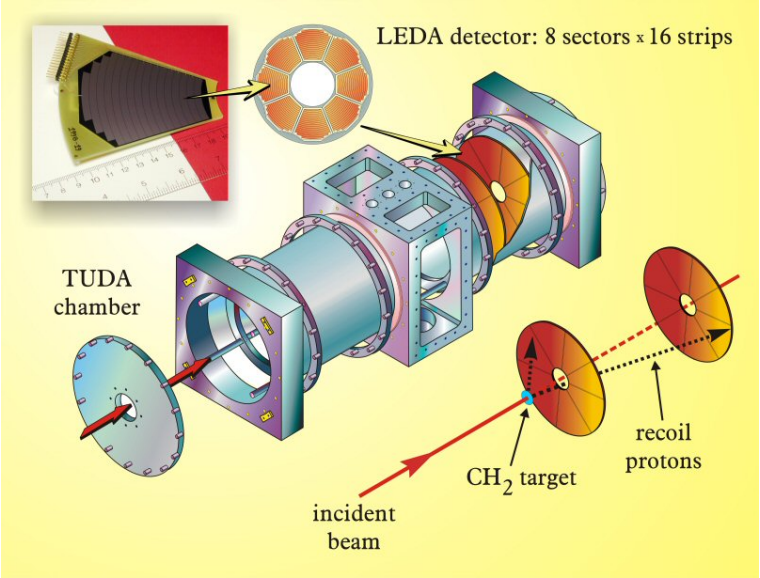

Figure 8.3: *TUDA design where LEDA detector has been positioned [104].*

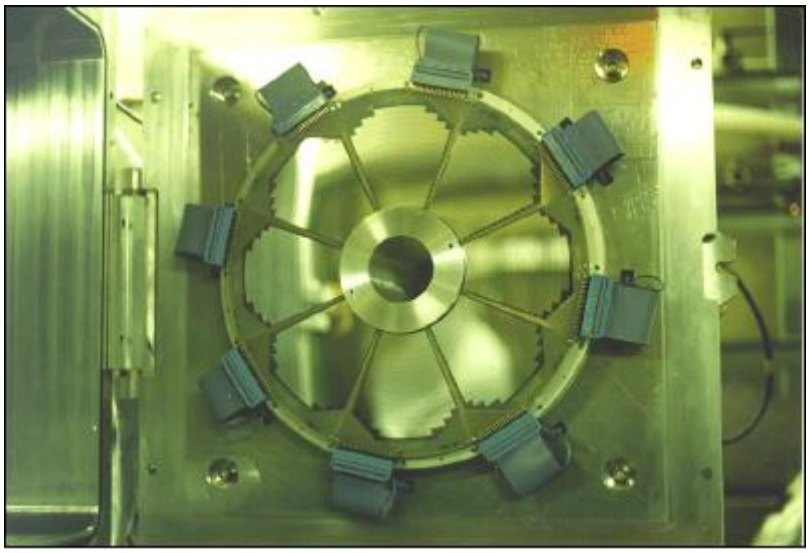

Figure 8.4: *Photograph showing a LEDA array [105]*

8.4 Micron S2 Detectors

The Micron S2 detector is a doubled sided silicon strip detector consisting of 48 annular rings and 16 segments. S2 is circular and has an active outer diameter of 70 mm and an active inner diameter of 22 mm. It has an active area of 35 cm^2 with a separation width of 100 μm [106]. Figure 8.5 shows a design of the micron S2 detector.

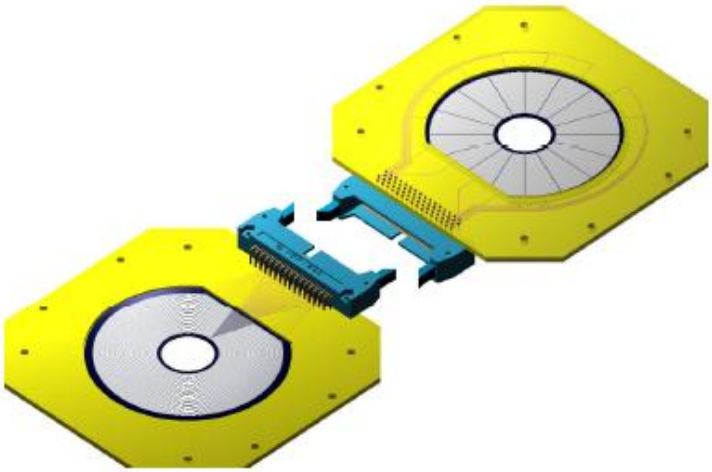

Figure 8.5: *S2 design where the front strips and back segments can be seen [106].*

8.5 Experimental Configuration

There were two experiments carried out, the first in 2005, followed by a further measurement in April 2006. For both experiments, $^{12}C^{3+}$ was used, with an intensity of, 10^{11} pps, and an enriched carbon target of either 10 or 20 $\mu g/cm^2$.

The setup in 2005, shown in Figure 8.6, consisted of one upstream and one downstream S2 detector; and one upstream and one downstream LEDA detector.

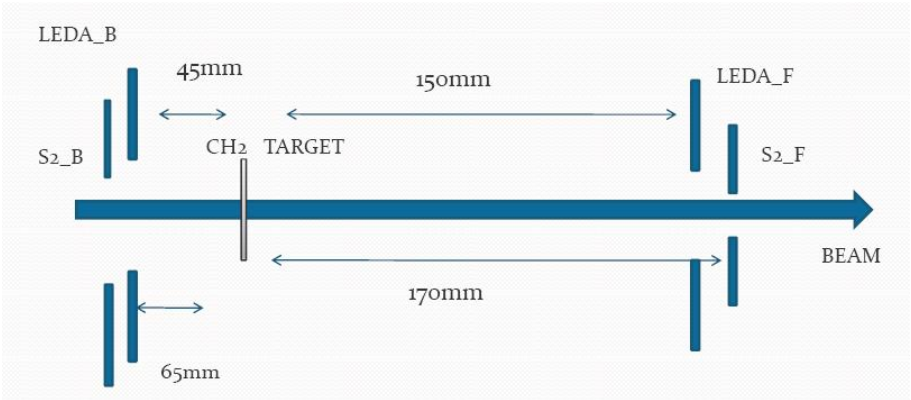

Figure 8.6: *2005 Experimental setup with upstream and downstream S2 detectors.*

In 2006, however, the downstream S2 detector was removed due to obstruction to the beam and the following set up, shown in Figure 8.7 was used.

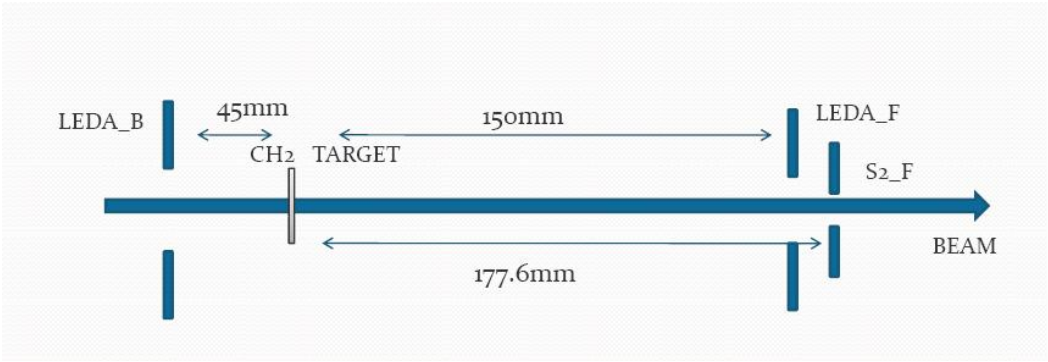

Figure 8.7: *2006 Experiment setup with only upstream S2 detector due to beam obstruction.*

With this configuration, the downstream LEDA had a thickness of $1000\mu m$ and the upstream LEDA had a thickness of $300\mu m$. There was good angle coverage, θ=3-11° for S2_F, θ =19-40° for LEDA_F and θ=109-130° for LEDA_B. There were aluminium shields placed in front of the detectors to stop scattering of heavy elements at small angles. One of the sector of the downstream LEDA was used as monitor detector. For that purpose,

there was a 3mm×5 hole in the shielding to allow ^{12}C +^{12} C elastic scattering to go through. The yield was measured at 45° to the beam axis.

8.5.1 Experimental Difficulties

During the run of the experiments, there were a few challenges expected such as the requirement of a very good beam energy determination, proton contamination on the target due to water and hydrocarbons and the danger of target thickness being affected by build-up.

Subsequently during the experiment, in order to monitor beam intensity and target thickness, a photodiode was added. The scattering at 50° was also monitored. In order to reduce the target contamination with hydrogen and deuterium, a cryopump was installed and to reduce the condensation of water vapour on the carbon surface, the target was heated.

8.6 Data Acquisition

Signals were processed by various electronic modules before the data acquisition system. In summary, the signals were shaped, amplified and digitised by the Analog to Digital Converter (ADC) which then gives energy information for a given event. Logical signals were also used. The logical signal was passed through a Time to Digital Converter (TDC). The TUDA AcQuisition system (DAQ) is VME- based and capable of acquiring up to 512 electronic channels. The data were acquired online, event by event and monitored using a Sun workstation [104]. It is important to underline that various technical difficulties were encountered during the 2005 experiment and some adjustments were needed for the 2006 experiment. Therefore, this work mainly focuses on the analysis on the subsequent 2006 experiment.

CHAPTER 9

^{12}C +^{12} C Data Analysis

This chapter gives details on the different stages of this data analysis carried out with the aim of extracting the yields and calculating the differential and total cross section of the ^{12}C +^{12} C reaction. The steps and problems encountered during the analysis are also described. Therefore, data conversion from MIDAS to ROOT is described, alongside data calibration, further details of the main sort code and different cuts applied to the data.

9.1 Data Format Conversion from the Multi Instance Acquisition System (MIDAS) to ROOT

An existing conversion of the data from MIDAS to ROOT alongside a sort code had been performed by the experimental team (in which the author was not involved). ADC calibrations were performed earlier on in MIDAS [99] and later included in a set of ROOT codes. Therefore, when the analysis began it revealed numerous inconsistencies, in particular the fact that either the ROOT sort code or the conversion from MIDAS to ROOT had led to an inconsistency with the original MIDAS data. This drove to the reconversion of the MIDAS data to ROOT by modifying another existing subroutine [107].

Thereafter, a new main sorting code was created and written by the author. The code was first initiated by creating a new ROOT class. The code allowed the extraction of the uncalibrated data.

9.2 Data Calibration

After extraction, the following step was to proceed with calibration of the 512 strips. The different detectors output signal were converted into digital signals by the ADC which gives the energy information and the TDC which gives the timing information. Outputs from each detector given in terms of channel number were converted in the main sorting code into energy (MeV) and timing information using

$$\text{Energy(channel)} = \text{ADC(channel)} \times \text{Gain(channel)} + \text{Offset(channel)} \ / \ 1000 \qquad (9.1)$$

$$\text{Time(channel)} = \text{TDC(channel)-Offset(channel)} \qquad (9.2)$$

9.2.1 Energy Calibration

There were, in total, 320 ADC channels in which the S2 detector data were located at channels < 64, LEDA_F at $63 <$ channel < 192 and LEDA_B at $191 <$ channel < 320. For the energy calibration data, a triple alpha source of ^{239}Pu,^{241}Am and ^{244}Cm with 5.156 MeV, 5.486 MeV and 5.805 MeV respectively was used to obtain the gain and offset. A program modified for sorting α-particle data was used whose ascii output files can be read by the main sorting code. A Gaussian was automatically fitted to each peak region which then allowed the calculation of a gain and an offset for each channel. Figure 9.1 shows the calibration run where the alpha peaks, after correction, can be seen as a function of the energies (MeV) for LEDA_F $\equiv$LEDA_1. Figure 9.2 shows the same run for all ADC channel numbers.

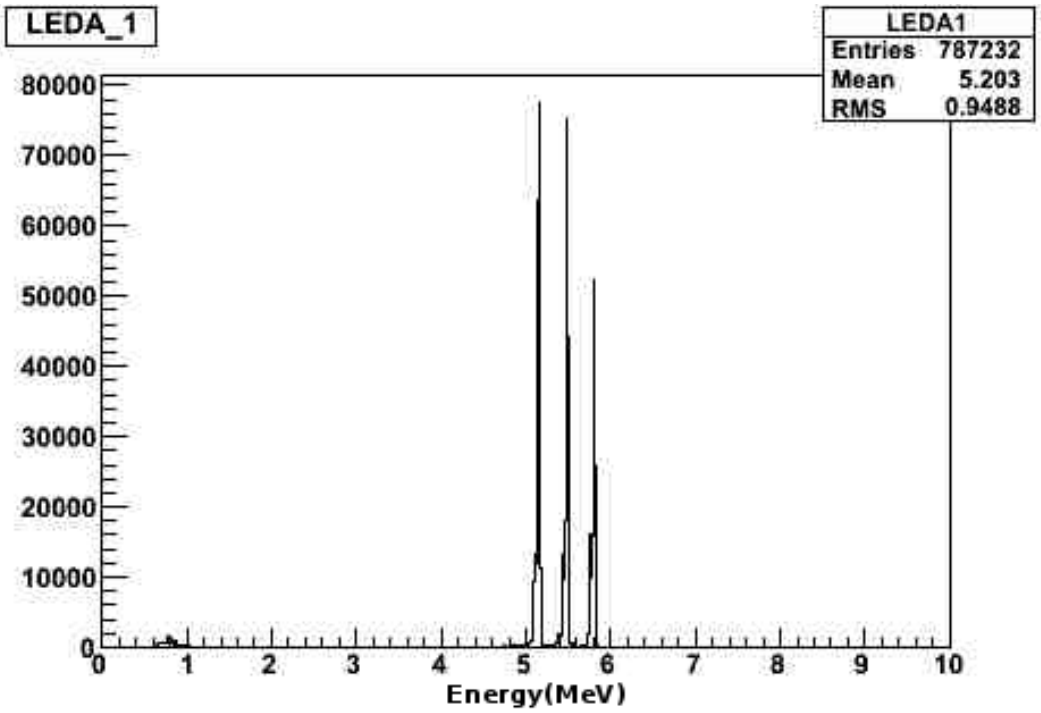

Figure 9.1: *Example of energy calibration file corresponding to LEDA_1. This figure shows the triple alpha source of* ^{239}Pu,^{241}Am *and* ^{244}Cm *with 5.156 MeV, 5.486 MeV and 5.805 MeV.*

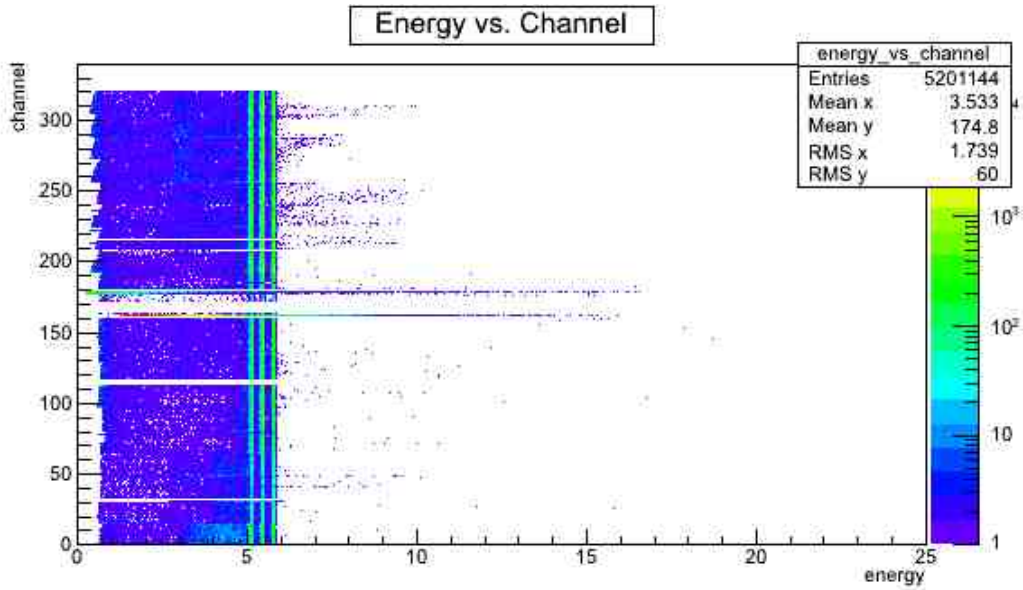

Figure 9.2: *Example of energy calibration file corresponding to LEDA_1 where energy(MeV) can be seen against channel number.*

9.2.2 Timing Data Calibration

Calibration of the timing information (TDC data) was performed manually for each TDC channel using a gold run (^{12}C +^{12} C+^{197}Au) for LEDA_2 after having checked that the difference on the time-of-flight (TOF) of ^{12}C between two different angles was not significant (a difference of 1.17 *ns* was found). A program was written and a Gaussian fitted to the one dimensional raw TDC value spectrum. For S2 front and LEDA_1 calibrations, pulser runs were used given the lack of gold runs with no shields for either of these detectors. Pulser walk-through and alpha calibration runs were taken at the very start and the vey end of the experiment in order to make sure that the calibration was still accurate. Pulser runs were used in this case after having checked that for each detector, both pulser runs located at the start and at the end of the experiment have their energies located at the same place.

For both detectors, by manually fitting a Gaussian, the peak centroid and widths were found. This then allowed offsets to be calculated based on considering an arbitrary value as the central TDCs centroid. Figures 9.3 and 9.4 show before and after calibration for LEDA1.

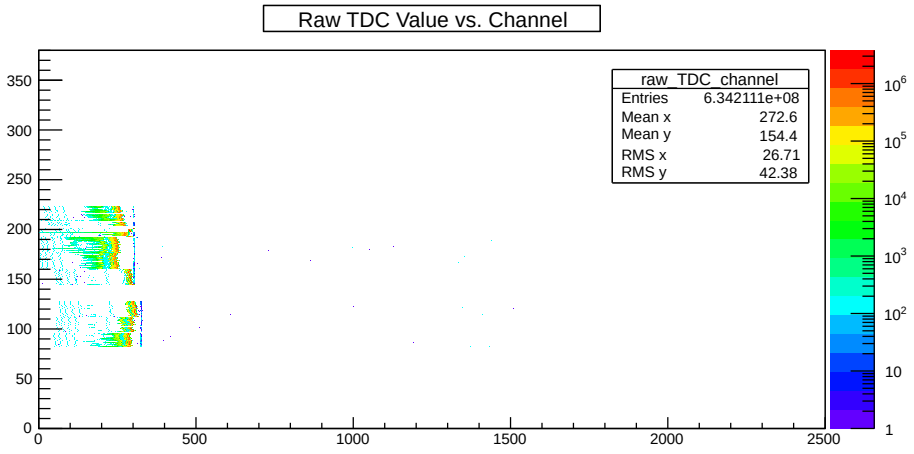

Figure 9.3: *Run 141. Calibration run for LEDA_1 shown before calibration offsets are applied.*

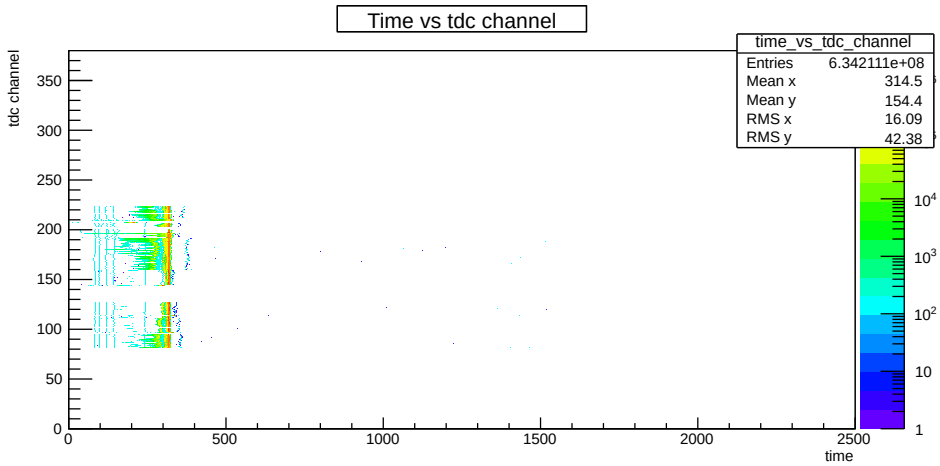

Figure 9.4: *Run 141. Calibration run for LEDA_1 shown after calibration.*

9.3 Energy Loss Correction

In order to take into account the loss of energy encountered by the detected particle when passing through the target and aluminium shield, energy loss corrections were performed using the Stopping and Range of Ions in Matter (SRIM) software [108]. SRIM is a program which performs calculations of the interaction of ions with matter. The energy measured was therefore adjusted by taking into account energy lost through the aluminium shield and up to halfway through the target thickness meaning $E = E_{meas.} + \Delta E_{Al} + \Delta E_{target}$. The energy loss dE/dx was calculated using SRIM in a 5 keV step. Two different outputs were obtained for both detected helium and protons products. The outputs obtained were plotted and a fit applied. A six order polynomial was found to have the best fit. In figures 9.5, 9.6, 9.7 and 9.8, a plot of the outputs can be seen alongside the fitted analytic expressions for hydrogen and helium respectively through aluminium and carbon.

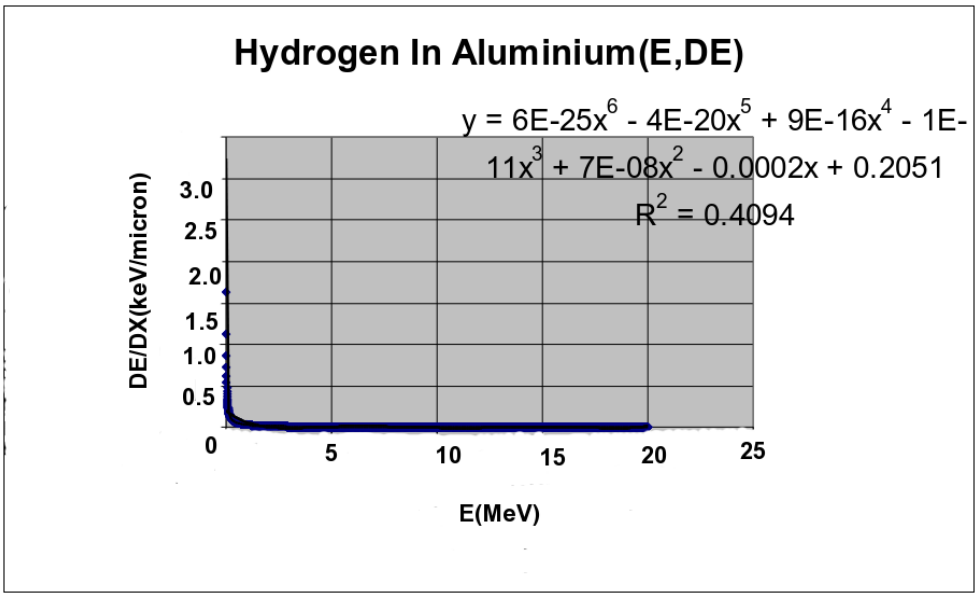

Figure 9.5: *Energy Losses for proton through Aluminium where the fitting polynomial curve can be seen.*

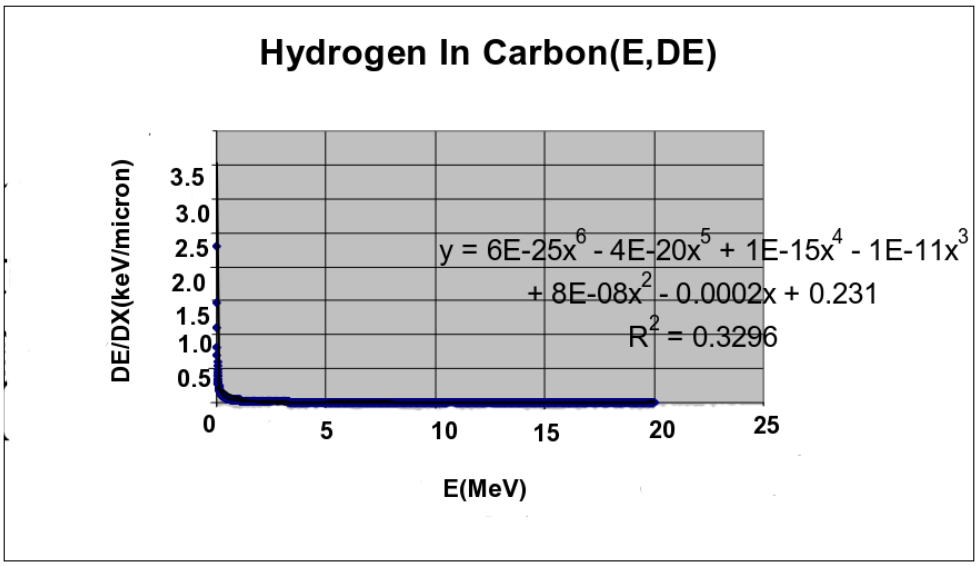

Figure 9.6: *Energy Losses for proton through Carbon where the fitting polynomial curve is seen.*

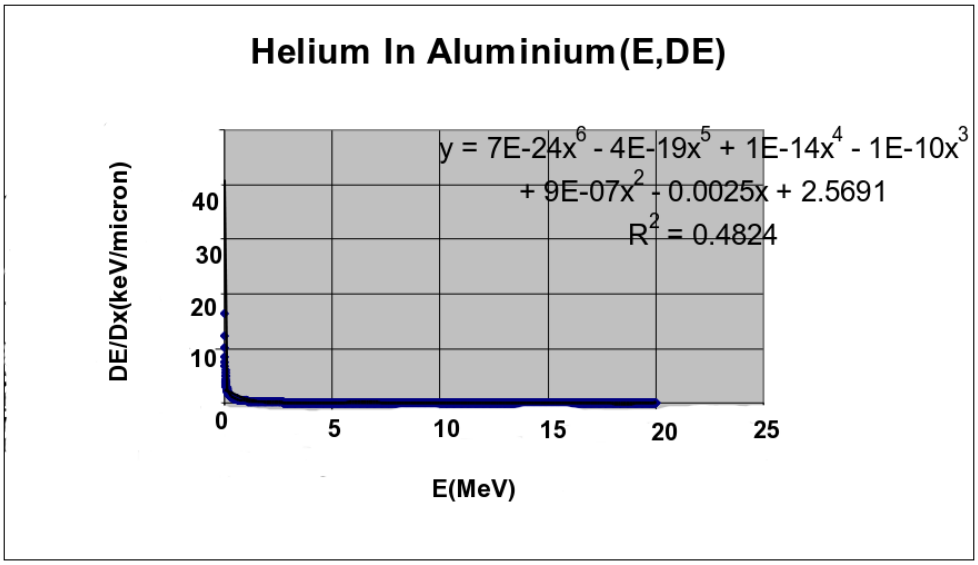

Figure 9.7: *Energy Losses for Alpha through Aluminium with polynomial fit shown.*

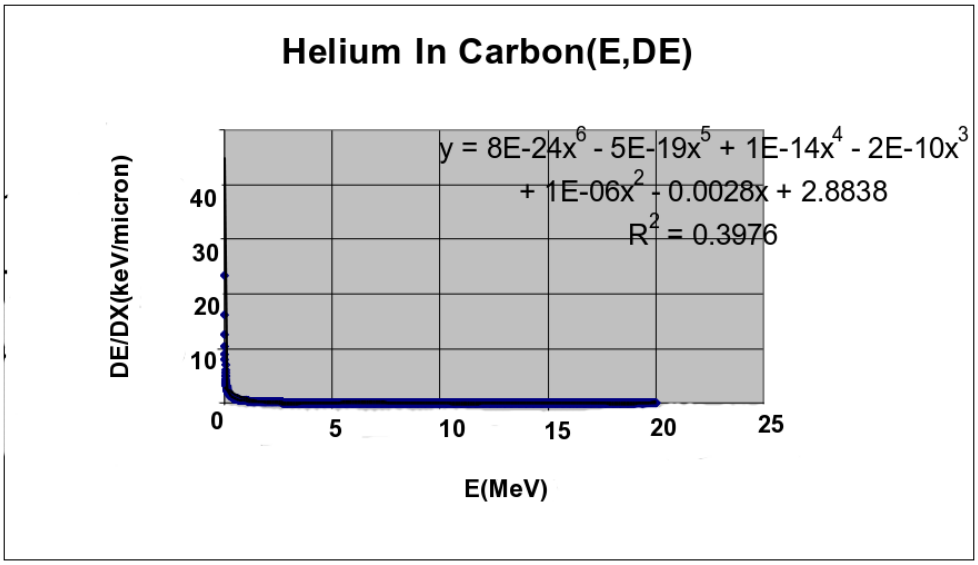

Figure 9.8: *Energy Losses for Alpha through Carbon where polynomial fit is shown.*

Both hydrogen and helium expressions were then included in the code. Corrections were performed for LEDA forward and for S2. Two target thicknesses of 10 and 20 μgcm^2 were used for different sets of energies and therefore taken into account.

9.4 On the Way for Yield Extraction

9.4.1 On the Way for Particle Identification

The first step toward the yield extraction was to clean up the data and only select good events. As a starting point, only events beyond 250 keV were to be considered in order to avoid low energies noise.

9.4.2 Good Events Selection

All detected events are not necessarily characterised as good events. The S2 detector uses the same silicon wafer for its front side and back side, which means that the expectation was for a good event to be characterised as one hitting the active area of this detector. Therefore for a good event on the S2 detector it is expected to have a close to identical energy between the front and back of the detector. Any events where this energy significantly differed were rejected. This coincidence helped in further reducing the background as well. Thus since only events which went through the front and the back of S2 detector at relatively close energies had to be selected, the exact range to be considered for the cut needed to be investigated. At this stage, a few features such as multiplicity of different detectors for ADC and TDC data were also investigated and the main code modified to prevent an inconsistent match between event of multiplicity greater than one.

For this purpose, the energy difference between the front and the back of the S2 detector for a gold run (^{12}C +^{12} C +^{197} Au) with no shield (run 20) was studied. The energy difference + offset of 2048 were investigated. Figure 9.9 shows the energy difference peak between the front and the back for run 20.

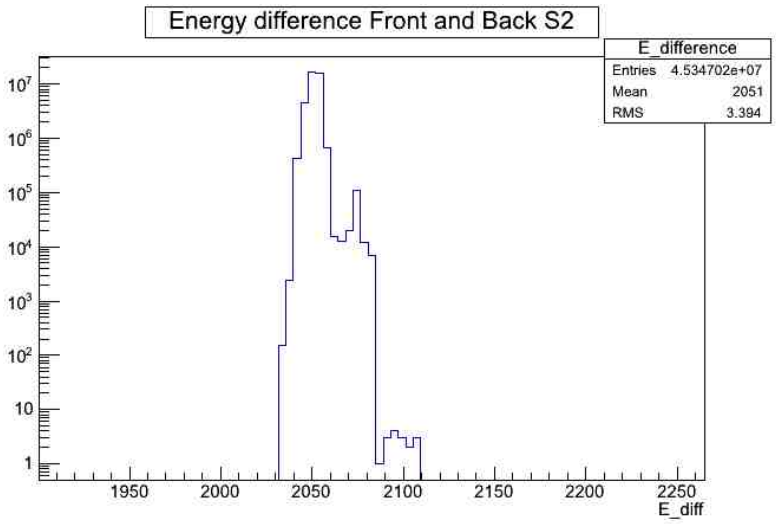

Figure 9.9: *Gold run with no shield on. This figure shows the energy difference between S2 front energy and S2 back energy. Energy difference+ 2048 were plotted.*

The peak was divided into three different sub-peaks and cuts on S2 were performed for each subdivision. Sub-peak I energy range was of [-160 keV, 220 keV], sub-peak II energy range varied from [220 keV, 360 keV] and sub-peak III range was [360 keV, 620 keV]. For each sub-peak, graphs such as Energy versus theta and S2 front energy versus S2 back energy were investigated. The conclusion came to take into account both sub-peaks for the for S2 energy cut. This brought the range to be [-160 keV, 620 keV].

The next set of spectra, Figure 9.10 and Figure 9.11 show respectively S2 energy front versus energy back before and after the cut for a ^{12}C +^{12} C run with the shield on (run 21).

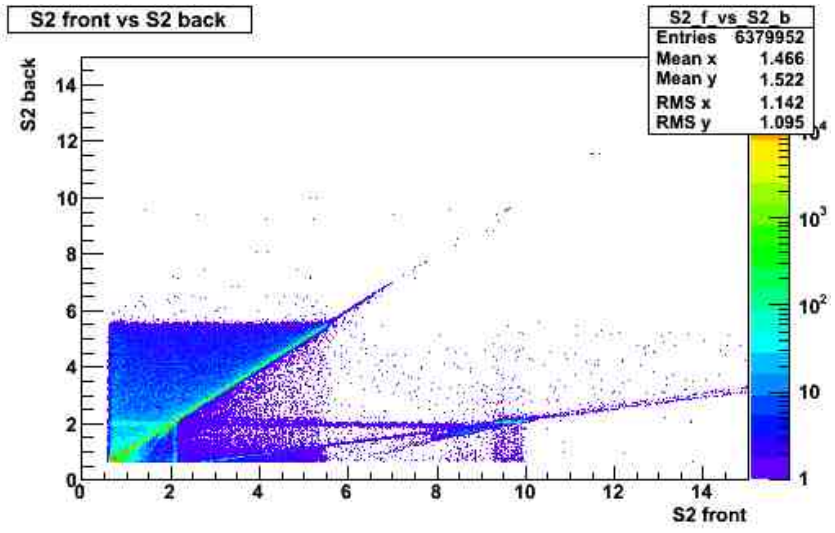

Figure 9.10: *Run 21, $^{12}C+^{12}$ C run with shield on. This figure shows S2 energy front versus S2 energy back before cut.*

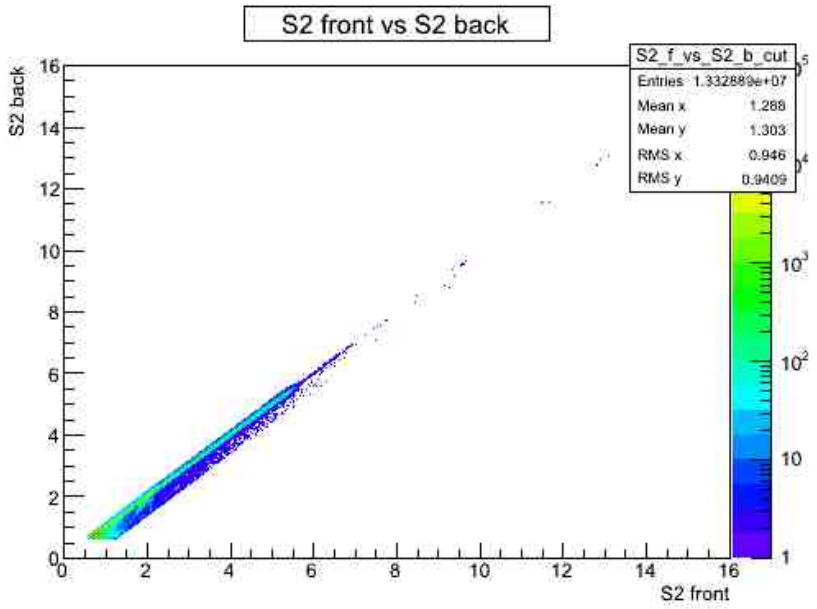

Figure 9.11: *Run 21, $^{12}C+^{12}$ C run with shield on. This figure shows S2 energy front versus S2 energy back after cut.*

9.4.3 Further Selection

A further consideration of good event selection was to take into account only event where there was data both for the ADC and the TDC channels. In other words consider events where for one ADC, there is a given TDC correspondence. The main code was updated accordingly.

CHAPTER 10

$^{12}C + ^{12}C$ Preliminary Results and Discussions

This chapter presents a brief overview of the preliminary results. This result does not encompass the end aim of cross section values, however it presents what was obtained after all analysis problems encountered were fixed and discuss the work that would have been performed if not for time constraint.

10.1 Energy versus theta

As discussed in chapter 9, applying different cuts to the data reduced the background in the energy versus theta spectra. Energy versus theta spectra, shown respectively in Figures 10.1 and 10.2 show as an example the background reduction of a gold run with no shield on.

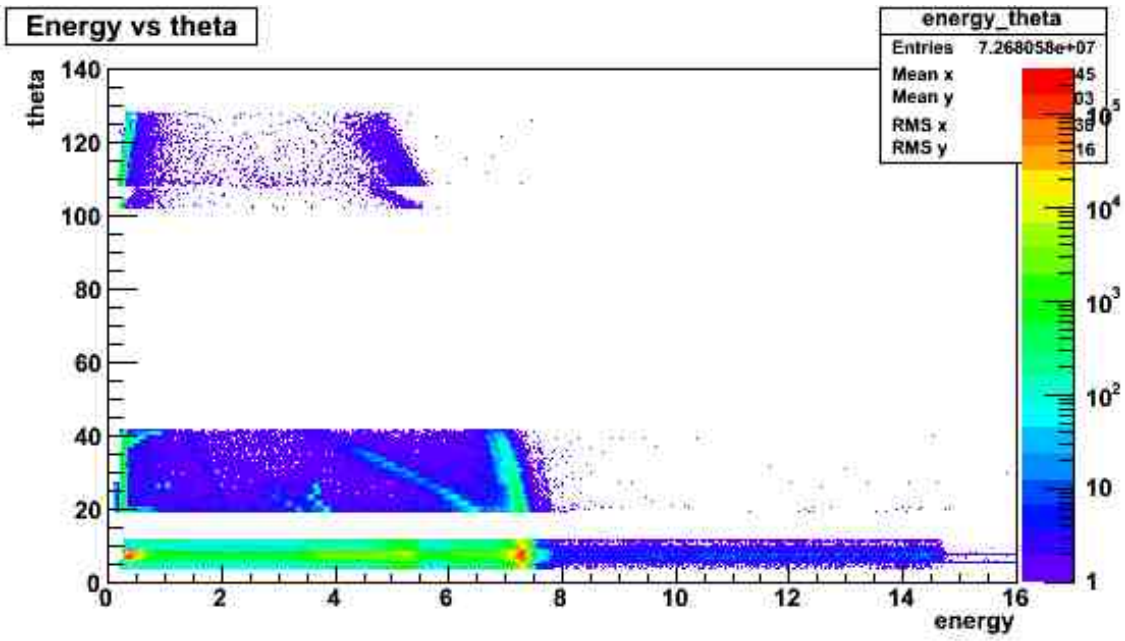

Figure 10.1: *Spectrum representing theta versus energy for a* $^{12}C+^{12}C+^{197}Au$ *run with no shield on, run20.*

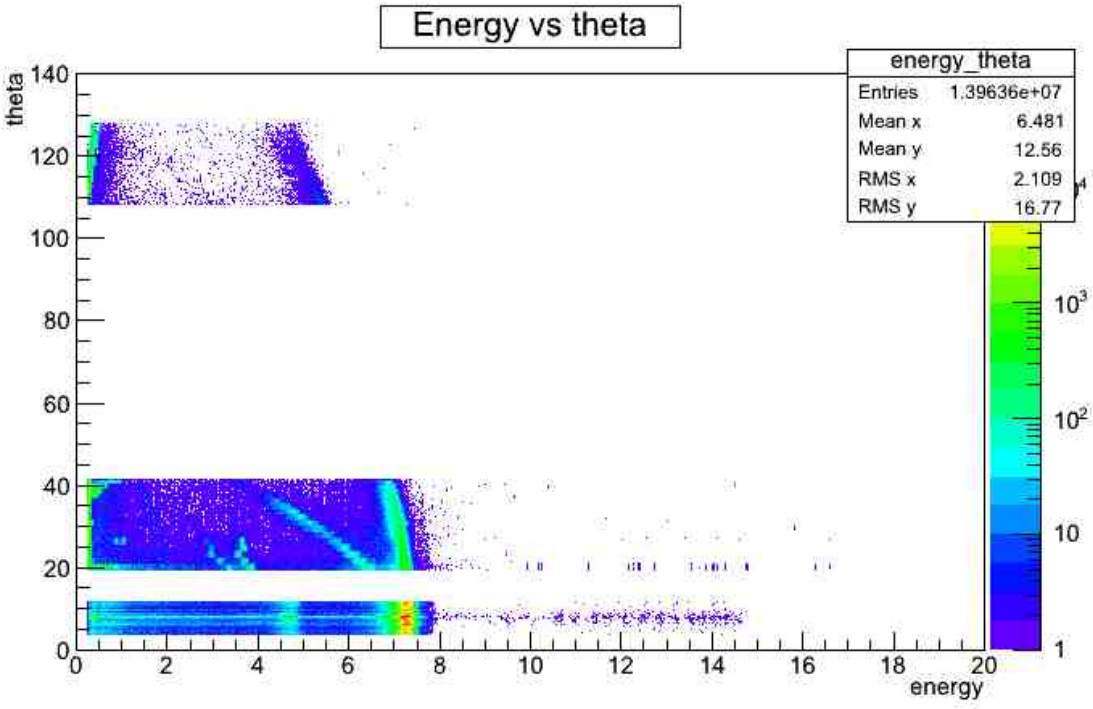

Figure 10.2: *Spectrum representing theta versus energy for a* $^{12}C+^{12}C+^{197}Au$ *run with no shield on, run20.*

10.2 Energy versus time

Work has been done to identify features in different TOF versus energy graphs of different runs for particle identification. The energy versus TOF for a $^{12}C + ^{12}C$ run with shield on for LEDA1 detector, here run 21 is shown in 10.3. Along with energy versus TOF for different detectors in different runs, energy versus TOF for Each individual strip of LEDAs and for S2 were also studied.

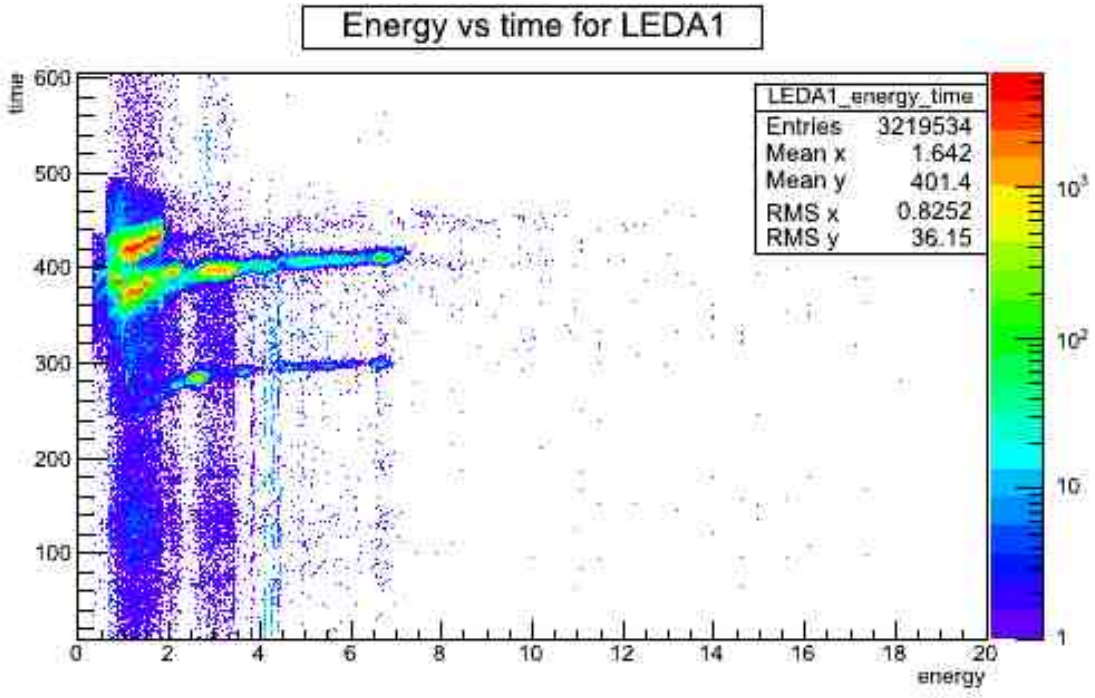

Figure 10.3: *This figure represents energy vs TOF for a $^{12}C + ^{12}C$ run with shield on, run21.*

So far, features such as proton scattering have been clearly identified but for other features however further analysis is required. Analysis was investigating energy versus strip for all strips in order to decide on further possible cuts. The different cuts such as $LEDA_1$ versus S2 coincidence or energy versus time gate, which are yet to be perfomed, would allow to further clean the data leading to proton and alpha identification and yield extraction.

10.3 Cross section Determination

As it can be seen in previous Chapter, there were numerous problems encountered during the analysis up to the stage that it reached. Due to time constraint, full particles identification has yet to be achieved.

As an overview of the work that remains doing for this data are the extraction of further parameters corresponding to the variables required to calculate the differential cross section.

The cross section can be written as

$$\frac{d\sigma}{d\Omega} = \frac{Y\left(E\right)}{IN\left(d\Omega_{lab} \times \frac{lab}{com} ratio\right)} \tag{10.1}$$

with Y(E) referring to the energy-dependent yield, I to the beam intensity, N the number of target atoms and dΩ the solid angle. As described in the previous Chapter, the following steps have already been carried out

- Resolution of ROOT to MIDAS conversion problems
- Calibration of ADC and TDC data
- Energy loss correction. This allowed to add to the measured energy, losses encountered through the aluminium shield and through the target.
- Kinematic curves which correspond to each state [1].
- Coincidence gate for good events selection and background reduction : S2 front versus S2 back coincidence cuts, low energies events, selection of event where both ADC and TDC fired.

However, further analysis are required in order to calculate the cross section

- Finishing on identification of different particle groups and extracting yields of detected protons and alphas.
- Calclulation of the differential cross section for each state.
- Experimental solid angle calculation using the experimental ^{12}C+^{12}C+^{197}Au scattering runs.
- This should thus allow the determination of the total cross section through the integration over differential cross section.

[1] ground state + different excited states

CHAPTER 11

Summary and Future Work

> Consider the blameless, observe the upright; a future awaits those who seek peace.
>
> Psalm

In this thesis, two different experiments including the state of their respective analysis have been described. That is the experiment and analysis involved for the ^{20}Ne(d,p)^{21}Ne transfer reaction and the ^{12}C $+^{12}$ C fusion reaction.

In order to proceed with the conclusion of this work, it is necessary to revisit the different objectives set at the beginning. For the first part of this work, that is the ^{20}Ne(d,p)^{21}Ne transfer reaction, the motive involved investigating spectroscopic information around the Gamow window of the ^{17}O(α,γ)^{21}Ne states located between E_x = 7.65-8.05 MeV. That is studying the excitation energies of states around that region such as identifying new state and spin-parity assignments as, for most states around that region no spectroscopic information is available.

With that in mind, an experiment was performed using the Munich Q3D magnetic spectrograph using ^{20}Ne implanted targets with carbon as backing. This experiment covered the region of excitation energies varying from 6.9 MeV to 8.5 MeV. This work went then on describing the different difficulties encountered during the experiment, which can be summarised as no knowledge of carbon true thickness and background estimation higher related uncertainties. Two different targets were in this case used, referred to as Dresden5 and Dresden2 throughout the work. The analysis of this work carried on by

"correcting" these issues by renormalising the data to a state with known spin-parity.

As results, in total sixteen states were identified in this work, only thirteen of which are found in literature meaning three, the 8.328(6) MeV, 6.977(17) MeV and 6.960(2) MeV have first been observed in this work. Within the Gamow window however, even if in literature, six states are present, only one state, the 7.955(2) MeV by correspondence to the 7.9603(10) has been identified.

Spin-parity were firmly assigned for some of the measured states and for others, only tentative assignments were made. Although Dresden5 was the target mainly used during the experiment, assignments were made using both Dresden5 and Dresden2 (where available). Dresden2 for example allowed to further discriminate between two different suggested assignments made using Dresden5 or the other way around. Even spin-parity suggestions are beneficial as absolutely no spectroscopic information was available for a total of eight states within this region. Five other states only had unconfirmed spin-parity. Out the sixteen identified states, this work made eleven firm assignments and two tentative assignments.

The use of implanted target constituted the main problem faced during the experiment as there were suggested neon leakage. The leakage was not monitored. That added to the uncertainties during analysis. A way of directly reducing uncertainties would be target monitoring and background estimation using backing materials during the experiment.

The identification of only one state within the Gamow window out of the six presently known could be due to two non excluding factors. The first of which could simply be a difficulty for the (d,p) to populate states around that region. As mentioned previously, this work is the first of its kind, in the way that no other ^{20}Ne(d,p)^{21}Ne reaction has ever reached excitation energies this high. This work was indeed the first ^{20}Ne(d,p)^{21}Ne reaction performed beyond E$_{ex}$= 6 MeV. Every state previously measured within the Gamow window have been performed, as detailed in the Chapter three on the astrosphysical purpose of this part (section 3.2.4), through a range of different reactions.
This work was also the first to have used an implanted target for the ^{20}Ne(d,p)^{21}Ne transfer reaction. Past experiments have all used gas target, not possible with the Munich setup.

The second non excluding factor for the observation of a unique state within the Gamow window could lead to the consideration of the possibility of a weak neutron width. Consideration which could be indicative of a neutron channel of weak strength around that region. This trend would definitely seems to agree with both previous experimental work on ^{17}O(α,γ)^{21}Ne ([31], [48], [29]) that agreed on an increase in strength of the (α,γ)

channel than the one predicted by the Descouvemont's calculations (ratio of 10^{-4} over all relevant energies) and a weaker strength of the (α,n) channel than previously thought as described in NACRE [30] and CF88 [27]. Weaker neutron channel could then indicate less recycled neutrons.

However, it is also primordial to indicate that the debate on ^{16}O as either neutron poison or absorber is not as simple as saying, in this case, less recycled neutron therefore "^{16}O = neutron poison". As explained by Taggart in [48], although, it is tempting to draw this initial conclusion, there exist a well described stellar model calculations which have indication that the weak s-process would only be sensitive to the loss of free neutrons through the ^{17}O(α,γ)^{21}Ne beyond a factor of two orders of magnitude or more than the (α,n) channel [12]. Based on present knowledge, it is therefore difficult to state neutron poison or otherwise as it is significant to underline that both previous experimental work on ^{17}O(α,γ)^{21}Ne used assumptions of different possible scenarios on level densities properties of ^{21}Ne around the Gamow window of ^{17}O(α,γ)^{21}Ne. Without further spectroscopic information of these ^{21}Ne states relevant within this region, meaning those with potentially low angular momentum transfers, it would not be possible to draw an informed conclusion on the debate.

Having only identified one state around that region does not allow to shed direct light on the actual levels densities of ^{21}Ne between E_x = 7.65-8.05 MeV. However, the lack of states detection by using the ^{20}Ne(d,p)^{21}Ne around that region could give a hint into the state of the neutron width around that region.

Future planned work for further study of spectroscopic information of ^{21}Ne around the ^{17}O(α,γ)^{21}Ne Gamow window will consist on using inverse kinematic, that is neon beam on deuteron target using the TUDA chamber at TRIUMF, Vancouver in Canada. This future experiment should not only hopefully help with the spectroscopic information around that region, but may also allow to shed further lights on the suggestion of the possibility of having a weak neutron width.

The second part of this work described the ^{12}C +^{12} C fusion reaction, performed in TRIUMF, Canada using the TUDA chamber. The experiment was based on charged particle detection, ^{12}C(^{12}C,α)^{20}Ne and ^{12}C(^{12}C,p)^{23}Na at the centre of mass 3.40 - 4.02 MeV. This experiment covered the high energy end of the Gamow Window and was meant to set ground for work at lower energies. The aim of this work was the determination of the cross section, which would help, at these energies, reduce uncertainties presently observed in literature. Analysis such new sort code writing that solved sorting problems initially encountered, ADCs and TDCs calibrations, different cuts selection necessary for particle

identification and preliminary results have been performed and were presented. The future direct work for this data is finishing identifying spectra features, yield extractions which will then allow the cross section calculation.

APPENDIX A

Detailed Data Details

The following table A.1 gives a detailed description on the data by giving Characteristics such as target used, angle alongside excitation energies on which the Q3D was centred. If as referenced in chapter 4, Table 4.1, both implanted ^{20}Ne used target are Dresden2 and Dresden5, the silicon target used for calibration purpose would simply be referenced as "silicon" and the carbon meant to be used for background estimation as "carbon". During the experiment for few runs, 24 MeV was used as beam energy. These set of data were taken before the beam energy was changed and fixed to 22 MeV. Those 24 MeV data were discarded during the analysis but still recorded for information purpose.

Recorded are as well some of the 22 MeV data for which runs were deemed faulty during the experiment. Such runs have obviously been discarded during anlysis but are also still recorded for information purpose.

E_{beam} (MeV)	**Run Number**	**Target**	**Angle (θ)**	**E_x(MeV)**	**Additional Note**
22	224	Dresden5	8	7.700	Faulty run. Wrong V_a used, run stopped.
22	225	Dresden5	8	7.700	Faulty run. V_a changed during run.

Continued on next page

E_{beam} (MeV)	Run Number	Target	Angle (θ)	E_x(MeV)	Additional Note
22	226	Dresden5	8	7.700	Faulty run. Large correction factor.
22	227	carbon	8	7.700	
22	228	silicon	8	7.700	Calibration
22	219	Dresden5	11	7.700	
22	220	Dresden5	11	7.700	
22	221	Dresden5	11	0.00	
22	223	silicon	11	7.700	Calibration
22	178	Dresden5	13	0.00	
22	211	Dresden5	13	0.00	
22	212	Dresden5	13	0.00	
22	213	Dresden5	13	0.00	
22	217	Dresden5	13	0.00	
22	216	Dresden5	13	7.700	
22	210	silicon	13	7.700	Calibration
22	214	silicon	13	7.700	Calibration
22	215	silicon	13	7.700	Calibration
24	138	Dresden5	14	7.700	Before beam energy change.
24	139	Dresden5	14	7.700	Before beam energy change.
22	166	Dresden5	15	7.700	
22	170	Dresden5	15	7.700	
22	275	Dresden5	15	7.700	Faulty run
22	276	Dresden5	15	7.700	Faulty run
22	277	Dresden2	15	7.700	
22	167	Dresden5	15	0.00	
22	168	Dresden5	15	5.700	
22	169	Dresden5	15	5.700	
22	172	carbon	15	5.700	
22	171	silicon	15	7.700	Calibration
22	177	Dresden5	15	5.700	
22	218	Dresden5	15	5.700	
22	222	Dresden5	15	5.700	

Continued on next page

$\mathbf{E}_{beam}$ (MeV)	Run Number	Target	Angle (θ)	$\mathbf{E}_x$(MeV)	Additional Note
24	142	Dresden5	20	7.700	Before beam energy change.
24	143	Dresden5	20	0.00	Before beam energy change.
24	144	Dresden5	20	0.00	Before beam energy change.
22	175	Dresden5	20	7.700	
22	278	Dresden2	20	7.700	
22	279	Dresden2	20	7.700	
22	280	Dresden2	20	7.700	
22	174	Dresden5	20	0.00	
22	281	Dresden2	20	5.700	
22	176	silicon	20	7.700	Calibration
22	179	Dresden5	25	0.00	
22	180	Dresden5	25	7.700	
22	282	Dresden2	25	7.700	
22	283	Dresden2	25	7.700	
22	284	Dresden2	25	7.700	
22	285	Dresden2	25	5.700	
22	182	silicon	25	7.700	Calibration
22	184	Dresden5	30	0.00	
22	185	Dresden5	30	7.700	
22	286	Dresden2	30	7.700	
22	287	Dresden2	30	7.700	
22	288	Dresden2	30	7.700	
22	289	Dresden2	30	5.700	
22	186	silicon	30	7.700	Calibration
22	291	Dresden2	35	7.700	
22	290	carbon	35	7.700	

Table A.1: *Details on all (d,p) data run along with target used. The corresponding laboratory angle can also be seen alongside the Excitation Energies on which was made the focus.*

APPENDIX B

Laboratory Frame to Centre of Mass Conversion

The following mathematical development, inspired by the development in Ref.[109] where in that case A FORTRAN code was used, were recorded to show the derivation that let to the appropriate conversion between the centre of mass and laboratory frame. The results as in the differential cross section along with the angle, as emphasised in chapter 6 were converted from the laboratory frame to the Centre of mass frame. A ROOT code was written for that purpose based on the presented set of equations. Only main steps will be shown but further details can be found in [109].

If in the laboratory frame, beam particle of mass m_1 and of velocity V_1 strikes a target of mass m_2. The total linear momentum can be written as

$$P_{lab} = m_1 V_1 \tag{B.1}$$

And the total kinetic energy can then be written as

$$E_{lab} = \frac{1}{2} m_1 V_1^2 \tag{B.2}$$

In the centre of mass frame, two interacting particles with respective velocity of v_1 and v_2 have the relationship which can be written as

$$m_1 v_1 = -m_2 v_2 \tag{B.3}$$

as their centre of mass is at rest.

The velocity of the centre of mass frame in the laboratory frame can be written as

$$V_{c.m} = -V_2 \tag{B.4}$$

This lead the centre of mass energy, after few steps (again not explicitly given) to be written as

$$E_{c.m} = \frac{1}{2}(m_1 + m_2)V_{c.m}^2 \tag{B.5}$$

If in the laboratory frame, the reactions products are considered to have the velocities of V_3 and V_4 with respective angles of ψ_3 and ψ_4 and in the centre of mass frame, the ejectile has a velocity v_3 with an angle of θ_3

The final equation linking the centre of mass angle to the laboratory frame angle will be written as

$$\tan\theta_3 = \frac{\sin\psi_3}{\cos\psi_3 - \frac{V_{c.m}}{V_3}} \tag{B.6}$$

With V_3 being defined as

$$V_3 = V_{c.m}\cos\psi_3 \pm (v_3^2 - V_{c.m}^2\sin^2\psi_3)^{\frac{1}{2}} \tag{B.7}$$

and where v_3 is defined as

$$v_3 = V_{c.m}^2 + V_3^2 - 2V_{c.m}V_3\cos\psi_3 \tag{B.8}$$

The final equation linking the differential cross section of both frame will then be written as

$$\frac{d\sigma}{d\Omega_{c.m}} = \frac{(1-\gamma^2\sin^2\psi)^{\frac{1}{2}}}{\left[\gamma\cos\psi \pm (1-\gamma^2\sin^2\psi)^{\frac{1}{2}}\right]^2} \times \frac{d\sigma}{d\Omega_{lab}} \tag{B.9}$$

where $\gamma = \frac{V_{c.m}}{v_3}$.

It is important to note that v_3 can also be written as

$$v_3 = \sqrt{\left(\frac{2}{M_p + M_{21Ne}}\right) \times \left(\frac{M_{21Ne}}{M_p}\right) \times \left(\frac{E_{c.m}}{Q}\right)} \tag{B.10}$$

where M_p represents the mass of the proton, M_{21Ne} is the mass of the ^{21}Ne nuclei and Q is the Q value of the reaction. For conversion purpose, the Q value of 4.53654 MeV was used, which therefore corresponds to an excitation of energy of 0 MeV.

Both set of those final equations (B.6 and B.9) were used for the conversion from the laboratory frame to the centre of mass frame.

APPENDIX C

Data Differential Cross section Details

The following table C.1 gives differential cross section details of different ^{21}Ne states at different angles. The differential cross section of each state was, as explained in chapter 10, separately calculated for each run. This table gives cross section before the CoM conversion and the weighted average cross section used for different target of different states at different angles. The "Yield related" error on the table is the error obtained with Yield only related uncertainties, while the "Total" error includes all related uncertainties (meaning the yield, acceptance and beam intensity related uncertainties). The weighted average for each target at each angle has been calculated using only the yield related errors. The error resulting from this process has then been combined in quadrature with a contribution of 10% for beam intensity and 10% for target thickness (as described on page 78, section 6.3) to give the final error which has been used in the angular momentum determination.

The weighted mean and weighted mean error have been calculated by using the following expressions

$$\hat{\mu} = \frac{\sum_{i=1}^{n} \left(\frac{x_i}{\sigma_i^2}\right)}{\sum_{i=1}^{n} \left(\frac{1}{\sigma_i^2}\right)} \tag{C.1}$$

and

$$\sigma^2(\mu) = \frac{1}{\sum_{i=1}^{n} \left(\frac{1}{\sigma_i^2}\right)} \tag{C.2}$$

with x_i being the value of the CoM $\sigma/\mathrm{d}\Omega$ and σ_i the associated total uncertainties (Total $\Delta(\mathrm{d}\sigma/\mathrm{d}\Omega)$).

^{21}Ne	Run Number	Laboratory Angle(θ)	Laboratory ($d\sigma/d\Omega$) (b/sr)	Yield related $\Delta(d\sigma/d\Omega)$	Total $\Delta(\ d\sigma/d\Omega)$	Additional Comment
1	Run 166	15	1.052e-08	1.168e-09 (11.1%)	18.0%	Dresden 5.
1	Run 170	15	6.985e-09	7.188e-10 (10.3%)	17.5%	Dresden 5.
1	Weighted average	15	8.000e-9	6.122e-10 (7.7%)	16.1%	Dresden 5, both runs.
1	Run 277	15	7.287e-08	1.164e-08 (15.9%)	21.3%	Dresden 2.
1	Run 216	13	4.186e-09	1.253e-09 (29.9%)	33.1%	Dresden 5.
1	Run 219	11	2.062e-09	5.583e-10 (27.1%)	30.6%	Dresden 5.
1	Run 220	11	3.495e-09	3.098e-10 (8.9%)	16.7%	Dresden 5.
1	Weighted average	11	3.1577e-09	2.7089e-10 (8.6%)	16.5%	Dresden 5, both runs.
1	Run 226	8	2.823e-08	5.730e-09 (20.3%)	24.7%	Dresden 5.
2	Run 291	35	7.570e-09	4.930e-09 (65.1%)	66.6%	Dresden 2.
2	Run 185	30	2.599e-09	1.559e-09 (59.9%)	61.5%	Dresden 5.
2	Run 286	30	1.005e-08	2.442e-09 (24.3%)	28.1%	Dresden 2.
2	Run 287	30	6.611e-09	2.052e-09 (31.0%)	34.1%	Dresden 2. Within error.
2	Run 288	30	4.426e-09	1.207e-09 (27.3%)	30.7%	Dresden 2. Within error.
2	Weighted average	30	5.7653e-09	1.000e-09 (17.3%)	22.4%	Dresden 2, both 3 runs.
2	Run 180	25	2.189e-09	6.291e-10 (28.7%)	32.0%	Dresden 5.
2	Run 282	25	5.846e-09	1.295e-09 (22.2%)	26.3%	Dresden 2.
2	Run 283	25	1.041e-08	3.435e-09 (32.9%)	35.8%	Dresden 2. Within error.
2	Run 284	25	5.095e-09	2.235e-09 (43.8%)	46.0%	Dresden 2. Within error.

Continued on next page

^{21}Ne	Run Number	Laboratory Angle(θ)	Laboratory ($d\sigma/d\Omega$) (b/sr)	Yield related $\Delta(d\sigma/d\Omega)$	Total $\Delta(\ d\sigma/d\Omega)$	Additional Comment
2	Weighted average	25	6.1143e-09	1.0653e-09 (17.4%)	22.4%	Dresden 2, both 3 runs.
2	Run 175	20	2.437e-09	2.386e-09 (97.9%)	98.9%	Dresden 5.
2	Run 278	20	2.081e-08	1.881e-09 (9.0%)	16.8%	Dresden 2.
2	Run 279	20	4.694e-08	4.082e-09 (8.7%)	16.6%	Dresden 2.
2	Run 280	20	2.685e-08	2.756e-09 (10.3%)	17.5%	Dresden 2.
2	Weighted average	20	2.5793e-08	1.4520e-09 (5.6%)	15.2%	Dresden 2, both 3 runs.
2	Run 166	15	5.811e-09	3.932e-09 (67.7%)	69.2%	Dresden 5.
2	Run 170	15	1.680e-09	1.680e-09 (100.0%)	100.0%	Dresden 5. Within error.
2	Weighted Average	15	2.3177e-09	1.5449e-09 (66.7%)	68.1%	Dresden 5, both runs.
2	Run 277	15	3.291e-08	8.737e-09 (26.5%)	30.0%	Dresden 2.
2	Run 216	13	1.919e-09	5.737e-10 (29.9%)	33.1%	Dresden 5.
2	Run 219	11	1.706e-09	4.062e-10 (23.8%)	27.7%	Dresden 5.
2	Run 220	11	1.911e-09	2.205e-10 (11.5%)	18.2%	Dresden 5. Within error.
2	Weighted average	11	1.8643e-09	1.9379e-10 (10.4%)	17.6%	Dresden 5, both runs.
2	Run 226	8	1.183e-08	7.002e-09 (59.2%)	60.9%	Dresden 5.
3	Run 291	35	1.038e-08	1.015e-09 (9.8%)	17.2%	Dresden 2.
3	Run 185	30	2.259e-09	9.935e-10 (43.9%)	46.1%	Dresden 5.
3	Run 286	30	1.044e-08	7.160e-09 (68.6%)	70.0%	Dresden 2.
3	Run 287	30	5.725e-09	6.144e-10 (10.7%)	17.7%	Dresden 2. Within error.

Continued on next page

^{21}Ne	Run Number	Laboratory Angle(θ)	Laboratory ($d\sigma/d\Omega$) (b/sr)	Yield related $\Delta(d\sigma/d\Omega)$	Total $\Delta(\ d\sigma/d\Omega)$	Additional Comment
3	Run 288	30	1.253e-08	8.540e-09 (68.2%)	69.7%	Dresden 2. Within error.
3	Weighted average	30	5.7941e-09	6.1058e-10 (10.5%)	17.6%	Dresden 2, both 3 runs.
3	Run 180	25	2.015e-09	5.650e-10 (28.0%)	31.4%	Dresden 5.
3	Run 282	25	1.132e-08	1.249 e-09 (11.0%)	17.9%	Dresden 2.
3	Run 283	25	1.712e-08	8.321e-09 (48.6%)	50.6%	Dresden 2. Within error.
3	Run 284	25	1.114e-08	2.909e-09 (26.1%)	29.7%	Dresden 2. Within error.
3	Weighted average	25	1.1401e-08	1.1369e-09 (9.9%)	17.3%	Dresden 2, both 3 runs.
3	Run 175	20	4.065e-09	7.435e-10 (18.3%)	23.1%	Dresden 5.
3	Run 278	20	5.946e-08	1.752e-08 (29.5%)	32.7%	Dresden 2.
3	Run 279	20	5.238e-08	1.644e-08 (31.3%)	34.3%	Dresden 2. Within error.
3	Run 280	20	4.051e-08	1.627e-08 (40.2%)	42.6%	Dresden 2. Within error.
3	Weighted Averaged	20	5.0351e-08	9.6513e-09 (19.2%)	23.8%	Dresden 2, both 3 runs.
3	Run 216	13	1.607e-09	3.986e-10 (24.8%)	28.5%	Dresden 5.
3	Run 219	11	3.028e-09	1.466e-09 (48.4%)	50.4%	Dresden 5.
3	Run 220	11	7.527e-09	3.517e-09 (46.7%)	48.8%	Dresden 5. Within error.
3	Weighted average	11	3.6940e-09	1.3532e-09 (36.6%)	39.3%	Dresden 5, both runs.
3	Run 226	8	3.294e-08	1.910e-09 (5.8%)	15.3%	Dresden 5.
4	Run 219	11	5.975e-09	2.0680e-09 (34.6%)	37.4%	Dresden 5.

Continued on next page

^{21}Ne	Run Number	Laboratory Angle(θ)	Laboratory ($d\sigma/d\Omega$) (b/sr)	Yield related $\Delta(d\sigma/d\Omega)$	Total $\Delta(\ d\sigma/d\Omega)$	Additional Comment
4	Run 220	11	8.567e-09	1.016e-09 (11.9%)	18.5%	Dresden 5. Within error.
4	Weighted average	11	8.0630e-09	9.1189e-10 (11.3%)	18.1%	Dresden 5, both runs.
4	Run 226	8	2.523e-08	1.100e-08 (43.6%)	45.8%	Dresden 5.
5	Run 291	35	9.938e-09	3.167e-09 (31.9%)	34.9%	Dresden 2.
5	Run 185	30	3.247e-09	2.353e-09 (72.5%)	73.9%	Dresden 5.
5	Run 286	30	1.340e-08	6.466e-09 (48.2%)	50.2%	Dresden 2.
5	Run 287	30	7.396e-09	2.407e-09 (32.5%)	35.4%	Dresden 2. Within error.
5	Run 288	30	8.679e-09	3.455e-09 (39.8%)	42.2%	Dresden 2. Within error.
5	Weighted average	30	8.2919e-09	1.8888e-09 (22.8%)	26.8%	Dresden 2, both 3 runs.
5	Run 175	20	1.023e-08	4.237e-09 (41.4%)	43.7%	Dresden 5.
5	Run 278	20	1.461e-07	1.707e-08 (11.7%)	18.4%	Dresden 2.
5	Run 279	20	1.333e-07	3.746e-08 (28.1%)	31.5%	Dresden 2. Within error.
5	Run 280	20	1.161e-07	1.018e-08 (8.8%)	16.7%	Dresden 2. Within error.
5	Weighted average	20	1.2445e-07	8.5144e-09 (6.8%)	15.7%	Dresden 2, both 3 runs.
5	Run 166	15	4.035e-08	1.276e-08 (31.6%)	34.6%	Dresden 5.
5	Run 170	15	6.675e-08	1.310e-08 (19.6%)	24.2%	Dresden 5.
5	Weighted average	15	5.3203e-08	9.1405e-09 (17.2%)	22.3%	Dresden 5, both runs.
5	Run 277	15	6.071e-07	2.029e-07 (33.4%)	36.3%	Dresden 2.
5	Run 216	13	3.620e-09	4.074e-10 (11.3%)	18.1%	Dresden 5.

Continued on next page

^{21}Ne	Run Number	Laboratory Angle(θ)	Laboratory ($d\sigma/d\Omega$) (b/sr)	Yield related $\Delta(d\sigma/d\Omega)$	Total $\Delta(\ d\sigma/d\Omega)$	Additional Comment
5	Run 219	11	3.798e-09	6.074e-10 (15.9%)	21.3%	Dresden 5.
5	Run 220	11	1.159e-08	2.394e-09 (20.7%)	25.1%	Dresden 5.
5	Weighted average	11	4.2693e-09	5.8875e-10 (13.8%)	19.8%	Dresden 5, both runs.
5	Run 226	8	2.354e-08	1.323e-09 (5.6%)	15.2%	Dresden 5.
6	Run 175	20	2.743e-09	2.070e-09 (75.5%)	76.8%	Dresden 5.
6	Run 278	20	2.083e-08	2.462e-09 (11.8%)	18.4%	Dresden 2.
6	Run 279	20	1.528e-08	2.142e-09 (14.0%)	19.9%	Dresden 2.
6	Run 280	20	1.371e-08	8.482e-10 (6.2%)	15.4%	Dresden 2. Within error.
6	Weighted average	20	1.4565e-08	7.5103e-10 (5.2%)	15.1%	Dresden 2, both 3 runs.
6	Run 166	15	3.850e-09	1.668e-09 (43.3%)	45.6%	Dresden 5.
6	Run 170	15	1.990e-09	7.937e-10 (39.9%)	42.3%	Dresden 5. Within error.
6	Weighted average	15	2.3334e-09	7.1670e-10 (30.7%)	33.8%	Dresden 5, both runs.
6	Run 277	15	4.436e-08	8.675e-09 (19.6%)	24.2%	Dresden 2.
6	Run 216	13	3.882e-09	1.305e-09 (33.6%)	36.5%	Dresden 5.
6	Run 219	11	2.675e-09	1.024e-09 (38.3%)	40.8%	Dresden 5.
6	Run 220	11	3.145e-09	2.067e-09 (65.7%)	67.2%	Dresden 5. Within error.
6	Weighted average	11	2.7676e-09	9.1757e-10 (33.2%)	36.0%	Dresden 5, both runs.
6	Run 226	8	6.677e-09	1.376e-09 (20.6%)	25.0%	Dresden 5.
7	Run 291	35	8.018e-09	3.649e-09 (45.5%)	47.6%	Dresden 2.
7	Run 185	30	5.128e-09	1.126e-09 (21.9%)	26.1%	Dresden 5.

Continued on next page

^{21}Ne	Run Number	Laboratory Angle(θ)	Laboratory ($d\sigma/d\Omega$) (b/sr)	Yield related $\Delta(d\sigma/d\Omega)$	Total $\Delta(\ d\sigma/d\Omega)$	Additional Comment
7	Run 286	30	1.996e-08	4.604e-09 (23.1%)	27.1%	Dresden 2.
7	Run 287	30	2.180e-08	1.611e-08 (73.9%)	75.2%	Dresden 2. Within error.
7	Run 288	30	2.172e-08	5.945e-09 (27.4%)	30.8%	Dresden 2. Within error.
7	Weighted average	30	2.0677e-08	3.5506e-09 (17.2%)	22.3%	Dresden 2, both 3 runs.
7	Run 180	25	9.280e-09	2.262e-09 (24.4%)	28.2%	Dresden 5.
7	Run 282	25	7.261e-08	5.788e-09 (7.9%)	16.2%	Dresden 2.
7	Run 283	25	6.924e-08	6.848e-09 (9.9%)	17.3%	Dresden 2. Within error.
7	Run 284	25	5.564e-08	1.295e-08 (23.3%)	27.3%	Dresden 2. Within error.
7	Weighted average	25	6.9582e-08	4.1835e-09 (6.0%)	15.4%	Dresden 2, both 3 runs.
7	Run 175	20	1.459e-08	1.271e-09 (8.7%)	16.6%	Dresden 5.
7	Run 278	20	2.260e-07	1.187e-08 (6.5%)	15.6%	Dresden 2.
7	Run 279	20	1.778e-07	1.165e-08 (6.5%)	15.6%	Dresden 2.
7	Run 280	20	1.397e-07	1.234e-08 (8.8%)	16.7%	Dresden 2.
7	Weighted average	20	1.8217e-07	6.8953e-09 (3.8%)	14.6%	Dresden 2, both 3 runs.
7	Run 166	15	3.493e-08	3.364e-09 (9.6%)	17.1%	Dresden 5.
7	Run 170	15	3.994e-08	1.143e-08 (28.6%)	31.9%	Dresden 5. Within error.
7	Weighted average	15	3.5329e-08	3.2268e-09 (9.1%)	16.8%	Dresden 5, both runs.
7	Run 277	15	5.521e-07	7.482e-08 (13.6%)	19.6%	Dresden 2.

Continued on next page

^{21}Ne	Run Number	Laboratory Angle(θ)	Laboratory ($d\sigma/d\Omega$) (b/sr)	Yield related $\Delta(d\sigma/d\Omega)$	Total $\Delta(\ d\sigma/d\Omega)$	Additional Comment
7	Run 216	13	4.540e-09	4.429e-10 (9.8%)	17.2%	Dresden 5.
7	Run 219	11	8.439e-09	1.217e-09 (14.4%)	20.2%	Dresden 5.
7	Run 220	11	1.671e-08	1.257e-09 (7.5%)	16.0%	Dresden 5.
7	Weighted average	11	1.2441e-08	8.7435e-10 (7.0%)	15.8%	Dresden 5, both runs.
7	Run 226	8	3.938e-08	3.416e-09 (8.7%)	16.6%	Dresden 5.
8	Run 291	35	4.778e-09	1.473e-09 (30.8%)	33.9%	Dresden 2.
8	Run 185	30	7.091e-09	7.016e-10 (9.9%)	17.3%	Dresden 5.
8	Run 286	30	2.267e-08	1.002e-08 (44.2%)	46.4%	Dresden 2.
8	Run 287	30	1.662e-08	1.297e-09 (7.8%)	16.2%	Dresden 2. Within error.
8	Run 288	30	1.421e-08	3.627e-09 (25.5%)	29.2%	Dresden 2. Within error.
8	Weighted average	30	1.6439e-08	1.2123e-09 (7.4%)	15.9%	Dresden 2, both 3 runs.
8	Run 180	25	2.029e-09	5.056e-10 (24.9%)	28.6%	Dresden 5.
8	Run 282	25	1.162e-08	1.214e-09 (10.4%)	17.6%	Dresden 2.
8	Run 283	25	8.464e-09	2.875e-09 (33.9%)	36.7%	Dresden 2. Within error.
8	Run 284	25	8.798e-09	1.008e-09 (11.5%)	18.2%	Dresden 2. Within error.
8	Weighted average	25	9.8489e-09	7.4876e-10 (7.6%)	16.1%	Dresden 2, both 3 runs.
8	Run 175	20	3.316e-09	7.920e-10 (23.9%)	27.7%	Dresden 5.
8	Run 278	20	2.791e-08	5.675e-09 (20.3%)	24.7%	Dresden 2.
8	Run 279	20	2.124e-08	2.769e-09 (13.0%)	19.2%	Dresden 2. Within error.

Continued on next page

^{21}Ne	Run Number	Laboratory Angle(θ)	Laboratory ($d\sigma/d\Omega$) (b/sr)	Yield related $\Delta(d\sigma/d\Omega)$	Total $\Delta(\ d\sigma/d\Omega)$	Additional Comment
8	Run 280	20	2.170e-08	8.717e-09 (40.2%)	42.6%	Dresden 2. Within error.
8	Weighted average	20	2.2461e-08	2.3930e-09 (10.7%)	17.7%	Dresden 2, both 3 runs.
9	Run 291	35	3.984e-09	6.822e-10 (17.1%)	22.2%	Dresden 2.
9	Run 185	30	4.651e-09	1.957e-09 (42%)	44.3%	Dresden 5.
9	Run 286	30	1.293e-08	8.196e-09 (63.4%)	64.9%	Dresden 2.
9	Run 287	30	1.059e-8	1.0387e-8 (98.0%)	99.0%	Dresden 2. within error.
9	Run 288	30	1.515e-08	8.437e-09 (55.7%)	57.5%	Dresden 2. Within error.
9	Weighted average	30	1.3179e-08	5.1162e-09 (38.8%)	41.3%	Dresden 2, both 3 runs.
9	Run 180	25	1.112e-09	2.665e-10 (23.9%)	27.8%	Dresden 5.
9	Run 282	25	1.379e-08	5.069e-09 (36.8%)	39.4%	Dresden 2.
9	Run 283	25	1.209e-08	4.131e-09 (34.2%)	37.0%	Dresden 2. Within error.
9	Run 284	25	1.283e-08	6.459e-09 (50.3%)	52.3%	Dresden 2. Within error.
9	Weighted average	25	1.2781e-08	2.8690e-09 (22.4%)	26.5%	Dresden 2, both 3 runs.
9	Run 175	20	6.241e-10	6.111e-10 (97.9%)	98.9%	Dresden 5.
9	Run 278	20	3.003e-08	1.119e-08 (37.0%)	39.6%	Dresden 2.
9	Run 279	20	3.224e-08	8.674e-09 (26.9%)	30.4%	Dresden 2. Within error.
9	Run 280	20	2.171e-08	5.439e-09 (25.1%)	28.8%	Dresden 2. Within error.

Continued on next page

^{21}Ne	Run Number	Laboratory Angle(θ)	Laboratory ($d\sigma/d\Omega$) (b/sr)	Yield related $\Delta(d\sigma/d\Omega)$	Total $\Delta(\ d\sigma/d\Omega)$	Additional Comment
9	Weighted average	20	2.5457e-08	4.2609e-09 (16.7%)	21.9%	Dresden 2, both 3 runs.
10	Run 180	25	2.231e-09	5.792e-10 (25.9%)	29.5%	Dresden 5.
10	Run 282	25	9.771e-09	3.538e-09 (36.2%)	38.9%	Dresden 2.
10	Run 283	25	6.919e-09	2.559e-09 (36.9%)	39.5%	Dresden 2. Within error.
10	Run 284	25	7.055e-09	1.744e-09 (24.7%)	28.5%	Dresden 2. Within error.
10	Weighted average	25	7.4045e-09	1.3347e-09 (18.0%)	22.9%	Dresden 2, both 3 runs.
10	Run 175	20	2.368e-09	1.489e-09 (62.8%)	64.4%	Dresden 5.
10	Run 278	20	5.708e-08	1.436e-08 (25.2%)	28.9%	Dresden 2.
10	Run 279	20	4.070e-08	1.141e-08 (28.0%)	31.4%	Dresden 2. Within error.
10	Run 280	20	3.559e-08	8.546e-09 (24.0%)	27.9%	Dresden 2. Within error.
10	Weighted average	20	4.1061e-08	6.1754e-09 (15.0%)	20.6%	Dresden 2, both 3 runs.
10	Run 166	15	9.351e-09	1.377e-09 (14.7%)	20.4%	Dresden 5.
10	Run 170	15	1.284e-08	8.175e-10 (6.4%)	15.5%	Dresden 5.
10	Weighted average	15	1.1931e-08	7.0296e-10 (5.9%)	15.3%	Dresden 5, both runs.
10	Run 216	13	1.753e-09	1.099e-09 (62.7%)	64.3%	Dresden 5.
10	Run 219	11	3.625e-09	1.140e-09 (31.4%)	34.4%	Dresden 5.
10	Run 220	11	3.788e-09	1.641e-09 (43.3%)	45.6%	Dresden 5. Within error.
10	Weighted average	11	3.6781e-09	9.3625e-10 (25.5%)	29.1%	Dresden 5, both runs.

Continued on next page

^{21}Ne	Run Number	Laboratory Angle(θ)	Laboratory ($d\sigma/d\Omega$) (b/sr)	Yield related $\Delta(d\sigma/d\Omega)$	Total $\Delta(\ d\sigma/d\Omega)$	Additional Comment
10	Run 226	8	1.498e-08	7.942e-09 (53%)	54.9%	Dresden 5.
11	Run 291	35	2.155e-08	9.354e-10 (4.3%)	14.8%	Dresden 2.
11	Run 185	30	5.159e-09	5.667e-10 (10.9%)	17.9%	Dresden 5.
11	Run 286	30	1.519e-08	7.809e-10 (5.1%)	15.0%	Dresden 2.
11	Run 287	30	1.370e-08	4.230e-09 (30.9%)	34.0%	Dresden 2. Within error.
11	Run 288	30	1.354e-08	3.778e-09 (27.9%)	31.3%	Dresden 2. Within error.
11	Weighted average	30	1.5077e-08	7.5254e-10 (5.0%)	15.0%	Dresden 2, both 3 runs.
11	Run 180	25	3.362e-09	3.925e-10 (11.7%)	18.4%	Dresden 5.
11	Run 282	25	2.448e-08	1.762e-09 (7.2%)	15.9%	Dresden 2.
11	Run 283	25	2.334e-08	1.582e-09 (6.8%)	15.7%	Dresden 2. Within error.
11	Run 284	25	2.077e-08	1.926e-09 (9.3%)	16.9%	Dresden 2. Within error.
11	Weighted average	25	2.300e-08	1.000e-09 (4.3%)	14.8%	Dresden 2, both 3 runs.
11	Run 175	20	2.434e-09	5.544e-10 (22.8%)	26.8%	Dresden 5.
11	Run 278	20	3.877e-08	2.531e-09 (6.5%)	15.6%	Dresden 2.
11	Run 279	20	2.960e-08	6.064e-09 (20.5%)	24.9%	Dresden 2.
11	Run 280	20	2.435e-08	9.302e-09 (38.2%)	40.7%	Dresden 2. Within error.
11	Weighted average	20	3.664e-08	2.265e-09 (6.2%)	15.4%	Dresden 2, both 3 runs.
11	Run 166	15	3.123e-09	7.499e-10 (24.0%)	27.9%	Dresden 5.

Continued on next page

^{21}Ne	Run Number	Laboratory Angle(θ)	Laboratory ($d\sigma/d\Omega$) (b/sr)	Yield related $\Delta(d\sigma/d\Omega)$	Total $\Delta(\ d\sigma/d\Omega)$	Additional Comment
11	Run 170	15	4.090e-09	4.538e-10 (11.1%)	18.0%	Dresden 5.
11	Weighted average	15	3.831e-09	3.883e-10 (10.1%)	17.4%	Dresden 5, both runs.
11	Run 226	8	1.498e-08	2.207e-09 (14.7%)	20.4%	Dresden 5.
12	Run 291	35	3.583e-08	1.637e-09 (4.6%)	14.9%	Dresden 2.
12	Run 185	30	1.066e-08	2.259e-09 (21.2%)	25.5%	Dresden 5.
12	Run 286	30	6.232e-08	1.238e-08 (19.9%)	24.4%	Dresden 2.
12	Run 287	30	6.150e-08	1.136e-08 (18.5%)	23.3%	Dresden 2. Within error.
12	Run 288	30	5.433e-08	1.726e-08 (31.8%)	34.8%	Dresden 2. Within error.
12	Weighted average	30	6.0438e-08	7.5313e-09 (12.5%)	18.8%	Dresden 2, both 3 runs.
12	Run 180	25	1.625e-08	1.364e-09 (8.4%)	16.4%	Dresden 5.
12	Run 282	25	1.521e-07	2.562e-09 (1.7%)	14.2%	Dresden 2.
12	Run 283	25	1.481e-07	2.165e-08 (14.6%)	20.3%	Dresden 2. Within error.
12	Run 284	25	1.191e-07	9.676e-09 (9.9%)	17.3%	Dresden 2. Within error.
12	Weighted average	25	1.4991e-07	2.4606e-09 (1.6%)	14.2%	Dresden 2, both 3 runs.
12	Run 175	20	2.497e-08	2.219e-09 (8.9%)	16.7%	Dresden 5.
12	Run 278	20	4.569e-07	1.309e-08 (2.9%)	14.4%	Dresden 2.
12	Run 279	20	3.699e-07	5.194e-09 (1.4%)	14.2%	Dresden 2.
12	Run 280	20	3.054e-07	1.568e-08 (5.1%)	15.0%	Dresden 2.
12	Weighted average	20	3.7512e-07	4.6141e-09 (1.2%)	14.2%	Dresden 2, both 3 runs.

Continued on next page

^{21}Ne	Run Number	Laboratory Angle(θ)	Laboratory ($d\sigma/d\Omega$) (b/sr)	Yield related $\Delta(d\sigma/d\Omega)$	Total $\Delta(\ d\sigma/d\Omega)$	Additional Comment
12	Run 166	15	5.439e-08	2.684e-09 (4.9%)	15.0%	Dresden 5.
12	Run 170	15	7.454e-08	1.859e-09 (2.5%)	14.4%	Dresden 5.
12	Weighted average	15	6.800e-08	1.5282e-09 (2.2%)	14.3%	Dresden 5, both runs.
12	Run 277	15	7.146e-07	4.507e-08 (6.3%)	15.5%	Dresden 2.
12	Run 216	13	8.885e-09	6.204e-10 (6.9%)	15.7%	Dresden 5.
12	Run 226	8	3.404e-08	6.847e-09 (20.1%)	24.6%	Dresden 5.
13	Run 291	35	1.158e-07	6.654e-09 (5.7%)	15.2%	Dresden 2.
13	Run 185	30	4.006e-09	6.238e-10 (15.6%)	21.1%	Dresden 5.
13	Run 286	30	3.569e-08	4.005e-09 (11.2%)	18.0%	Dresden 2.
13	Run 287	30	2.880e-08	6.563e-09 (22.8%)	26.8%	Dresden 2. Within error.
13	Run 288	30	3.816e-08	9.599e-09 (25.2%)	28.9%	Dresden 2. Within error.
13	Weighted average	30	3.4309e-08	3.2206e-09 (9.4%)	17.0%	Dresden 2, both 3 runs.
13	Run 180	25	8.225e-09	6.537e-10 (7.9%)	16.2%	Dresden 5.
13	Run 282	25	1.068e-07	2.973e-08 (27.4%)	30.8%	Dresden 2.
13	Run 283	25	1.073e-07	2.414e-08 (22.5%)	26.6%	Dresden 2. Within error.
13	Run 284	25	9.233e-08	2.459e-08 (26.6%)	30.1%	Dresden 2. Within error.
13	Weighted average	25	1.0167e-07	1.4905e-08 (14.7%)	20.4%	Dresden 2, both 3 runs.
13	Run 175	20	1.075e-08	1.161e-09 (10.8%)	17.8%	Dresden 5.
13	Run 278	20	3.118e-07	1.812e-08 (5.8%)	15.3%	Dresden 2.

Continued on next page

^{21}Ne	Run Number	Laboratory Angle(θ)	Laboratory ($d\sigma/d\Omega$) (b/sr)	Yield related $\Delta(d\sigma/d\Omega)$	Total $\Delta(\ d\sigma/d\Omega)$	Additional Comment
13	Run 279	20	2.456e-07	3.753e-08 (15.3%)	20.8%	Dresden 2.
13	Run 280	20	2.166e-07	2.986e-08 (13.8%)	19.8%	Dresden 2. Within error.
13	Weighted average	20	2.8027e-07	1.4319e-08 (5.1%)	15.0%	Dresden 2, both 3 runs.
13	Run 166	15	3.750e-08	4.249e-09 (11.3%)	18.1%	Dresden 5.
13	Run 170	15	5.017e-08	6.138e-09 (12.2%)	18.7%	Dresden 5. Within error.
13	Weighted average	15	4.1604e-08	3.4936e-09 (8.4%)	16.4%	Dresden 5, both runs.
13	Run 277	15	4.677e-07	3.062e-08 (6.5%)	15.6%	Dresden 2.
13	Run 216	13	4.315e-09	4.372e-10 (10.1%)	17.4%	Dresden 5.
13	Run 219	11	4.409e-09	7.278e-10 (16.5%)	21.7%	Dresden 5.
13	Run 220	11	1.175e-08	7.817e-10 (6.7%)	15.6%	Dresden 5.
13	Weighted average	11	7.8177e-09	5.3267e-10 (6.8%)	15.7%	Dresden 5, both runs.
13	Run 226	8	3.589e-08	6.423e-09 (17.9%)	22.8%	Dresden 5.
14	Run 291	35	4.831e-09	1.259e-09 (26.0%)	29.6%	Dresden 2.
14	Run 185	30	5.857e-10	3.664e-10 (62.5%)	64.1%	Dresden 5.
14	Run 286	30	7.559e-09	1.774e-09 (23.5%)	27.4%	Dresden 2.
14	Run 287	30	6.533e-09	2.694e-09 (41.2%)	43.6%	Dresden 2. Within error.
14	Run 288	30	3.706e-09	1.133e-09 (30.6%)	33.7%	Dresden 2. Within error.
14	Weighted average	30	5.000e-09	9.0001e-10 (18.0%)	22.9%	Dresden 2. both 3 runs.
14	Run 180	25	1.873e-09	9.664e-10 (51.6%)	53.5%	Dresden 5.

Continued on next page

^{21}Ne	Run Number	Laboratory Angle(θ)	Laboratory ($d\sigma/d\Omega$) (b/sr)	Yield related $\Delta(d\sigma/d\Omega)$	Total $\Delta(\ d\sigma/d\Omega)$	Additional Comment
14	Run 282	25	2.990e-08	1.542e-08 (51.6%)	53.5%	Dresden 2.
14	Run 283	25	2.456e-08	1.013e-08 (41.3%)	43.7%	Dresden 2. Within error.
14	Run 284	25	2.265e-08	1.079e-08 (47.6%)	49.7%	Dresden 2. Within error.
14	Weighted average	25	2.4828e-08	6.6608e-09 (26.8%)	30.3%	Dresden 2, both 3 runs.
14	Run 175	20	1.654e-09	1.318e-09 (79.7%)	80.9%	Dresden 5.
14	Run 278	20	5.745e-08	1.284e-08 (22.3%)	26.4%	Dresden 2.
14	Run 279	20	4.374e-08	1.834e-08 (41.9%)	44.2%	Dresden 2. Within error.
14	Run 280	20	3.082e-08	9.371e-09 (30.4%)	33.5%	Dresden 2. Within error.
14	Weighted average	20	4.0609e-08	7.000e-09 (17.2%)	22.3%	Dresden 2, both 3 runs.
14	Run 166	15	1.925e-09	4.994e-10 (25.9%)	29.5%	Dresden 5.
14	Run 170	15	5.344e-09	1.563e-09 (29.4%)	32.6%	Dresden 5.
14	Weighted average	15	2.2417e-09	4.7571e-10 (21.2%)	25.5%	Dresden 5, both runs.
14	Run 277	15	4.006e-08	4.379e-09 (10.9%)	17.9%	Dresden 2.
14	Run 216	13	3.4402e-09	2.788e-09 (81.0%)	82.2%	Dresden 5.
14	Run 220	11	1.824e-09	2.382e-10 (13.1%)	19.3%	Dresden 5.
15	Run 291	35	3.535e-09	2.447e-10 (6.9%)	15.7%	Dresden 2.
15	Run 185	30	3.562e-09	4.447e-10 (12.5%)	18.9%	Dresden 5.
15	Run 286	30	2.570e-08	1.978e-08 (76.9%)	78.2%	Dresden 2.
15	Run 287	30	2.064e-08	2.322e-09 (11.2%)	18.0%	Dresden 2. Within error.

Continued on next page

^{21}Ne	Run Number	Laboratory Angle(θ)	Laboratory ($d\sigma/d\Omega$) (b/sr)	Yield related $\Delta(d\sigma/d\Omega)$	Total $\Delta(\ d\sigma/d\Omega)$	Additional Comment
15	Run 288	30	1.578e-08	3.877e-09 (24.6%)	28.4%	Dresden 2. Within error.
15	Weighted average	30	1.9421e-08	2.000e-09 (10.3%)	17.5%	Dresden 2, both 3 runs.
15	Run 180	25	4.447e-09	4.452e-10 (10.0%)	17.3%	Dresden 5.
15	Run 282	25	8.701e-08	2.612e-09 (3.0%)	14.5%	Dresden 2.
15	Run 283	25	7.672e-08	1.332e-08 (17.4%)	22.4%	Dresden 2. Within error.
15	Run 284	25	6.549e-08	5.838e-09 (8.9%)	16.7%	Dresden 2. Within error.
15	Weighted average	25	8.3213e-08	3.3469e-09 (4.0%)	14.7%	Dresden 2, both 3 runs.
15	Run 175	20	2.403e-09	4.937e-10 (20.5%)	24.9%	Dresden 5.
15	Run 278	20	2.232e-07	3.726e-09 (1.7%)	14.2%	Dresden 2.
15	Run 279	20	1.854e-07	2.964e-09 (1.6%)	14.2%	Dresden 2.
15	Run 280	20	1.528e-07	2.486e-09 (1.6%)	14.2%	Dresden 2.
15	Weighted average	20	1.7806e-07	1.6960e-09 (1.0%)	14.2%	Dresden 2, both 3 runs.
15	Run 166	15	2.326e-08	1.806e-09 (7.8%)	16.2%	Dresden 5.
15	Run 170	15	3.149e-08	1.371e-09 (4.4%)	14.8%	Dresden 5.
15	Weighted average	15	2.8481e-08	1.0920e-09 (3.8%)	14.7%	Dresden 5, both runs.
15	Run 277	15	2.760e-07	2.265e-08 (8.2%)	16.3%	Dresden 2.
15	Run 216	13	2.024e-09	2.991e-10 (14.8%)	20.5%	Dresden 5.
15	Run 219	11	2.968e-09	6.753e-10 (22.8%)	26.8%	Dresden 5.
15	Run 220	11	8.123e-09	5.321e-10 (6.5%)	15.6%	Dresden 5.

Continued on next page

^{21}Ne	Run Number	Laboratory Angle(θ)	Laboratory ($d\sigma/d\Omega$) (b/sr)	Yield related $\Delta(d\sigma/d\Omega)$	Total $\Delta(\ d\sigma/d\Omega)$	Additional Comment
15	Weighted average	11	6.1485e-09	4.1795e-10 (6.8%)	15.7%	Dresden 5, both runs.
16	Run 291	35	4.877e-09	1.139e-09 (23.4%)	27.3%	Dresden 2.
16	Run 180	25	4.564e-09	1.257e-09 (27.5%)	30.9%	Dresden 5.
16	Run 282	25	4.656e-09	1.139e-09 (24.5%)	28.3%	Dresden 2.
16	Run 283	25	4.452e-09	1.003e-09 (22.5%)	26.6%	Dresden 2. Within error.
16	Run 284	25	4.436e-09	1.971e-09 (44.4%)	46.6%	Dresden 2. Within error.
16	Weighted average	25	4.5277e-09	7.0320e-10 (15.5%)	21.0%	Dresden 2, both 3 runs.
16	Run 175	20	9.995e-10	3.459e-10 (34.6%)	37.4%	Dresden 5.
16	Run 278	20	6.578e-09	1.118e-09 (16.9%)	22.0%	Dresden 2.
16	Run 279	20	6.394e-09	9.776e-10 (15.3%)	20.8%	Dresden 2. Within error.
16	Run 280	20	6.539e-09	7.743e-10 (11.8%)	18.4%	Dresden 2. Within error.
16	Weighted average	20	6.5047e-09	5.3343e-10 (8.2%)	16.3%	Dresden 2, both 3 runs.
16	Run 170	15	7.594e-10	2.663e-10 (35.0%)	37.7%	Dresden 5.
16	Run 220	11	1.066e-09	1.660e-10 (15.6%)	21.1%	Dresden 5.

Table C.1: *Differential cross section (d,p) data alongside run number and target used for each ^{21}Ne states. Relevant comment on each cross section at different angle was also added.*

Bibliography

[1] G. Wallerstein *et al.* Synthesis of the elements in stars: forty years of progress. *Reviews of Modern Physics*, 69(4), October 1997.

[2] C.Rolfs and W.S.Rodney. *Cauldrons in the cosmos.* University of Chicago Press, 1988.

[3] J.Jose and C.Iliadis. Nuclear astrophysics: The unfinished quest for the origin of the elements. *Rep. Prog. Phys.*, 74(096901), 2011.

[4] R.A. Alpher, H. Bethe, and G. Gamow. The origin of chemical elements. *Physical Review C*, 73(7), April 1948.

[5] Ralph A. Alpher and Robert Herman. *Genesis of the Big Bang.* Oxford University Press, 2001.

[6] F.Hoyle. The synthesis of the elements from hydrogen. *Monthly Notices of the Royal Astronomical Society*, 106(343), 1946.

[7] A.G.W.Cameron. *Essays in Nuclear Astrophysics.* Cambridge University Press, 1982.

[8] J.Audouze and S.Vauclair. *An introduction to Nuclear Astrophysics:The Formation and the Evolution of Matter in the Universe.* D. Reidel Pub Co, 1980.

[9] J.R.De Laeter. Abundances for p-process nucleosynthesis. *Physical Review C*, 77(045803), 2008.

[10] E.M.Burbidge *et al.* Synthesis of the elements in stars. *Reviews of Modern Physics*, 29(4):547–650, 1957.

[11] Kenneth S.Krane. *Introductory Nuclear Physics.* John Wiley & Sons, 1988.

[12] U. Frischknecht, R. Hirschi, and F.-K. Thielemann. Non-standard s-process in low metallicity massive rotating stars. *Astronomy & Astrophysics*, 538, 2012.

[13] I. Baraffe, M.F. El Eid, and N. Prantzos. The s-process in massive stars of variable composition.

[14] R. Hirschi *et al.* Nugrid: *s*-process in massive stars. *POS(NIC X)*, 083, 2008.

[15] M. Taggart *et al.* The first direct measurement of $^{17}O(\alpha,\gamma)^{21}Ne$ and its impact upon s-process abundances. *POS(NIC XI)*, 045, 2010.

[16] A.C.Phillips. *The Physics of Stars.* John Wiley & Sons, 1999.

[17] Late evolution of low- and intermediate-mass stars. `http://www.astro.uni-bonn.de/nlanger/siuweb/ssescript/new/chapter10.pdf` as accessed on the 22/08/2011.

[18] The role of stellar clusters in empirically determining stellar evolution. `http://zebu.uoregon.edu/2003/ph122/lec15.html` as accessed on the 25/07/2013.

[19] Christian Iliadis. *Nuclear Physics of Stars.* Wiley-VCH Verlag Gmbh & Co. KGaA, 2007.

[20] The evolution of binary-star systems. `http://astronomy.nju.edu.cn/~lixd/GA/AT4/AT420/HTML/AT42006.htm` as accessed on the 21/07/2014.

[21] A. G. Riess *et al.* Observational evidence from supernovae for an accelerating universe and a cosmological constant. *The Astronomical Journal*, 116(3), 1998.

[22] A. J. Aspden, J. B. Bell, S. Dong, and S. E. Woosley. Burning thermals in type Ia supernovae. *The astrophysysical journal*, 738:94, August 2011.

[23] Stars - low mass stellar evolution. `http://astronomyonline.org/Stars/LowMassEvolution.asp?Cate=Home&SubCate=OG04&SubCate2=OG0401` as accessed on the 25/07/2013.

[24] Erik Kuulkersa. The observers view of (very) long x-ray bursts: they are super! *The astrophysysical journal*, 0310402v1, October 2003.

[25] Hotter than expected neutron star surfaces help explain superburst frequency. `http://www.spacedaily.com/reports/Hotter_Than_Expected_Neutron_Star_`

Surfaces_Help_Explain_Superburst_Frequency_999.html as accessed on the 25/07/2013.

[26] X. Tang *et al.* Upper limit on the molecular resonance strengths in the reaction ^{12}C +^{12} C fusion. *J. Phys.: Conf. Ser*, 337, 2012.

[27] Caughlan and Fowler. *Atomic Data and Nuclear Data Tables*, 40:2, 283–334, 1998.

[28] P.Descouvemont. Microscopic three-cluster study of the 21-nucleon systems. *Phys.Rev.*, C48:2746, 1993.

[29] A. Best *et al.* Measurement of the reaction ^{17}O(α,n)^{20}Ne and its impact on the s-process in massive stars. *Phys. Rev. C*, 87:045805, 2013.

[30] Nuclear astrophysics compilation of reaction rates. http://pntpm3.ulb.ac.be/Nacre/nacre.htm as accessed on the 1/09/2013.

[31] A Best *et al.* First direct measurement of resonance strengths in ^{17}O(α,γ)21Ne. *Phys Rev. C*, 83(052802(R)), 2011.

[32] John S. Lilley. *Nuclear Physics: Principles and Applications.* John Wiley & Sons, Ltd, 2002.

[33] Massive stars as thermonuclear reactors and their explosions following core collapse. http://inspirehep.net/record/827392/plots as accessed on the 22/07/2014.

[34] Training in advanced low energy nuclear theory course 6: Theory for exploring nuclear reaction experiments. 1 - 19 July 2013, GANIL, Caen, France http://www.nucleartheory.net/Talent_6_Course/index3.htm as accessed on the 02/05/2014.

[35] SAMUEL S.M. WONG. *Introductory Nuclear Physics.* Wiley-VCH Verlag GmbH & Co. KGaA, 1999.

[36] P.E. Hodgson. *Nuclear Reactions and Nuclear Structure.* John Wiley & Sons, 1971.

[37] Physics of the interaction of charged particles with nuclei. A.F. Gurbich. Institute of Physics and Power Engineering Obninsk, Russian Federation users.ictp.it/~pub_off/lectures/lns022/Gurbich_1/Gurbich_1.pdf as accessed on the 30/05/2014.

[38] Optical model calculations with the code ECIS95. B.V.Carlson. Lectures given at the Workshop on Nuclear Data and Nuclear Reactors: Physics, Design and Safety. Trieste, 13th March- 14th April 2000 as accessed on the 2/06/2014.

[39] Ian J. Thompson and Filomena M.Nunes. *Nuclear Reactions for Astrophysics: Principles, Calculation and Applications of Low-Energy Reactions.* Cambridge University Press, 2009.

[40] W. Elsasser. *Journal de Physique et le Radium 5*, 625, 1934.

[41] Alan John Mitchell. *Investigating high-j single-particle energies in Z = 51 nuclei.* PhD thesis, University of Manchester, School of Physics and Astronomy, 2012.

[42] T. Sawaguri and W. Tobocman. *Journ. Math. Phys. 8*, page 2223, 1967.

[43] Norman K. Glendenning. *Direct Nuclear Reactions.* Academic Press, Inc. (London) LTD., 1983.

[44] P.D. Kunz, D.A. Lind, and W.E. Brittin. *Lectures in Theoretical Physics. Volume VIII-C - Nuclear Structure Physics.* The University of Colorado Press and Gordon and Breach, Science Publishers, 1965.

[45] R.C. Johnson and P. J. R. Soper. *Phys. Rev. C 1*, 976, 1970.

[46] N. K. Timofeyuk and R. C. Johnson. Nonlocality in deuteron stripping reactions. *Phys. Rev. Lett.*, 110:112501, Mar 2013.

[47] N. K. Timofeyuk and R. C. Johnson. Nonlocality in the adiabatic model of A(d,p)B reactions. *Phys. Rev. C*, 87:064610, Jun 2013.

[48] Matt Taggart. *The first direct measurement of the $^{17}O(\alpha,\gamma)^{21}Ne$ reaction and its impact on heavy element production.* PhD thesis, The University of York, Department of Physics, 2012.

[49] P. Descouvemont. Microscopic models for nuclear reaction rates. *Journal of Physics G*, 19:S141S152(21), 1993.

[50] A. Denker. *Drei Neutronenerzeugungsreaktion in Sternen.* PhD thesis, PhD thesis, Universität Stuttgart, 1994.

[51] J. DAuria *et al.* Astrophysics with a DRAGON at ISAC. *Nuclear Physics A*, 701:625631, 2003.

[52] D. Hutcheon *et al.* The DRAGON facility for Nuclear Astrophysics at TRIUMF ISAC: design, construction and operation. *Nuclear Instruments and Methods in Physics Research A*, 498:190210, 2003.

[53] P. Descouvemont. Microscopic models for nuclear reaction rates. *Journal of Physics G*, 19:S141S152, 1993.

[54] D C Bailey *et al. Journal of Physics A*, 4(908), 1971.

[55] C. Rolfs *et al. Nuclear Physics A*, 3(641664):189, 1972.

[56] A.Hoffmann *et al. Z.Phys. A.*, 332(289), 1989.

[57] G. Andritsopoulo *et al. Nuclear physics A*, 372(1-2):281–300, 1981.

[58] J.C Lawson and P.R.Chagnon. *Phys. Rev. C*, 11(643-647), 1975.

[59] S Hinds and R Middleton. *Proc. Phys. Soc.*, 74(779), 1959.

[60] J.N. Hallock *et al. Nuclear Physics A*, 252(1):141–151, 1975.

[61] S Thummerer *et al. Journal of Physique G: Nucl. Part*, 29(3):509, 2003.

[62] M. A. Thaler *et al. Phys. Rev. C*, 69(3):035210, 2004.

[63] F.Hinterberger *et al. Nuclear Physics A*, 423(2):200–220, 1984.

[64] S.F.Mughabghab, M.Divadeenam, and N.E.Holden. *Academic Press, New York*, 1981.

[65] B.Chambon *et al.* Study of 5.69 and 5.78 MeV states in ^{21}Ne through the ^{20}Ne(d,p)^{21}Ne reaction. *Physical Review C*, 9(1), 1974.

[66] A.J.Howard *et al.* Studies on ^{21}Ne and ^{23}Na via the ^{20}Ne(d,p)^{21}Ne and ^{22}Ne(d,p)^{23}Nereactions. *Nuclear Physics A*, 152:317–336, 1970.

[67] M. Lambert *et al.* ^{20}Ne(d,p)^{21}Ne et etats excités. *Nuclear Physics A*, 112:161–184, 1968.

[68] National nuclear data center. `http://www.nndc.bnl.gov/ensdf` as accessed on the 09/01/2014.

[69] D.W.Heikkinen and R.E.Pixley. (d, p) reaction on ^{20}Ne. *Phys. Rev. C*, 3(4), 1971.

[70] L. Vegh and A. Valek. Investigation of the ^{20}Ne(d,p_0)^{21}Ne reaction at E$_d$=0.500-0.662 MeV. *J.Phqs. G : Nucl. Pliys.*, 4(4), 1978.

[71] Maier-leibnitz laboratorium homepage. http://www.bl.physik.uni-muenchen.de/ as accessed on the 12/06/2013.

[72] M.Weber and C.Herlitzius. Graduate laboratory notes experiment nr 52: Heavy ion scattering at the tandem accelerator, April 2010.

[73] R.Gernhauser and T.Christ. Graduate laboratory notes experiment nr 52: Heavy ion scattering at the tandem accelerator, November 2003.

[74] Encyclopedia britannica. http://www.britannica.com/ as accessed on the 23/07/2014.

[75] L.Rohrer and tandem staff. Status report of the munich tandem accelerator. *American Institute of Physics Conference Proceedings*, 473(1), 1999.

[76] J.Ott *et al.* A position sensitive cathode strip detector with single strip readout. *Nuclear Instruments and Methods in Physics Research A*, 367(280-28), 1995.

[77] Stephan Paul. Physik department e18: Q3D magnetic spectrograph, 2009.

[78] M.Loffler *et al.* The ion optical properties of the munich Q3D-spectrograph investigated by means of a special experimental ray tracing method. *Nuclear Instruments and Methods III*, 1-12, 1973.

[79] Harald A. Enge. Magnetic spectrograph for nuclear reaction studies. *Nuclear Instruments and Methods III*, 162(161-180), 1979.

[80] H.-F.Wirth *et al.* A position sensitive cathode strip detector with single-strip readout for the munich Q3D magnetic spectrograph. Preprint submitted to Elsevier, April 2008.

[81] nukesim-classes: Java Classes for Nuclear Physics Simulation. http://nukesim-classes.sourceforge.net/software_index.html as accessed on the 13/05/2014.

[82] J. A. Tostevin, University of Surrey version of the code TWOFNR (of M. Toyama, M. Igarashi and N.Kishida) and code FRONT (private communication). http://www.nucleartheory.net/NPG/code.htm as accessed on the 22/05/2014.

[83] F. D. Becchetti Jr and G. W. Greenlees. Nucleon-Nucleus Optical-Model Parameters, A$>$ 40, E$<$ 50 MeV. *Phys. Rev. 182*, 1190, June 1969.

[84] Brookhaven national laboratory. National Nuclear Data Center `http://http://www.nndc.bnl.gov/ensdf` as accessed on the 04/03/2014.

[85] Anuj Parikh. Private Communications.

[86] Christian A. Diget. Private Communications.

[87] Thomas Faestermann. Private Communications.

[88] S. Seuthe *et al.* Production and properties of implanted targets. *Nuclear Instruments and Methods in Physics Research Section A: Accelerators, Spectrometers, Detectors and Associated Equipment*, 260(1):33 – 42, 1987.

[89] T.A.D. Brown, K. Deryckx, A. Garca, A.L. Sallaska, K.A. Snover, D.W. Storm, and C. Wrede. Properties of ^{23}Na implanted targets. *Nuclear Instruments and Methods in Physics Research Section B: Beam Interactions with Materials and Atoms*, 267(19):3302 – 3308, 2009.

[90] C. Wrede, K. Deryckx, B.M. Freeman, A. Garca, G.C. Harper, A.S.C. Palmer, D.A. Short, and D.I. Will. Preparation of ^{20}Ne, ^{24}Mg, ^{28}Si, ^{32}S, and ^{36}Ar targets by ion implantation into thin carbon foils. *Nuclear Instruments and Methods in Physics Research Section B: Beam Interactions with Materials and Atoms*, 268(23):3482 – 3484, 2010.

[91] W.H. Geist, Z. Ayer, A.C. Hird, E.J. Ludwig, M. Wood, and K.A. Fletcher. Ion implanted ^{3}He targets for very low energy experiments. *Nuclear Instruments and Methods in Physics Research Section B: Beam Interactions with Materials and Atoms*, 111(12):176 – 180, 1996.

[92] H.Y. Lee, J. Grres, H.-W. Becker, E. Stech, E. Strandberg, and M. Wiescher. Production and characterization of oxygen-reduced implanted ^{21}Ne targets. *Nuclear Instruments and Methods in Physics Research Section B: Beam Interactions with Materials and Atoms*, 267(2122):3539 – 3544, 2009.

[93] L. Barrn-Palos, E.F. Aguilera b, J. Aspiazu b, A. Huertaa, E. Martnez-Quiroz b, R. Monroy a, E. Morenob, G. Murillo b, M.E. Ortiz a, R. Policroniades b, A. Varelab, and E. Chveza. Absolute cross sections measurement for the ^{12}C + ^{12}C system at astrophysically relevant energies. *Nuclear Physics A*, 779:318332, 2006. available online at www.ScienceDirect.com.

[94] Michael G. Mazarakis and William E. Stephens. Experimental measurements of the ^{12}C $+^{12}$ C nuclear reactions at low energies. *Physical Review C*, 7, April 1973.

[95] T. M. Cormier *et al.* Gamma rays from ^{23}Na states excited in the $^{12}\mathrm{C}\left(^{12}\mathrm{C},p\right)$ reaction at E = 38.6 MeV. *Nuclear Physics A*, 247:377–381, 1975.

[96] T. Spillane *et al.* Recent results on the ^{12}C $+^{12}$ C reactions. *AIP Conf. Proc.*, 1012,:144–149, May 2008.

[97] T. Spillane *et al.* ^{12}C+^{12}C fusion reactions near the Gamow Energy. *Phyical Review Letters*, 98:122501, May 2007.

[98] M. D. High and B. H. Ujec. The ^{12}C+^{12}C sub-coulomb fusion cross section. *Nuclear Physics A*, 282:181–188, 1977.

[99] Clare Madeleine Tunstall. Cross section measurements for the ^{12}C $+^{12}$ C fusion reaction at low energies. Master's thesis, University of York, 2008.

[100] H.W.Becker, K.U.Kettner, C.Rolfs, and H.P.Trautvetter. The ^{12}C $+^{12}$ C reaction at sub-coulomb energies. *Z.Phys.*, A303, 1981.

[101] E. F. Aguilera *et al.* New Gamma-ray measurements for ^{12}C $+^{12}$ C sub-coulomb fusion: Toward data unification. *Physical Review C*, 73:064601, June 2006.

[102] K. Jayamanna. Off line ion source terminal. *Springer Science+Business Media Dordrecht*, DOI 10.1007/s10751-013-0881-y, 2013.

[103] Resonant Elastic Scattering Studies at TUDA and Exploding Stars in the Lab! Nuclear Astrophysics with TUDA and DRAGON. `http://tuda.triumf.ca` as accessed on the 18/07/2014.

[104] Charged-particle exit channels from the ^{12}C $+^{12}$ C fusion reaction at astrophysical energies. `http://tuda.triumf.ca` as accessed on the 18/07/2014.

[105] Alison Laird For the TUDA collaboration. Nuclear Astrophysics at TRIUMF with the TUDA facility. `https://indico.cern.ch/event/328/material/slides` as accessed on the 18/07/2014.

[106] 2011 catalogue micron semiconductor limited. `www.micronsemiconductor.co.uk` as accessed on the 06/06/2014.

[107] James Brown. Private Communications.

[108] James F. Ziegler SRIM AND TRIM: particle interactions with matter. http://www.srim.org/ as accessed on the 23/07/2014.

[109] Kinematics II: A Nonrelativistic Kinematics FORTRAN program to aid analysis of nuclear reaction angular distribution data. By J. B. Ball, Oak Ridge National Laboratory, www.ornl.gov/info/reports/1962/3445605484295.pdf as accessed on the 02/05/2014.